Experimental Investigation of Nucleate Boiling on Microstructured and Smooth Surfaces

Dissertation

Matthias Zimmermann

TECHNISCHE
UNIVERSITÄT
DARMSTADT

Experimentelle Untersuchung des Blasensiedens auf mikrostrukturierten und glatten Oberflächen

Experimental Investigation of Nucleate Boiling on Microstructured and Smooth Surfaces

Doctoral thesis
by Matthias Zimmermann

submitted in fulfillment of the requirements for the
degree of Doktor-Ingenieur
(Dr.-Ing.)

at the Department of Mechanical Engineering
of the Technische Universität Darmstadt

First Examiner: Prof. Dr.-Ing. Peter Stephan
Second Examiner: Dr.-Ing. Lena Schnabel

Darmstadt 2022

Matthias Zimmermann:
Experimental Investigation of Nucleate Boiling on Microstructured and Smooth Surfaces

Darmstadt, Technische Universität Darmstadt

Date of oral exam: February 22, 2022
Thesis published online on TUprints in 2022

Please cite this thesis as:
URN: urn:nbn:de:tuda-tuprints-196738
URI: https://tuprints.ulb.tu-darmstadt.de/id/eprint/19673

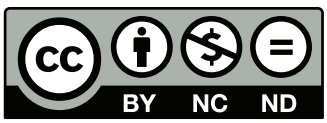

Danksagung

Diese Dissertationsschrift entstand während meiner Anstellung als Wissenschaftlicher Mitarbeiter am Institut für Technische Thermodynamik der Technischen Universität Darmstadt. Bei Herrn Prof. Dr.-Ing. Peter Stephan möchte ich mich herzlich für die Möglichkeit bedanken, die Promotion an seinem Institut durchzuführen. Ich bedanke mich zudem für die exzellente Betreuung und die interessanten wissenschaftlichen Diskussionen. Bei Frau Dr.-Ing. Lena Schnabel möchte ich mich für die Übernahme des Korreferats bedanken. Meinem Gruppenleiter Herrn Dr.-Ing. Axel Sielaff danke ich für die gute Zusammenarbeit, die konstruktiven Diskussionen und hilfreichen Anregungen.

Ich möchte mich außerdem bei allen Kolleginnen und Kollegen des Instituts für die gute Zusammenarbeit und den freundlichen Umgang bedanken. Für die produktive Arbeitsatmosphäre bedanke ich mich besonders bei meinen Bürokollegen Thomas Antritter und Dr.-Ing. Achim Bender, die mich bei vielen numerischen Problemen unterstützt und beraten haben. Zudem möchte ich mich bei Dr.-Ing. Niklas Preußer und Dr.-Ing. Timm Winterling für ihr offenes Ohr und die zahlreichen hilfreichen Ratschläge bedanken. Für die Durchsicht meiner Dissertation danke ich Michael Heinz, Johannes Kind, Kai Schweikert und Christian Wolf.

Ich möchte mich bei allen Beteiligten des Sonderforschungsbereichs 1194 für die gute Zusammenarbeit, die hilfreichen Impulse und erfolgreichen Kooperationen herzlich bedanken, insbesondere bei Alena Bell, Dr. Beatrice Fickel, Dr.-Ing. Maximilian Hartmann, Adnan Khalil und Dr. Benjamin Kresse. Ich bedanke mich ebenfalls bei der Deutschen Forschungsgemeinschaft für die Förderung meines Projekts C02 im Rahmen des Sonderforschungsbereichs 1194.

Neben dem wissenschaftlichen Personal gilt mein besonderer Dank dem Team der Werkstatt unter Herrn Roland Berntheisel und Herrn Robert Schrod. Ebenso möchte ich mich bei Frau Gaby Gunkel, Frau Heike Kagerbauer und Frau Monika Medina España für die Unterstützung bei den administrativen Aufgaben bedanken. Beim Team von Herrn Marcus Keiner bedanke ich mich für die schnelle Hilfe und Unterstützung bei IT-Problemen.

Zusätzlich möchte ich mich bei allen Studierenden bedanken, die mich während meiner Promotion unterstützt haben. Mein Dank gilt Leonard Edens und Tilman Frölich für ihre Unterstützung beim Aufbau meines Versuchsstandes, Simon Schwörer für das Aufsetzen des Steuerungsprogramms und Adrian Reuter für das Durchführen zahlloser Versuchsreihen. Mein besonderer Dank gilt allen Bachelor- und Masterarbeiter/innen, die im Rahmen ihrer Arbeiten, meine Promotion entscheidend vorangebracht haben: Marie-Theres Flietel, David Dexheimer, Paul Heckelmann, Julian Reitzel, Dominik Neumann, Felix Pfliegensdörfer, Felix Neubeck, Philipp Kaufmann und Irina Zhelezova.

Außerdem möchte ich mich bei Herrn Florian Weißenborn für die Fertigung der mikrostrukturierten Oberflächen bedanken. Ohne seinen Einsatz und die Bereitschaft, für eine Kleinstserie die Produktion anzupassen, wäre es zu deutlichen Verzögerungen meiner Dissertation gekommen. Bei Dorota Borovsky und Dr. Ashleigh McIntyre bedanke ich mich für die sprachliche Korrektur meiner Arbeit.

Mein größter Dank gilt jedoch meinen Eltern und meinem Bruder.

Darmstadt, den 19.11.2021

Matthias Zimmermann

Abstract

In the last decade, the focus of boiling research has shifted towards micro- and nanostructures. Both structures improve the boiling process significantly compared to smooth surfaces. The interactions between fluid and surface, however, are very complex and not well understood. This impedes the development of universally applicable correlations that incorporate the influence of those complex structures, which would enable the construction of more efficient evaporators.

In this thesis, a new experimental setup is constructed to enable boiling experiments at a large pressure, temperature, and heat flux range. FC-72, a refrigerant, and ethanol are chosen as boiling fluids. The boiling process is analyzed on various length scales using two different heater modules. A copper heater module is used to determine mean heat transfer coefficients and critical heat fluxes. An infrared transparent heater module is utilized to examine local heat transfer phenomena beneath growing bubbles. Two copper microneedle surfaces with a needle diameter of 1 µm and different lengths of 10 and 20 µm are manufactured and characterized according to their roughness, their wetting, and wicking behavior. Two uncoated copper surfaces with different roughness are produced for comparison.

The experimental data of the uncoated surfaces obtained with the new setup is validated by comparing the data to correlations and data published by other researchers. The two microstructured surfaces increase the heat transfer coefficients by a maximum factor of 2.8 compared to the smoother uncoated surface. The critical heat fluxes obtained for the microstructured surfaces, on the other hand, are reduced. Possible reasons are identified and analyzed, narrowing down the causes. This enabled the construction of an optimized, hierarchical surface, which shows higher critical heat fluxes than the uncoated surfaces.

An increase in the heat transfer coefficient occurs at small system pressures, when using a smooth surface and ethanol as boiling fluid compared to FC-72. This is likely due to the formation of an evaporating microlayer, while the measurements using FC-72 show mostly contact line evaporation. These experiments also successfully verify the applicability of correlations distinguishing contact line and microlayer evaporation that were developed using generic non-isothermal dewetting experiments [127].

Zusammenfassung

Mikro- und Nanostrukturen werden seit einigen Jahren verstärkt in der Siedeforschung untersucht. Dabei hat sich gezeigt, dass Mikro- und Nanostrukturen den Siedeprozess deutlich verbessern können im Vergleich mit einer glatten Oberfläche. Die Wechselwirkungen zwischen dem Fluid und diesen Oberflächen sind jedoch sehr komplex und noch wenig verstanden. Dies erschwert die Entwicklung universell einsetzbarer Korrelationen, die den Einfluss von Mikro- und Nanostrukturen berücksichtigen und zur Auslegung effektiverer Verdampfer genutzt werden können.

Im Rahmen dieser Dissertation wird ein neuer Versuchsaufbau konstruiert, mit dem Siedeexperimente in einem großen Druck-, Temperatur- und Wärmestromdichtenbereich möglich sind. Als Versuchsfluide werden Ethanol und das Kältemittel FC-72 eingesetzt. Unterschiedliche Heizeraufbauten ermöglichen die Untersuchung des Blasensiedens auf verschiedenen Längenskalen. Mit Hilfe eines Kupferheizers können die kritische Wärmestromdichte und der mittlere Wärmeübergangskoeffizient bestimmt werden. Ein infrarot transparenter Heizer ermöglicht die Untersuchung der lokalen, unter einer wachsenden Blase auftretenden Wärmetransportvorgänge. Zwei mikrostrukturierte Oberflächen werden gefertigt, die aus Kupfernadeln mit identischen Durchmessern von 1 µm und unterschiedlichen Längen von 10 and 20 µm bestehen. Die Oberflächen werden anhand ihrer Rauheit, ihres Benetzungs- und ihres Imbibitionsverhaltens charakterisiert, da die daraus gewonnenen Parameter zur Interpretation des Siedeverhaltens wichtig sind. Als Vergleichsoberflächen dienen zusätzlich zwei unbeschichtete Kupferoberflächen mit unterschiedlichen Rauheiten.

Die in dem neuen Versuchsaufbau gemessenen Ergebnisse der unbeschichteten Kupferoberflächen können durch einen Vergleich mit den Ergebnissen anderer Forscher und mit Blasensiedekorrelationen validiert werden. Die beiden mikrostrukturierten Oberflächen können den Wärmeübergangskoeffizienten um den Faktor 2,8 im Vergleich mit der glatteren unbeschichteten Oberfläche verbessern. Die kritischen Wärmestromdichten der mikrostrukturierten Oberflächen sind hingegen kleiner als die Werte auf den unbeschichteten Oberflächen. Die dafür verantwortlichen Phänomene werden analysiert und diskutiert. Anhand dieser Überlegungen wird eine optimierte hierarchische Oberfläche gefertigt, deren kritische Wärmestromdichten größer sind als die der unbeschichteten Oberflächen.

Beim Vergleich der beiden Versuchsfluide kann eine Verbesserung des Wärmeübergangskoeffizienten bei niedrigen Systemdrücken mit Ethanol festgestellt werden. Dies könnte auf die Bildung eines effektiv verdampfenden Dünnfilms zurückzuführen sein. Die Messungen mit FC-72 zeigen hingegen hauptsächlich Kontaktlinienverdampfung. Darüber hinaus ist es möglich, die Anwendbarkeit fluidspezifischer Korrelationen zur Dünnfilm- und Kontaktlinienverdampfung [127] auf das Blasensieden zu verifizieren.

Contents

Nomenclature

Latin Symbols

Symbol	Description	Unit
A	area	m^2
a, b, n	exponents	-
B, C, D	calibration coefficients	
c_p	specific heat capacity	$J\,kg^{-1}\,K^{-1}$
C_{sf}	constant in the Rohsenow correlation [124]	-
d	diameter	m
F_p, F_q, F_w	factors in the Gorenflo correlation [140]	-
g	gravitational acceleration	$m\,s^{-2}$
Δh_v	specific enthalpy of vaporization	$J\,kg^{-1}$
I	electric current	A
K, L	constants	-
l	length	m
l_c	characteristic length	m
$\dot{M}$	mass flow	$kg\,s^{-1}$
n	number of entities	-
p	pressure	Pa
P	center-to-center distance between smooth copper strips	m
$\dot{q}$	heat flux	$W\,m^{-2}$
$\dot{Q}$	heat flow	W
r	roughness factor according to Wenzel [156]	-
R	radius	m
$\overline{R}$	specific gas constant	$J\,kg^{-1}\,K^{-1}$
Ra	arithmetical mean roughness	m
s	distance	m
Sa	arithmetical mean area roughness	m
Sm	mean spacing of the surface roughness	m

Sp	maximum peak height above the mean level	m
Spd	mean peak density of the surface	m
Sv	maximum valley depth below the mean level	m
t	time	s
T	temperature	K
u	velocity	$m\,s^{-1}$
U	voltage	V
$\dot{V}$	volume flow	$m^3\,s^{-1}$
x, y, z	coordinate	m

Greek Symbols

Symbol	Description	Unit
α	heat transfer coefficient	$W\,m^{-2}\,K^{-1}$
γ	microlayer thickness	m
δ	inclination of the boiling surface	deg
Δ	difference	-
η	dynamic viscosity	Pa s
Θ	contact angle	deg
λ	thermal conductivity	$W\,m^{-1}\,K^{-1}$
Λ_{RT}	Rayleigh-Taylor wavelength	m
Λ_{H}	Helmholtz wavelength	m
ρ	density	$kg\,m^{-3}$
σ	surface tension	$N\,m^{-1}$
φ	resistance density	$Ohm\,m^{-2}$
Ψ	intensity	-

Subscripts

Symbol	Description
0	reference state
01,02,03	thermometer position

10cu	short microstructured surface
20cu	long microstructured surface
al	algorithm
b	bubble
c	critical
cav	cavity
CHF	critical heat flux
cl	contact line
cond	condensation
cont	contrast
conv	convection
Cr	chromium
Cu	copper
el	electricity
EtOH	ethanol
evap	evaporation
exp	expansion
FC-72	perfluorohexane
G	Gaussian distribution
high	high parameter range
K	Kandlikar
l	liquid
lc	local
le	lens
low	low parameter range
max	maximum
m	mean value
mc	microconvection
ml	microlayer
nc	natural convection
nd	needle
nucl	nucleation
num	numerically calculated value

Opt	optimized, hierarchical surface
PEEK	polyether ether ketone
pm	pixel to millimeter conversion
poly	polynomial
R	rectangular distribution
ran	random
rec	receding
rg	rough
s	solid
sat	saturation
Scu	smooth copper surface
sed	sediments
sl	superheated layer
sm	smooth
so	silicone oil
sup	superheat
sys	system
T	Theofanous
tc	transient conduction
Tcu	technical copper surface
therm	thermometer
v	vapor
vc	vapor convection
w	wall
Y	Yagov
Z	Zuber

Abbreviations

Symbol	Description
10cu	short microstructured surface
20cu	long microstructured surface
Au	gold

b&w	black and white
CAD	computer-aided design
CaF_2	calcium fluoride
CHF	critical heat flux
Cr	chromium
CrN	chromium nitride
Cu	copper
Cu-OFE	oxygen-free, pure copper
EtOH	ethanol
In	indium
ir	infrared
Opt	optimized, hierarchical surface
PEEK	polyether ether ketone
Scr	smooth chromium surface
Scu	smooth copper surface
SiO_2	silicon dioxide
Tcu	technical copper surface
UV	ultraviolet

Non-dimensional parameters

Symbol	Description	Unit
Ca	capillary number	$\eta_\mathrm{l} u_\mathrm{b}/\sigma$
Ja	Jakob number	$c_{p,\mathrm{l}} \Delta T_\mathrm{sup}/\Delta h_\nu$
Nu	Nusselt number	$\alpha_\mathrm{l} l_c/\lambda_\mathrm{l}$
Pr	Prandtl number	$\eta_\mathrm{l} c_{p,\mathrm{l}}/\lambda_\mathrm{l}$
p_r	reduced pressure	$p_\mathrm{sys}/p_\mathrm{c}$
Re	Reynolds number	$u\rho_\mathrm{l} l_c/\eta_\mathrm{l}$

CHAPTER 1

Introduction

Most of us come into contact with nucleate boiling on a daily basis. It is a commonly observed physical phenomenon easily created with a fluid, a container and a heat source; nonetheless, it is still not fully understood. Boiling research was started in the early 1900s by Nukiyama, Jakob and Linke, and others. In the 1940s and 50s the first empirical and semi-empirical correlations for nucleate boiling were developed, enabling the dimensioning of boiling vessels. Since then, several important parameters were identified and incorporated in state of the art correlations. However, large deviations between calculated and actual boiling performance are still common to this day. This is mostly because important interactions between wall and fluid are not fully understood and an analytical description of the boiling phenomena is still missing.

In recent years, new applications for nucleate boiling, like the cooling of microelectronics, require the transfer of high heat fluxes at low wall temperatures. Thus, the focus of boiling research shifted towards microstructures, nanostructures, and nanofluids. While enabling the transfer of significantly higher heat fluxes compared to smooth surfaces, the interactions between those structured surfaces and fluids are very complex. This results in large deviations between the correlations for micro and nanostructured surfaces and experimental data. Thus, understanding the interactions between structured surfaces and liquids and their influence on nucleate boiling is important. The surface structure, the wettability of the fluid-surface combination, as well as the wickability of the fluid into the surface have to be determined, as they have a huge impact on boiling behavior. Their characterization is vital for the understanding and interpretation of the latter. In addition to measuring heat transfer coefficients and critical heat fluxes, bubble diameters, bubble frequencies and nucleation site densities should be investigated. Together with the dynamics of the three-phase contact line, these parameters provide important information for the understanding of the nucleate boiling process on micro and nanostructures. In conclusion, multiscale and multiphenomena investigations are necessary to analyze the influence of micro and nanostructured surfaces on nucleate boiling.

This thesis investigates the influence of microstructured and hierarchically structured surfaces on nucleate boiling. The bubble diameters and evaporation regimes in the region of the three-phase contact line are analyzed, alongside the measurement of heat transfer coefficients and critical heat fluxes. Additional measurements are performed to characterize the roughness, the wettability, and the wickability of the fluid-surface combinations, all of which act in combination with the observed bubble dynamics as the basis for the interpretation of the observed boiling behavior.

The thesis is structured into the following chapters:

- **Chapter 1: Introduction**
  A short introduction on the topic of nucleate boiling is provided and the motivation for this thesis is exemplified.

- **Chapter 2: Fundamentals and State of the Art**
  Important influencing factors of nucleate boiling are presented in the context of the fundamentals of the research field. Models describing the boiling process and the critical heat flux, as well as the corresponding correlations are shown. Additionally, the influence of micropillars, nanowires, and hierarchical structures on the boiling process are depicted, leading to the positing of the three scientific questions governing this thesis.

- **Chapter 3: Experimental Methods**
  This chapter presents the experimental setup and the boiling surfaces. These are characterized regarding their roughness, wettability, and wickability in combination with the boiling fluids used in this thesis.

- **Chapter 4: Data Evaluation**
  This chapter shows the data evaluation and the corresponding uncertainties.

- **Chapter 5: Experimental Results and Discussion**
  Firstly, this chapter presents the results using two uncoated copper surfaces. This provides a comparison for the microstructured surfaces. Afterwards, the results of a hierarchical structure are presented, which was manufactured based on the findings of the microstructured surfaces. Finally, the influence of the boiling fluid is examined on two different length scales.

- **Chapter 6: Summary, Conclusion, and Outlook**
  The concluding chapter provides a summary of the thesis and an outlook concerning future investigations.

CHAPTER 2

Fundamentals and State of the Art

In this chapter, an overview on the state of the art of nucleate boiling research is provided, as well as a short summary of the necessary fundamentals. After a presentation of the fundamentals of nucleate boiling and bubble nucleation, the chapter continues with a focus on influencing parameters. Afterwards, commonly used correlations are discussed, before focusing on the influence of micro and nanostructures on nucleate boiling. The chapter is concluded with a summary and the postulation of the scientific questions that drive this thesis.

2.1 Fundamentals of pool boiling

This section provides a short overview on the fundamentals of pool boiling. A more detailed description and explanation can be found in [6, 16, 140].

2.1.1 Boiling curve

The term boiling describes the phase change of a liquid into vapor if the vapor pressure of the liquid is equal to the system pressure. This phenomenon, as described in the introduction, is often used as a method of heat transfer. Similar to convective heat transfer and based on Fourier's law, the transferred heat flux can be calculated with a temperature difference, which is shown in Equation 2.1:

$$\dot{q} = \alpha \left(T_{\mathrm{w}} - T_{\mathrm{sat}} \right). \tag{2.1}$$

α is the heat transfer coefficient and the main parameter judging the efficiency of the boiling process. In pool boiling, where heat is typically transferred from a solid wall into a fluid, the temperature difference, the so-called "wall superheat", consists of the wall temperature T_{w} and the saturation temperature of the fluid T_{sat}. For pool boiling experiments, the relation between heat flux and wall superheat is typically

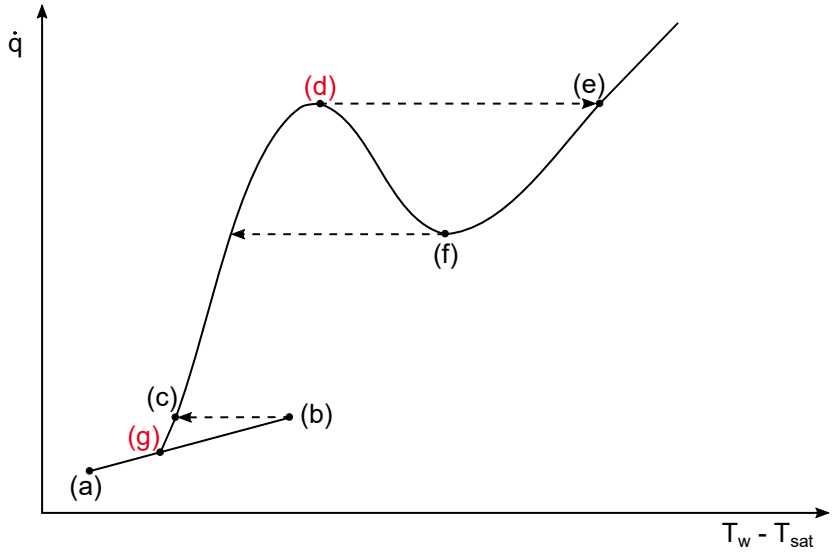

Figure 2.1: Sketch of a boiling curve: Point (a) is still in the natural convection regime until the onset of nucleate boiling is reached at (b). Between (c)/(g) and (d) is the nucleate boiling regime, which ends at the critical heat flux, point (d). There, a transition into the film boiling regime occurs, (e), for constant heat flux. For decreasing heat fluxes, the surface will stay in the film boiling regime until point (f) is reached, the Leidenfrost point, before jumping back into the nucleate boiling regime.

displayed in the boiling curve (Figure 2.1), which was first published by Nukiyama [109] and is named after him. At low heat fluxes (a-b), heat is solely transferred by natural convection without phase change. The heat transfer coefficient is significantly lower in this regime, which is seen by the smaller gradient of the boiling curve. For rising heat flux at point (b), which is the onset of nucleate boiling, the first bubbles nucleate, which leads to a jump in the wall superheat to point (c) for a constant heat flux because the heat transfer coefficients are significantly larger in the nucleate boiling regime. A further increase in heat flux results in an increase in the nucleation site density, bubble size, frequency, and the once isolated bubbles start to coalesce, creating so-called "slugs and columns". A further increase in heat flux eventually leads to burnout at the critical heat flux (d). At this heat flux, a part of the surface is irreversibly covered by a vapor film. This film instantaneously spreads over the entire surface for a constant heat flux and the wall superheat jumps to point (e) into the stable film boiling regime as the heat transfer coefficient is significantly reduced due to the blanketing vapor film. When the heat flux is reduced again, the system does not jump back from point (e) to (d), but stays in the film boiling regime until point (f), the Leidenfrost point, is reached. Then, the vapor film breaks up and the wall superheat jumps back into the nucleate boiling regime. The region between point (d) and (f), the transition boiling regime, cannot be reached with a heat flux controlled heater, such as that used in this thesis. The letters in red (d-g) show the section of the boiling curve that is covered by the experiments in this thesis. Most of the experiments are performed for decreasing heat fluxes, which extends the nucleate boiling regime from point (c) until point (g) as once activated nucleation sites stay active until lower heat fluxes. The hysteresis (g-b-c) is caused by the difference in the superheat necessary to activate and sustain a nucleation site. This circumstance is discussed in the following section.

2.1.2 Nucleation

Heterogeneous nucleation is the observed and studied nucleation mode in boiling research. The necessary superheats for homogeneous nucleation are only reached using very smooth, glassy walls. In heterogeneous nucleation, the bubbles nucleate in so-called "nucleation sites", which are scratches and cavities in the surface. Depending on the wetting behavior of the fluid-surface combination and the percentage of dissolved gases inside the liquid, those cavities have likely entrapped vapor or gas embryos. Those embryos start growing, if the necessary superheat is reached. This superheat depends on the thermodynamics of curved interfaces, the wetting behavior, and the geometry of the cavity. According to thermodynamics, a vapor bubble with the radius R_b needs the following minimal superheat compared to the saturation temperature T_sat to exist [16]:

$$\Delta T_\mathrm{sup} = \frac{2\sigma T_\mathrm{sat}\left(\frac{1}{\rho_\mathrm{v}} - \frac{1}{\rho_\mathrm{l}}\right)}{\Delta h_\upsilon R_\mathrm{b}}. \tag{2.2}$$

In Equation 2.2 σ is the surface tension at the liquid-vapor interface, ρ_v and ρ_l are the densities of vapor and liquid, respectively, and Δh_υ is the specific enthalpy of vaporization. In case of a deep, narrow cavity and average wettability of the surface, the cavity mouth radius R_cav is equal to the bubble radius R_b according to Lorenz [94]. The wall superheat necessary to keep a cavity with a mouth radius of R_cav active is calculated by:

$$\Delta T_\mathrm{w,sup} = \frac{2\sigma T_\mathrm{sat}\left(\frac{1}{\rho_\mathrm{v}} - \frac{1}{\rho_\mathrm{l}}\right)}{\Delta h_\upsilon R_\mathrm{cav}}. \tag{2.3}$$

However, for perfectly wetting or degassed fluids, which are often used in pool boiling research, most cavities will not have gas embryos. To activate those cavities, higher wall superheats are necessary, compared to an already active cavity. There, a vapor embryo remains inside the cavity after the previous bubble departed, which will start to grow forming the next bubble. This explains the difference in the superheat needed to activate a nucleation site and to keep it active.

2.1.3 Bubble departure diameters and frequencies

Once the necessary superheat is reached, the vapor embryo will start to grow and the new formed bubble will spread upon the surface until adhesion forces are smaller than repulsion forces. Then, the contact line will advance until the bubble finally departures. Thus, the diameter of departing bubbles is dependent on adhesion and repulsion forces. Good examples showing this relation, are the bubble sizes at different gravitational levels captured during parabolic flight, as shown in Figure 2.2. It is obvious that the bubble diameters are much larger under reduced gravity since gravity has a huge impact on buoyancy, one of the repulsion forces. Buoyancy and surface tension forces were considered by Fritz to establish his famous correlation [37][1]. Several other researchers have proposed correlations, considering different

[1] The final correlation is not displayed in this publication, but it is possible to deviate it from Abb.4 in [37]

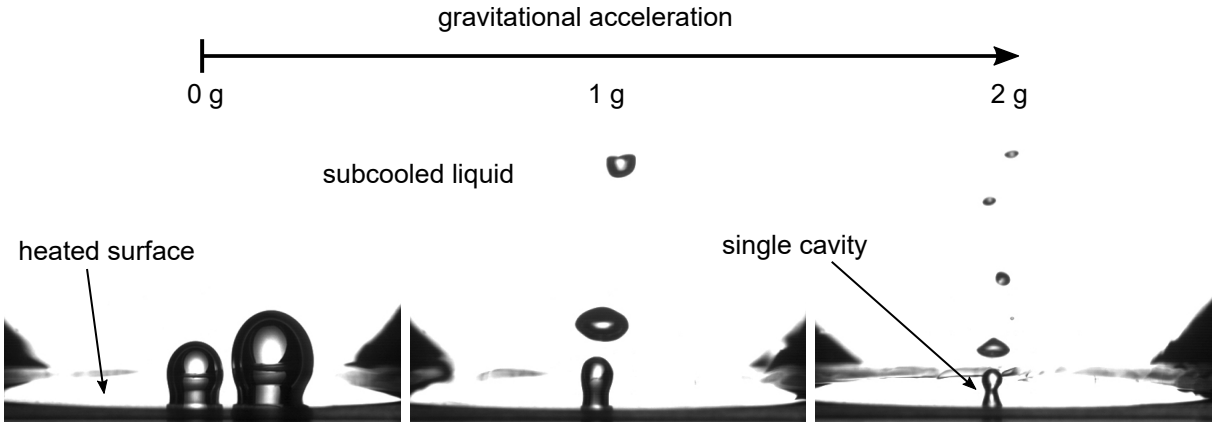

Figure 2.2: Images of nucleating bubbles at different gravitational acceleration levels obtained during the 70th ESA parabolic flight campaign [2].

forces into their force balance. A thorough overview of their approaches is provided by Carey [16]. In recent years, the complexity of the models increased, incorporating additional forces and phenomena into the equations [5, 24, 29, 165].

The bubble departure frequency is affected by the bubble departure diameter, the bubble growth rate, and waiting time, which is the time period between departure of a bubble and the nucleation of a subsequent bubble. Since even more parameters influence bubble frequency compared to diameter, developing a model that predicts bubble frequencies accurately is much more difficult. Several models are described by Carey [16].

2.1.4 Heat transfer by a single bubble

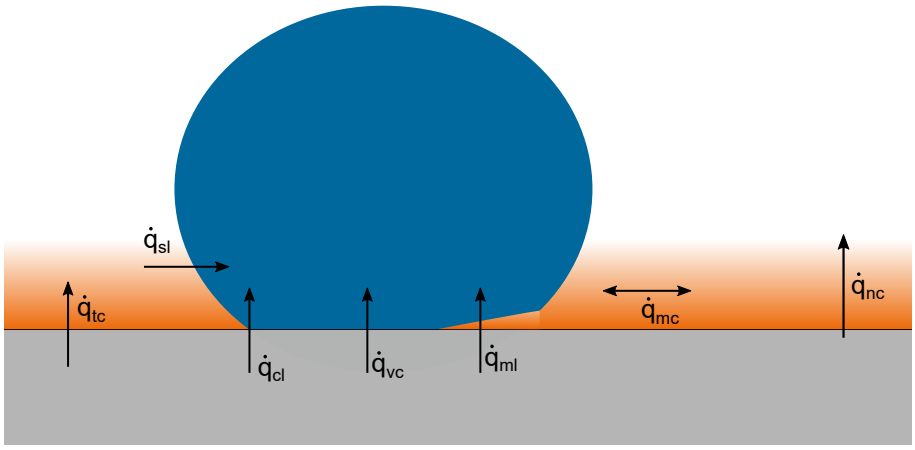

Figure 2.3: Sketch showing different heat transfer mechanisms adapted from Kim [67] and Stephan et al. [139].

During the bubble ebullition cycle, heat is constantly transferred from the wall into the fluid by different heat transfer mechanisms. Adapted from Kim [67] and Stephan et al. [139], the next section and Figure 2.3 describe and demonstrate some of the proposed mechanisms. Depending on the bubble expansion velocity, a liquid microlayer can be formed between bubble and wall. The evaporation of this microlayer $\dot{q}_{\mathrm{ml}}$ contributes to the bubble growth. Heat is also transferred at the three-phase contact line through contact line evaporation $\dot{q}_{\mathrm{cl}}$. In case the microlayer is completely evaporated, or it did not form in the first place, heat is transferred from the surface to the bubble by convection and conduction though an adsorbed thin film, $\dot{q}_{\mathrm{vc}}$. This adsorbed thin film does not evaporate, since the adhesion forces or the so-called "disjoining pressure", respectively, between liquid and wall reduce the vapor pressure of the fluid significantly. Additionally, superheated liquid in the boundary layer surrounding the bubble evaporates, $\dot{q}_{\mathrm{sl}}$, and natural convection $\dot{q}_{\mathrm{nc}}$ transports heat from the superheated boundary layer into the bulk of the liquid. During bubble growth and departure, the bubble motion induces microconvection, $\dot{q}_{\mathrm{mc}}$, and once the bubble is fully departed, cooler liquid will be transported to the wall and the disturbed thermal boundary layer will regrow through transient conduction $\dot{q}_{\mathrm{tc}}$. The next sections discuss the contributions of microlayer and contact line evaporation to the overall heat transfer in further detail.

2.1.4.1 Contact line heat transfer

In the 1970s, Wayner's group studied evaporating menisci experimentally [153] and numerically [116, 154] and developed a model, which was further advanced by Stephan and Hammer for nucleate boiling (Figure 2.4) [138]. This microregion model was continuously enhanced by Kunkelmann [76], Batzdorf [8] and Schlawitschek [126]. The model assumes that there is a non-evaporating, adsorbed thin film beneath a growing bubble, as shown in Figure 2.4b. In the non-evaporating thin film region, the disjoining pressure reduces the vapor pressure of the fluid preventing evaporation, as mentioned in the previous section. As the film thickness gradually increases in the microregion, the influence of the disjoining pressure decreases and the thin film starts to evaporate. In the interline or microregion, the model predicts high heat fluxes due to the efficient evaporation of this thin film, which is shown in

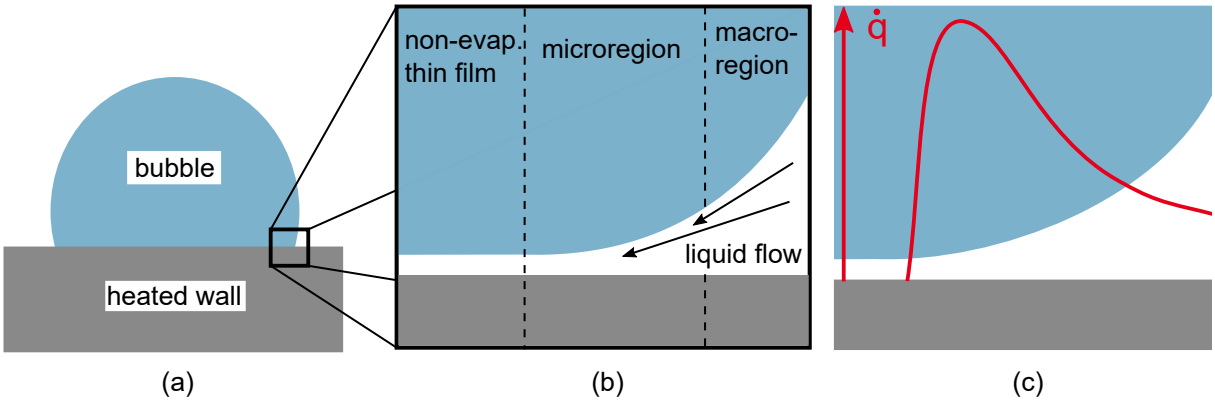

Figure 2.4: Sketch showing a bubble growing on a heated wall (a), the microregion (b), and qualitative heat flux (c) adapted from Stephan and Hammer [138].

Figure 2.4c. The results of this model are in agreement with experimental results obtained using refrigerants like FC-72 [130] and FC-3284 [151] as boiling fluids. Especially, if the bubble expansion velocities are small, for example at higher system pressures [135] or under low gravitational acceleration [130] good agreement is observed. At higher bubble expansion or receding contact line velocities, respectively, microlayer formation was observed for those fluids as well [33, 128, 135].

2.1.4.2 Microlayer heat transfer

In 1961, Hsu and Schmidt [51] and Moore and Mesler [106] observed wall temperature fluctuations during nucleate boiling. Each traced the fluctuations back to the ebullition cycle. Hsu and Schmidt assumed that the fluctuations are caused by bubble departure and the subsequent quenching of the wall. Moore and Mesler, on the other hand, argued that it must be caused by an evaporating thin film below the bubble. Through synchronous temperature and visual analysis of the bubble ebullition cycle, Hendricks and Sharp [49] proved that the large decrease in wall temperature coincides with bubble nucleation and, therefore, should be caused by microlayer evaporation. The experimental proof was adduced by Sharp [131], who measured the shape and evolution of microlayers forming beneath growing bubbles by interferometry. Sharp used water and methanol as boiling fluids and observed that the complete evaporation of the microlayer depends on the input heat flux. He also saw a clear influence of the surface on microlayer evaporation. Jawurek [54] did similar measurements using ethanol and methanol as boiling fluids. He determined the microlayer shape to be wedge-like. In recent years, several groups have measured the local temperature profile beneath growing bubbles by infrared thermography and calculated the heat flux profile of an evaporating microlayer [59, 135, 142]. Advances were also made by the group of Utaka [21, 147] determining the shape of the microlayer beneath a growing bubble.

Using generic non-isothermal dewetting experiments, Schweikert et al. [129] were able to determine the critical dewetting velocity necessary to form a microlayer. They also measured the heat flux profile caused by an evaporating microlayer and compared it to contact line evaporation [128]. They observed that the heat flux transferred by microlayer evaporation is significantly higher compared to contact line evaporation.

2.2 Influential parameters

In this section, the influence of several important parameters on nucleate boiling are presented, including surface roughness, wettability, and system pressure.

2.2.1 Surface roughness

The influence of surface roughness on nucleate boiling heat transfer is a well-studied phenomenon. In 1931, three years before Nukiyama published his famous work, Jakob and Fritz [53] observed an increase in the heat transfer coefficient with increasing surface roughness. Similar results were obtained

by Kurihara and Myers [78] and Berenson [9]. The heat transfer is enhanced due to cavities on the rough surface. These cavities lead to a higher number of possible nucleation sites compared to a smooth surface. Berenson measured an increase in the heat transfer coefficient by up to 600 % due to surface roughness. He also saw that the heat transfer coefficient does not increase monotonously with increasing surface roughness. He assumed that thinner and smaller cavities on the surface are preferable nucleation sites, since they cannot be wetted by the liquid easily compared to larger and wider cavities. For large roughness values, the increase of the area in contact with the fluid can have a large impact on the heat transfer. A positive effect on the bubble departure diameter and frequency was observed by McHale and Garimella [98].

The surface roughness is commonly characterized by the roughness parameter *Ra*. However, this parameter does not offer any information on the cavity size distribution of the surface [99]. McHale and Garimella used a filtered roughness parameter that only incorporates surface features whose length scales are below a certain threshold. They used the contact diameter of the bubble base prior to detachment as the threshold value. Other researchers [34, 160, 162] used fractal surface analysis to correlate their data to a roughness parameter. Those studies show that there are more suitable parameters to account for the influence of roughness on nucleate boiling. However, the determination of those parameters requires a considerable effort, meaning that they are impractical for industry.

2.2.2 Wettability

Like surface roughness, the influence of the wettability of a surface on nucleate boiling has been studied by Jakob and Fritz in 1931 [53]. They observed different bubble dynamics depending on the wettability of the surface. Studying the influence of wettability is very complicated because a change in fluid or surface will also change several other parameters that have significant influence on the boiling process as well. To avoid this problem, Bourdon et al. [14] used very smooth glass substrates and applied hydrophobic monolayers onto them without changing their surface roughness. They observed that the onset of nucleate boiling was at much lower wall superheats for a poorly wetting surface compared to a highly wetting one. The heat transfer coefficients of the poorly wetting surface were also increased for specific heat fluxes, but the critical heat fluxes were significantly reduced compared to a highly wetting surface.

Takata et al. [141] and Zhang et al. [166] used a different approach. They manufactured a nanostructure whose wettability could be changed by exposure to UV-light. They observed the same behavior for highly and poorly wetting surfaces as Bourdon et al. [14]. The lower onset of nucleate boiling temperatures of a poorly wetting surface are presumably caused by the higher number of vapor or gas embryos trapped in the surface roughness because the liquid cannot wet those cavities, as shown in section 2.1.2. Phan et al. [113] used different coatings to change static contact angles between 22° and 112°. They measured increasing bubble departure diameters, waiting times, critical heat fluxes, and decreasing bubble departure frequencies for highly wetting surfaces. Additionally, they observed differences in the bubble shape and growth, depending on the wettability. The bubbles do not detach easily from a poorly wetting

surface coalescing into a film, which causes burnout at low heat fluxes. However, the influence of those different coatings on the boiling process might not be limited to the change in wettability.

It is obvious that the wettability of fluid-surface combinations has a huge impact on the boiling phenomena. Using the positive impacts of highly and poorly wetting surfaces on the boiling process, several researchers [56, 132, 159] manufactured surfaces with poorly wetting spots on a highly wetting surface. They could increase the heat transfer coefficient significantly compared to a homogeneous highly wetting surface, while maintaining a similar critical heat flux. The poorly wetting spots act as favorable nucleation sites, increasing the heat transfer coefficient at low heat fluxes. According to Jo et al. [56], the waiting times of these poorly wetting spots are very low compared to a well wetting surface, which increases the overall heat transfer because the heat flux transferred during waiting time is low. However, since most of the surface is highly wetting, the critical heat flux is higher compared to a poorly wetting surface.

Typically, the wettability of a fluid-surface combination is characterized by static contact angles measured under atmospheric conditions. However, several researchers [31, 63, 83, 123] have observed a significant increase of the static contact angles of a highly wetting fluid under superheated conditions. Additionally, since the three-phase contact line is moving on the surface during bubble growth, the advancing and receding contact angles measured under saturated superheated conditions should be used to characterize the wettability and its impact on nucleate boiling.

2.2.3 System pressure

In saturated boiling, the system pressure and, therefore, the temperature influences the physical properties of the boiling fluid significantly. The physical properties of the fluid, in turn, govern the boiling process. Several researchers [10, 11, 27, 42, 45, 97, 102] have studied the influence of system pressure on nucleate boiling. They found that the boiling curves are shifted to the left to smaller wall superheats with increasing pressure. This implies an increase in the heat transfer coefficient and a lower superheat at the onset of nucleate boiling for higher system pressures. Kutateladze [79], Borishansky [13], and Gorenflo [41] observed a maximum critical heat flux for a specific reduced pressure, which is the ratio of system pressure to critical pressure. According to Gorenflo, this reduced pressure is approximately $p_r = p_{\mathrm{sys}}/p_{\mathrm{c}} = 0.38$ [140]. Additionally, an influence on nucleation site density [32], bubble departure diameter [32, 135], bubble frequency [32, 135], and bubble growth rate [150] can be observed.

The influence of those three parameters (surface roughness, wettability, and system pressure) on the boiling process is accounted for directly or indirectly by correlations for nucleate boiling.

2.3 Correlations for nucleate boiling

Most correlations for nucleate boiling focus either on the heat transfer coefficient or on the critical heat flux. Knowledge of both parameters is vital for designing evaporators as the heat transfer coefficient is

a measure of efficiency of the boiling process and the critical heat flux limits the maximum transferable heat flux by the evaporator.

2.3.1 Correlations for the heat transfer coefficient

The correlations presented in this section were developed to predict the heat transfer coefficient of uncoated smooth and rough surfaces, for various system pressures and fluids. However, there are notable differences in heat transfer coefficients predicted by different correlations, as the experimental data used to obtain those correlations are also scattered. The differences in the experimental data can be traced back to imprecise surface characterizations, measurement uncertainties, non-condensable gases, purity of the fluids, and other minor parameters. A deviation of up to 20 % between experimentally determined and calculated heat transfer coefficients is, in the author's opinion, nothing out of the ordinary.

There are multiple correlations available [13, 36, 79, 80, 84, 90, 103, 108, 117, 124, 137, 140] which differ in their approach [16], such as analogy to convective heat transfer [36, 80, 124], corresponding state [13, 79, 140], and dimensional analysis [117, 137]. One of the most famous and frequently used, is the correlation of Rohsenow [124], which is based on an analogy to convective heat transfer. Rohsenow assumed that nucleate boiling heat transfer is dominated by forced convection resulting from bubble departure. Similar to convective heat transfer, he used the following Equation 2.4 as a basis for his correlation:

$$Nu = C\, Re^{a} Pr^{b}. \tag{2.4}$$

Besides the Prandtl number Pr, Rohsenow [124] used the bubble diameter, which is calculated using the correlation of Fritz [37][1], as the characteristic length of the Nusselt Nu and Reynolds number Re. The final correlation includes, among others, three fitted parameters, the two exponents a, b, and the factor C_{sf}, as well as the specific heat capacity $c_{p,\mathrm{l}}$, the dynamic viscosity η_{l}, and the thermal conductivity λ_{l} of the liquid:

$$\frac{c_{p\mathrm{l}}\left(T_{\mathrm{w}} - T_{\mathrm{sat}}\right)}{\Delta h_{v}} = C_{\mathrm{sf}}\left[\frac{\dot{q}}{\eta_{\mathrm{l}} \Delta h_{v}} \sqrt{\frac{\sigma}{g\left(\rho_{\mathrm{l}} - \rho_{\mathrm{v}}\right)}}\right]^{a} \left(\frac{\eta_{\mathrm{l}} c_{p,\mathrm{l}}}{\lambda_{\mathrm{l}}}\right)^{b}. \tag{2.5}$$

Based on the data used for fitting, Rohsenow recommended the values of $a = 0.33$, $b = 1.7$, and $C_{\mathrm{sf}} = 0.013$, but stated that these do not have to be the true values. Different values for the parameters have been proposed by other researchers like Vachon et al. [148], Pioro [114], and Priarone [118], among others.

Another important correlation, which can be found in the *VDI-Wärmeatlas* [140], was developed by Gorenflo:

$$\frac{\alpha}{\alpha_{0}} = F_{q} F_{p} F_{w}, \tag{2.6a}$$

[1] The final correlation is not displayed in this publication, but it is possible to deviate it from Abb.4 in [37]

$$F_q = \frac{\dot{q}}{\dot{q}_0}^n, \qquad n = 0.95 - 0.3 p_r^{0.3}, \tag{2.6b}$$

$$F_p = 0.7 p_r^{0.2} + 4 p_r + \frac{1.4 p_r}{1 - p_r}, \tag{2.6c}$$

$$F_w = \left(\frac{Ra}{Ra_0}\right)^{2/15} \left(\frac{\lambda_\mathrm{w} \rho_\mathrm{w} c_\mathrm{w}}{\lambda_{\mathrm{w},0} \rho_{\mathrm{w},0} c_{\mathrm{w},0}}\right)^{0.25}. \tag{2.6d}$$

This correlation uses a reference case, index 0, to calculate the desired heat transfer coefficient. Three empirical factors, F_q, F_p, and F_w, consider the influence of the heat flux, the system pressure, and the wall on the heat transfer coefficient, respectively. The parameters with the index 0 correspond to the reference case of a copper wall at $\dot{q}_0 = 20\,\mathrm{kW\,m^{-2}}$, $p_{r,0} = 0.1$, and $Ra_0 = 0.4$. The reference heat transfer coefficient α_0 should be determined experimentally or calculated using the equations in the *VDI-Wärmeatlas* [140].

Besides correlations for the heat transfer coefficient, there are multiple correlations for determining the critical heat flux that will be discussed in the next section.

2.3.2 Correlations for the critical heat flux

There are several different theories and, therefore, correlations for the critical heat flux. This includes the premise that burnout is triggered by

- reaching a critical bubble packing on the surface [125],
- the evaporation of a liquid macrolayer formed beneath a large vapor bubble [47],
- the lift-off of a liquid macrolayer due to vapor flow from the surface [38, 43],
- the instability of hydrodynamic vapor jets leaving the surface [168],
- vapor recoil exceeding the holding forces of a bubble on the surface [62],
- the formation of an irreversible dry spot on the surface [149].

The last three theories will be discussed in detail, as they are the most relevant for this thesis, starting with the correlation of Zuber [168]:

$$\dot{q}_\mathrm{CHF,Z} = K \rho_\mathrm{v} \Delta h_\nu \left[\frac{\sigma\, g\, (\rho_\mathrm{l} - \rho_\mathrm{v})}{\rho_\mathrm{v}^2}\right]^{0.25}, \tag{2.7a}$$

$$\frac{\pi}{24} < K < \frac{\pi}{16}. \tag{2.7b}$$

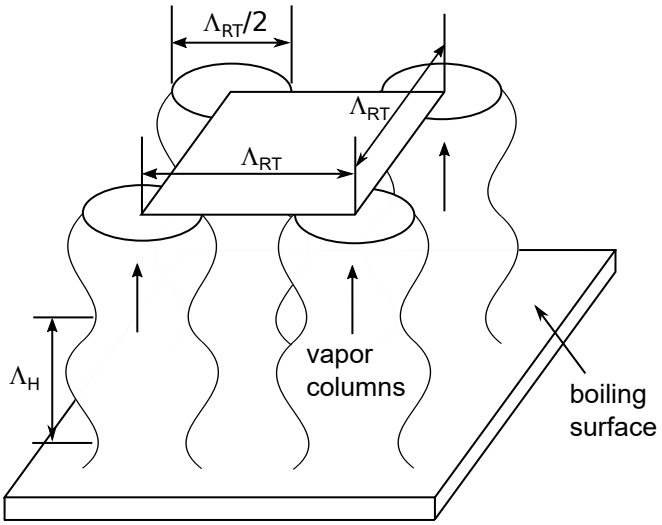

Figure 2.5: Sketch showing the boiling surface and the liquid-vapor interface displaying the Rayleigh-Taylor wavelength (Λ_{RT}) and Helmholtz instability wavelength (Λ_H) according to Zuber's model, adapted from Carey [16].

According to Carey [16], a similar equation was proposed by Kutateladze in 1948 based on an analogy to flooding distillation columns. However, Zuber developed an analytical model to describe the critical heat flux. His model is based on several assumptions, which are visible in Figure 2.5 [16]. Vapor leaves the surface in columns, which are arranged in a chessboard pattern. The dimensions of a unit cell are equal to the Rayleigh-Taylor wavelength Λ_{RT} and the diameter of the vapor columns is half the wavelength. Critical heat flux is reached if the vapor columns become Helmholtz unstable. Zuber assumed that the Helmholtz instability wavelength Λ_H equals the Rayleigh-Taylor wavelength. However, according to Lienhard and Dhir [91], Zuber did not have suitable experimental data to determine whether the critical or the most susceptible Rayleigh-Taylor wavelength would be formed on the surface. This is expressed by the inequation in Equation 2.7b. According to Lienhard and Dhir [91] the most susceptible wavelength is formed on the surface, which results in a factor of $K = \frac{\pi}{16} = 0.149$. A more detailed description and derivation of the model is undertaken by Carey [16].

The correlation of Zuber is widely used and it fits a significant amount of data reasonably well; however, it does not account for any influence of the boiling surface on the critical heat flux. It is well known that the wettability of the surface has a huge impact on the critical heat flux, which is shown in section 2.2.2. Kandlikar [62] included the wetting behavior into his correlation,

$$\dot{q}_{\mathrm{CHF,K}} = \rho_{\mathrm{v}} \Delta h_v \left[\frac{\sigma\, g\, (\rho_{\mathrm{l}} - \rho_{\mathrm{v}})}{\rho_{\mathrm{v}}^2} \right]^{0.25} \left(\frac{1 + \cos\Theta_{\mathrm{rec}}}{16} \right) \left[\frac{2}{\pi} + \frac{\pi}{4} (1 + \cos\Theta_{\mathrm{rec}}) \cos\delta \right]^{0.5}, \tag{2.8}$$

which is based on a force balance for a growing bubble on the surface. The surface tension force and the gravitational force keep the bubble horizontally in place. At the sides of the bubble, the momentum change of the evaporating fluid, due to the density difference between liquid and vapor, induces a vapor recoil force. If this force is larger than the surface tension force and gravitational force, the bubbles will expand horizontally along the surface, which will result in vapor blanketing and burnout. Since burnout is triggered by expanding vapor on the surface, the receding contact angle Θ_{rec} is used to calculate the surface tension force [62]. δ accounts for the surface orientation, being $\delta = 0$ for a horizontal surface. While this correlation incorporates the effect of wettability of the surface, the measurement of the receding contact angle in a saturated atmosphere is complicated. This hinders the applicability of this correlation.

According to van Ouwerkerk [149], Kirby and Westwater and Gaertner[1] established a connection between critical heat flux and dry spots on the surface. Van Ouwerkerk investigated the formation of dry spots beneath growing bubbles using the difference in refraction indices between liquid and vapor. He observed that dry spots are periodically formed beneath growing bubbles, which are rewetted after bubble departure. The formation of those reversible dry spots already starts at a heat flux of 20 % of critical heat flux. For increasing heat fluxes, he observed that the size and lifespan of reversible dry spots did not change dramatically, but they occurred more frequently. Once the critical heat flux is reached, several dry spots cannot be completely rewetted, which in turn start to grow and trigger burnout.

Similar observations were made by Theofanous et al. [144, 145], while examining the back of a boiling surface with an infrared camera. They observed that hot spots became more numerous and their superheat increased from 5 - 10 to 50 - 60 K for increasing heat fluxes. Contrary to the observations made by van Ouwerkerk [149], Theofanous et al. also saw an increasing lifespan of those hotspots. Through comparison to theoretical, adiabatic heat up rates of their surface, they deduced that the hotspots have to be covered by vapor. Burnout is eventually triggered by multiple dry spots spreading across the surface covering 10 % of the boiling surface. The growth of dry spots seemed to be influenced and confined by nearby nucleation sites, which results in a positive effect of nucleation site density on critical heat flux.

In a follow-up publication, Theofanous and Dinh [143] developed a correlation, which is based on the findings in their previous publications. This correlation is formally similar to the correlation of Zuber [168], but the derivations differ:

$$\dot{q}_{\mathrm{CHF,T}} = K^{-0.5} \rho_{\mathrm{v}} \Delta h_{\nu} \left[\frac{\sigma \; g \, (\rho_{\mathrm{l}} - \rho_{\mathrm{v}})}{\rho_{\mathrm{v}}^2} \right]^{0.25} . \tag{2.9}$$

The parameter K should be determined by simulating the contact line region [143]. However, to the author's knowledge, a value for K has not been provided by Theofanous and Dinh. An expression for K was developed by Kim et al. [72]:

$$K = \left(1 - \frac{\sin\Theta}{2} - \frac{\pi/2 - \Theta}{2\cos\Theta} \right)^{-0.5} . \tag{2.10}$$

[1] Unfortunately, the original sources could not be obtained

According to Liang and Mudawar [89], Yagov also developed a correlation based on dry spots triggering burnout in 1988[1]. In 2014, Yagov [158] published an updated correlation:

$$\dot{q}_{\mathrm{CHF,Y,low}} = 0.5 \frac{\Delta h_\nu^{81/55} \sigma^{9/11} \rho_\mathrm{v}^{13/110} \lambda_\mathrm{l}^{7/110} g^{21/55} f(Pr)}{\nu_\mathrm{l}^{0.5} c_{p,\mathrm{l}}^{3/10} \overline{R}^{79/110} T_\mathrm{sat}^{21/22}} \quad \text{for} \quad p_r < 0.001, \tag{2.11a}$$

$$f(Pr) = \left(\frac{Pr^{9/8}}{1 + 2Pr^{0.25} + 0.6Pr^{19/24}} \right)^{4/11}, \tag{2.11b}$$

$$\dot{q}_{\mathrm{CHF,Y,high}} = 0.06 \Delta h_\nu \rho_\mathrm{v}^{0.6} \sigma^{0.4} \left[\frac{g(\rho_\mathrm{l} - \rho_\mathrm{v})}{\eta_\mathrm{l}} \right]^{0.2} \quad \text{for} \quad p_r > 0.03, \tag{2.11c}$$

$$\dot{q}_{\mathrm{CHF,Y}} = \left(\dot{q}_{\mathrm{CHF,Y,low}}^3 + \dot{q}_{\mathrm{CHF,Y,high}}^3 \right)^{1/3} \quad \text{for} \quad 0.03 < p_r < 0.001. \tag{2.11d}$$

Depending on the system pressure, the critical heat flux is calculated using empirical equations, which consider the physical properties of liquid and vapor, such as the kinematic viscosity of the liquid ν_l and the specific gas constant of the fluid $\overline{R}$.

2.4 Influence of micropillars and nanowires on nucleate boiling

In the last 20 years, the focus of boiling research has shifted towards micro and nanostructures. Compared to a smooth surface, those structures enable a significant improvement of the critical heat flux [22, 66, 70, 85, 92] as well as the heat transfer coefficient [25, 28, 61, 75, 85]. The surface modifications range from nanoparticles, nanograss, and nanowires on the nanoscale to microchannels, micropillars, and microporous surfaces, among others on the microscale. The influence of nanowires and micropillars is especially interesting, since the structures are both of cylindrical shape. However, the length scale of the cylinders is very different. First, an overview of the influence of nanowires is provided, followed by an overview of surfaces with micropillars.

2.4.1 Nanowires

Typically, nanowires are either made of copper, silicon, or carbon and the experiments are usually performed at atmospheric pressure using various boiling fluids. Several researchers have observed an increased heat transfer coefficient [20, 65, 82, 133, 161] and critical heat flux [20, 65, 82, 133, 161]. This enhancement is due to an increase in surface roughness [82, 161], wettability [20, 86, 133, 161], and wickability [20, 65, 75, 86] of the nanowire surfaces. Additionally, bubble diameters [65, 82, 86] are decreased and bubble departure frequencies increased [65, 82, 86].

[1] Unfortunately, the original source could not be obtained

Nanowires increase the surface roughness and, therefore, the nucleation site density [75, 82, 86, 161]. This effect is enhanced by an increasing nanowire length [52, 65, 133] and diameter [75]. Longer nanowires start to collapse, forming larger cavities, which act as favorable nucleation sites. However, according to Im et al. [52] and Kumar et al. [75], there is an optimum nanowire length and diameter. Longer or thicker nanowires increase the cavity density and size up to a point, as well as the capillary flow. On the other hand, the flow resistance of liquid and vapor inside the nanostructure is also increased.

Nanowires improve the wettability of a surface, as well. This enhanced wettability could be traced back to the increased roughness. According to Wenzel [156], the contact angle of a fluid on a rough surface, Θ_{rg}, is either reduced or increased depending on the contact angle of the same fluid on a smooth surface, Θ_{sm}:

$$\cos\Theta_{rg} = r\cos\Theta_{sm}. \tag{2.12}$$

Roughness factor r in Equation 2.12 is the ratio of the surface area in contact with liquid to the surface area of a smooth surface with the same macroscopic dimensions. Additionally, the wickability of nanowire surfaces has a significant impact, especially on critical heat flux. The capillary pressure caused by small menisci in the nanostructure helps to rewet the surface, preventing burnout until higher heat fluxes [75, 161].

Thiagarajan et al. [146] and Li et al. [86], however, observed lower critical heat fluxes using nanostructured surfaces compared to smooth surfaces. Thiagarajan et al. [146] assumed that their nanostructured surface could not benefit from an enhancement in wettability because a highly wetting fluid HFE 7100 was used. However, this cannot be the sole reason, since Kumar et al. [75] and Im et al. [52] observed an increase in critical heat flux working with similarly well wetting fluids like FC-72 or PF-5060. At first, Li et al. [86] observed comparable critical heat fluxes to a smooth surface, which decreased during further test runs. They proposed that oxidation and impurities are responsible for decreasing the critical heat flux. For nanowire lengths exceeding 30 µm, Lu et al. [95] observed lower heat transfer coefficients for a specific heat flux, compared to a smooth surface. Unfortunately, they do not offer an explanation. The increased flow resistance in the nanostructure, which is presumably responsible for lower critical heat fluxes, might also cause decreasing heat transfer coefficients. On the other hand, Chen et al. [20] used similarly long and thick silicon nanowires and water as boiling fluid, and observed an increase in heat transfer coefficient.

2.4.2 Micropillars

Similar to experiments using nanowires, a surface with micropillars typically increases critical heat flux. The reason for this enhancement is subject of much discussion. According to Chu et al. [22], the increase in roughness factor r and the resulting higher wettability results in a longer total length of the three-phase contact line. Following the critical heat flux mechanism described by Kandlikar [62], the resulting increase in surface tension allows for higher evaporation rates and, therefore, higher critical heat fluxes. Dhillon et al. [26], Kim et al. [66], Li et al. [87], and Yu et al. [163] assumed that the wickability

of microstructures and the resulting additional liquid supply to the surface increase critical heat flux. However, the effect triggering burnout is subject of debate. Dhillon et al. [26] proposed that burnout is triggered by irreversible dry spots growing on the surface, and Kim et al. [66] assumed that it is triggered by the complete evaporation of a liquid macrolayer below a large bubble. Li et al. [87] mentioned that microstructures could decrease the Rayleigh-Taylor wavelength, which would in turn increase the critical heat flux.

Chu et al. [22] observed higher critical heat fluxes on surfaces with smaller pillar diameters and pitches. A similar behavior was reported by Dong et al. [28] and Yu et al. [163]. Yu et al. [163] and Dhillon et al. [26] observed the existence of an optimum pillar diameter and pitch for critical heat flux enhancement due to the simultaneously increasing capillary flow and flow resistance for smaller pillar diameters and pitches.

The reasons for an increase in heat transfer coefficient are similarly a subject of debate. Moita et al. [104] used surfaces with low roughness factors r, due to large pitches. They assumed that the enhanced bubble dynamic is responsible for an improved boiling behavior. Dong et al. [28] and Li et al. [87] claimed that the larger wetted area, is responsible for the increase in heat transfer coefficient. Furthermore, higher nucleation site densities could be responsible for increased heat transfer coefficients, according to Ho et al. [50] and Dong et al. [28]. The latter also observed smaller bubble departure diameters and higher frequencies. On the other hand, Chu et al. [22] did not observe increased heat transfer coefficients for specific heat fluxes. Additionally, they did not see a significant influence of the pillar size and pitch on the heat transfer coefficient. Dong et al. [28] and Li et al. [87] reported that the heat transfer coefficient increases for smaller micropillar diameters and pitches due to higher surface roughness [71], increased nucleation site densities [28], and an increase in the wetted area [87]. A contrary observation was made by Kim et al. [69], although their pillar geometries were similar to those of Dong et al. [28].

All in all it is clear, that the influence of nanowires and micropillars on the boiling process is still a subject of debate. If surfaces with nanowires and micropillars are compared directly, the surfaces with nanowires show slightly higher heat transfer coefficients compared to surfaces with micropillars [28, 87]. In case of critical heat flux, however, it is the other way round [26, 87].

2.4.3 Hierarchical surface

In recent years, several researchers have been using hierarchical surfaces to enhance the boiling process even further and to study the interactions between the different length scales. The hierarchical surfaces can be divided into three groups, depending on their length scale:

- a combination of a microstructure and a nanostructure [23, 87, 105, 134, 155],
- a combination of a macrostructure and a microstructure [44, 157],
- a combination of a macrostructure and a nanostructure [18, 120].

Starting off with the combination of a microstructure and a nanostructure, Li et al. [87] manufactured a copper micropillar array and coated the surface with copper nanowires. They used water as boiling fluid at atmospheric pressure. At low heat fluxes, the boiling behavior was similar to the boiling behavior of a surface with micropillars. At higher heat fluxes, however, the hierarchical surfaces showed the highest heat transfer coefficients and critical heat fluxes of the three surfaces (microstructured, nanostructured, and hierarchical). This delayed heat transfer coefficient improvement is presumably caused by smaller cavities in the nanostructure that need higher wall superheats to be activated. The higher critical heat flux is explained by the enhanced capillary flow inside the hierarchical structure. The nanowires increase the capillary flow and the flow resistance inside the structure due to their small dimensions. The downside of a higher flow resistance is counteracted by the larger spacing between the micropillars. Wen et al. [155] used a similar surface consisting of copper nanowires, whose length were augmented to create a micropillared surface made of nanowires. They also performed their experiments with water as boiling fluid at atmospheric pressure. They observed a similar boiling behavior to Li et al., where the heat transfer coefficient exceeds those of homogeneously coated nanowire surfaces at high heat fluxes. A similar explanation is given for this phenomenon. Contrary to Li et al. [87], Wen et al. [155] assumed that the separation of liquid and vapor pathways is responsible for the critical heat flux enhancement, since the bubbles are mostly formed in the valleys besides the pillars. Chu et al. [23] and Moon et al. [105] observed a similar boiling behavior on their surfaces. Shin et al. [134] manufactured a surface made of copper nanowires with larger cavities (approx. 10 µm), using water as boiling fluid at atmospheric pressure. They observed higher heat transfer coefficients but lower critical heat fluxes compared to a surface with homogeneously distributed nanowires. The increase in heat transfer coefficient is caused by larger cavities acting as favorable nucleation sites. However, the critical heat flux decreases because the surface of the larger cavities is not covered with nanowires, resulting in a missing capillary flow. This is augmented by the larger cavities being favorable nucleation sites.

Ha and Graham [44] manufactured a porous surface made of sintered copper particles and created channels with various depths inside the microporous layer. They observed a significant enhancement of the heat transfer coefficient and critical heat flux with increasing channel depth compared to the homogeneous microporous surface. The vapor bubbles can escape the microporous layer through the channels preventing dry-out inside the layer, which, in turn, increases the heat transfer coefficient and prevents burnout. If the channels are deeper, they affect the entire thickness of the microporous layer resulting in a further enhancement of the boiling process. Witte [157] used surfaces with porous metallic cylinders consisting of copper fibers. He observed a higher heat transfer coefficient compared to the ones obtained using a homogenous porous surface made of the same copper fibers at low heat fluxes. He deduced that vapor escapes and liquid enters the porous cylinders easier due to the cylinders finite diameter compared to a homogeneous porous surface, which, in turn, increases the heat transfer coefficient.

Rahman and McCarthy [120] manufactured a copper surface covered periodically with a hydrophobic nanostructure made of PTFE, followed by a copper nanostructure, a groove filled with epoxy, and the same copper nanostructure again. This setup should ensure the separation of liquid flow to the surface and capillary wicking inside the copper nanostructure, nucleation and vapor outflow at the PTFE nanostructure. While the critical heat flux was higher for a surface without the PTFE nanostructure, the

heat transfer coefficients of the described hierarchical surface were the highest. This can be explained by favorable nucleation sites in the hydrophobic PTFE nanostructure, which increase heat transfer while decreasing critical heat flux, because the nucleation sites are not spread homogeneously on the surface. The employment of epoxy filled grooves leads to an overall improvement compared to a homogeneously nanostructured surface caused by the separation of liquid inflow and vapor outflow. Chen and Li [18] manufactured copper surfaces, where channels create square areas with different dimensions covered by nanowires. They observed a slight increase in critical heat flux due to capillary wicking inside the nanostructure compared to a surface with similar microgrooves. They also reported an increase in critical heat flux with smaller square sizes. They assumed that this is due to smaller modulated wavelengths, which prevent burnout, similar to the findings of Liter and Kaviany [92].

In conclusion, hierarchical surfaces have proven to improve the boiling process by combining beneficial effects caused by surface structures on different length scales.

2.5 Summary and scientific questions of this thesis

It is clear that the influence of microstructures and nanostructures on nucleate boiling is still a subject of active research. However, most of the experiments using microstructured or nanostructured surfaces are performed using water as boiling fluid at atmospheric pressure. This limits the possibility of identifying and analyzing important parameters, like the interactions between surface and fluid. Although the results obtained using surfaces with micropillars and nanowires are similar, several important phenomena, such as the interaction of capillary wicking and flow resistance governing critical heat flux, are dependent on the length scales of the structures.

Hierarchical structures benefit from those differences by adding another geometrical length scale, increasing the overall boiling performance. However, to design such a surface, detailed knowledge of the dominant phenomena on different length scales is necessary. This shows the necessity of investigating the boiling process on different length scales.

Furthermore, it is clear that the influences of system pressure, surface roughness, and wettability are considered by state of the art correlations. Although microlayer and contact line evaporation have a significant impact on the overall heat transfer, their influence is not incorporated directly. This is mostly because a regime map was not developed until recently [15].

Considering this summary, three scientific questions for this thesis are developed:

1. How is the boiling process affected by a microstructure, whose geometrical length scale is between the well-studied micropillars and nanowires?
2. Is it possible to improve the boiling performance of said microstructure by adding a macrostructure, creating a hierarchical structure?
3. Can an investigation of the boiling process on different length scales enable a better understanding of the occurring boiling phenomena?

In order to answer these questions, a new experimental setup has to be constructed. This experimental setup should allow measurements using different fluids over a large range of system pressures and heat fluxes to enable a thorough investigation of the microstructured surfaces. To analyze the boiling process on different length scales, different heater modules and measuring devices are necessary.

Chapter 3

Experimental Methods

This chapter explains the experimental setup and the necessary measurement equipment followed by a characterization of the used boiling surfaces. The chapter then concludes with a description of the experimental procedure.

3.1 Overview of the experimental setup

Answering the scientific questions formulated in the previous chapter requires the experimental setup to meet certain requirements.

- **Experimental investigation of nucleate boiling in a wide pressure and temperature range with different fluids.**

  In order to meet the requirement, a pressure vessel made of stainless steel is necessary. A low leakage rate must be ensured as non-condensable gases have a significant impact on nucleate boiling. Typically, three different classes of fluids are used for boiling investigations: refrigerants; water; and other hydrocarbons whose physical properties and applications differ from one another. FC-72, or perfluorohexane, is a refrigerant with a low specific enthalpy of vaporization and surface tension. Its boiling point $\left(T_{\mathrm{sat}} = 56.6\,^{\circ}\mathrm{C} \;@\; p_{\mathrm{sys}} = 1\,\mathrm{bar}\right)$ enables experiments in a wide pressure range. Additionally to FC-72, ethanol is chosen as the second boiling fluid, belonging to the hydrocarbon class. Its physical properties are significantly different compared to FC-72 but its boiling point $\left(T_{\mathrm{sat}} = 78.1\,^{\circ}\mathrm{C} \;@\; p_{\mathrm{sys}} = 1\,\mathrm{bar}\right)$ is similar to enable measurements at the same system pressures.

- **The boiling process should be analyzed on different length scales.**

  To analyze the boiling process on different length scales, distinct heater modules are necessary. A heater module should enable measurements that are comparable to industrial scale applications. Therefore, the heater surface area has to be large enough to avoid having an impact on the boiling process. The heater focusing on a smaller length scale should be infrared transparent in order to

analyze the local heat transfer phenomena beneath a growing bubble. The studied microstructures should be applied onto both heater modules. Additionally, the influence of the surfaces on bubble sizes and dynamics should be analyzed. Therefore, a high speed b&w camera, as well as optical access to the boiling surface are necessary. A modular experimental setup should ease the installation of different surfaces and heater modules, and enable necessary adaptions.

Based on these two requirements, the experimental setup was designed and constructed. The entire setup is shown in Figure 3.1. The flowchart shows the main components of the setup: the boiling cell and a heater module, which is situated inside; condenser; cameras; and, corresponding equipment necessary for experiments. The single components will be described in greater detail in the following sections starting with the boiling cell.

3.1.1 Boiling cell

The boiling cell without insulation is shown in Figure 3.2a. To satisfy the principle goal of flexibility, a modular system with different flanges was designed, each of them having a different functionality. This ensures easy alterations of the system in case a different function is desired. To ensure a high leak tightness, the CF[1] sealing system was chosen, which belongs to the metal-metal sealing systems. Besides the low leakage rate of CF sealing systems, it requires bulky components, to apply the necessary stress onto the seal. Thus, they are able to withstand greater internal pressures. The manufacturers of these components, however, guarantee safety up to an absolute pressure of 1.5 bar, which is lower than the desired 6 bar. Therefore, the pressure safety had to be established with the help of the AD 2000 datasheets [1]. These datasheets provide guidelines for the safe construction of pressure vessels. To prevent external auditors and annual tests, the experimental setup has to be categorized into the A1 category, which limits the pressure and volume of the experimental setup. Thus, the flanges, seals, screws, and their materials were constructed or chosen with the help of the AD 2000 datasheets. The larger components were designed using the simulation tool of NX10, a CAD software by *Siemens*.

The base body of the boiling cell is a stainless steel cube with an edge length of 305 mm, shown in Figure 3.2b. Three holes with diameters of 200 mm, one in each space coordinate, create the volume of the boiling cell. Additionally, further holes and channels are drilled into the sides of the cube, which are covered by metal plates to create a double jacket around the cube. This double jacket is connected to a thermostat (Unistat Tango by *Huber Kältemaschinenbau*) and filled with silicone oil (M20.195/235.20 supplied by *Huber Kältemaschinenbau*) in order to control the temperature of the boiling cell and, therefore, the temperature of the boiling fluid within. The openings on each side of the cube are covered with stainless steel flanges, which serve different purposes.

Windows are embedded into two flanges covering opposite sides to observe the boiling process with a b&w camera (MotionXtra N4 by *IDT*) and a backlight. Two different lenses are used to capture the boiling phenomenon, depending on the heat flux. At low heat fluxes $\left(\dot{q} < 40\,\mathrm{kW\,m^{-2}}\right)$ a microscope lens (LMZ45T3 by *Kowa*) is used to observe the boiling process close to the surface. This data is used to

[1] ConFlat

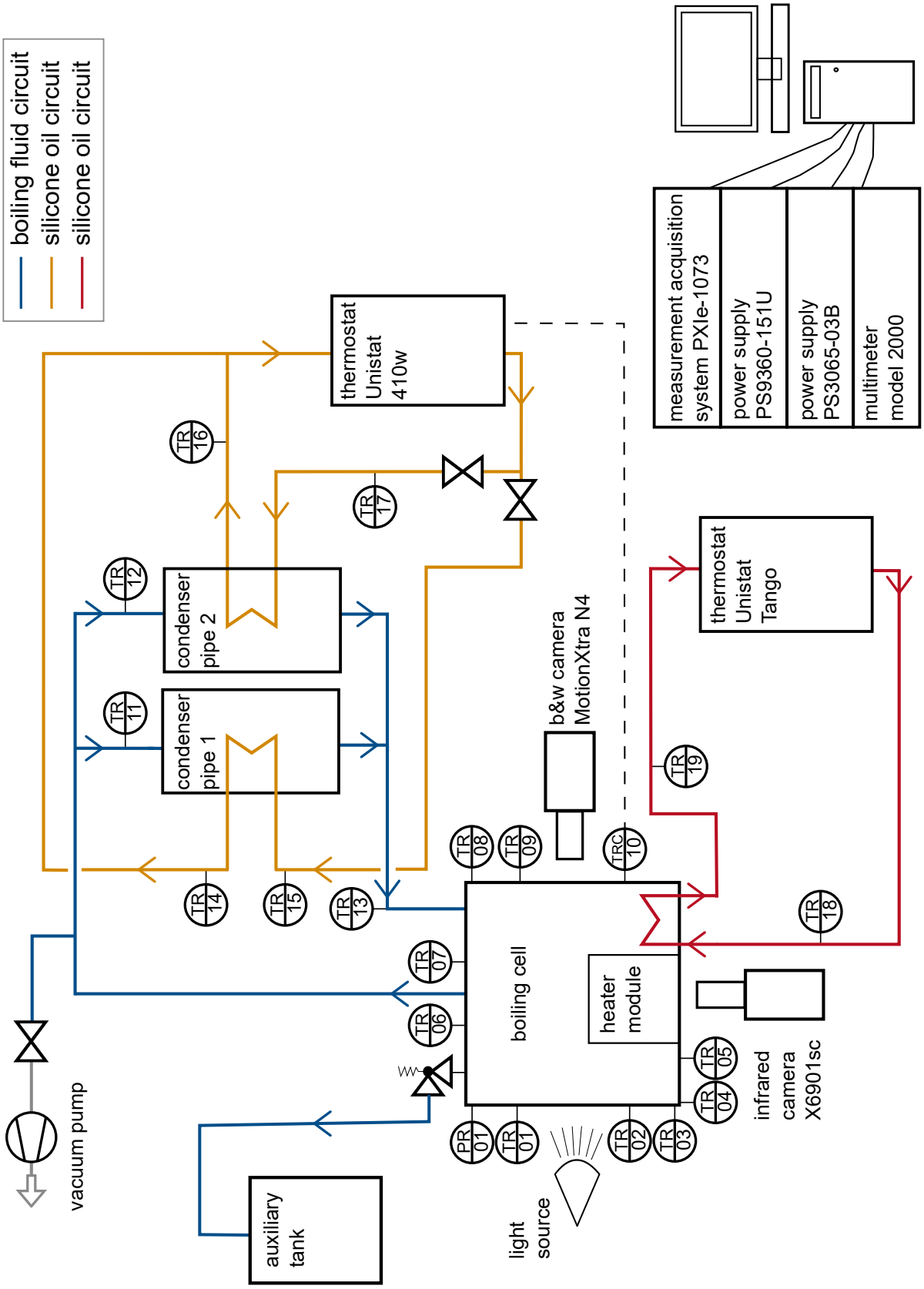

Figure 3.1: Flowchart of the experimental setup.

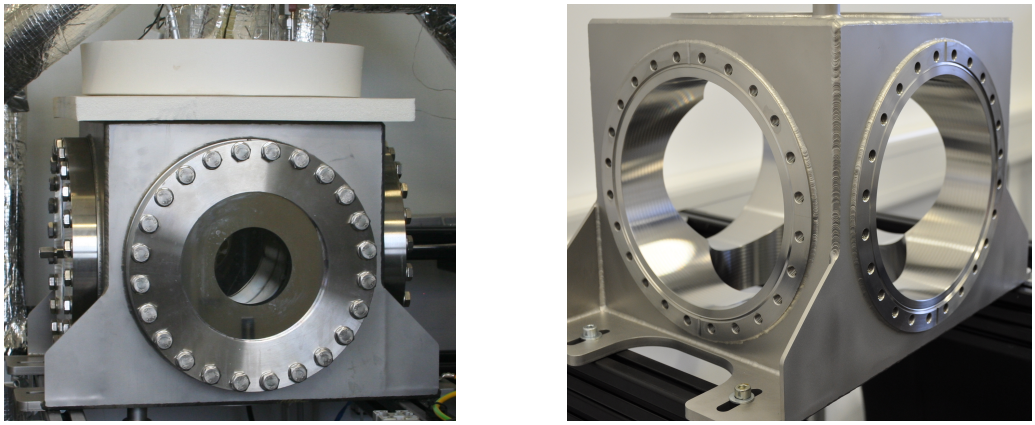

(a) (b)

Figure 3.2: Images of the boiling cell (a) and its base body (b) without insulation.

evaluate the bubble diameter. For heat fluxes greater than $\dot{q} > 40\,\mathrm{kW\,m^{-2}}$ a Navitron 50 mm F1.3 lens by *D.O. Industries* is used to distinguish the different boiling regimes, like isolated bubble regime or the slugs and columns regime.

A pressure sensor (P-30 by *WIKA*) and an auxiliary cartridge heater are installed into two separate horizontal flanges without windows. The pressure sensor is connected to the flange via a 500 mm long pipe, which is filled completely by the boiling fluid. The length of the pipe is determined by a simplified calculation, balancing the incoming and outgoing heat flux. The incoming heat flux is calculated using 1-dimensional Fourier's law in the pipe and fluid. The outgoing heat flux is approximated by a correlation for natural convection on the outside of the pipe. This design ensures a temperature below 60 °C at the pressure sensor as the measurement uncertainty of the pressure sensor would increase by at least 100 % at elevated temperatures. During experiments, the temperature of the pipe close to the pressure sensor never exceeded 40 °C.

Four resistance thermometers and one thermocouple measuring the liquid temperature in different locations inside the cell and a thermocouple measuring the vapor temperature are connected to the top flange. The thermometers are connected to the measurement acquisition system (PXIe-1073 by *National Instruments*) and the entire experimental setup is controlled by a LabVIEW program. Aside from the thermometers, a pipe for filling the boiling cell and a pressure relief valve are connected to the top flange. To prevent hot vapor from entering the laboratory, in case of overpressure, a pipe is coupled to the outlet of the pressure relief valve. The opposite end of this pipe is submerged in an auxiliary tank (shown in Figure 3.1) filled with water (30 l) and a porous metal cylinder is connected to the pipe, splitting the vapor flow into smaller bubbles. These bubbles condense easily, which prevents a significant pressure increase inside the tank and the laboratory, since the tank is open to the environment.

3.1.2 Condenser

Two pipes connect the boiling cell to the condenser, via the top flange. The larger vapor pipe is mounted centrically on the top flange and the smaller liquid pipe is connected at a minimum distance of 80 mm

from the center of the flange. This ensures that condensed, colder liquid does not disturb the boiling process, since the heater surface is centered below the top flange. The diameters of the vapor pipe (60.3 mm × 3 mm) and liquid pipe (12 mm × 2 mm) are chosen to ensure fluid velocities below 1 m s^{-1} and 10 m s^{-1}, respectively. The calculations were done using FC-72 as boiling fluid, since it has the lowest specific enthalpy of vaporization of the boiling fluids used in this thesis and, thus, the highest mass and volume flow for a specific heat flow. The condenser consists of two, 1 m long pipes with outer shells. These outer shells are connected to another thermostat (Unistat 410w by *Huber Kältemaschinenbau*), which uses silicone oil (M40.165/220.10 supplied by *Huber Kältemaschinenbau*) as working fluid.

A well-designed condenser is crucial for repeatable boiling experiments, since the condenser controls the boiling process by setting the system pressure and, therefore, the temperature of the boiling fluid. The condenser is designed to work with ethanol and FC-72, whose physical properties like thermal conductivity and specific enthalpy of vaporization differ significantly. It should also be able to transfer heat fluxes ranging from 10 to 1000 kW m^{-2} for boiling fluid temperatures ranging from 30 to 180 °C. It should be noted that only commonly available pipe diameters were considered and since the diameter of the pipe, leading to the condenser is 60.3 mm × 3 mm, the same diameter and thickness were chosen for the condenser pipes themselves. The maximum pressure drop for the chosen pipe diameter was calculated to be negligible.

Considering the large range of heat fluxes that need to be transferred and the different physical properties of ethanol and FC-72, it was established that the higher heat transfer resistance had to be on the silicone oil side. The temperature of the silicone oil flowing through the outer shells can be altered between 10 and 150 °C and the flowrate between 5 and 50 l min^{-1}. The diameter and thickness of the shell were chosen to be 76.1 mm × 3 mm, creating a gap between the condenser pipe and the outer shell of 4.9 mm. The necessary condenser length of 1 m for each pipe was calculated using a piecewise 2-dimensional calculation. Further details can be found in section A.4 in the appendix.

3.1.3 Infrared transparent heater module

In order to investigate the boiling process on different length scales, two distinct heater modules are designed. The larger heater module is used to determine the critical heat flux and the mean heat transfer coefficient, which is the parameter judging the efficiency of the boiling process. Knowing the critical heat flux is crucial for safety reasons, as the temperature jump associated with the transition to film boiling can cause damage to the boiling surface. Additionally, the heat transfer coefficient typically increases with increasing heat flux. Thus, a high critical heat flux allows for a more efficient boiling process. The smaller infrared transparent heater module is used to investigate the local heat transfer beneath a growing bubble and to distinguish between the two regimes of microlayer and contact line evaporation. This knowledge is helpful for understanding the phenomena visible on the large heater module.

The infrared transparent heater module, visible in Figure 3.3, consists of the infrared transparent heater itself and two flanges, a mounting flange and a distance flange (Figure 3.3a). The distance flange reduces the risk of damage to the seal of the boiling cell because the direct connection to the boiling cell does

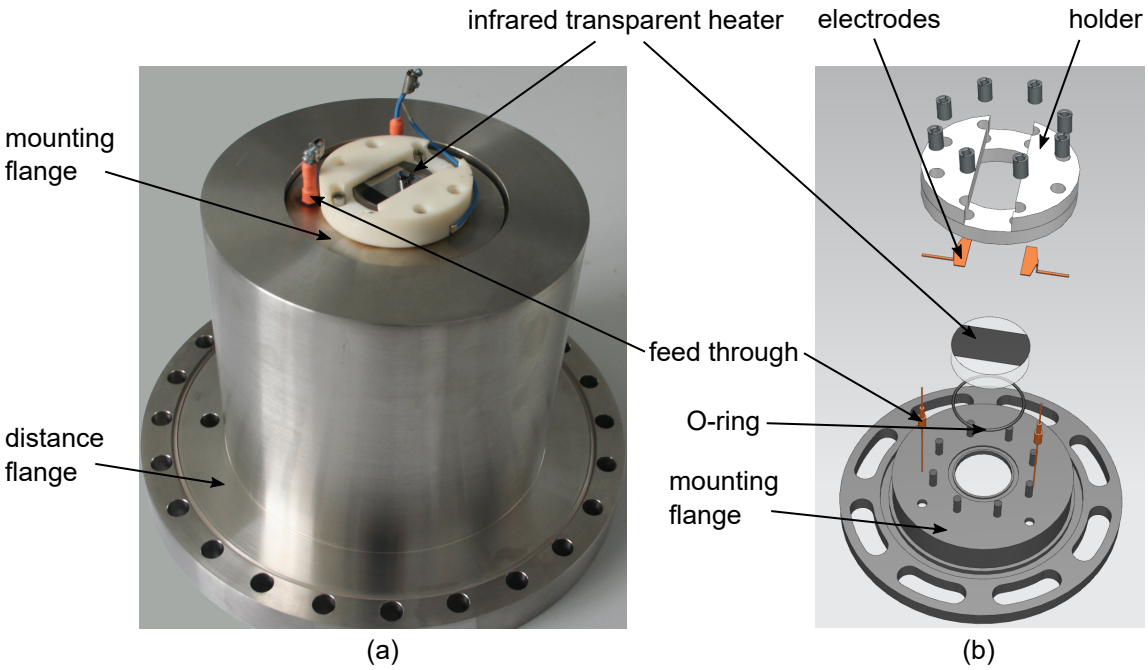

Figure 3.3: Image (a) and CAD image (b) of the infrared transparent heater module.

not have to be opened in case a different boiling surface is studied. To change the boiling surface, the heater and the mounting flange have to be removed while the distance flange stays connected to the boiling cell. Additionally, this distance flange is used to get the infrared transparent heater closer to the center of the boiling cell, enabling the observation of the boiling process via the windows in the horizontal flanges of the boiling cell (Figure 3.2a). The mounting flange is a lot smaller than the distance flange for easier installation, as shown in Figure 3.3b. The infrared transparent heater is pressed onto the mounting flange by a ceramic filled polymer holder. The holder is designed to apply pressure on a large area of the infrared transparent heater, reducing the risk of damage to the heater, while ensuring an even deformation of the O-ring seal between heater and flange. Furthermore, the holder offers an unobstructed view onto the boiling surface from the side windows of the boiling cell, while pressing electrodes onto the infrared transparent heater. Those electrodes are attached to copper wires, which are connected via feed throughs to a power supply (PS3065-03B by *Elektro-Automatik*) and multimeter (model 2000 by *Keithley*).

The infrared transparent heater is visible in Figure 3.4a. It consists of a CaF_2 crystal (37 mm diameter and 10 mm height), a CrN layer for better emissivity and a Cr layer on top of the CrN, which are visible in Figure 3.4b. Both layers, each approximately 400 nm thick, are applied to the CaF_2 crystal by physical vapor deposition. The Cr layer is used as a resistance heater, supplying the boiling heat flux. As mentioned earlier, two electrodes are connected to the Cr layer on each side for power supply. To reduce contact resistance, the electrodes consist of a copper sheet, a copper mesh, and indium foil, as shown in Figure 3.4b. As it does not form an oxide layer, a thin layer of gold is sputtered onto the Cr layer beneath the electrodes to minimize contact resistance further. This reduction in contact resistance is necessary to minimize the amount of parasitic boiling in the contact area between electrode and Cr layer. There are two reasons why parasitic boiling is prone to happen in this region. For one, the contact

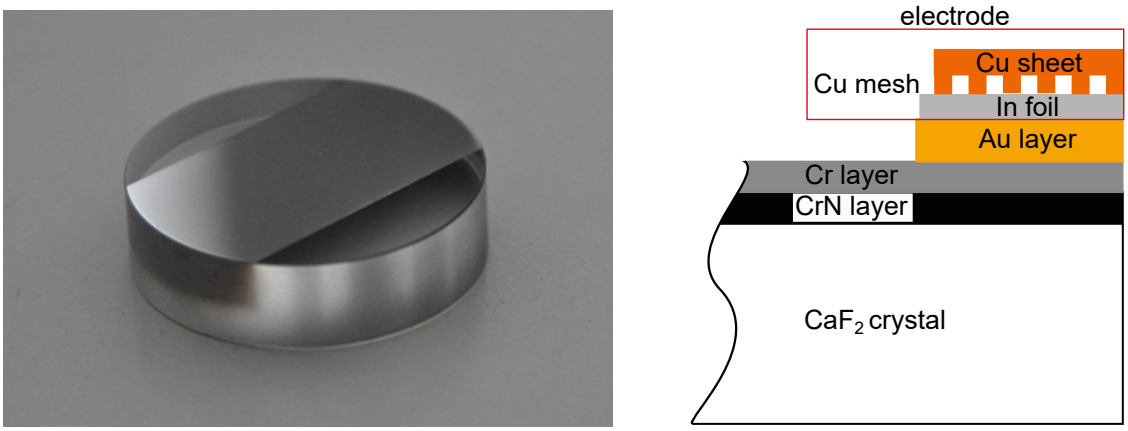

Figure 3.4: Image (a) and sketch (b) of the infrared transparent heater.

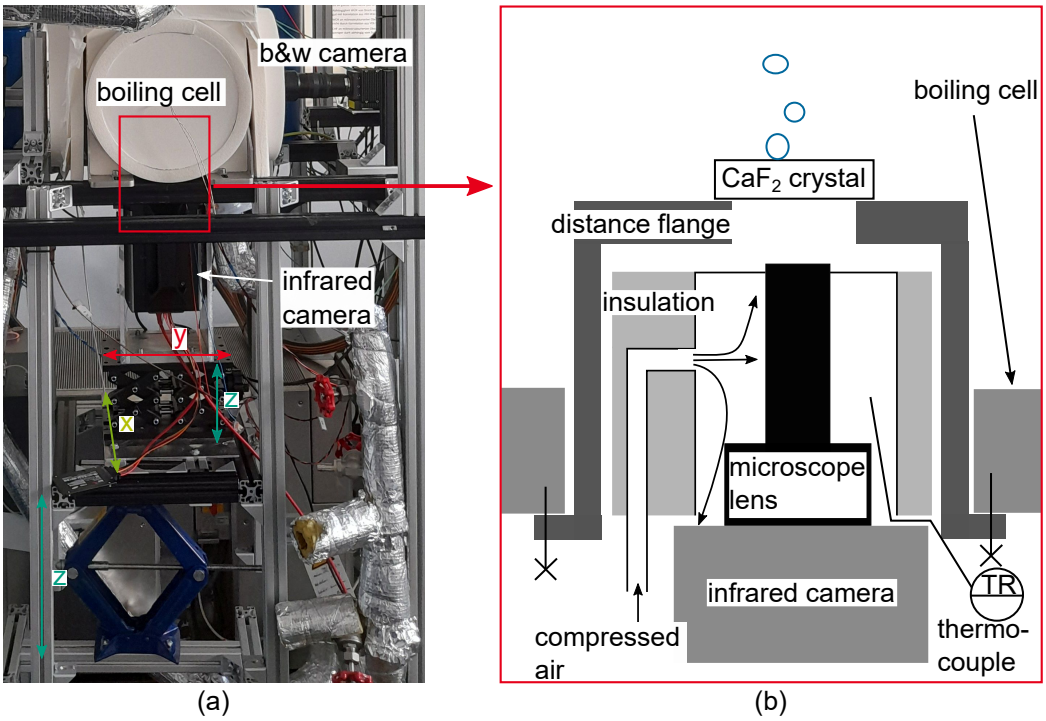

Figure 3.5: Image (a) of the infrared camera mount and sketch (b) of the microscope lens temperature control system.

area is usually the hottest part of the surface due to the aforementioned contact resistance for the current to pass through, generating additional heat. The second reason is that gaps and cavities are formed by pressing the electrode to the surface, which act as favorable nucleation sites. This parasitic boiling reduces the possible heat flux range because the critical heat flux is reached in the contact area sooner, since the liquid flow to the gap between the surface and the electrode is hindered by the bubbles and the electrode itself.

The infrared transparent heater is positioned on top of an opening through the mounting flange, allowing the observation of the backside of the CrN layer by the infrared camera. The infrared camera (X6901sc

by *FLIR*) is attached to a special mount below the boiling cell, enabling a 3-dimensional local adjustment of the camera, as shown in Figure 3.5a. Due to the small working distance of 50.8 mm of the microscope lens, it has to be inserted into the hollow of the distance flange, which is visible in Figure 3.5b. A simple cooling system utilizing compressed air is installed to prevent the lens from heating up. Controlling the temperature of the microscope lens is important, since the infrared radiation of the lens can alter the measurement results, in case the lens' temperature differs from the calibration temperature. The temperature between lens and insulation is monitored by a thermocouple.

3.1.4 Copper heater module

The large heater module, called copper heater module, is visible in Figure 3.6a. It consists of the copper heater itself, a mounting flange, and a distance flange, which connects the mounting flange to the boiling cell. The mounting flange of the copper heater module has three stakes to hold the copper heater and feed throughs for five thermometers and two copper wires.

The copper heater itself consists of two parts, which are screwed together, as shown in Figure 3.6b. The upper part is a copper cylinder (35 mm diameter and 35 mm height) thermally pressed into a PEEK (Polyether-ether-ketone) cylinder for thermal insulation. There are four drilling holes for thermometers inside the copper cylinder. One thermocouple is used to measure the temperature 2 mm below the boiling surface, two Pt100s are distanced 7 mm from each other in the middle of the copper cylinder and one thermocouple is located at the bottom of the cylinder. This last thermocouple is installed for safety reasons, since the PEEK insulation must not become hotter than 300 °C, which is the highest short term operating temperature of PEEK. A 2-dimensional simulation in COMSOL Multiphysics showed that the hottest temperatures inside the PEEK insulation would be in the area the thermocouple is placed in; that is, above the copper disk at the bottom of the copper cylinder.

The lower part of the copper heater is also made of PEEK. It contains a spring, a flat ceramic heater, and feed throughs for copper wires to connect the ceramic heater to the power supply (PS9360-151U by *Elektro-Automatik*). If both parts of the copper heater are connected, the spring presses the ceramic

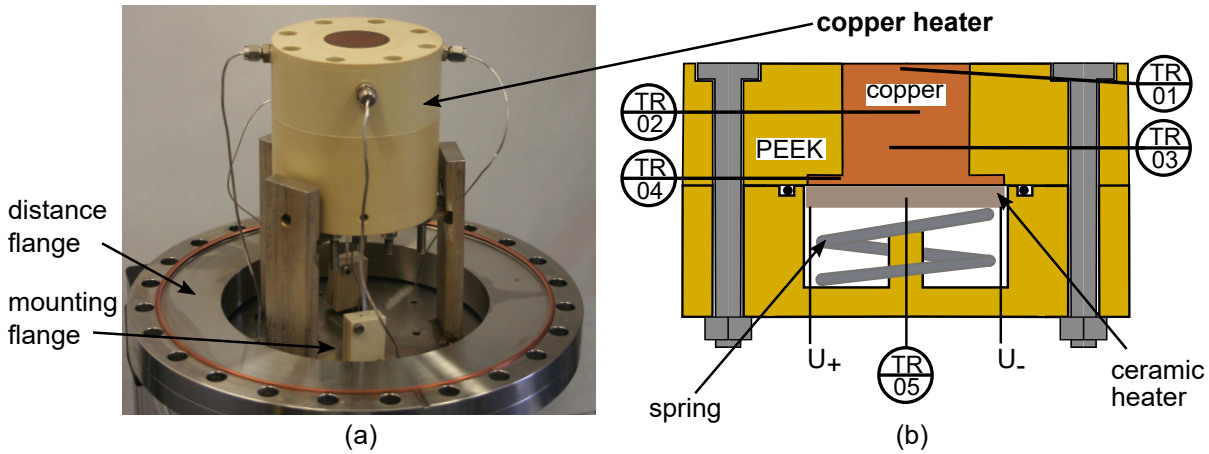

Figure 3.6: Image (a) of the copper heater module and sketch (b) of the copper heater.

heater against the copper cylinder ensuring thermal contact between both components at all times. This design was chosen because conventional cartridge heaters are prone to thermal runaway, due to different thermal expansion coefficients resulting in a lack of thermal contact. A thermocouple is used to monitor the temperature at the bottom of the ceramic heater.

Contrary to most other pool boiling experiments, the entire heater is submerged in the liquid. The main reason for this design is operational safety in case of elevated system pressures. The AD 2000 datasheets used to design this setup prohibit the use of plastics as pressure bearing components. However, a plastic insulation is necessary to prevent boiling in undesirable places, like the shell of the copper cylinder due to the low thermal conductivity of most plastics.

3.2 Boiling surfaces

The six different boiling surfaces used in this thesis are shown in Table 3.1. There, the name, the abbreviation, and a short description of the surfaces are presented. More detailed descriptions and characterizations of the surfaces are given in the following sections.

It was shown in the sections 2.4.1 and 2.4.2 that, although their common geometrical shape is cylindrical, micropillars and nanowires influence the boiling process differently due to their differing geometrical length scales. In order to investigate this further, a microstructure whose geometrical length scale is between the well-studied micropillars and nanowires was chosen for this thesis. The desired microstructures are manufactured by *Nanowired*, a spin-off company of TU-Darmstadt. The company keeps the exact manufacturing process secret, but a brief overview can be given. After cleaning, a membrane is glued to the surface. This membrane has holes with the desired diameters and center-to-center distances of the finished microstructure. The membrane is used as a template and copper is electrochemically deposited through the membrane until the desired length of the microneedles is reached. The membrane

Table 3.1: Boiling surfaces used in this thesis.

name	abbr.	description
long microstructured surface	20cu	smooth copper surface coated with 20 µm long copper needles
short microstructured surface	10cu	smooth copper surface coated with 10 µm long copper needles
optimized, hierarchical surface	Opt	smooth copper surface with alternating strips of 20 µm long copper needles and strips without needles
technical copper surface	Tcu	rough uncoated copper surface
smooth copper surface	Scu	smooth uncoated copper surface
smooth chromium surface	Scr	smooth chromium surface of the infrared transparent heater

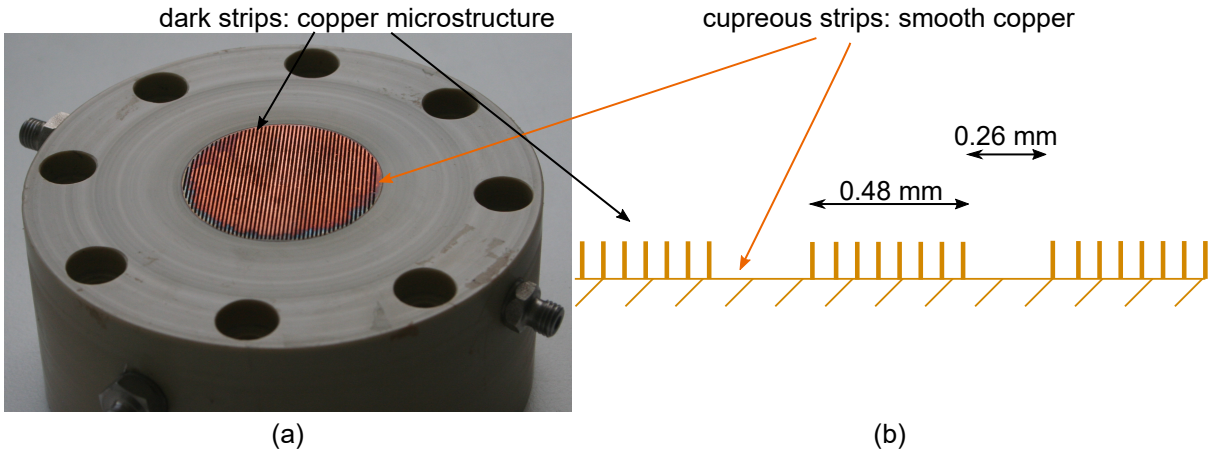

Figure 3.7: Image (a) and sketch (b) of the optimized, hierarchical boiling surface.

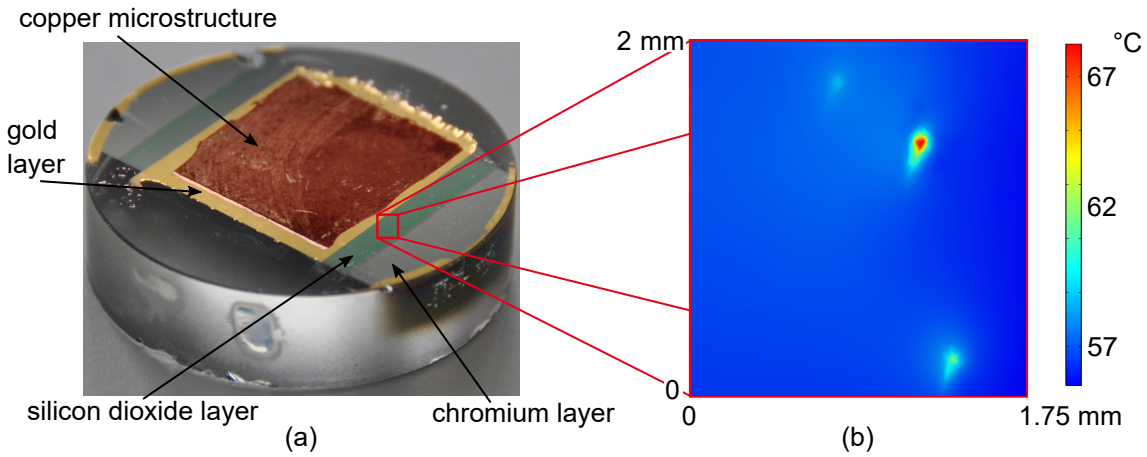

Figure 3.8: Image (a) of the microstructured infrared transparent heater and measured surface temperature field (b) showing hotspots in the SiO_2 layer.

is then dissolved, leaving the copper microstructure on the surface. Using this manufacturing technique, three microstructured surfaces were created.

20cu is the abbreviation for the long microstructured surface, the reference microstructured surface of this thesis, since the surface is manufactured onto a copper heater and the length of the microneedles is $l_{\mathrm{nd}} = 20\,\mu\mathrm{m}$. The diameter and center-to-center distance could not be varied systematically, as *Nanowired* did not have suitable membranes. The short microstructured surface, 10cu, though, has a reduced needle length of $l_{\mathrm{nd}} = 10\,\mu\mathrm{m}$. Opt is an optimized, hierarchical surface on top of the copper heater, which is visible in Figure 3.7a. The surface has a line pattern with a microstructure ($l_{\mathrm{nd}} = 20\,\mu\mathrm{m}$) and smooth copper surface alternating. The microneedle strips are $0.48\,\mathrm{mm} \pm 0.02\,\mathrm{mm}$ thick and the smooth surface strips are $0.26\,\mathrm{mm} \pm 0.03\,\mathrm{mm}$, as shown in Figure 3.7b.

To analyze the boiling process on a smaller length scale, a microstructured infrared transparent heater was manufactured, which is visible in Figure 3.8a. The microstructure is identical to the long microstructured surface. However, the manufacturing process was a lot more complicated compared to that of the copper heaters. For the copper heaters, the microstructure can be applied directly onto the surface. For the infrared transparent heater, auxiliary layers are necessary. Since the infrared transparent heater is

heated by Joule heating, an additional electrically isolating layer has to be applied between the Cr layer and the copper microstructure. Otherwise, the high conductivity of copper would result in the current passing through the microstructure. This isolating layer is made of SiO_2 and was applied by Julijan Cesar of the Institute for *Mikrowellentechnik und Photonik* of TU-Darmstadt. In addition to the isolating layer, a gold layer had to be deposited as adhesion agent, as shown in Figure 3.8a. This complicated new manufacturing process, in addition to the frailty of the CaF_2 crystal, resulted in the successful manufacturing of a single surface. On other heaters, the SiO_2 layer did not isolate perfectly or the crystal was destroyed in the manufacturing process of the microstructured surface. Unfortunately, the Cr layer of this successfully manufactured heater was damaged during the manufacturing of the SiO_2 layer, which later resulted in hot spots appearing on the surface during the experiments, which is shown in Figure 3.8b. There, a section of the surface temperature field determined with the infrared camera for the microstructured infrared transparent heater is presented. This particular section is situated below the SiO_2 layer and spots are visible that have significantly higher temperatures compared to the rest of the surface. These hot spots also caused the rupture of the CaF_2 crystal before bubbles could appear on the microstructured surface. As such, no data could be obtained using this microstructured infrared transparent heater.

3.2.1 Structural characterization

It was shown in section 2.2.1 that the surface characteristics have a significant impact on the boiling process [9, 78, 98]. The surface characteristics of the boiling surfaces are investigated using a scanning electron microscope (SEM) and a confocal microscope. The confocal microscope measurements are used to measure the mean roughness of the surfaces and the SEM measurements are used to confirm the dimensional accuracy of the production process. Unfortunately, SEM measurements could not be performed for the actual boiling surfaces because the heater geometry is too large. Thus, a smaller copper cylinder was coated with the same microstructure ($d_{\mathrm{nd}} = 1\,\mu\mathrm{m}, l_{\mathrm{nd}} = 20\,\mu\mathrm{m}$) as the actual boiling surface. The SEM images shown in Figure 3.9 were used to determine the diameter of the microneedles, the center-to-center distance between the needles, and the roughness factor r. r is the ratio of the surface area in contact with the fluid to the area of a smooth surface with the same dimensions [156].

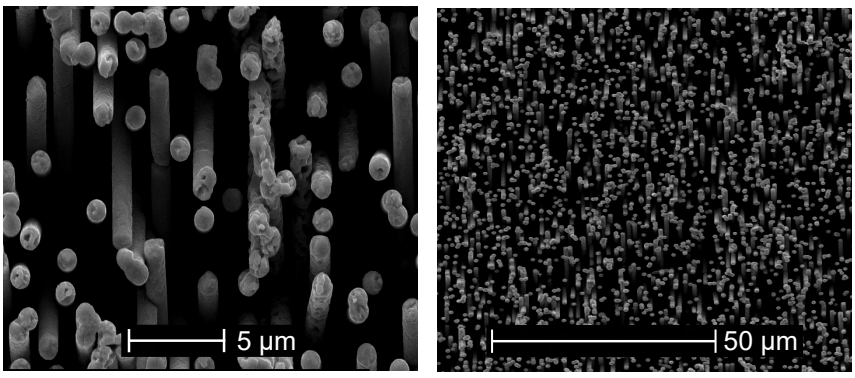

Figure 3.9: SEM images of a microstructured surface ($d_{\mathrm{nd}} = 1\,\mu\mathrm{m}, l_{\mathrm{nd}} = 20\,\mu\mathrm{m}$).

Table 3.2: Surface characteristics determined by SEM images.

	20cu	10cu	Opt
needle diameter in µm	1.006	1.006	1.006
center-to-center distance in µm	1.946	1.946	1.946
roughness factor r	17.59	9.29	11.76

Table 3.3: Mean roughness values of the boiling surfaces.

	20cu	10cu	Opt	Tcu	Scu	Scr
Sa in µm	1.56 ± 0.5	1.4 ± 0.08	6.5 ± 0.35	0.50 ± 0.04	0.009 ± 0.001	0.002 ± 0.0004
Sp in µm	10.8 ± 3.0	6.0 ± 0.52	23.7 ± 4.1	2.55 ± 0.47	0.10 ± 0.02	0.017 ± 0.008
Sv in µm	14.3 ± 0.8	5.8 ± 0.57	16.1 ± 1.5	5.10 ± 1.16	0.44 ± 0.24	0.023 ± 0.008

The parameters for the other microstructured surfaces (20cu, 10cu, and Opt) are determined using the measured parameters of this test surface, as shown in Table 3.2. The values determined from the SEM images confirm the dimensional accuracy of the production process. The area covered by needles is calculated to be 20.7 %, which is very close to the membrane porosity of 20 %, and the diameter of the copper needles is roughly 1 µm, which is the desired value. As can be seen in Figure 3.9, most of the copper needles are not standing upright but are slightly tilted to random directions. This is probably resulting from the membrane pores or the drying process. All in all, the copper needles are homogenously distributed among the surface, which is reason to believe that the actual boiling surfaces look similar to the tested one. It is assumed that the given values in Table 3.2 are in the same order of magnitude as the real ones, even though, the exact values of the actual boiling surfaces are unknown.

In addition to the geometrical parameters of the microstructures, the mean arithmetical roughness is a typical parameter to describe a surface and its impact on boiling heat transfer, since it is a parameter that is easy to measure and widespread in industry. Several researchers have shown a surface roughness dependency of the boiling process, which resulted in correlations incorporating a roughness parameter. A confocal microscope (µsurf expert by *Nanofocus*) is used to measure the roughness parameters. Besides the arithmetical mean area roughness (Sa), this device can evaluate the maximum peak height (Sp) and valley depth (Sv) above and below the mean level, respectively. The results for the microstructured surfaces are shown in Table 3.3.

The surface parameters of the long microstructured surface, 20cu, are expectedly higher compared to the short microstructured surface, 10cu, due to the longer copper needles. Since the hierarchical surface, Opt, is not homogeneous, the roughness parameters cannot be easily compared to the other surfaces. Sa and Sp of the hierarchical surface are larger because the copper surface below the microstructured strips and the remaining smooth copper surface have different heights, which results in larger values of Sa und Sp. The height difference is caused by the manufacturing process of the surface. In order to prevent deposition on the smooth surface area, it is coated with photoresist. When the membrane is placed on the surface, there is a small gap with the height of the photoresist layers between the membrane and

the precipitative copper surface. This area is then filled with copper, before the copper needles grow on top of it, resulting in an additional height difference between the smooth surface and the peaks of the microstructure.

The roughness values of three additional uncoated surfaces are also shown in Table 3.3. Tcu is the abbreviation for the technical copper surface, which emulates a copper surface found in evaporators. Scr is the smooth chromium surface of the infrared transparent heater and Scu stands for smooth copper surface. The latter surface was created because the surface roughness differs significantly between the technical copper surface and the smooth chromium surface. This would have made a comparison of the boiling results between the two surfaces difficult, since roughness has a large impact on the boiling process. Thus, an additional smooth copper surface was created having a significantly lower mean surface roughness compared to the technical copper surface. The uncertainties of the roughness parameters are due to the uncertainty of the confocal microscope and the standard deviation of the measurements.

3.2.2 Wettability and wickability characterization

Besides the surface roughness, the wetting and wicking behavior of fluid-surface combinations have a significant impact on the boiling process, as shown in the sections 2.2.2 and 2.4. The wetting and wicking behavior are analyzed using contact angle and imbibition measurements. The static and dynamic contact angles are determined using the drop shape analyzer DSA100 by *Krüss*. The static and dynamic contact angles for all the combinations of fluids (FC-72 and ethanol) and surfaces are smaller than 10° (visible in Figure 3.10) and, therefore, not measureable without large measurement uncertainties.

The imbibition or wicking of fluids into structures is investigated using the experimental setup of Michael Heinz, a colleague at the institute and collaboration partner in the CRC 1194. The collaborative research center 1194 focuses on the interactions between transport and wetting processes and there are three projects at the institute, besides the author's [1]. The entire setup and the experimental procedure are

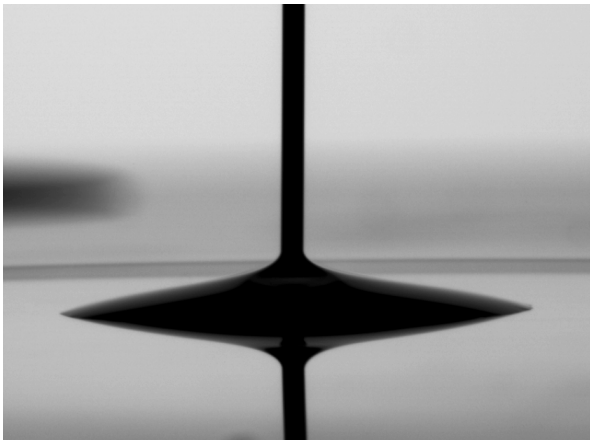

Figure 3.10: Image showing a contact angle measurement on the smooth copper surface Scu using ethanol.

[1] C02: Multiscale Investigations of Boiling of Complex Fluids on Complex Surfaces

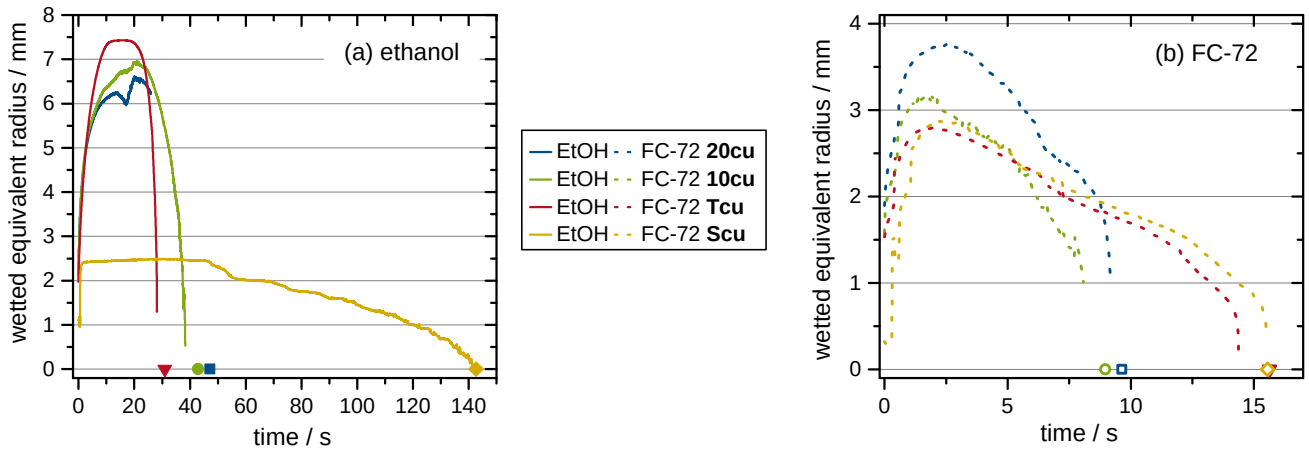

Figure 3.11: Evolution of the wetted equivalent radii of 2 µl drops of ethanol (a) and FC-72 (b) on four different surfaces.

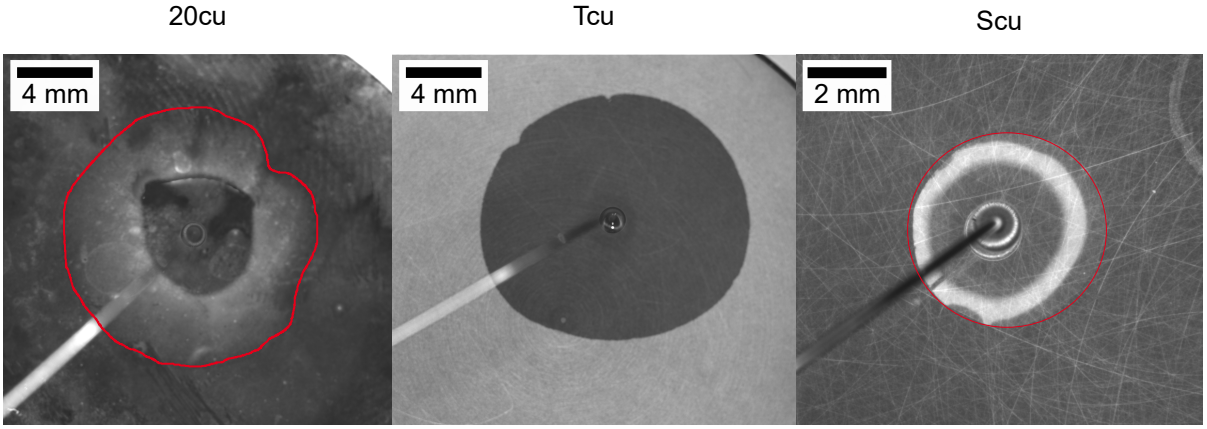

Figure 3.12: Images showing maximum expansions of ethanol drops (indicated by the red lines in case of poor contrast) on different surfaces.

explained in detail in [48], but a short overview will be given. The experimental setup allows drop impact and wicking experiments in a controlled air atmosphere. A syringe pump and cannulas of different diameters are used to generate drops of various volumes. A camera situated above the test subject visualizes the wicking process from above, enabling the measurement of maximum spreading radii and complete evaporation times, as well as imbibition velocities. The side camera is used to visualize the contact line dynamic during the drop impact phase, spreading, and evaporation phase. The images are evaluated using an algorithm described in [48]. The experiments are performed with 2 µl drops and a distance between the cannula and surface that is smaller than the drop diameter. Thus, the kinetic energy of the drops should be comparable.

The results of the measurements using ethanol (a) and FC-72 (b) are shown in Figure 3.11. The evolution of wetted equivalent radii are calculated based on the wetted surface area over time on the long and short microstructured surfaces 20cu, 10cu and the two uncoated surfaces Tcu and Scu. The curves correspond to the data, which is evaluated by an algorithm. However, if the contrast between wall and liquid is too low, the algorithm stops. Thus, the complete evaporation times are determined manually

and are presented by the symbols in Figure 3.11. For the measurements using ethanol, a significant difference can be seen in the spreading behavior on the smooth and technical copper surface. This is probably due to the increased roughness of the technical surface. The liquid can imbibe into the larger scratches and grooves, which results in the largest equivalent wetted radius and, therefore, the shortest evaporation time of all surfaces. On the smooth copper surface the contact line pins shortly after the drop impacts on the surface, which causes a significantly longer evaporation time. While ethanol imbibes into the microstructures, which is visible in Figure 3.12, the maximum wetted area is surprisingly smaller compared to the technical copper surface. A higher flow resistance to the wicking liquid might be causing this difference. The experiments using FC-72 drops do not show additional spreading on the technical copper surface. The wetted radius evolution is similar to the one of the smooth copper surface. The lower surface tension resulting in a lower capillary force, in addition to the faster evaporation rate, might cause the inability of the liquid to imbibe into the grooves of the technical copper surface. On the microstructured surfaces, slightly larger wetted radii are observed, resulting in shorter evaporation times.

In conclusion, the imbibition results would suggest significantly increased critical heat fluxes on the two homogeneously microstructured surfaces and the technical copper surface compared to the smooth copper surface, especially when using ethanol as boiling fluid. For FC-72, the critical heat fluxes of the two uncoated surfaces should be comparable, as no imbibition into the grooves of the technical copper surface is observable.

3.3 Experimental procedure

This section explains the experimental procedure of the conducted experiments. Since the procedure differs depending on the heater module, they will be introduced separately.

After a change of the boiling surface or fluid, the latter is degassed for at least five hours. Inert gases have a significant impact on nucleate boiling experiments and it is, therefore, necessary to remove them beforehand. Otherwise, the inert gases that entered the system overnight are removed by evacuation. Since the boiling cell has a high leak tightness of $2.5 \times 10^{-5}\,\mathrm{mbar\,l\,s^{-1}}$, an evacuation of the system once per day is deemed sufficient. The pressure inside the setup increases by a maximum of $\Delta p = 1.1 \times 10^{-4}\,\mathrm{bar}$ per day due to inert gases. Additionally, the amount of inert gases present inside the boiling cell is monitored by a pressure sensor and the fluid temperature, which is used to calculate the saturation pressure.

3.3.1 Experimental procedure using the copper heater module

A measurement campaign is typically a week long. After a change of surface and degassing of the fluid, the experiments start with the lowest system pressure of 0.4 bar. Experiments at system pressures of 0.4 bar, 0.7 bar, 1.0 bar, 3.0 bar, and 5.0 bar are performed throughout the week. The experiments for a specific system pressure are done throughout the day and measurements with an increased system

pressure are carried out the next day. The daily measurement routine is completely automated once the desired fluid temperature/system pressures, as well as heat fluxes, have been uploaded into the LabVIEW program, which controls the setup. Typically, the heat flux is incrementally increased and measurements are taken after the system reaches stationary state for each increment. Stationary state is reached once the liquid and wall temperatures averaged over the last 10 seconds is less than 0.04 K compared to the average liquid and wall temperatures five minutes prior. The data is then saved for one minute with a data collection rate of 30 Hz. Afterwards, b&w images of the boiling phenomena are taken with a framerate of 1000 Hz, followed by a further increase of heat flux. This process continues until the critical heat flux is reached. However, the actual value is not measured. The highest heat fluxes shown in the results are the last measured heat fluxes before burnout. After reaching burnout, the heat flux is set to zero until the surface is no longer in the film boiling regime. Since reaching critical heat flux leads to a rapid increase in the wall temperature, it is important to switch off the power supply to the heater as soon as possible. For this purpose, the program compares the temperatures measured inside the copper cylinder to the temperatures measured three seconds prior. If a single difference is larger than 2 K, the power supply is stopped. Two additional safety switches are implemented in case this first one malfunctions. If the copper temperature exceeds 250 °C or if the controlling program does not respond anymore due to an error message, the power supply is turned off automatically. This ensures the safety of the experiments and prevents the destruction of the surfaces. After the boiling regime transforms back to nucleate boiling, the heat flux is increased close to the critical heat flux and then decreased incrementally taking measurements along the way. Unless otherwise mentioned, the data shown in the results are the measurements taken with decreasing heat fluxes, as they are not influenced by boiling hysteresis.

3.3.2 Experimental procedure using the infrared transparent heater module

The measurement campaigns using the infrared transparent heater module are shorter compared to the copper heater module because the experiments covering the three system pressures (0.4 bar, 0.7 bar, and 1.0 bar) can be performed in a day. After degassing the liquid the day before, the temperature of the boiling fluid is increased until the system pressure reaches the highest desired pressure. After reaching steady state, the resistance of the transparent heater is measured, followed by a slow increase in the heat flux of the heater. Burnout must not be reached with this heater because it would result in its destruction. Due to the electrodes on the heater surface, burnout can occur at much lower heat fluxes compared to the copper heater. As such, the heat flux is only increased until $\dot{q} = 116\,\mathrm{kW\,m^{-2}}$ for the experiments with ethanol and $\dot{q} = 62\,\mathrm{kW\,m^{-2}}$ for FC-72. After reaching steady state, the infrared camera and the b&w camera are triggered simultaneously. The heat flux is then decreased step by step, taking measurements alongside until the part of the surface, which is observed by the infrared camera, is no longer in the nucleate boiling regime. Then, the fluid temperature is reduced until the system reaches the next desired system pressure and the procedure is repeated. The temperature inside the boiling cell is monitored during the experiments.

To ensure minimum calibration error, the infrared camera must not be moved between calibration and experiments. Furthermore, the temperature of the microscope lens should be the same and the intensity

range during calibration must exceed the intensity range of the experiments. To comply with these requirements, the infrared camera is calibrated alongside the experiments. The calibration process starts at the highest temperature observed during test measurements at the highest desired system pressure of 1.0 bar. A second temperature level is chosen between the highest calibration temperature level and highest experimental temperature level, which corresponds to a system pressure of 1.0 bar. After the calibration measurement at a system pressure of 1.0 bar, the heat flux is increased and the experiments are conducted. The system pressure and, therefore, the temperature is then reduced to 0.7 bar. Following the calibration and experimental measurements, the system pressure is reduced to 0.4 bar, where calibration and experimental measurements are also taken. Contrary to experiments using the large copper heater, no experiments at elevated pressures are performed as it is deemed unsafe due to the fragility of the infrared transparent heater.

Chapter 4

Data Evaluation

This chapter presents the data obtained by the b&w camera, the infrared transparent heater module and the copper heater module. Additionally, the data processing, the calculation of derived values, and their uncertainties are shown. Firstly, the data evaluation of the b&w images is presented, since b&w images are evaluated for both heater modules. Afterwards, the data evaluation of the infrared transparent heater module is followed by the data evaluation of the copper heater module.

4.1 Data evaluation for b&w imaging

As mentioned in section 3.1.1, a b&w camera is used to visualize the boiling process. Two different lenses are used to either calculate the bubble diameters or visually differentiate between boiling regimes. No further post processing except cropping of the image is necessary to do the latter.

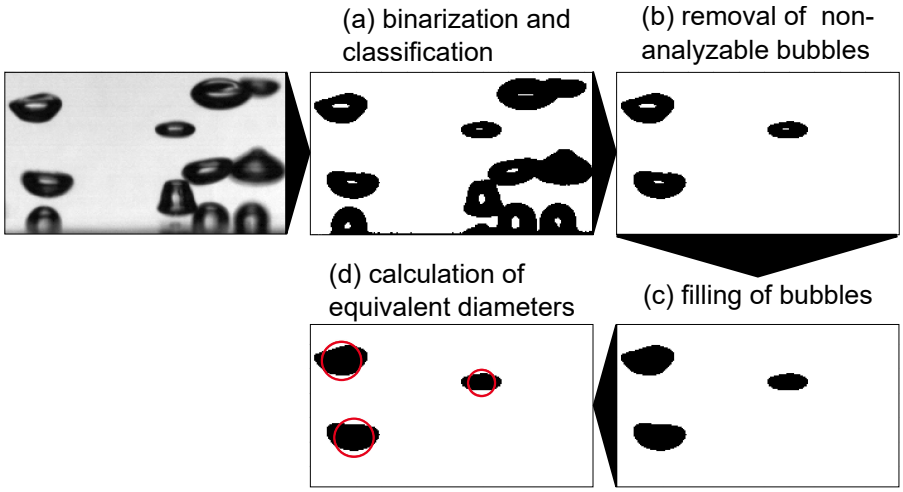

Figure 4.1: The equivalent bubble diameters are determined through image processing: (a) binarization and classification (black pixels are vapor, white pixels are liquid), (b) removal of non-analyzable bubbles, (c) filling of bubbles, and (d) calculation of equivalent diameters.

To extract bubble diameters from images, additional post processing is performed in Matlab, which is presented in Figure 4.1. Firstly, the image is binarized, as shown in Figure 4.1a. The bubbles appear dark in the images, whereas the liquid is greyish; therefore, binarization is achieved using a specific grey scale threshold. The center of larger bubbles can appear lighter due to less curvature and, therefore, weaker refraction of light. This results in wrong classification, which is seen in Figure 4.1a, because black pixels (1) are classed as vapor and white pixels (0) are classed as liquid.

Secondly, bubbles which should not be analyzed are discarded, as shown in Figure 4.1b. The reasons why bubbles might be removed are coalescing bubbles, bubbles partially leaving the image, and bubbles overlapping with each other. The incorporation of overlapping or coalescing bubbles would result in a significant error of the mean bubble diameter. Five criteria are used to determine if the bubbles should be removed or not. The first and second criteria are based on the size of the bubble. Reasons for a bubble being too small after binarization could be a bad pixel or a contamination inside the liquid. Multiple overlapping bubbles will be removed since the conglomeration is larger than a defined threshold value. Bubbles being partially outside of the image are removed by the third criterion. The fourth criterion checks the symmetry of the bubble. Significantly unsymmetrical bubbles could be caused by either overlapping or coalescing bubbles. The fifth criterion addresses this issue as well, by checking for inhomogeneous patterns inside the bubble. The algorithm checks if there are multiple white pixel clusters, inside the supposed bubble. This might be the case, if multiple large bubbles are overlapping with each other, since the bubble centers are wrongly classed as liquid (white pixels), which is explained in the previous paragraph. Thirdly, after the removal of the unwanted bubbles, the centers of the bubbles are set to unity, which corresponds to vapor, making the bubbles homogeneous, as shown in Figure 4.1c.

Fourthly, the center of a bubble is calculated and its area is assessed. This area is used to calculate an equivalent bubble diameter, which is presented in Figure 4.1d. For a typical experiment the number of evaluated bubbles is larger than a hundred, therefore, a mean diameter is calculated for each experiment. A conversion factor, which is described in the next section, is used to translate the diameters from pixels into millimeter.

The thresholds determining the binarization and the bubble removal are set manually before evaluating each experiment. A computer generated set of threshold values is not viable, due to significant differences in boiling behavior depending on fluid, system pressure, and heat flux.

Measurement uncertainties and uncertainties of derived values

The measurement uncertainties and the uncertainties of the derived values presented in the following sections are standard deviations. In some cases, where the actual distribution is unknown, a rectangular distribution is chosen, which is indicated by R, and in the other cases a Gaussian distribution (G) is assumed [55]. The error propagation is calculated using the Gaussian error propagation.

The bubble diameter error results from different individual errors. One error is due to low contrast in the images, which is shown in Figure 4.2. Another error occurs due to an imprecise translation between

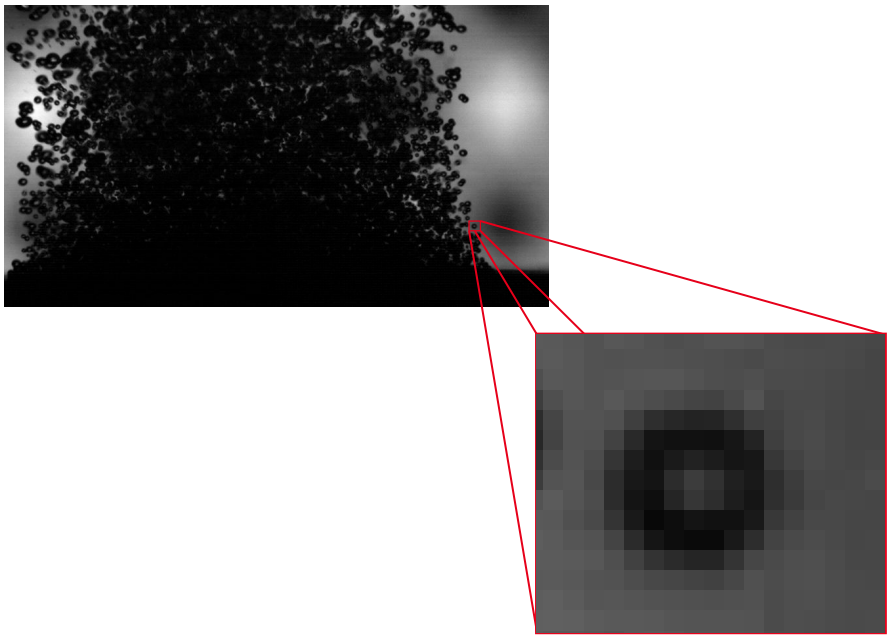

Figure 4.2: B&w image and a zoomed in part of the latter image, showing a bubble and the lack of contrast.

pixels and millimeter. Furthermore, an error occurs due to wrong classification or incorrect bubble size calculation of the algorithm.

Concerning the error due to low contrast, Figure 4.2 shows a b&w image and a zoomed in image of one bubble. It is observable that the greyscale gradient between bubble and liquid extends over four pixels. Since the binarization of the image would result in a bubble boundary inside this gradient, the error of the diameter due to the lack of contrast is four pixels, which is approximately $\Delta d_{\mathrm{b,cont,R}} = \pm 0.12\,\mathrm{mm}$.

Concerning the error due to an imprecise translation between pixels and millimeter, the conversion factor between pixel and millimeter can be calculated using three different reference geometries, as shown in Figure 4.3. A thermometer could be used as a reference that is inside the depth of focus of the lens (Figure 4.3a). The holder of the infrared transparent heater module (Figure 4.3b) or the heated area of the copper heater module (Figure 4.3c) could be also used as references. Since the images are obtained during the experiments, the error stems from a lack of contrast similar to the first error and faulty assumptions of the geometric dimensions of the reference geometries. For measurements using the reference thermometer, this error is $\Delta d_{\mathrm{b,pm,therm,R}} = \pm 0.052 d_{\mathrm{b,pm,therm}}$ (Figure 4.3a), which is larger than the error caused by using the holder of the infrared transparent heater module as reference $\Delta d_{\mathrm{b,pm,Cr,R}} = \pm 0.029 d_{\mathrm{b,pm,Cr,}}$ (Figure 4.3b). If the heated area of the copper heater module is used to determine the conversion factor, the error is $\Delta d_{\mathrm{b,pm,Cu,R}} = \pm 0.04 d_{\mathrm{b,pm,Cu}}$ (Figure 4.3c).

Another error is due to classification and faulty bubble size calculations of the Matlab script. This error is estimated by comparing the mean bubble diameters evaluated by the script compared to a manual eval-

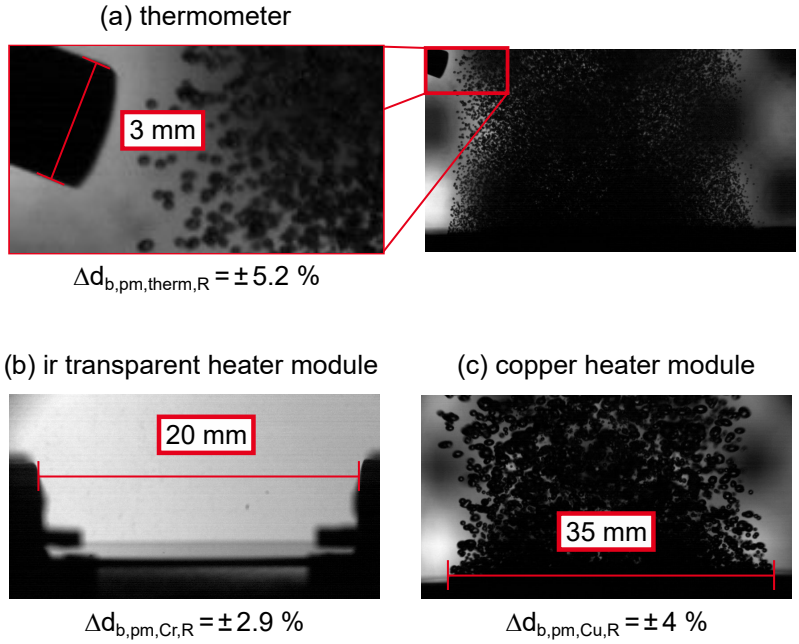

Figure 4.3: B&w images of the two heater modules showing the geometrical dimensions of the reference geometries used to calculate the conversion factor between pixel and millimeter ((a) reference thermometer, (b) holder of the infrared transparent heater module, and (c) heated area of the copper heater module). Additionally, the percental bubble diameter errors are depicted resulting from inaccuracies in determining the conversion factor.

uation. Five different experiments were compared and the resulting mean error is $\Delta d_{\mathrm{b,al,G}} = \pm 0.06 d_{\mathrm{b,al}}$. The combined uncertainty of the mean bubble diameter is calculated accordingly:

$$\Delta d_{\mathrm{b}} = \sqrt{\Delta d^2_{\mathrm{b,cont,R}} + \Delta d^2_{\mathrm{b,pm,R}} + \Delta d^2_{\mathrm{b,al,G}}}. \tag{4.1}$$

As an example, for bubbles with a mean diameter of $d_{\mathrm{b}} = 1.05\,\mathrm{mm}$ that are evaluated using the heated area of the copper heater, the error is $\Delta d_{\mathrm{b}} = \pm 0.136\,\mathrm{mm}$.

4.2 Data evaluation for the infrared transparent heater module

As mentioned previously, the infrared camera is used to investigate the local wall temperatures of the infrared transparent heater. The infrared camera does not measure temperature directly; rather, it measures the photon count per pixel. This means the intensity signal has to be converted into a temperature signal, which is achieved by calibrating the infrared camera. A pixel-wise in situ calibration is chosen because the accuracy of the resulting temperature signal is much higher, compared to a global calibration according to Sielaff [135]. Assuming that the heater surface has fluid temperature during the calibration measurements, the measured intensity data is fitted by a polynomial to the fluid temperature data measured during calibration. This is done for every pixel individually. In the polynomial, which is based on

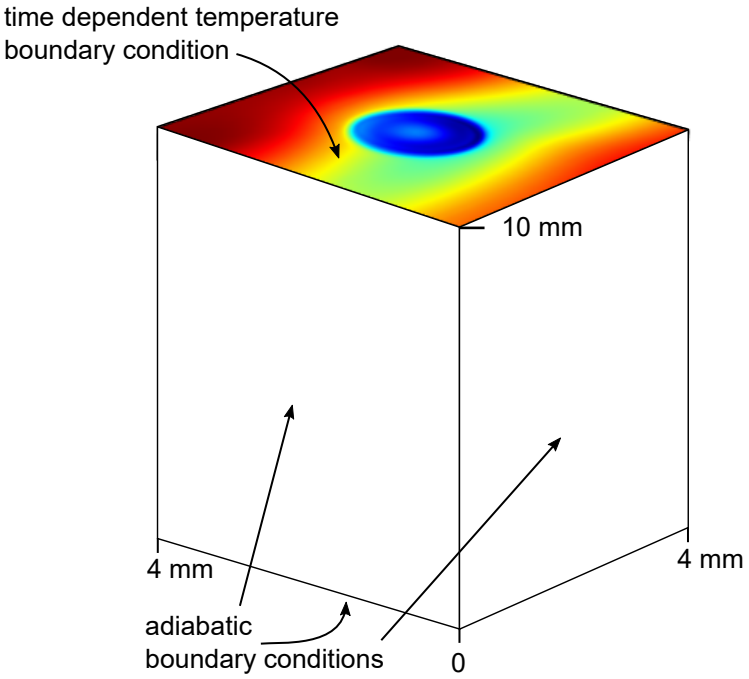

Figure 4.4: Evaluated section of the infrared transparent crystal with boundary conditions.

the Stefan-Boltzmann equation, the temperature is proportional to the intensity Ψ to the power of 0.25 [135]:

$$T = D\left[(\Psi + B)^{0.25} + C\right], \tag{4.2}$$

B, C, and D are the calibration coefficients, whose physical interpretation can be found in [33].

As previously discussed, the local heat fluxes can be calculated using the local temperature data. The local heat fluxes are determined using a simulation in COMSOL Multiphysics. In order to save computation time, only a section of the entire heater is simulated. Depending on the bubble sizes a 2 x 2, 4 x 4, or 6 x 6 mm^2 section, each 10 mm thick is generated in COMSOL Multiphysics. Figure 4.4 shows a 4 x 4 mm^2 section with the corresponding boundary conditions. The side and the bottom boundaries are adiabatic. This assumption is discussed in the following measurement uncertainty section (Figure 4.11). The top boundary is the local temperature field obtained from the intensity data. As the temperature data consists of a matrix with discrete temperatures corresponding to individual pixels, the temperature field has to be smoothened by a linear interpolation for the simulation. The two sputtered Cr and CrN layers are both excluded from the simulation since the thermal capacities and conductivities of the layers are negligible due to the small thickness of the layers (approximately 400 nm each). The initial temperature is the average temperature over the first 10 ms of the corresponding analyzed data set. The thermal boundary layer inside the evaluated section will form in the first time steps of the simulation. This results in large heat fluxes at the beginning of the simulation and, thus, the results of the first 50 ms are discarded from further evaluation steps.

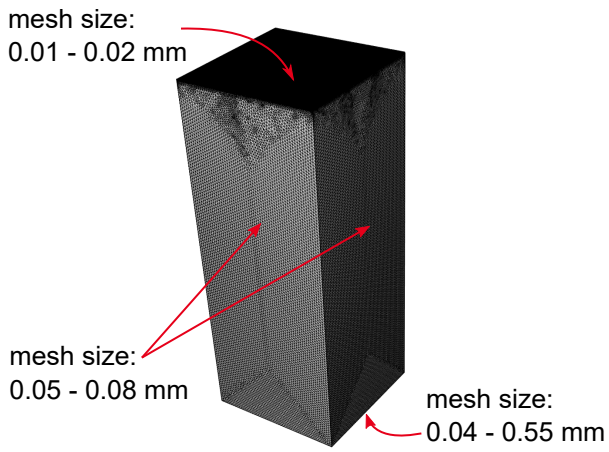

Figure 4.5: 3-dimensional mesh and its dimensions used for local heat flux calculations in COMSOL Multiphysics.

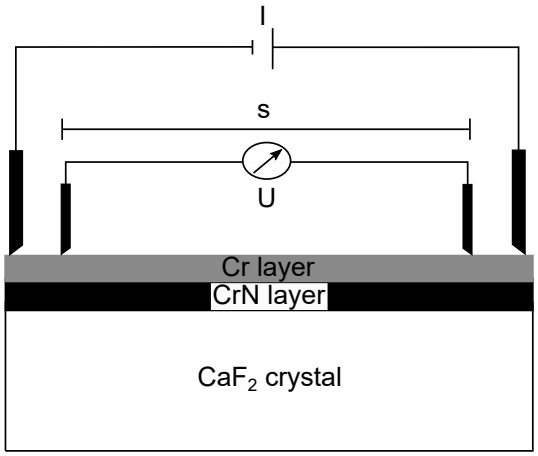

Figure 4.6: Sketch of the four-point measuring device with the parameters necessary to calculate φ.

The mesh, shown in Figure 4.5, consists of an unstructured tetrahedral mesh. The mesh size on top is 10 to 20 µm, which is smaller than the pixel size of 25 µm. The mesh size at the sides is between 50 and 80 µm. The bottom mesh size is between 40 and 550 µm with a high elemental growth rate of 1.4. The results calculated in COMSOL Multiphysics are transferred into Matlab and converted into 3-dimensional (x, y, t) arrays similar to the input temperature data. Since the Cr and CrN layers were not implemented in the simulations, the input heat flux, which is generated in the Cr and CrN layers due to their electrical resistance, is not included in the numerically calculated heat flux $\dot{q}_{\mathrm{num}}$. The overall local heat flux is then calculated by Equation 4.3:

$$\dot{q}_{\mathrm{lc}} = \dot{q}_{\mathrm{el}} + \dot{q}_{\mathrm{num}}. \tag{4.3}$$

The heat flux generated by Joule heating $\dot{q}_{\mathrm{el}}$ requires the resistance density φ of the Cr and CrN layer to be calculated:

$$\dot{q}_{\mathrm{el}} = \varphi\, I^2. \tag{4.4}$$

The resistance density of the Cr and CrN layers is calculated using a four-point measuring device, which is shown in Figure 4.6. The resistance density is calculated using the measured current I, voltage U, Cr layer width l, and distance between the two edges s of the resistance measuring device:

$$\varphi = \frac{U}{I\, l\, s}. \tag{4.5}$$

Since the resistance of the Cr and CrN layers is dependent on the temperature, it is assessed for five different temperatures up to 120 °C and a quadratic equation is fitted to the measurement points. The different temperatures of the infrared transparent heater are achieved by placing the latter in an oven.

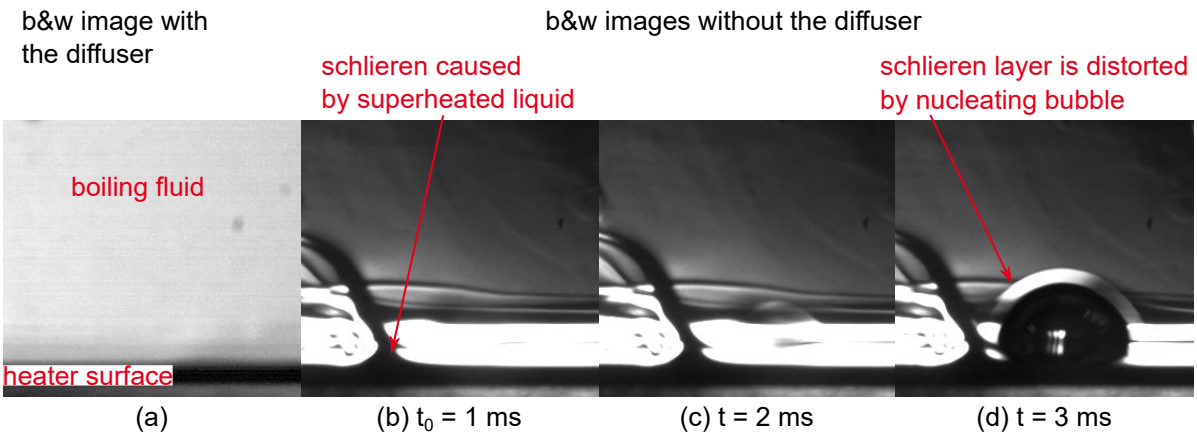

Figure 4.7: B&w images with (a) and without the diffuser for three consecutive time steps (b), (c), and (d) showing the smooth chromium surface and schlieren caused by the superheated liquid.

Besides temperature and local heat flux, the bubble expansion velocity is the third parameter, which is determined based on the measured intensity data. As shown in section 2.1.4.1, the bubble expansion velocity is one of the deciding parameters governing the microlayer formation. To determine the bubble expansion velocity, the position of the macroscopic contact line has to be known. Unfortunately, its position cannot be measured using b&w images, since the heater surface is not visible, which can be seen in Figure 4.7. Figure 4.7a shows a b&w image captured with a diffuser, which is used for homogeneous illumination of the heater surface. The boiling fluid and the heater surface can be distinguished and no fluidic inhomogeneity is visible. The latter is revealed if the diffuser is removed, as shown in Figure 4.7b. During the measurements, a thermal boundary layer is formed, whose refraction index differs from the surrounding cooler liquid due to its elevated temperature. This causes schlieren, which make the precise localization of the contact line in the b&w images impossible, as seen in Figure 4.7b, c, and d. There, b&w images without the diffuser for three consecutive time steps are shown. As the bubble is still submerged in the thermal boundary layer, a distortion of the latter might be visible in Figure 4.7c, while no bubble related disturbance is observable in Figure 4.7b. In the following time step (Figure 4.7d) the bubble and the surrounding superheated liquid layer are visible, the contact line of the bubble, though, is still submerged inside the thermal boundary layer.

Thus, the bubble expansion velocity is determined using the local heat flux data, as shown in Figure 4.8. The bubble expansion velocity is determined via the temporal extent of the microlayer, shortly after bubble nucleation. As seen in Figure 4.8a, the heat fluxes transferred by the microlayer and the contact line are higher compared to the rest of the surface. It is assumed that the microlayer beneath the bubble causes an increased heat flux over its entire length and the microlayer extent visible in the local heat flux field corresponds to the bubble extent close to the surface. Via a heat flux threshold, the bubble extent close to the surface is determined, as shown in Figure 4.8b and c. For the first three bubbles, the threshold is manually iterated to fit the visually detected bubble extent as good as possible, which is shown in Figure 4.8c. If a satisfying threshold is found, the data set is analyzed.

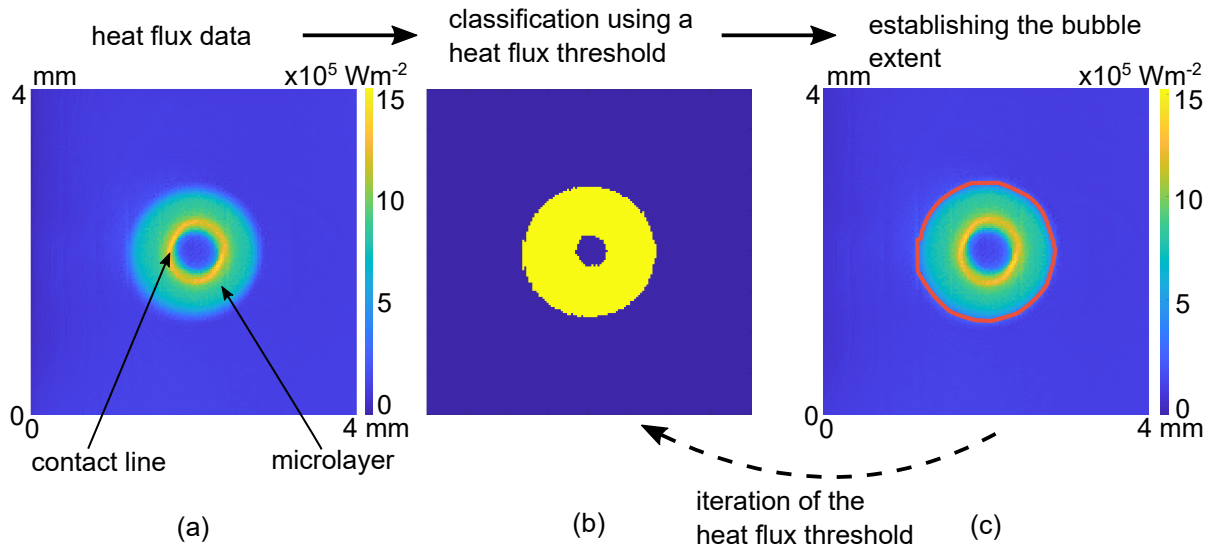

Figure 4.8: Heat flux threshold iteration: (a) heat flux field showing the bubble footprint, contact line and microlayer, of a growing ethanol bubble, (b) classification of the bubble extent, (c) heat flux field and calculated bubble extent (red line) on the surface.

Measurement uncertainties and uncertainties of derived values

Uncertainties of the intensity and wall temperature

The measurement uncertainty of the intensity of the infrared measurements is due to noise of the detector chip of the infrared camera. While the examined wall temperature is constant, a random intensity fluctuation is visible. The maximum standard deviation of all pixels of a specific calibration file is calculated to evaluate the measurement uncertainty caused by the intensity fluctuations. After the evaluation of each calibration file, the mean value of the maximum standard deviations is calculated to obtain an average value $\Delta\Psi_G = \pm 20.88$ counts for the intensity error due to noise, over the entire calibrated intensity range. The uncertainty of the intensity causes an error in the calculated temperature data. By calculating the product between the measurement uncertainty of intensity and the mean gradient of the polynomials used for calibration, the temperature error due to the intensity noise is $\Delta T_{\Psi,G} = \pm 0.2\,\mathrm{K}$.

The assumption that the temperature of the boiling surface is equal to the temperature and intensity measured at the back of the CrN layer causes an error in the temperature data. However, since the Cr and CrN layers are very thin (400 nm each), the error is assumed to be negligible. Additionally, due to a lack of ideal conditions during calibration, the measurement uncertainty of the thermometers used for calibrating the intensity data, and deviations from the fitted polynomial cause errors in the temperature data. During calibration, it is important that the temperatures of the infrared camera, its microscope lens, and its surroundings do not change, as temperature differences result in intensity variations, while the observed object has the same temperature. A cooling system is implemented as the microscope lens is surrounded by heated walls, which is shown in Figure 3.5b. With the aid of this system, the temperature of the lens only varies by 2 K, while the temperature of the observed object changes in total by 70 K. The impact of this discrepancy is, however, hard to quantify. The error is assumed to be

around $\Delta T_{\mathrm{le,R}} = \pm 0.02 T_{\mathrm{w}}$. The temperature error of the thermometers used for calibration is $\Delta T_{\mathrm{therm,G}} = \pm 0.079\,\mathrm{K}$. To account for deviations between the fitted polynomials and calibration data, the intensity data sets obtained during calibration are calibrated themselves and the resulting temperature values are compared to the reference temperatures. The mean deviation is $\Delta T_{\mathrm{poly,R}} = \pm 0.04\,\mathrm{K}$. The total error is then calculated by a quadratic summation of the single errors:

$$\Delta T_{\mathrm{w}} = \sqrt{\Delta T_{\Psi,\mathrm{G}}^2 + \Delta T_{\mathrm{le,R}}^2 + \Delta T_{\mathrm{therm,G}}^2 + \Delta T_{\mathrm{poly,R}}^2}. \tag{4.6}$$

As an example, the temperature error is $\Delta T_{\mathrm{w}} = \pm 1.42\,\mathrm{K}$ for a wall temperature of $T_{\mathrm{w}} = 70\,^{\circ}\mathrm{C}$.

Uncertainty of the local heat flux

The uncertainty of the local heat flux can be attributed to uncertainties of the temperature boundary condition, the assumption of adiabatic boundary conditions on the remaining surfaces, the mesh size, numerical errors, and errors due to the starting condition. Since the heat flux on the surface is calculated using the temporal changes of the wall temperature, only the error due to intensity noise has to be taken

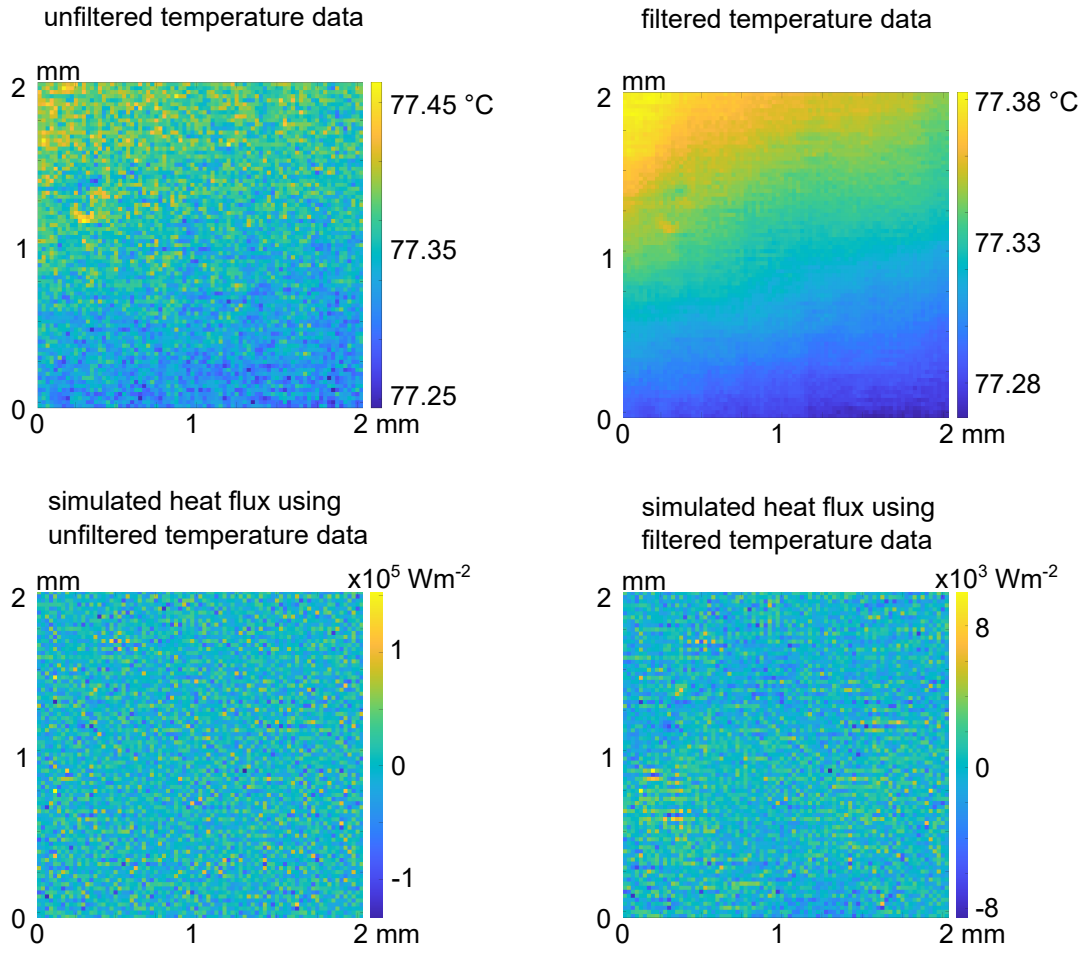

Figure 4.9: Comparison between simulated heat flux data using filtered and unfiltered temperature data and the temperature data themselves showing a calibration case.

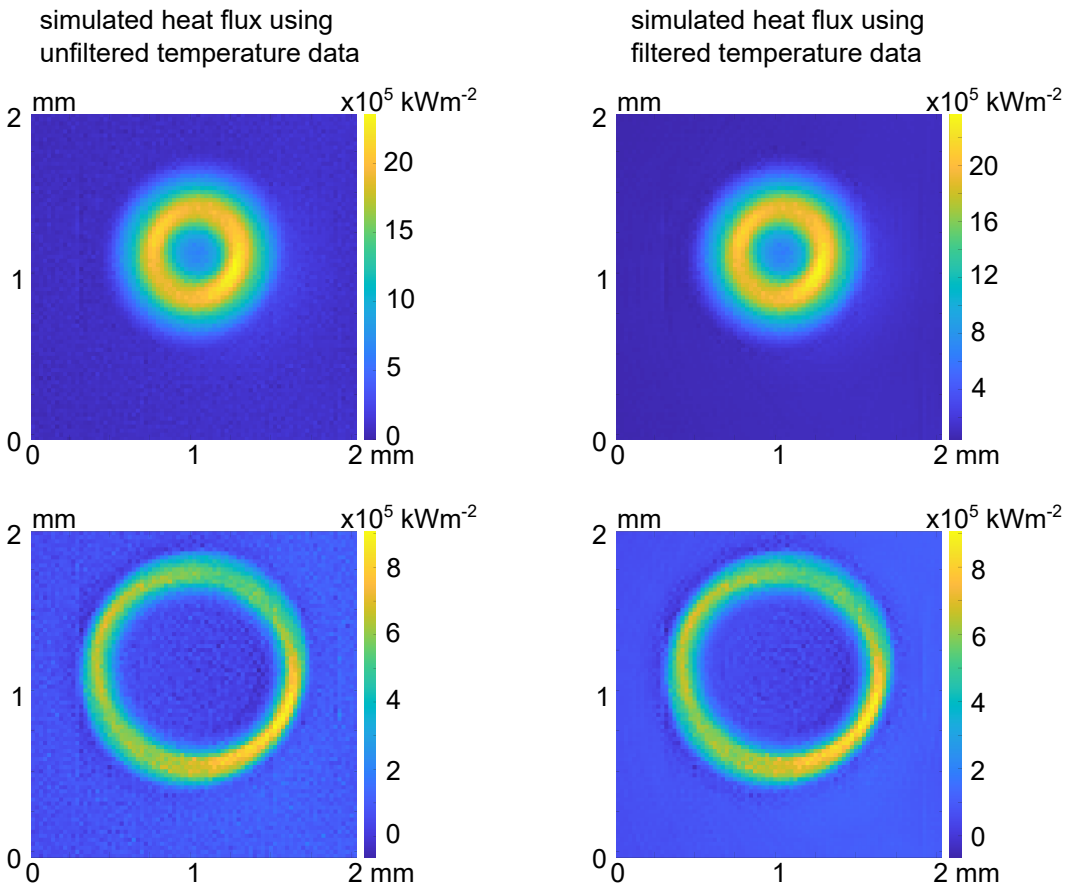

Figure 4.10: Comparison between simulated heat flux data using filtered and unfiltered temperature data showing a bubble footprint at two specific time steps.

into consideration. However, in the scope of this thesis it is impossible to calculate the resulting heat flux uncertainty analytically based on the temperature noise. Thus, the heat flux noise is analyzed independently.

In order to reduce the error, the input temperature data is filtered using a Gaussian filter. Figure 4.9 shows an unfiltered temperature data set and the corresponding filtered temperature data set of a calibration measurement (isothermal) alongside the calculated local heat fluxes. The Gaussian filter reduces the observed noise in the local heat flux data by an order of magnitude. Although the noise is reduced significantly, the mean temperature and heat flux difference between the two shown temperature and heat flux data sets are negligible, with 0.0002 K and 90.94 W m^{-2}, respectively.

In case a heated measurement is evaluated similar to the aforementioned calibration measurement, Figure 4.10 shows that the heat flux profile below a bubble does not seem to be influenced by the filter gravely. The difference in mean heat fluxes between the presented images is very small, as expected (12 W m^{-2}). Thus, it is assumed that the Gaussian filter does not influence the temperature and heat flux data negatively. The reduction in input temperature noise, however, reduces the resulting heat flux noise by a factor of 10, which reduces the mean uncertainty of the heat flux due to noise to $\Delta\dot{q}_{\mathrm{lc,ran,G}} = \pm 21.50\,\mathrm{kW\,m^{-2}}$.

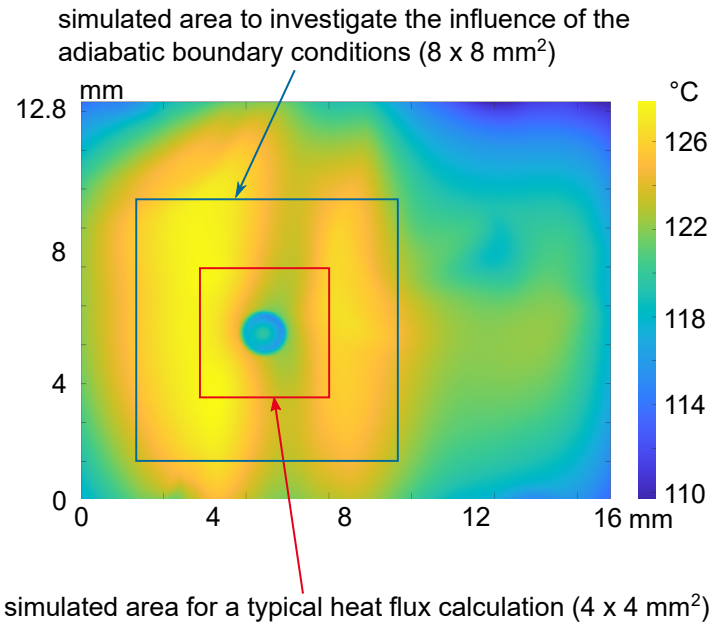

Figure 4.11: Local temperature data of the entire field of view of the infrared camera and red and blue rectangles indicating areas, which are used for simulations.

Figure 4.11 shows a temperature field, which is evaluated based on the intensity data in the field of view of the infrared camera. It is obvious that the temperature field is not homogeneous, which is due to the inhomogeneous distribution of nucleation sites on the surface. Due to a more efficient heat transfer at the nucleation sites, the temperature is lower in comparison to the rest of the surface. To save computation time, only a small area (4 x 4 mm^2) around a bubble is used to calculate local heat fluxes, which is indicated by the red rectangle in Figure 4.11. The inhomogeneous temperature field suggests heat fluxes, which are transferred inside the CaF_2 crystal through the boundaries of the simulated volume. However, as shown in Figure 4.4, adiabatic boundary conditions are applied to all boundaries except for the top boundary, which uses the temporal temperature field. This causes an additional error in the heat flux data, which is evaluated by an additional simulation. For this simulation, a larger area of 8 x 8 mm^2, indicated by the blue rectangle in Figure 4.11, is used and the results are compared to the ones of the 4 x 4 mm^2 simulation.

Figure 4.12 shows the results of the 4 x 4 (a) and 8 x 8 mm^2 simulations (b). For comparison, only a 4 x 4 mm^2 section of the 8 x 8 mm^2 simulation is presented. It is obvious that the heat flux profiles do not differ dramatically either quantitatively or qualitatively. The difference in the mean heat flux is 777 $W\,m^{-2}$. The results of the 8 x 8 mm^2 simulation, however, show larger and smaller maximum and minimum heat fluxes compared to the 4 x 4 mm^2 results. The minimum and maximum heat flux values differ by 26.4 $kW\,m^{-2}$ and 61.0 $kW\,m^{-2}$, respectively. However, only 2 out of 25600 pixels are smaller and 2 are larger, respectively, than the minimum and maximum values of the 4 x 4 mm^2 simulation. Therefore, it is assumed that those differences are due to numerical errors, as there is no physical explanation for those differences. Such numerical errors could be caused by e.g. interpolation between the discrete temperature nodes of the temporal boundary condition by COMSOL Multiphysics. In conclusion, although the

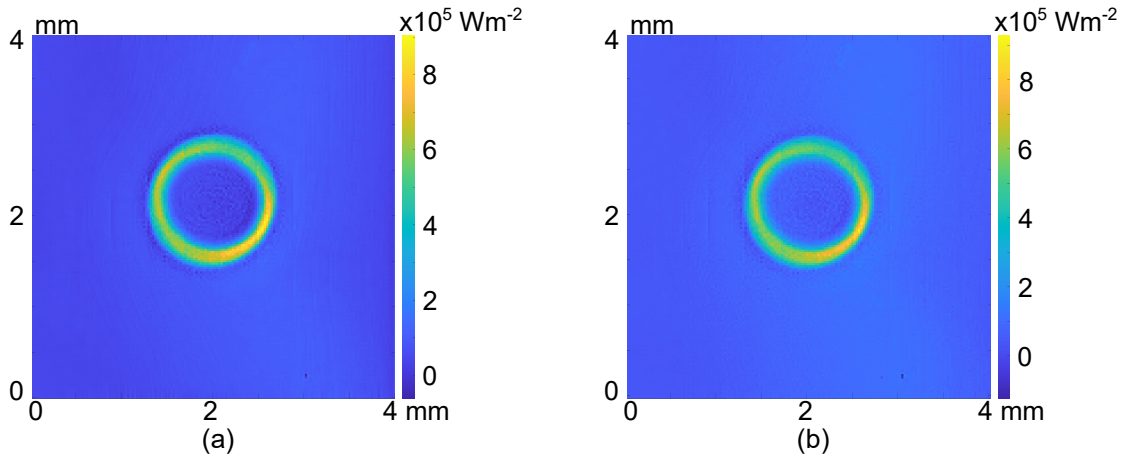

Figure 4.12: 4 x 4 mm^2 sections of the heat flux fields calculated using a 4 x 4 mm^2 area (a) and an 8 x 8 mm^2 area (b) for the simulations.

local temperature distribution is notably inhomogeneous in this data set (Figure 4.11), the mean heat flux error due to the adiabatic boundary conditions is significantly smaller than the error due to the random temperature noise. Although the mean heat flux error caused by the adiabatic boundary conditions is negligible, larger deviations of the maximum and minimum heat fluxes of a few pixels are observable. The deviations are significant for each pixel; however, large deviations are limited to a few pixels. Since the maximum or minimum heat fluxes are not used in this thesis and their influence on the average heat flux below a bubble is negligible, the influence of this numerical error is deemed insignificant. Thus, the errors due to the adiabatic boundary conditions are negligible.

Additional numerical errors are analyzed by calculating the mean heat flux of the data sets. Since there is no heat source included in the simulations and the mean temperature of the heater should not change due to the measurements being performed at steady state, the mean heat fluxes should be zero. A deviation can be attributed to numerical errors. The standard deviation of the mean heat flux deviations is $\Delta\dot{q}_{\mathrm{lc,num,G}} = \pm 908.41\,\mathrm{W\,m^{-2}}$ for all datasets.

The influence of the mesh size on the calculated heat fluxes is analyzed by a mesh study. The results of the mesh study are shown in Table 4.1 and Figure 4.13. The heat flux fields in Figure 4.13 visually indicate that no improvement of the qualitative results could be achieved for smaller mesh sizes than medium (Table 4.1). However, quantitatively, no clear trend is visible in Table 4.1. The mean heat fluxes of the entire data set and the mean heat fluxes of an exemplary frame do not show a clear trend. It is unknown, why a clear trend is missing. It might be possible that the used mesh sizes are too similar. However, the mesh size chosen for evaluation should not be larger than the medium sized mesh in Table 4.1, as the heat flux fields showed qualitative differences for larger mesh sizes as shown in Figure 4.13. Using even smaller mesh sizes is also not recommendable, as the computation time (20 days for a data set) for the finest mesh size is already impractical. Additionally, the pixel size of the infrared camera and, therefore, the distance between the temperature nodes of the temporal boundary condition is 25 µm, which is significantly larger compared to the finest mesh size. Using an even finer mesh size should not significantly increase the quality of the simulation results. It is assumed that the differences between the heat fluxes in Table 4.1 are partially due to errors caused by the data transfer between the

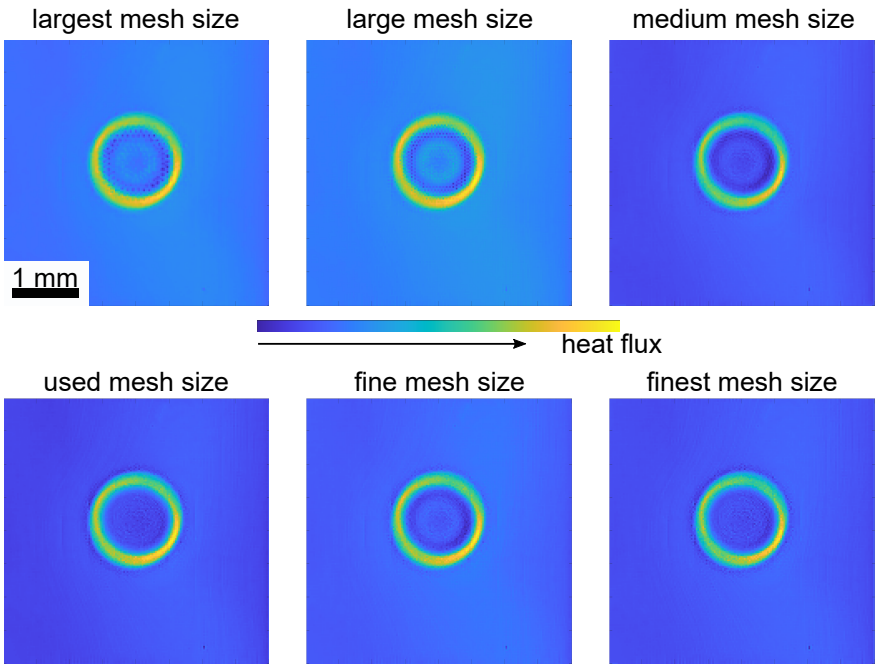

Figure 4.13: Heat flux fields of an exemplary frame for different mesh sizes.

Table 4.1: Results of the mesh study.

	largest	large	medium	used mesh size	fine	finest
number of elements	331k	416k	663k	1,244 k	3,459k	6,662k
max. element size top surface in µm	70	45	25	15	15	7
$\dot{q}_m$ entire data set in kW m^{-2}	3.45	3.44	3.55	3.47	3.64	3.52
$\dot{q}_m$ exemplary frame[1] in kW m^{-2}	15.3	14.3	14.9	19.5	15.0	18.5

Matlab script and COMSOL Multiphysics, as discussed above, since the results are reproducible using the same mesh size. Quantifying these numerical errors is not possible because the real heat flux value is unknown. Nevertheless, it can be concluded that the used mesh size does not lead to significant qualitative and quantitative deviations compared to finer mesh sizes.

The starting condition of the heat flux simulation can also lead to errors of the calculated heat flux. Typically, the mean wall temperature of the first 10 frames (10 ms) is used as the initial temperature. However, a difference in the mean heat flux of the 200th frame of 1.4 kW m^{-2} is observable, if the heat fluxes are calculated using the mean wall temperature of the 200th until the 210th frame or the mean wall temperature of the first 10 frames as initial conditions. However, the assessment of the error due to the initial condition is not possible because the true value cannot be defined. Thus, it is not calculated in this thesis. The reader, however, should keep this deviation in mind, when the results of the infrared transparent heater module are discussed. The uncertainties of the local numerically determined heat

[1] Corresponds to the exemplary frame shown in Figure 4.13.

flux $\Delta\dot{q}_{\mathrm{num}}$ are, therefore, dominated by the random heat flux noise caused by the intensity noise of the detector chip $\dot{q}_{\mathrm{lc,ran,G}}$:

$$\Delta\dot{q}_{\mathrm{num}} = \sqrt{\Delta\dot{q}^2_{\mathrm{lc,ran,G}} + \Delta\dot{q}^2_{\mathrm{lc,num,G}}} = 21.52\,\mathrm{kW\,m^{-2}}. \tag{4.7}$$

Compared to the mean heat flux ranges observed for the measurements using ethanol (approx. $2.1 \times 10^3\,\mathrm{kW\,m^{-2}}$) and FC-72 (approx. $3.7 \times 10^2\,\mathrm{kW\,m^{-2}}$), this error is small (±1 % and ±5.7 %, respectively).

The uncertainty of the heat flux $\Delta\dot{q}_{\mathrm{el}}$ is due to an uncertainty of the resistance density of the Cr and CrN layers and the uncertainty of the current. The current supplied to the heater is measured by a multimeter (model 2000 by *Keithley*). According to the datasheet [64], the uncertainty is $\Delta I_{\mathrm{R}} = \pm 1.45 \times 10^{-3}\,\mathrm{A}$, which is negligible. Similarly, the uncertainties of the current and voltage used to calculate the resistance of the Cr and CrN layers are negligible. As described in section 4.2, the resistance of the heater was measured at five different temperatures. To increase the temperature of the heater, it was placed in an oven. For the resistance measurement, the heater had to be removed from the latter. Thus, the exact temperature of the heater during the measurement is unknown. The temperatures are assumed to be in a five Kelvin range to the oven's temperatures. The area used to calculate the resistance density has an uncertainty of $\Delta A_{\mathrm{Cr,R}} = \pm 2.89 \times 10^{-3}\,\mathrm{mm^2}$. This results in an overall uncertainty of the resistance density of $\Delta\varphi_{\mathrm{R}} = \pm 0.1\varphi$. The uncertainty of the heat flux is calculated using Equation 4.8:

$$\Delta\dot{q}_{\mathrm{el}} = \Delta\varphi_{\mathrm{R}}\, I^2_{\mathrm{R}}. \tag{4.8}$$

Compared to the mean heat flux ranges observed for the measurements using ethanol (approx. $2.1 \times 10^3\,\mathrm{kW\,m^{-2}}$) and FC-72 (approx. $3.7 \times 10^2\,\mathrm{kW\,m^{-2}}$), this error is ±3.8 % and ±10.8 %, respectively. The uncertainties of the local heat flux $\Delta\dot{q}_{\mathrm{lc}}$ are calculated using the following equation:

$$\Delta\dot{q}_{\mathrm{lc}} = \sqrt{\Delta\dot{q}^2_{\mathrm{num}} + \Delta\dot{q}^2_{\mathrm{el}}}. \tag{4.9}$$

Compared to the mean heat flux ranges observed for the measurements using ethanol and FC-72, which are shown above, this error is ±3.9 % and ±12.2 %, respectively.

Uncertainty of the bubble expansion velocity

There are several uncertainties influencing the bubble expansion velocity, which cannot be quantified. The defined heat flux threshold, which is necessary for the determination of the expansion velocity, could lead to a deviation in the latter, however, Figure 4.14 shows a reasonable agreement between the visually observable bubble extents and the calculated ones (red circle). More importantly, the exact nucleation event cannot be determined due to the finite frame rate of the infrared camera. Thus, the expansion velocity shortly after nucleation, which causes the formation of a microlayer, can only be approximated. It is assumed that the velocities measured in this thesis are determined once a microlayer is already formed. The presence of a microlayer, however, presumably increases the expansion velocity shortly

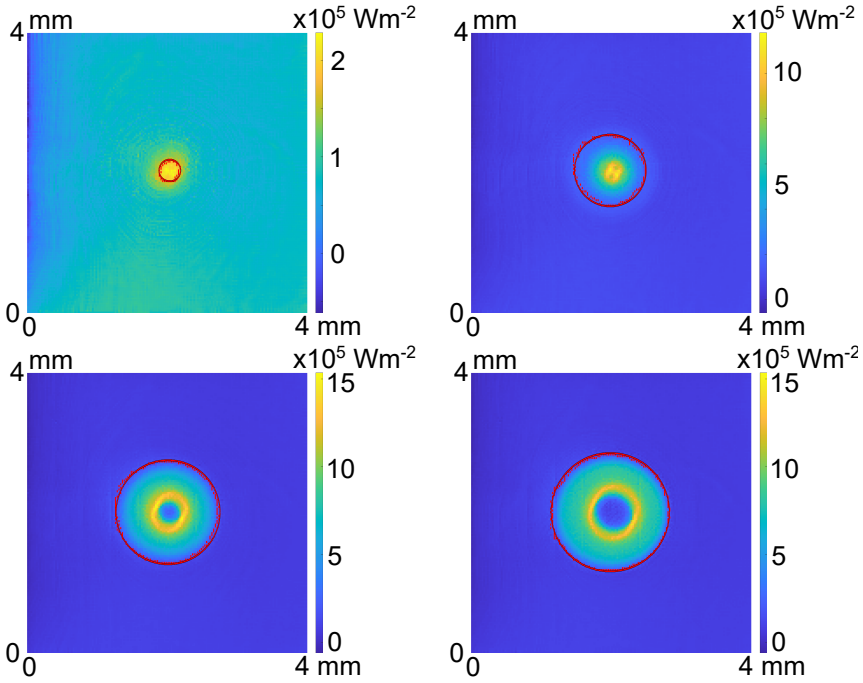

Figure 4.14: Local heat flux fields and bubble extents (red circles) of a growing bubble.

after nucleation, under the assumption of a small receding contact angle, due to high evaporation rates of the microlayer. Thus, it is assumed that the actual expansion velocity that causes the formation of a microlayer is lower compared to the measured bubble expansion velocity in this thesis. However, quantifying this error is not possible, as the true bubble expansion velocity is unknown.

4.3 Data evaluation for the copper heater module

As previously mentioned, the copper heater module is used to investigate the boiling process on a large length scale. One key parameter judging the boiling process is the mean heat transfer coefficient. It is calculated using the input heat flux and the wall and saturation temperature of the fluid. The heat flux

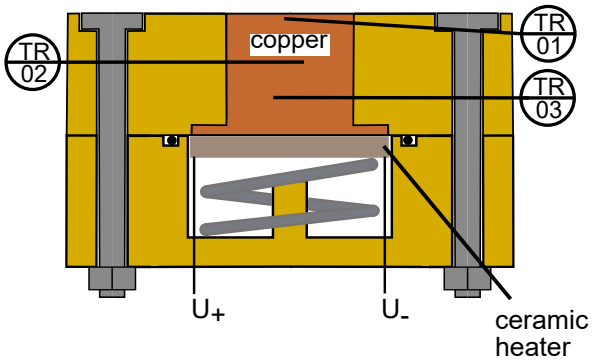

Figure 4.15: Sketch of the copper heater showing important measured parameters.

can be obtained using two different approaches. For the first approach, the heat flux is calculated using the current I and voltage U supplied to the ceramic heater, which is shown in Equation 4.10:

$$\dot{q}_{\mathrm{el}} = \frac{U\ I}{A_{\mathrm{Cu}}}, \tag{4.10}$$

where $A_{\mathrm{Cu}} = 9.621 \times 10^{-4}\,\mathrm{m}^2$ is the cross-section area of the copper cylinder close to the surface.

The second approach utilizes the measured temperatures of two Pt100s (TR02, TR03), which are $s_{\mathrm{Cu}} = 7\,\mathrm{mm}$ apart from each other inside the copper cylinder, to determine the heat flux:

$$\dot{q}_{\mathrm{therm}} = \frac{\lambda_{\mathrm{Cu}}}{s_{\mathrm{Cu}}} \left(T_{03} - T_{02}\right). \tag{4.11}$$

λ_{Cu} is the thermal conductivity of copper, which is temperature dependent. The following equation is found for the thermal conductivity of copper[1] [73]:

$$\lambda_{\mathrm{Cu}} = 8.99 \times 10^{-5}\,\mathrm{T}^2 - 0.137\,\mathrm{T} + 425.24 \quad \text{in } \mathrm{W\,m^{-1}\,K^{-1}}. \tag{4.12}$$

A temperature dependency of $T^{-0.5}$ would be physically correct [101]. However, this general dependency is valid in a wide temperature range, covering low temperatures where the thermal conductivity rises drastically. To fit the relevant data points more effectively, a quadratic equation was chosen.

Both approaches assume that the temperature profile in the copper cylinder is 1-dimensional, which is examined using a simulation in COMSOL Multiphysics. Figure 4.16 shows a sketch of the copper heater on the left hand side and the results of a simulation on the right hand side. Indicated by the red rectangles, only the simulation results of the relevant part of the copper heater are presented. The simulation shows the isotherms inside the copper cylinder and part of the PEEK body for a heat flux of $\dot{q}_{\mathrm{el}} = 860\,\mathrm{kW\,m^{-2}}$ at the boiling surface, which is the highest heat flux employed in the experiments. The temperature difference between each isotherm is 1 K. In addition to the isotherms, the locations of the thermometers inside the copper cylinder are indicated. The results show that the temperature profile inside the copper cylinder should be homogeneous in the areas of the temperature measurements. In the simulation, a heat transfer coefficient of $\alpha_{\mathrm{nucl}} = 60\,\mathrm{kW\,m^{-2}\,K^{-1}}$ is used on top of the copper cylinder, which corresponds to the measured heat transfer coefficients. A heat transfer coefficient of $\alpha_{\mathrm{conv}} = 4\,\mathrm{kW\,m^{-2}\,K^{-1}}$ is used at the interface between PEEK body and liquid, assuming natural and forced convection as no nucleate boiling is observed on the PEEK body in the experiments.

However, besides the homogeneous temperature profile, the uncertainties of the heat fluxes calculated via the two Pt100s inside the cylinder are always larger than those calculated via the electrical power. This is shown in the following section. This is why the heat fluxes in this thesis are determined by the electrical power of the ceramic heater.

[1] Cu-OFE, an oxygen-free, pure copper, which is used in this thesis

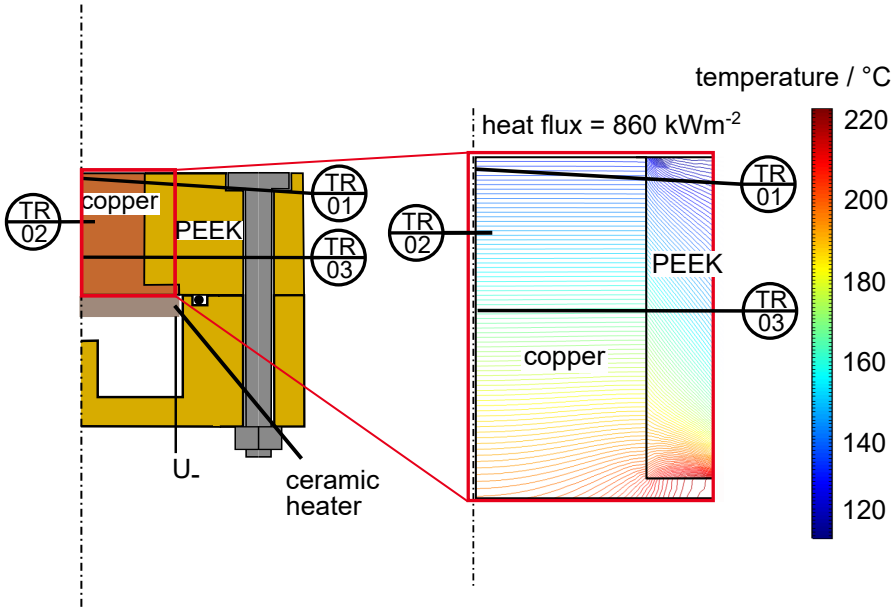

Figure 4.16: Sketch and simulation result of the copper heater showing isotherms inside the copper cylinder for a heat flux of $\dot{q}_{\mathrm{el}} = 860\,\mathrm{kW\,m^{-2}}$.

Since the fluid is pure and degassed, the mean temperature of the four resistance thermometers located inside the liquid is used as the saturation temperature of the fluid. The wall temperature is calculated by an extrapolation of the temperature measurement T_{01} of the thermocouple located $s_{\mathrm{w}} = 2\,\mathrm{mm}$ below the surface (TR01 in Figure 4.15) and the heat flux calculated by Equation 4.10. The wall temperature is determined for all surfaces equally, independent of the surface structure:

$$T_{\mathrm{w}} = T_{01} - \frac{\dot{q}_{\mathrm{el}} s_{\mathrm{w}}}{\lambda_{\mathrm{Cu}}}. \tag{4.13}$$

The mean heat transfer coefficient is then determined using the calculated heat flux, the wall and saturation temperature T_{sat}:

$$\alpha_{\mathrm{m}} = \frac{\dot{q}_{\mathrm{el}}}{T_{\mathrm{w}} - T_{\mathrm{sat}}}. \tag{4.14}$$

The vapor volume flow, which is used to compare the results of the two boiling fluids, is calculated by the following equation:

$$\dot{V}_{\mathrm{v}} = \frac{\dot{q}_{\mathrm{el}} A_{\mathrm{Cu}}}{\Delta h_{\nu} \rho_{\mathrm{v}}}. \tag{4.15}$$

Measurement uncertainties and uncertainties of derived values

The measured parameters with relevant uncertainties are current, voltage, temperature, and pressure. The pressure sensor used to verify a pure saturated state of the fluid has an error of $\Delta p_{\mathrm{R}} = 15\,\mathrm{mbar}$.

According to the power supply's datasheet [30], the errors of the current and voltage measurements are $\Delta I_R = \pm 0.017\,\mathrm{A}$ and $\Delta U_R = \pm 0.208\,\mathrm{V}$, respectively. As mentioned in section 3.3.1, measurements are taken for one minute with a collection rate of 30 Hz at steady state. For further evaluation, the mean values of the measured temperatures, current, and voltage are calculated, for each one-minute-long measurement. The standard deviation of these mean values are negligible for current $\Delta I_{m,G} = \pm 3.24 \times 10^{-5}\,\mathrm{A}$, voltage $\Delta U_{m,G} = \pm 1.89 \times 10^{-3}\,\mathrm{V}$, and temperature $\Delta T_{m,G} = \pm 2.96 \times 10^{-3}\,\mathrm{K}$.

Uncertainty of the temperature

The Pt100s and thermocouples employed in the boiling cell and condenser, as well as the corresponding data acquisition system, are calibrated prior to the experiments using a reference Pt100 in the temperature range of 20 and 130 °C. This reference Pt100 is calibrated in-house, resulting in an error of $\Delta T_{low,G} = \pm 0.063\,\mathrm{K}$. Polynomials are utilized to fit the measurement data of the Pt100s and thermocouples to the data of the reference Pt100. The maximum deviation between the fitted polynomials to the reference temperatures is $\Delta T_{poly,low,R} = \pm 0.046\,\mathrm{K}$. The thermometers inside the copper heater are additionally calibrated in the temperature range of 130 and 300 °C using a reference thermocouple whose measurement error is $\Delta T_{high,G} = \pm 0.07\,\mathrm{K}$. The maximum deviation between the fitted polynomials and the reference temperatures is $\Delta T_{poly,high,R} = \pm 0.22\,\mathrm{K}$.

An additional uncertainty occurs due to the setup of the copper heater module. As seen in Figure 4.15, the measurement tips of the thermometers TR01, TR02 and TR03 are located inside the copper cylinder. This requires their removal and reinstallation when the boiling surface is changed. Although, the diameter differences between the thermometers and their corresponding drill holes are very small, this reinstallation process could result in slightly different positions of the thermometers. This results in an additional temperature uncertainty of $\Delta T_{therm,R} = \pm 0.17\,\mathrm{K}$. Furthermore, temperature measurement uncertainties occur due to sedimentation on the boiling surface for the experiments using ethanol as boiling fluid. During the design of the experimental setup, great care was taken to ensure that all employed materials are chemically resistant to ethanol. The sediments prove that this is not the case. However, the origin of the sediments remains unknown. To evaluate this additional error, test measurements were performed beforehand. The error due to sedimentation is determined by a weeklong test measurement to $\Delta T_{sed,R} = \pm 0.58\,\mathrm{K}$.

In addition to the temperature error, the uncertainty of the wall temperature is dependent on the uncertainty of the heat flux, the manufacturing error of the thermocouple's distance to the surface, and the uncertainties of the physical properties of copper. The uncertainty of the physical properties, independent of the material, is assumed to be ±5 %. The manufacturing error is $\Delta s_{w,R} = \pm 0.1\,\mathrm{mm}$. The wall temperature uncertainty is calculated using Equation 4.16:

$$\Delta T_w = \sqrt{(\Delta T_{01})^2 + \left(-\frac{s_w}{\lambda_{Cu}}\Delta \dot{q}_{el}\right)^2 + \left(-\frac{\dot{q}_{el}}{\lambda_{Cu}}\Delta s_w\right)^2 + \left(\frac{\dot{q}_{el} s_{w,R}}{\lambda_{Cu}^2}\Delta \lambda_{Cu}\right)^2}. \tag{4.16}$$

This results in mean wall temperature errors of approximately $\Delta T_{\mathrm{w,EtOH}} = \pm 0.68\,\mathrm{K}$ and $\Delta T_{\mathrm{w,FC\text{-}72}} = \pm 0.31\,\mathrm{K}$ for the measurements with ethanol and FC-72, respectively.

Uncertainty of the heat flux, heat transfer coefficient, and vapor volume flow

The uncertainty of the heat flux $\Delta\dot{q}_{\mathrm{el}}$ calculated using the electrical power supply to the ceramic heater consists of two errors:

$$\Delta\dot{q}_{\mathrm{el}} = \sqrt{\left(\Delta\dot{q}_{\mathrm{el,Cu}}\right)^2 + \left(\Delta\dot{q}_{\mathrm{el,PEEK}}\right)^2}. \tag{4.17}$$

$\Delta\dot{q}_{\mathrm{el,Cu}}$ is determined with the measurement uncertainties of voltage, current, and the manufacturing error of the copper cylinder. $\Delta\dot{q}_{\mathrm{el,PEEK}}$ is caused by heat loss through the insulating PEEK body surrounding the copper cylinder. Overall, the heat flux error is approximately $\Delta\dot{q}_{\mathrm{el}} = \pm 4\,\%\ \dot{q}_{\mathrm{el}}$ for all measurements with a heat flux higher than $\dot{q}_{\mathrm{el}} = 35\,\mathrm{kW\,m^{-2}}$. The error increases to $\pm 10\,\%$ for the measurements at the lowest heat flux of approximately $\dot{q}_{\mathrm{el}} = 2\,\mathrm{kW\,m^{-2}}$.

The error due to manufacturing and measurement uncertainties is calculated by the following equation,

$$\Delta\dot{q}_{\mathrm{el,Cu}} = \sqrt{\left(\frac{I}{A_{\mathrm{Cu}}}\Delta U_{\mathrm{R}}\right)^2 + \left(\frac{U}{A_{\mathrm{Cu}}}\Delta I_{\mathrm{R}}\right)^2 + \left(-\frac{U\,I}{A_{\mathrm{Cu}}^2}\Delta A_{\mathrm{Cu,R}}\right)^2}, \tag{4.18}$$

assuming that the manufacturing error of the copper cylinder diameter is $\Delta d_{\mathrm{Cu,R}} = \pm 0.2\,\mathrm{mm}$. This results in an error of the cross-section area of $\Delta A_{\mathrm{Cu,R}} = \pm 11\,\mathrm{mm^2}$.

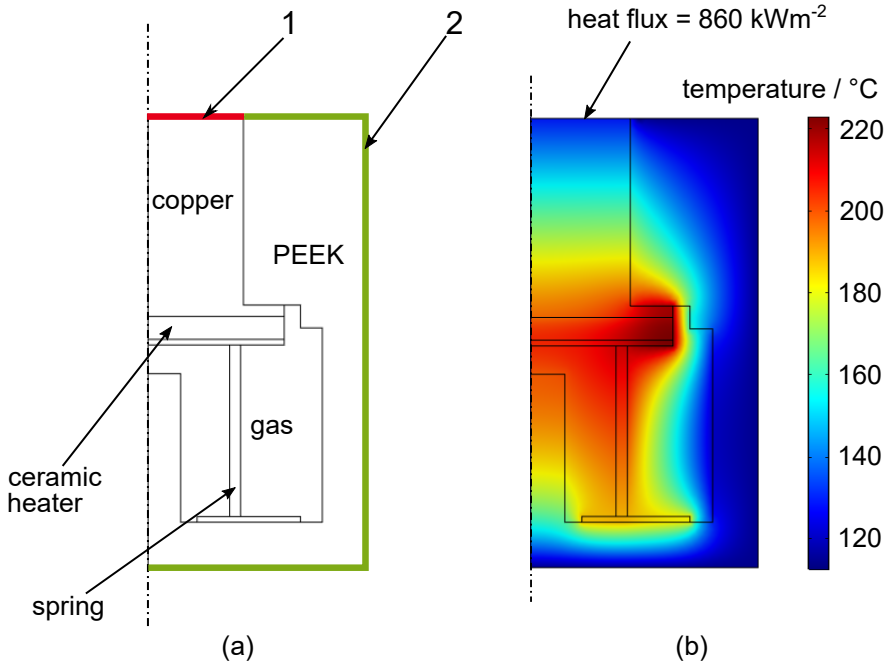

Figure 4.17: Sketch (a) and simulation result (b) of the copper heater dissipating a heat flow of $\dot{Q}_{\mathrm{el}} = 830\,\mathrm{W}$, which corresponds to a heat flux of $\dot{q}_{\mathrm{el}} = 860\,\mathrm{kW\,m^{-2}}$ at the boiling surface (surface 1). Surface 2 corresponds to the area of the PEEK body in contact with the fluid.

The error due to heat loss through the PEEK body is determined by a simulation in COMSOL Multiphysics. Figure 4.17 shows a sketch (a) and simulation result (b) of the copper heater. A heat flow of $\dot{Q}_{\mathrm{el}} = 830\,\mathrm{W}$ is supplied by the ceramic heater, which corresponds to a heat flux of $860\,\mathrm{kW\,m^{-2}}$ at the boiling surface indicated by a 1 in Figure 4.17a. $\dot{q}_{\mathrm{el}} = 860\,\mathrm{kW\,m^{-2}}$ is the highest heat flux used in the experiments in this thesis. The boundaries are treated as Cauchy boundary conditions, meaning that heat transfer coefficients were dictated. The heat transfer coefficient at surface 1, $\alpha_{\mathrm{nucl}} = 60\,\mathrm{kW\,m^{-2}\,K^{-1}}$, corresponds to the heat transfer coefficients observed during the experiments at similar heat fluxes. The heat transfer coefficient at surface 2 (PEEK insulation) is $\alpha_{\mathrm{conv}} = 4\,\mathrm{kW\,m^{-2}\,K^{-1}}$, which is significantly lower, since heat transfer on the PEEK body is dominated by natural convection. To analyze the heat flux loss through the PEEK insulation (surface 2 in Figure 4.17a), the heat flow dissipated through surface 1 is compared to surface 2. The maximum heat flux loss through the PEEK insulation obtained by this method is $\dot{q}_{\mathrm{el,PEEK}} = \pm 3.7\,\% \cdot \dot{q}_{\mathrm{el}}$.

The alternative method of calculating the heat flux via the two resistance thermometers inside the copper cylinder (Figure 4.15) results in heat flux uncertainties between ±4.5 and ±340 %, depending on the wall superheat. Thus, the heat fluxes shown in the results are calculated via the electrical power supplied to the ceramic heater.

The error of the mean heat transfer coefficient is due to temperature measurement uncertainties and the error of the heat flux, which is shown in Equation 4.19:

$$\Delta\alpha_{\mathrm{m}} = \sqrt{\left(\frac{1}{T_{\mathrm{w}} - T_{\mathrm{sat}}}\Delta q_{\mathrm{el}}\right)^2 + \left(-\frac{q_{\mathrm{el}}}{(T_{\mathrm{w}} - T_{\mathrm{sat}})^2}\Delta T_{\mathrm{w}}\right)^2 + \left(\frac{q_{\mathrm{el}}}{(T_{\mathrm{w}} - T_{\mathrm{sat}})^2}\Delta T_{\mathrm{sat}}\right)^2}. \tag{4.19}$$

Depending on the heat flux, fluid, surface, and system pressure, this error is between ±4 and ±28 % of the calculated mean heat transfer coefficient.

The error of the vapor volume flow is due to the error of the cross-section area of the copper cylinder $\left(\Delta A_{\mathrm{Cu}} = \pm 11\,\mathrm{mm^2}\right)$, the uncertainties of the physical properties (±5 % of the corresponding values), and the error of the heat flux:

$$\Delta\dot{V} = \sqrt{\left(\frac{A_{\mathrm{Cu}}}{\Delta h_v \rho_{\mathrm{v}}}\Delta q_{\mathrm{el}}\right)^2 + \left(\frac{q_{\mathrm{el}}}{\Delta h_v \rho_{\mathrm{v}}}\Delta A_{\mathrm{Cu}}\right)^2 + 2\left(0.05\frac{q_{\mathrm{el}} A_{\mathrm{Cu}}}{\Delta h_v \rho_{\mathrm{v}}}\right)^2}. \tag{4.20}$$

Depending on the heat flux, fluid, surface, and system pressure, this error is between ±4 and ±12 % of the vapor volume flow. In addition, the vapor volume flow is calculated under the assumption that the entire electrical heat flux is used for the evaporation of liquid. However, the exact amount of heat dissipated by natural and forced convection is not possible to determine. Thus, an exact value for this error cannot be given. For the corresponding diagrams, the reader should keep in mind that the vapor volume flows presented in this thesis are higher than the actual values.

Uncertainty of the critical heat flux

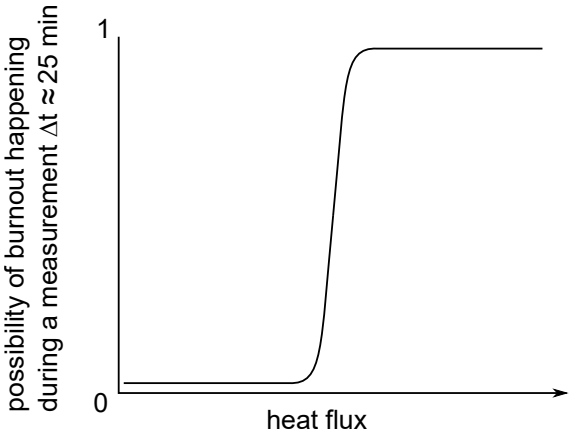

Figure 4.18: Sketch showing the chances of burnout happening during a measurement.

The exact value of the critical heat flux is impossible to determine in the scope of this thesis. Burnout is a slightly random event and it is assumed that the possibility of its occurrence in a certain time period rises significantly once a certain heat flux is reached, as shown in Figure 4.18. As mentioned in section 3.3.1, the first measurement point is taken at a slightly lower heat flux than the observed critical heat flux. However, it was observed during experiments that burnout sometimes happened at this first measurement point, after the measurements were already taken and the system was kept at the first measurement point ($t > 25\,\text{min}$). In this case, the first measurement point would be situated in the heat flux range showing the gradient in the possibility curve in Figure 4.18. Therefore, it is assumed that the critical heat flux is in a heat flux range, with the upper limit being the heat flux where burnout was observed and the lower limit being the second measurement point, where burnout was never observed.

Chapter 5

Experimental Results and Discussion

In this chapter, the experimental results are presented and the scientific questions of this thesis are answered. Since the experimental setup was constructed for this thesis, in the first step it is analyzed whether the experimental results obtained with this new setup are comparable to literature data or state of the art correlations. After establishing the validity of the experiments, the boiling process of the uncoated copper surfaces is analyzed, followed by the results of the homogeneously coated microstructured surfaces (20cu and 10cu). The first scientific question—How is the boiling process affected by a microstructure, whose geometrical length scale is between the well-studied micropillars and nanowires?—is answered and the necessity for an additional optimization of the microstructured surfaces is displayed in this section. This leads to the answer of the second scientific question—Is it possible to improve the boiling performance of said microstructure by adding a macrostructure, creating a hierarchical structure?—in the following section, where the results of the optimized, hierarchical surface are shown. Afterwards, the influence of the boiling fluid is discussed and a significant parameter, the evaporation mode at the three-phase contact line, is analyzed in further detail, using the infrared transparent heater. The third scientific question—Can an investigation of the boiling process on different length scales enable a better understanding of the occurring boiling phenomena?—is answered in this last section, as well.

5.1 Results of the uncoated copper surfaces

Firstly, the validity of the experimental setup is verified using the smooth copper surface. The results obtained using the latter are compared to literature data and the Rohsenow correlation (Equation 2.5) [124].

5.1.1 Verifying the validity of the experimental results

Figure 5.1 shows the Nukiyama curves for the smooth copper surface Scu at various system pressures. The results of ethanol as boiling fluid are visible in Figure 5.1a and the ones of FC-72 in Figure 5.1b. As mentioned before, the results are obtained for decreasing heat fluxes. Additionally, measured data by Dong et al. [28] and Rainey et al. [122] are presented in the figures, for reference. The data of Dong et al. and Rainey et al. at 1.0 bar fit the experimental data at higher heat fluxes well. Under the assumption that the boiling process does not change dramatically between 0.3 bar and 0.4 bar, the same is true for the data at 0.4 bar using FC-72. The larger deviations at lower heat fluxes and the comparison to further literature data will be addressed in section A.2 in the appendix.

In addition to literature data, the experimental results are compared to the well-known Rohsenow correlation (Equation 2.5) [124]. In Figure 5.2, the Nukiyama curves for the smooth copper surface Scu, various system pressures, and fluids ((a) ethanol, (b) FC-72) are compared to Rohsenow's correlation. In

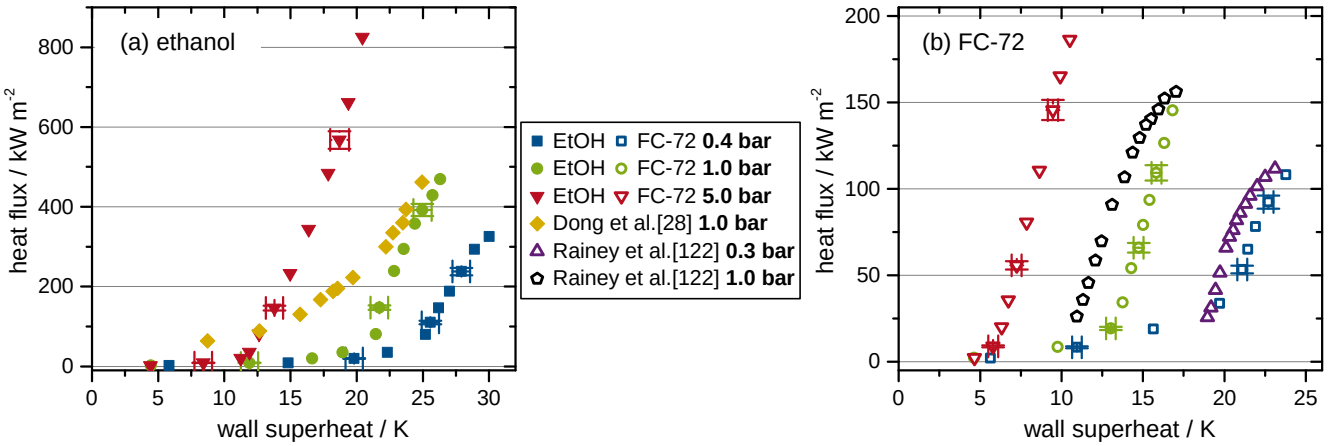

Figure 5.1: Nukiyama curves for the smooth copper surface Scu at various system pressures obtained with ethanol (a) and FC-72 (b) as well as literature data.

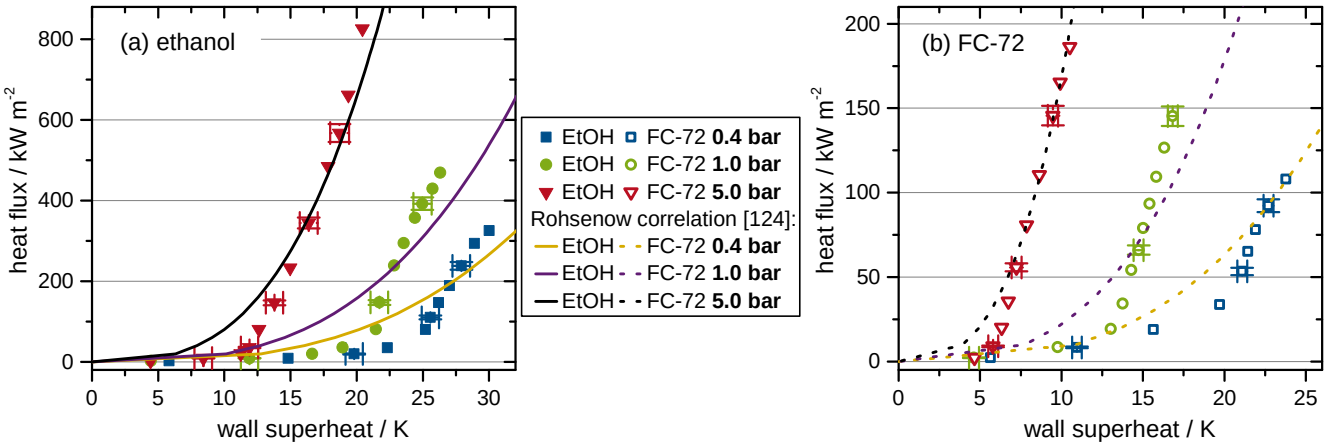

Figure 5.2: Nukiyama curves for the smooth copper surface Scu at various system pressures obtained with ethanol (a) and FC-72 (b) in comparison to the Rohsenow correlation [124].

said correlation, the factor C_{sf} accounts for the influence of fluid-surface combinations. This parameter was fitted onto the experimental data resulting in $C_{sf,EtOH} = 0.0095$ and $C_{sf,FC\text{-}72} = 0.0038$. For FC-72, the value of C_{sf} is very close to the one reported by Priarone [118] $C_{sf,Priarone} = 0.003\,93$. For ethanol, no suitable data for C_{sf} could be found. The value reported by Pioro [114] $C_{sf,Pioro} = 0.000\,79$ was evaluated for the heat flux range of 2.1 and 26 kW m^{-2}, which is significantly smaller compared to the heat flux data presented here, ranging up to 800 kW m^{-2}. In the experimental Nukiyama curves, bends are visible at low heat fluxes resulting from the increasing importance of natural convection at low heat fluxes, since parts of the surface are no longer in the nucleate boiling regime, which is shown in Figure A.1 in the appendix. For results obtained with ethanol as boiling fluid, those bends are at heat fluxes of approximately 20 to 40 kW m^{-2}, depending on the system pressure. The large discrepancy between the fitted $C_{sf,EtOH}$ value and the one reported by Pioro is probably due to the regime change at low heat fluxes present in the experimental data. Nevertheless, the fitted $C_{sf,EtOH}$ value is close to the universally recommended value of $C_{sf,Rohsenow} = 0.013$ [16].

The exponents a of the Rohsenow correlation were set to the recommended value [124] of 0.33 for both fluids, while the exponent b was set to the recommended value of 1.7 for FC-72. For ethanol, an exponent of $b = 1$, the recommended value for water [148], fits the data better than using a value of 1.7. The mean deviations between the experimental data and the correlations are approximately 17 % and 10.5 % for ethanol and FC-72, respectively. However, as mentioned before, there is a change in the boiling regime at lower heat fluxes. If only fully developed nucleate boiling is considered, the mean deviations drop to approximately 12 % for ethanol and 8.3 % for FC-72. The values of the exponents a and b are not fixed values [124], but were established by Rohsenow's available correlating data. Other researchers [114, 118, 148] report different values for the exponents. If the values of a, b, and C_{sf} are determined by fitting the presented heat flux data, the sets of parameters are $a_{EtOH} = 0.16$, $b_{EtOH} = 0.6$, and $C_{sf,EtOH} = 0.023$ for ethanol, and $a_{FC\text{-}72} = 0.2$, $b_{FC\text{-}72} = 1.49$, and $C_{sf,FC\text{-}72} = 0.0064$ for FC-72. For fully developed nucleate boiling, the mean deviations decrease to 3.5 % for ethanol and 5.5 % for FC-72, respectively.

In conclusion, the heat transfer data of the smooth copper surface obtained by this novel experimental setup are comparable to available literature data. Also, the results can be approximated by a well-known correlation with the typical accuracy ($< 20\,\%$ [16, 114, 115, 148]) of correlations for nucleate boiling. Thus, it is established that the results obtained with this setup are not impacted by larger systematic errors, caused by inert gases, contaminations, etc. Additionally, further differences in the data obtained with different boiling surfaces compared to the smooth copper surface can be attributed directly to the impact of the boiling surface on nucleate boiling.

5.1.2 Boiling performance of the uncoated copper surfaces

In this section, most of the results are presented for the technical copper surface, as the findings for the technical copper surface and the smooth copper surface are very similar. In case there are significant differences, the results of both surfaces are presented, otherwise the results of the smooth copper surface are shown in the appendix. The results of the technical copper surface using FC-72 at a system pressure

of 5.0 bar are obtained for increasing heat fluxes. However, the Nukiyama curves for the technical copper surface using FC-72 are very similar, whether they are obtained with increasing or decreasing heat fluxes, as shown in Figure A.2 in the appendix.

5.1.2.1 Nukiyama curves and heat transfer coefficients

Figure 5.3 shows the Nukiyama curves for the technical copper surface Tcu at various system pressures. The results for ethanol are presented in Figure 5.3a, while the ones for FC-72 are visible in Figure 5.3b. Similar to the results of the smooth copper surface, the wall superheat decreases and the critical heat flux increases as system pressure increases. This decrease of wall superheat increases the heat transfer coefficient for a specific heat flux, which is shown in Figure 5.4. The results obtained for the technical copper surface Tcu using ethanol are presented in Figure 5.4a and the ones using FC-72 are shown in Figure 5.4b. The results of the smooth copper surface Scu show the same phenomena and are presented in Figure A.3 in the appendix.

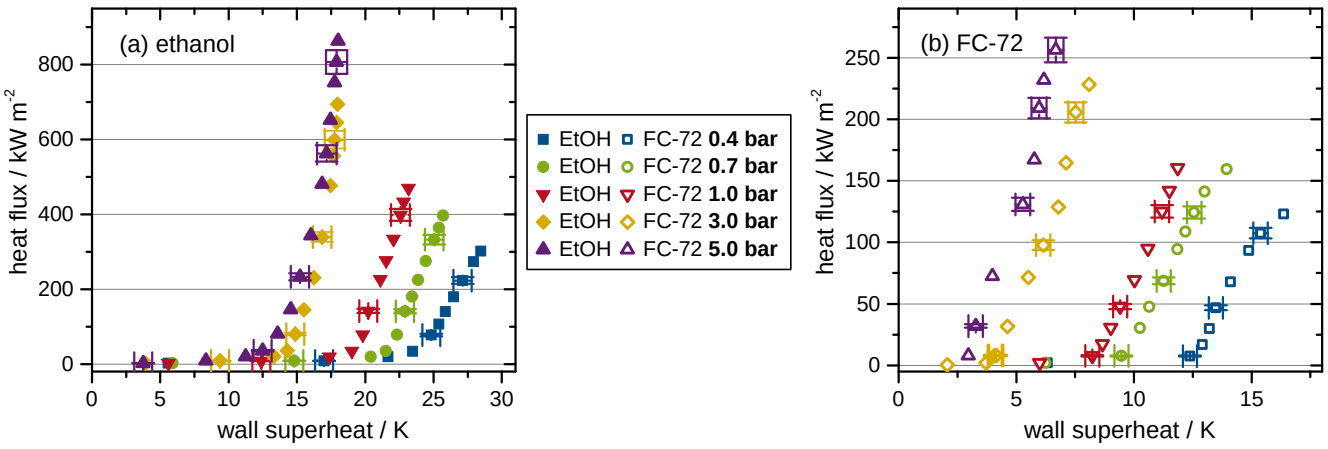

Figure 5.3: Nukiyama curves for the technical copper surface Tcu at various system pressures obtained with ethanol (a) and FC-72 (b).

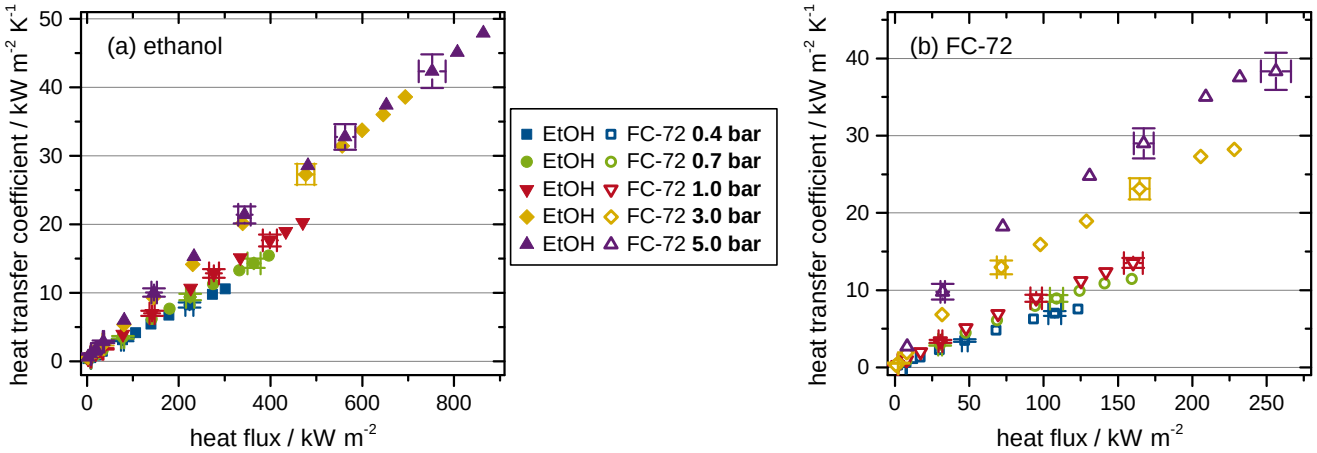

Figure 5.4: Heat transfer coefficients for specific heat fluxes obtained for the technical copper surface Tcu using ethanol (a) and FC-72 (b) at various system pressures.

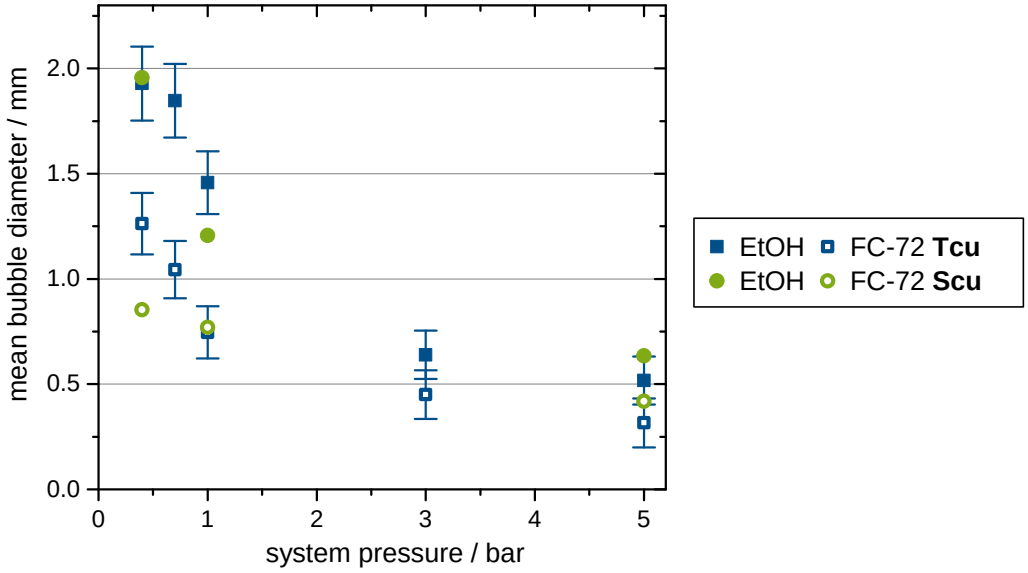

Figure 5.5: Mean bubble diameters at various system pressures obtained for the technical Tcu and smooth copper surface Scu using ethanol and FC-72 as boiling fluids.

One of the main reasons for the increase in heat transfer coefficient with higher system pressure for a specific heat flux is the increased nucleation site density. Based on Equation 2.3, the superheat necessary to activate a certain cavity size decreases with increasing pressure, leading to lower wall superheats for a given surface. Corresponding to the increased nucleation site densities, bubble diameters decrease with increasing pressure, which is shown in Figure 5.5 and is well documented in literature [4, 19, 39, 135, 136]. Smaller bubble diameters result in an increase in total three-phase contact line length for a specific heat flux, experimental parameters, and evaluated time period compared to diametrically larger bubbles. Due to thin liquid films being present in the vicinity of the three-phase contact line, high heat fluxes can be transferred [96, 130, 138, 142]. This could lead to lower wall superheats and in turn to higher heat transfer coefficients. Additionally, it is assumed that smaller bubbles also cause increased flow turbulence close to the wall, due to more rapid departure events, which further increases the heat transfer coefficient. The growth and departure of bubbles induce liquid motion due to the density difference between liquid and vapor. In case of small bubbles nucleating close to each other, it is assumed that this liquid motion is more turbulent, which increases heat transfer.

Besides the increased heat transfer coefficients for specific heat fluxes, the maximum heat transfer coefficients increase at higher system pressures, which corresponds to higher critical heat fluxes. At higher heat fluxes and, thus, higher wall superheats, additional nucleation sites can be activated. Additionally, as the bubble departure frequency increases, both phenomena cause an increasing heat transfer coefficient, until shortly before critical heat flux is reached.

For further evaluation, the experimental results are compared to the well-known Gorenflo correlation (Equations 2.6) [140]. The reference heat transfer coefficients of the correlation are experimental values at 30 and 80 $kW\,m^{-2}$ for FC-72 and ethanol, respectively, both at 1.0 bar. Figure 5.6 shows the ratios of heat transfer coefficients to the aforementioned references for specific heat fluxes and reduced pressures

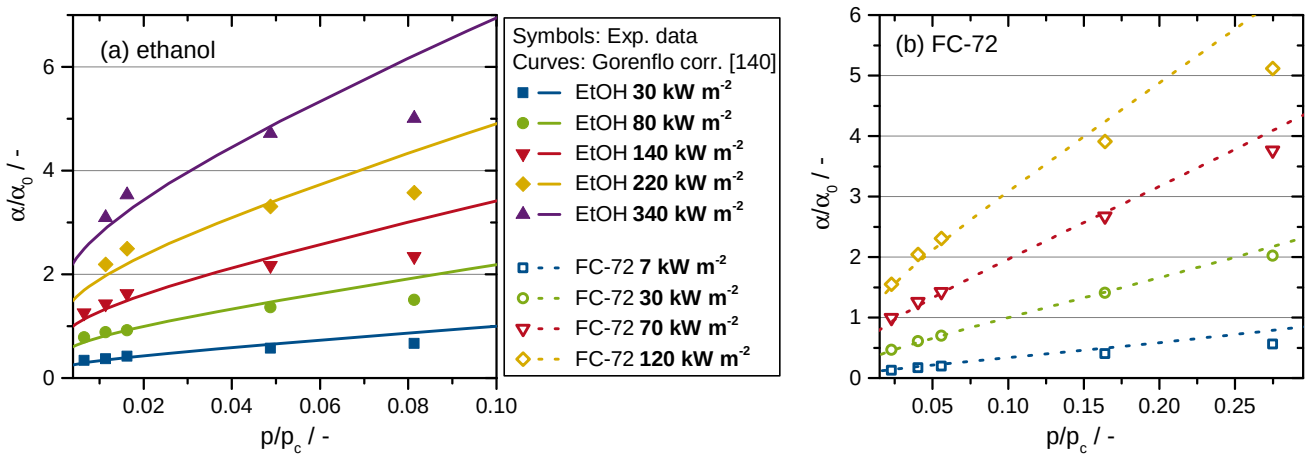

Figure 5.6: Ratio of heat transfer coefficient to reference heat transfer coefficient for specific heat fluxes at reduced pressures obtained for the technical copper surface Tcu using ethanol (a) and FC-72 (b) compared to Gorenflo's correlation [140].

($p_r = p/p_c$)[1]. The figure presents the data of the technical copper surface Tcu for both fluids. For ethanol and FC-72, the correlation fits the experimental data at lower reduced pressures well. However, the ratio of heat transfer coefficients at the highest reduced pressure is lower compared to the correlation for both fluids. The data of the smooth copper surface Scu can be found in Figure A.4 in the appendix. For both fluids, the results of the smooth copper surface show a similar trend to the results of the technical copper surface (Figure 5.6). At lower reduced pressures, the correlation mostly fits the experimental data for both fluids. However, at high reduced pressures the heat transfer coefficient ratios are significantly lower, when compared to the correlation.

5.1.2.2 Critical heat fluxes

Besides the heat transfer coefficient, the critical heat flux is the second important parameter judging the boiling performance of a surface. As mentioned before, the critical heat flux increases with rising system pressure. This increase in critical heat flux could be due to a lower vapor volume flow created on top of the boiling surface. At $p_{sys,EtOH} = 0.4\,bar$, the vapor volume flow shortly before critical heat flux is $\dot{V}_{EtOH,Scu} = 0.53\,l\,s^{-1}$ $\left(at\ \dot{q}_{EtOH,Scu} = 325.16\,kW\,m^{-2}\right)$, while at $p_{sys,EtOH} = 5.0\,bar$, the volume flow decreases to $\dot{V}_{EtOH,Scu} = 0.15\,l\,s^{-1}$ $\left(at\ \dot{q}_{EtOH,Scu} = 825.67\,kW\,m^{-2}\right)$. For FC-72, the values are $\dot{V}_{FC\text{-}72,Scu} = 0.20\,l\,s^{-1}$ $\left(at\ \dot{q}_{FC\text{-},Scu} = 108.07\,kW\,m^{-2}\right)$ and $\dot{V}_{FC\text{-}72,Scu} = 0.04\,l\,s^{-1}$ $\left(at\ \dot{q}_{FC\text{-},Scu} = 186.36\,kW\,m^{-2}\right)$, respectively. However, the vapor volume flow cannot be the only influencing parameter, or otherwise the critical heat fluxes would be even higher at increased system pressures. According to the hydrodynamic model of Zuber (Equations 2.7) [168], the unstable Helmholtz velocity and the Rayleigh-Taylor wavelength both decrease for increasing pressure, due to physical property changes of the fluid. Compared to the correlation of Zuber, the experimentally determined critical heat fluxes for the smooth copper surface Scu are smaller using ethanol as boiling fluid, which is shown in Figure 5.7a. The results obtained using FC-72 fit the correlation within the measurement uncertainties, as shown in Figure 5.7b.

[1] p_c is the critical pressure of the corresponding fluid

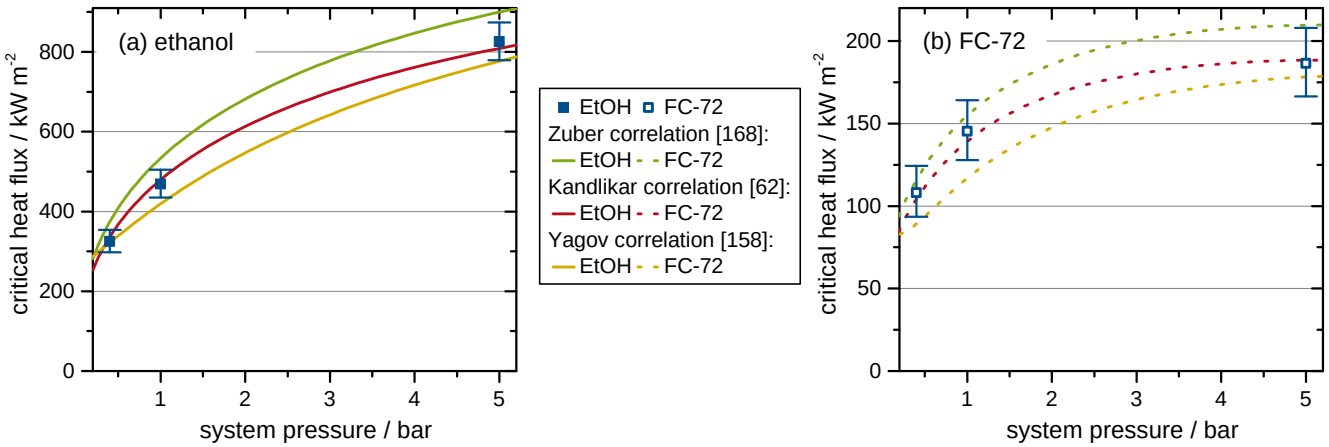

Figure 5.7: Critical heat fluxes for the smooth copper surface Scu at various system pressures using ethanol (a) and FC-72 (b) compared to the correlations of Zuber [168], Kandlikar [62], and Yagov [158].

Along with the correlation of Zuber, the correlations of Yagov (Equations 2.11) [158] and Kandlikar (Equation 2.8) [62] are compared to the experimental data as well. The latter incorporates the receding contact angle. This value, however, is not measureable with the necessary accuracy in this experimental setup. Thus, the correlation of Kandlikar has to be fitted onto the experimental data resulting in a receding contact angle of $\Theta_{rec,Scu} = 65°$ for both fluids. This receding contact angle might disagree with the contact angle measurements under ambient conditions, where both fluids wetted all copper surfaces well, as mentioned in section 3.2.2. However, contact angles can increase drastically under rapid evaporating conditions [123]. The correlation of Yagov assumes that burnout is triggered by formation and growth of dry spots beneath growing bubbles, which cannot be rewetted completely after bubble departure. The correlation predicts slightly lower critical heat fluxes compared to the other correlations and the experimental data for both fluids. The correlation of Theofanous and Dinh [143], which is described in section 2.3.2, does not fit the results of the copper surfaces well, hence it is not included in the corresponding figures. Although, the correlation is formally similar to the correlation of Zuber, the value of the parameter K differs, which is responsible for the discrepancy between the correlation and the experimental results.

Figure 5.8 shows the experimentally determined critical heat fluxes for the technical copper surface Tcu using ethanol (a) and FC-72 (b) as boiling fluids, compared to the correlations of Zuber [168], Kandlikar [62], and Yagov [158]. The results obtained with ethanol as boiling fluid show a similar trend compared to the smooth copper surface. The experimentally determined critical heat fluxes are smaller than the correlation of Zuber but larger than the correlation of Yagov. The same receding contact angle is used to fit the correlation of Kandlikar, $\Theta_{rec,Scu/Tcu,EtOH} = 65°$, as is used for the smooth copper surface. For FC-72, the results are significantly larger than the correlation of Yagov and comparable to the correlation of Zuber at system pressures below unity. Consequently, a smaller receding contact angle is used to fit the correlation of Kandlikar to the experimental data, $\Theta_{rec,Tcu,FC\text{-}72} = 43°$, which is significantly lower compared to the receding contact angle of the smooth copper surface $\Theta_{rec,Scu,FC\text{-}72} = 65°$. While it could be possible that the receding contact angle is much lower on the technical copper surface, the more likely

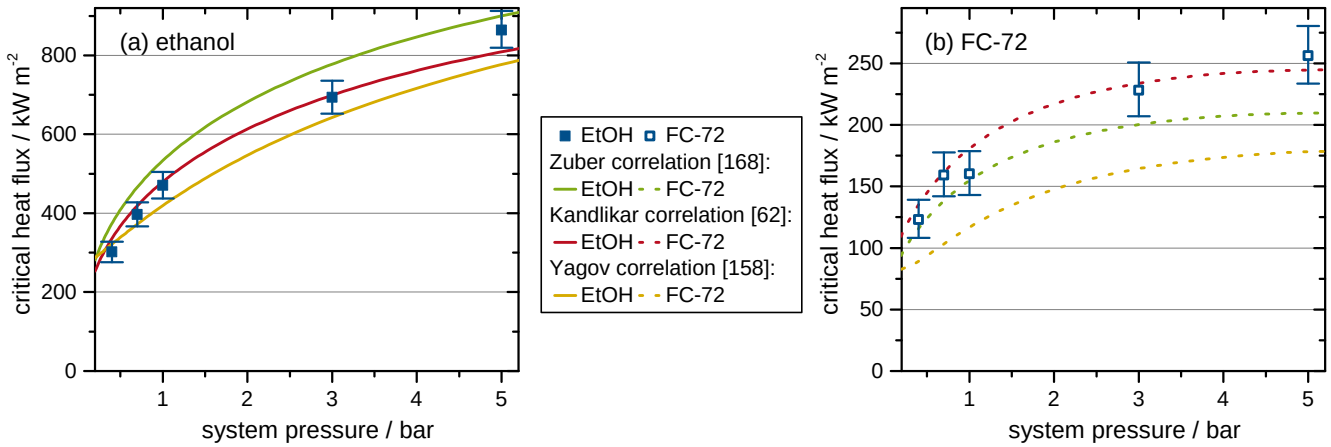

Figure 5.8: Critical heat fluxes for the technical copper surface Tcu at various system pressures using ethanol (a) and FC-72 (b) compared to the correlations of Zuber [168], Kandlikar [62], and Yagov [158].

explanation for the enhanced critical heat fluxes is the higher surface roughness of the technical copper surface. Although it is still a subject of debate, several researchers [7, 68] have linked their critical heat flux enhancements to surface roughness.

Based on the imbibition experiments in section 3.2.2, higher critical heat fluxes using ethanol were predicted for the technical copper surface compared to the smooth copper surface. The critical heat fluxes for FC-72 should be similar for the technical and the smooth copper surface. The opposite behavior is now observed in boiling experiments. This begs the question, whether the results of an isothermal imbibition experiment performed under atmospheric conditions are transferable to nucleate boiling.

5.1.2.3 Influence of surface roughness

To determine if the enhanced critical heat fluxes observed for the technical copper surface are due to a reduced receding contact angle or the higher surface roughness compared to the smooth copper surface, the results of the technical copper surface are compared to a correlation developed by Kim et al. [68]. Their correlation is based on Kandlikar's and incorporates surface roughness parameters, as shown in Equation 5.1:

$$\dot{q}_{\mathrm{CHF}} = K\Delta h_v \rho_{\mathrm{v}}^{0.5} \left[\sigma g \left(\rho_{\mathrm{l}} - \rho_{\mathrm{v}}\right)\right]^{0.25} \cdot \frac{1+\cos\Theta_{\mathrm{rec}}}{16} \left[\frac{2}{\pi} + \frac{\pi}{4}\left(1+\cos\Theta_{\mathrm{rec}}\right) + \frac{4L\cos\Theta_{\mathrm{rec}} Ra}{\left(1+\cos\Theta_{\mathrm{rec}}\right) Sm}\right]^{0.5}. \quad (5.1)$$

The factor K is set to unity, since it was introduced by Kim et al. to accommodate for differences in critical heat flux of their smooth surface compared to those of other researchers. Since the critical heat fluxes of the smooth copper surface presented in this thesis are comparable to several correlations, the inclusion of this adjustment parameter is deemed unnecessary. The fitted receding contact angle of the smooth copper surface $\Theta_{\mathrm{rec,Scu,FC\text{-}72}} = 65°$ is used in the correlation instead of the contact angle of the technical copper surface, since the enhancement of the critical heat flux of the technical copper surface is

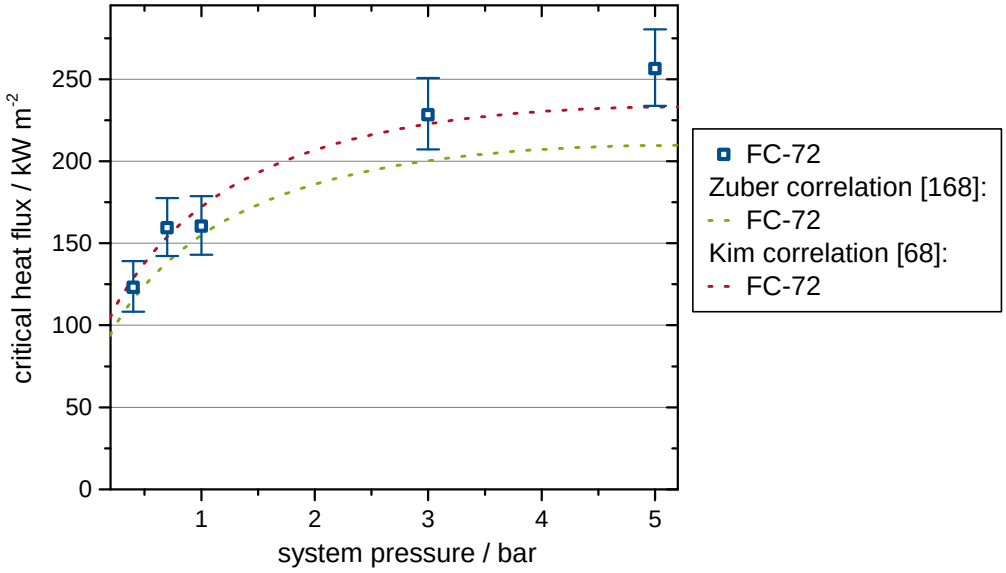

Figure 5.9: Critical heat fluxes for the technical copper surface Tcu at various system pressures obtained with FC-72 compared to Zuber's [168] and Kim's [68] correlations.

believed to result from the difference in roughness and not a difference in contact angle. A small mistake is undoubtedly made, since the contact angles on the technical copper surface should be smaller than the ones on the smooth copper surface, according to Wenzel [156]. However, since the receding contact angles are not measured but fitted, the additional error is deemed negligible. The roughness parameter Sa of the technical copper surface is used instead of the line roughness parameter Ra. According to Kim et al., Sm in Equation 5.1 is the mean spacing of the surface roughness. Since the technical copper surface lacks the oriented roughness of the surfaces presented by Kim et al. in their publication, the measured peak density $Spd = 38.1\,\mu\text{m}$ is employed as Sm.

In Figure 5.9, the critical heat fluxes measured using FC-72 for the technical copper surface Tcu at various system pressures are compared to the correlations of Zuber [168], which serves as a reference, and Kim et al. [68]. The correlation of Kim et al. fits the measured critical heat fluxes relatively well for the same empirical parameter $L = 87.8$, despite the fact that the surface roughness of the technical copper surface is not oriented, which made the determination of Sm difficult. Perhaps the peak density Spd is the equivalent parameter to Sm, when dealing with isotropic surface roughness. However, this has to be investigated with additional surfaces before a recommendation can be given.

Besides critical heat flux, the roughness difference of the two uncoated copper surfaces presumably also influences the wall superheat and, therefore, the heat transfer coefficient, which is visible in Figure 5.10. Independent of the system pressure, the wall superheats measured using FC-72 as boiling fluid of the technical copper surface Tcu are lower compared to corresponding superheats of the smooth copper surface Scu (Figure 5.10a). This in turn results in higher heat transfer coefficients, as shown in Figure 5.10b. The difference is likely due to increased nucleation site densities on the technical copper surface, which is shown in Figure 5.11. This figure shows b&w images of the boiling process at a specific heat flux of $\dot{q}_{\text{el}} = 20\,\text{kW m}^{-2}$ and various system pressures on the technical copper surface Tcu and the smooth

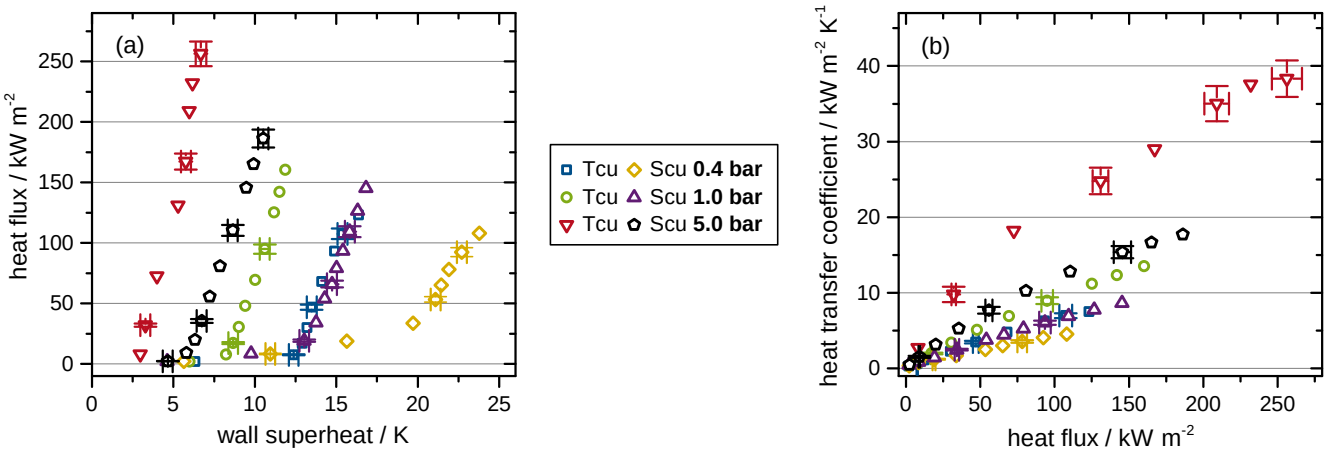

Figure 5.10: Comparison between the results obtained for the technical copper surface Tcu and the smooth copper surface Scu with FC-72 as boiling fluid at various system pressures. On the left hand side the Nukiyama curves are presented (a), while on the right hand side the heat transfer coefficients are shown (b).

copper surface Scu. At 0.4 bar, no visible difference can be noticed, but at higher pressures the bubble densities seem to be higher on the technical copper surface compared to the smooth copper surface. However, similar to the critical heat fluxes, this difference is only visible if FC-72 is used as boiling fluid. The corresponding figures using ethanol are presented in Figure A.5 in the appendix.

Assuming that the increased nucleation site densities are caused by additional cavities due to the higher roughness of the technical copper surface, the question remains why the measurements using ethanol are not similarly affected. A similar behavior was also observed by Jones et al. [58], using water and FC-72. This could be caused by the fact that the activated cavity size at a certain superheat is lower for FC-72 compared to ethanol $\left(R_{\mathrm{cav,FC\text{-}72}} = 1.5\,\mathrm{nm},\ \text{and}\ R_{\mathrm{cav,EtOH}} = 2.6\,\mathrm{nm}\ \text{at}\ 1.0\,\mathrm{bar}\ \text{and}\ 10\,\mathrm{K}\ \text{superheat}\right)$ (determined by Equation 2.3). Of course, this cavity radius is significantly smaller than the observable grooves, which cause the higher roughness value of the technical copper surface. However, small cavities could be formed in said grooves. Additionally, those values are based on thermodynamic equilibrium. However, processes happening during bubble growth are seldom in thermodynamic equilibrium. The actual wall superheats are significantly larger than the necessary superheats, which in turn, leads to the small cavity sizes [6]. In addition, the fluids were degassed and are well wetting, which might lead to discrepancies when using Equation 2.3 to calculate the cavity sizes, as discussed in section 2.1.2. Nevertheless, the different critical cavity radii could give an idea why a different behavior is observed for the two fluids. A decisive answer, however, cannot be given.

All in all, the experimental results of the two uncoated copper surfaces show a decrease in wall superheat and, therefore, an increase in heat transfer coefficient with increasing system pressure for both fluids. This pressure dependency is described reasonably well by well-known correlations, especially for the technical copper surface at lower system pressures. The critical heat fluxes observed for the two surfaces are comparable to values predicted by the correlations of Zuber and Yagov, with the exception of critical heat fluxes obtained for the technical copper surface and FC-72 at high system pressures. Presumably, due to the higher surface roughness, the critical heat flux increases. Similar to critical heat flux, higher

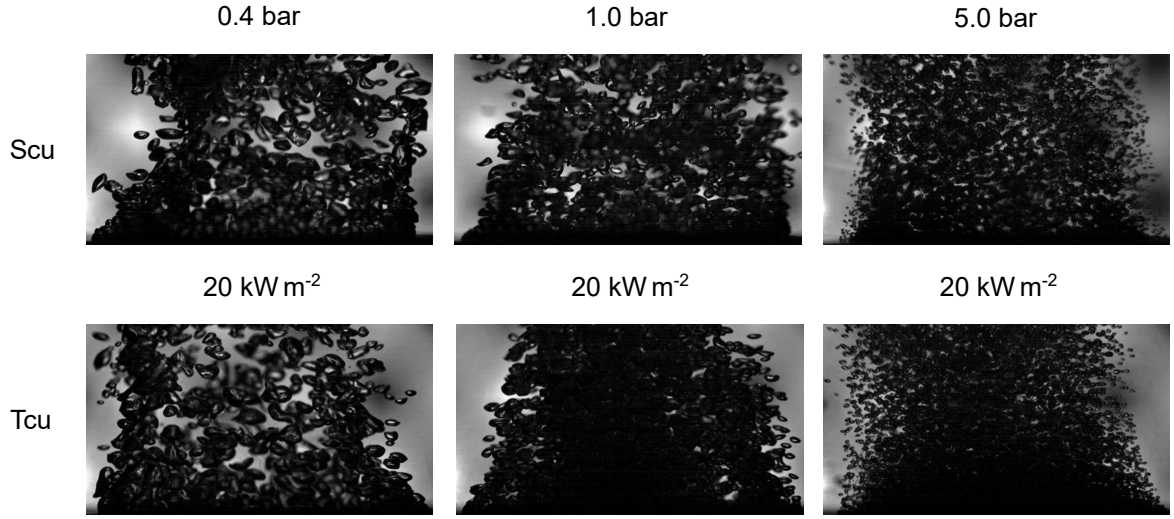

Figure 5.11: Images showing the boiling phenomenon at a heat flux of $20\,\mathrm{kW\,m^{-2}}$, at various system pressures obtained for the two uncoated copper surfaces, Scu and Tcu, using FC-72 as boiling fluid.

heat transfer coefficients are observed for the technical copper surface compared to the smooth copper surface if FC-72 is used as boiling fluid, which is presumably due to higher nucleation site densities. The reason for the different boiling behavior using ethanol and FC-72 remains unknown. It is possible that additional nucleation sites present on the technical copper surface could be activated more easily, if FC-72 is used.

5.2 Results of the homogeneously structured surfaces

As mentioned earlier, all the experiments were performed with decreasing heat fluxes starting close to critical heat flux, with the exception of the data of the technical copper surface with FC-72 and a system pressure of 5.0 bar. The reason for this procedure is explained in the following section.

5.2.1 Boiling performance for increasing heat fluxes

A more detailed description and analysis is presented in the author's paper dedicated to this topic [167]. During pilot tests, it was observed that the surface of the long microstructured heater was not fully activated until shortly before critical heat flux. This phenomenon was also discovered for the technical copper surface. Both boiling surfaces pass through the following boiling regimes with increasing heat flux:

(1) natural convection regime

(2) partially activated isolated bubble regime

(3) fully activated isolated bubble regime

(4) slugs and columns regime

(5) film boiling regime

However, the extent of each individual regime differs depending on the surface, which is shown in Figure 5.12. There, images are presented of the boiling phenomenon taking place on the technical copper surface Tcu and the long microstructured surface 20cu at various heat fluxes and a system pressure of $p_{sys} = 1.75\,\text{bar}$. At the lowest heat flux of $\dot{q} = 20\,\text{kW m}^{-2}$ both surfaces are in the partially activated isolated bubble regime (2), visible by the surfaces not being completely covered with nucleation sites. The technical copper surface transitions into the fully activated isolated bubble regime (3) at $\dot{q} = 50\,\text{kW m}^{-2}$ and transitions into the slugs and columns regime (4) at $\dot{q} = 110\,\text{kW m}^{-2}$. In contrast, the long microstructured surface stays in the partially activated isolated bubble regime and transitions either straight into the slugs and columns regime (4), which is shown in Figure 5.12(4) or exhibits a short fully activated isolated bubble regime before transitioning into the slugs and columns regime. This distinct behavior is also visible in the Nukiyama curves of the two different surfaces.

Figure 5.13 shows double logarithmic Nukiyama curves at various system pressures using FC-72 as boiling fluid. The results of the technical copper surface Tcu are presented in Figure 5.13a, while the results of the long microstructured surface 20cu are visible in Figure 5.13b. Furthermore, the extents of the partially activated isolated bubble regime are indicated by red solid lines. In contrast to the technical copper surface, the extents of the different regimes cannot be identified so easily for the long microstructured surface. For the technical copper surface, the partially activated isolated bubble regime (2) is clearly

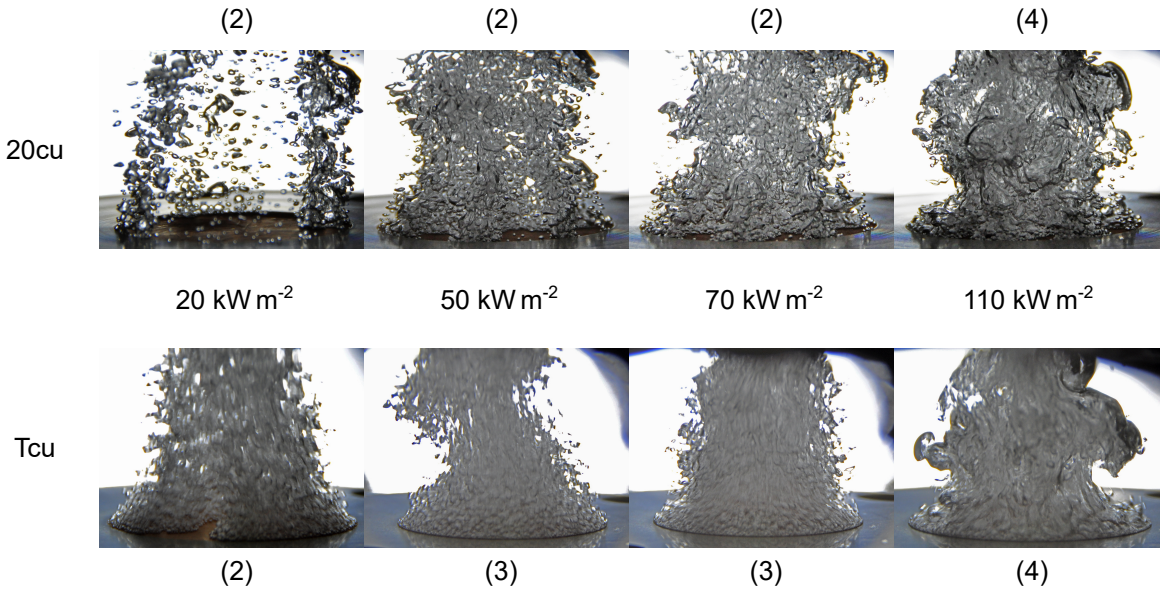

Figure 5.12: Images showing the boiling phenomenon at various heat fluxes on the technical copper surface Tcu and the long microstructured surface 20cu at a system pressure of $p_{sys} = 1.75\,\text{bar}$ using FC-72 as boiling fluid. The surfaces transition from (2) the partially activated isolated bubble regime via (3) the fully activated isolated bubble regime into (4) the slugs and columns regime.

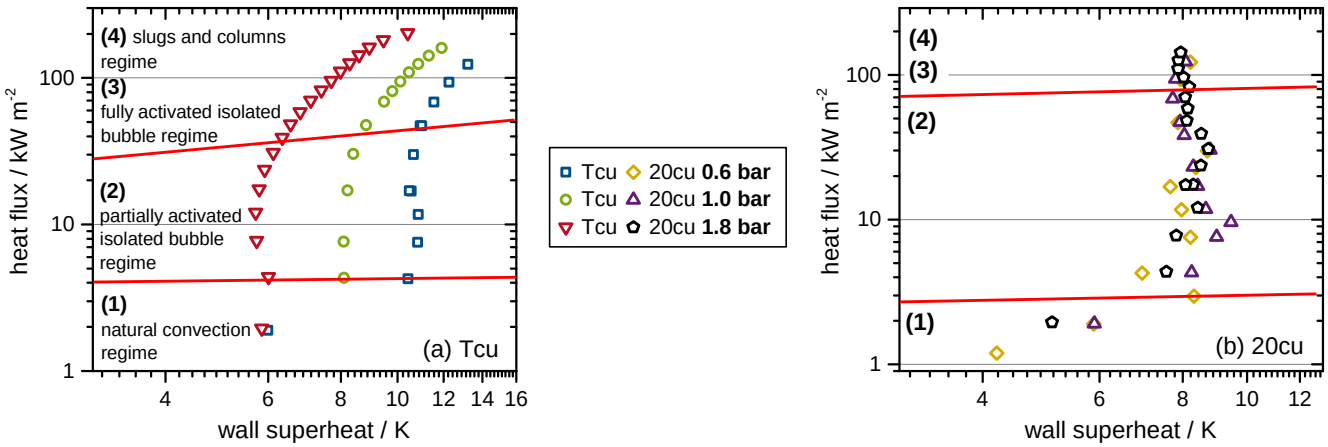

Figure 5.13: Nukiyama curves for the technical copper surface Tcu (a) and the long microstructured surface 20cu (b) at various system pressures obtained with FC-72 with corresponding boiling regimes. The solid red lines indicate the regime boundaries of the partially activated isolated bubble regime.

visible, since the wall superheat does not increase significantly in this regime. With increasing heat flux, additional nucleation sites are activated, while the superheat stays nearly constant. Once the entire surface is activated, the wall superheat starts to increase with rising heat fluxes. Besides the different extents of the boiling regimes, the differing pressure dependencies of the two surfaces are also shown in Figure 5.13. The results of the technical copper surface show a clear pressure dependency, similar to the results of decreasing heat fluxes, which are visible in Figure 5.3. The results of the long microstructured surface, however, show no distinct pressure dependency, which is in opposition to the results presented in Figure 5.14 for decreasing heat fluxes. The lack of pressure dependency is not caused by the presentation of the data in a double logarithmic diagram, since the linear diagrams show a similar trend, which are presented in Figure A.6 in the appendix. The presumed reason is the superposition of the effects causing the pressure dependency and the partially activated isolated bubble regime. Such an overlap of effects should be avoided, since it complicates the identification of parameters, which cause specific changes in the boiling process. This problem is avoided by starting at high heat fluxes slightly below critical heat flux, where the entire surface is activated and reducing the heat flux in a stepwise manner. The once activated nucleation sites stay active until much lower superheats, suppressing the partially activated isolated bubble regime.

5.2.2 Boiling performance of the homogeneously structured surfaces

This section focuses on the first scientific question of this thesis—How is the boiling process affected by a microstructure, whose geometrical length scale is between the well-studied micropillars and nanowires? To address this question, the boiling performance of the two homogeneously structured surfaces 20cu and 10cu are analyzed and compared to the phenomena observed on the two uncoated surfaces. In case the boiling behavior of both microstructured surfaces is very similar, the results of the short microstructured surface are shown in the following section, while the results of the long microstructured surface are presented in the appendix.

5.2.2.1 Nukiyama curves

In Figures 5.14 and 5.15 Nukiyama curves for the long and short microstructured surfaces, 20cu and 10cu, respectively, are presented. The results of the ethanol measurements are visible on the left (a), while the results using FC-72 are shown on the right (b). Similar to the results of the uncoated copper surfaces, critical heat flux increases with higher system pressure. In addition, the wall superheat decreases with increasing system pressure, with the exception of the measurements for the long microstructured surface using ethanol (Figure 5.14a). For ethanol, the wall superheat increases between 1.0 bar and 3.0 bar and reduces again at a system pressure of 5.0 bar. Additionally, the shapes of the Nukiyama curves change from a "sigmoid-shape" to a "power-law-shape" at higher pressures. The experiments using FC-72 show this "power-law-shape" as the typical shape of boiling curves over the entire pressure range. The results of the short microstructured surface using ethanol show a less pronounced change in shape of the boiling curve at 5.0 bar, which is accompanied by a less significant decrease in wall superheat.

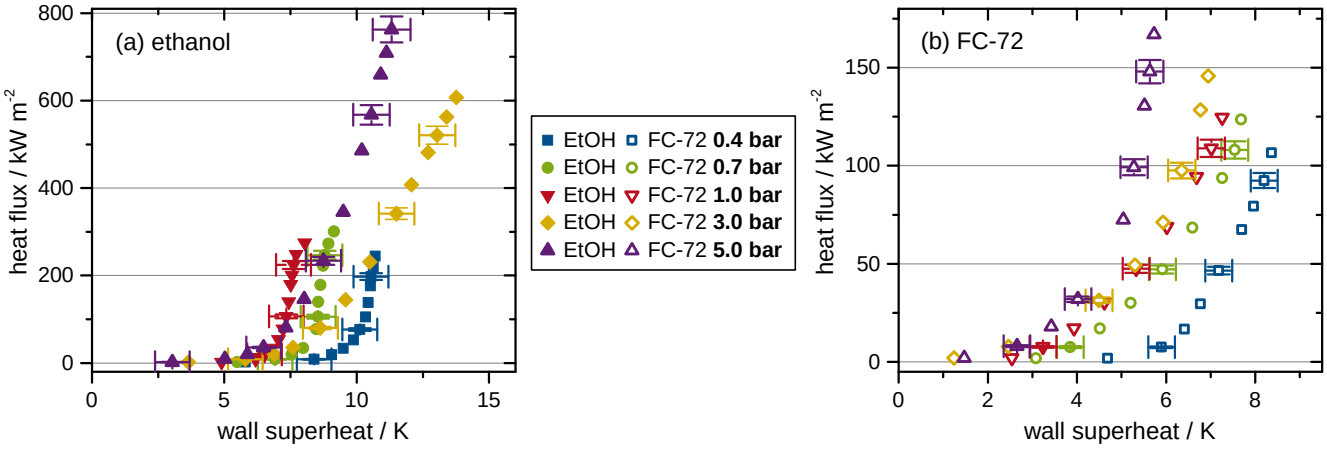

Figure 5.14: Nukiyama curves for the long microstructured surface 20cu at various system pressures obtained with ethanol (a) and FC-72 (b).

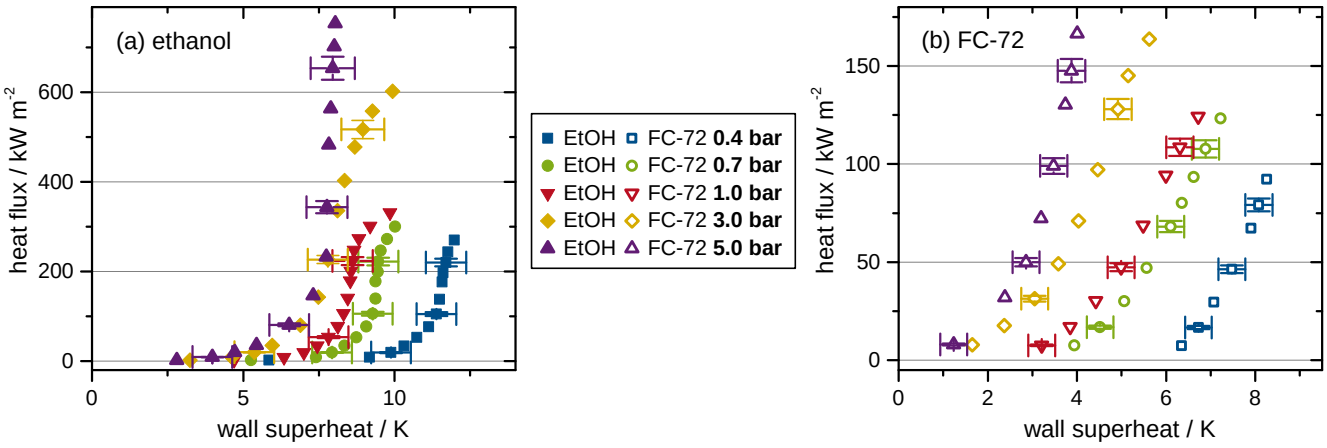

Figure 5.15: Nukiyama curves for the short microstructured surface 10cu at various system pressures obtained with ethanol (a) and FC-72 (b).

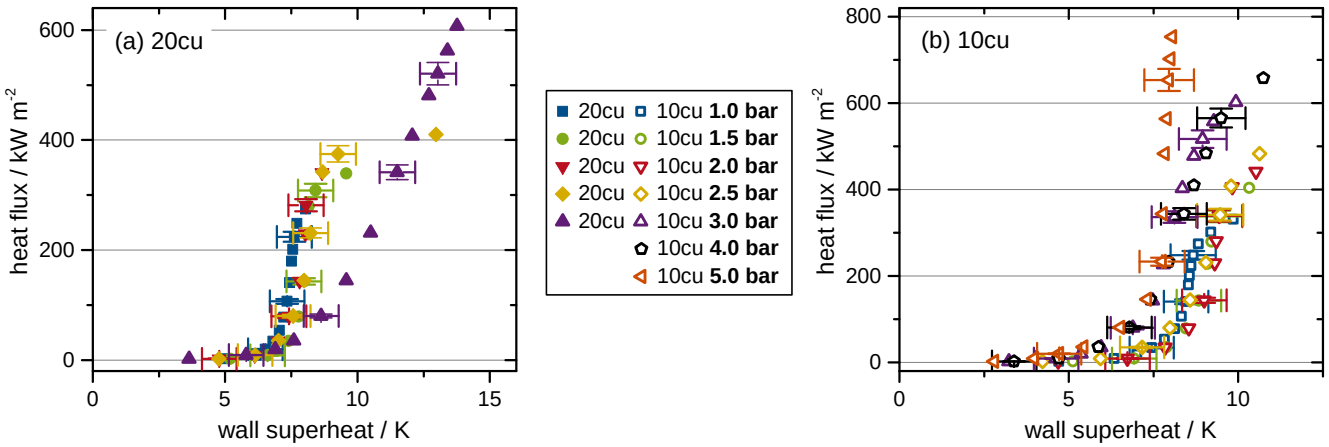

Figure 5.16: Nukiyama curves at various system pressures using ethanol for the long microstructured surface 20cu (a) and short microstructured surface 10cu (b).

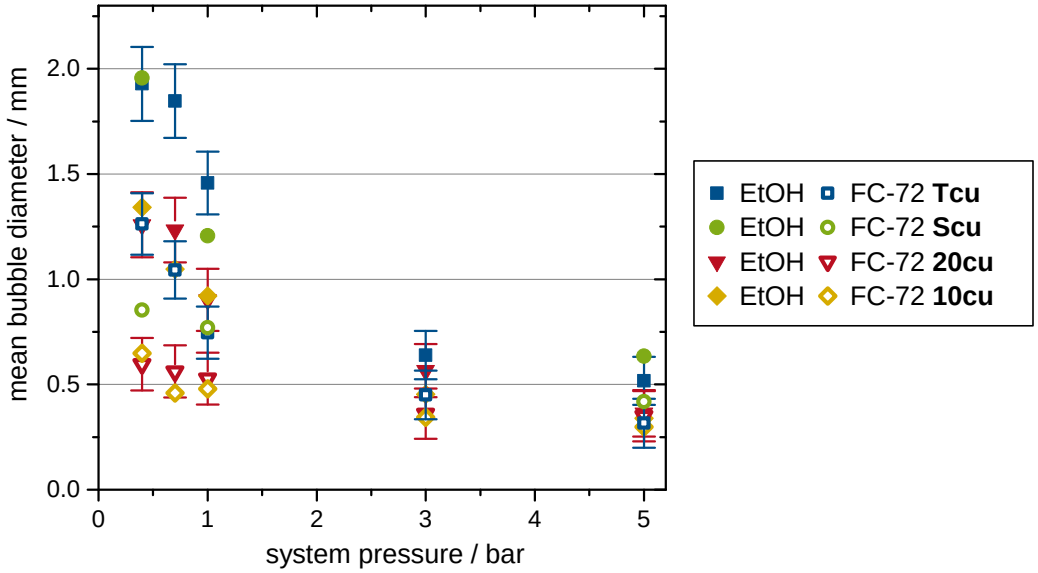

Figure 5.17: Mean bubble diameters at various system pressures using ethanol and FC-72 obtained for the technical Tcu, the smooth Scu, the long microstructured 20cu, and the short microstructured surface 10cu.

To establish whether this change in boiling behavior for the two surfaces is gradual or sudden, additional experiments between 1.0 bar and 3.0 bar (20cu) and 1.0 bar and 5.0 bar (10cu) were performed using ethanol (Figure 5.16). These experiments indicate that the change from a "sigmoid-shape" to a "power-law-shape" of the boiling curve happens between 2.5 bar and 3.0 bar for the long microstructured surface 20cu (Figure 5.16a) and between 4.0 bar and 5.0 bar for the short microstructured surface 10cu (Figure 5.16b). A reason for this change in the boiling behavior might be the existence of a critical bubble size to wire length ratio. At higher system pressures, the bubble diameters are smaller, which is shown for the uncoated and the homogeneously structured surfaces in Figure 5.17. Considering the smaller needle length of 10cu, this would result in a change in boiling curve shape at higher system pressures compared to the long microstructured surface, which is observed in the experiments. The absence of a change in the Nukiyama curves of FC-72 could be explained by the smaller bubble diameters. This theory, however,

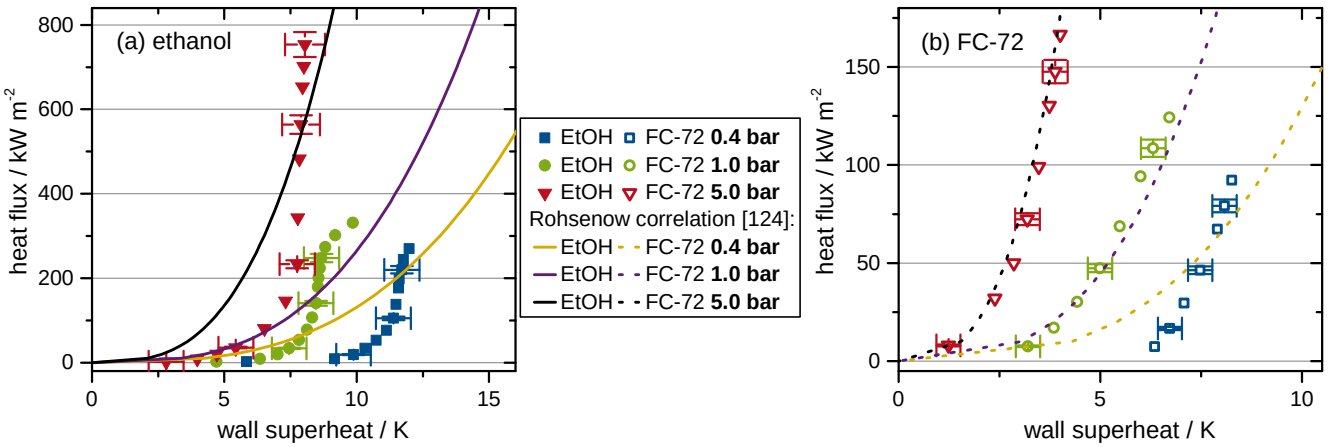

Figure 5.18: Nukiyama curves for the short microstructured surface 10cu at various system pressures obtained with ethanol (a) and FC-72 (b) in comparison to Rohsenow's correlation [124].

cannot be proven because the exact interactions between the growing bubbles and the needles cannot be visualized in the scope of this thesis.

To establish, how this change in the boiling behavior affects the comparability to a correlation, the boiling curves of the microstructured surfaces are compared to the correlation of Rohsenow (Equation 2.5) [124]. The results of the long microstructured surface 20cu are presented in Figure A.7 in the appendix. Figure 5.18 shows the Nukiyama curves for the short microstructured surface 10cu at various system pressures in comparison to Rohsenow's correlation [124]. The results for ethanol are shown in Figure 5.18a, while the ones using FC-72 are visible in Figure 5.18b. The experimental data, obtained with the short microstructured surface using FC-72, are in good agreement with Rohsenow's correlation. The deviations are between 5 and 14 % using the parameter set of $a_{\text{FC-72}} = 0.33$, $b_{\text{FC-72}} = 1.7$, and $C_{\text{sf,FC-72}} = 0.0015$. The deviations for the long microstructured surface are larger with 17 and 24 %. At least for the short microstructured surface, this suggests that the changes in wall superheat with increasing pressure are due to temperature and pressure dependencies of the physical properties of the fluid, and not interactions between the surface structure and nucleating bubbles.

However, the experimental data obtained with ethanol and both homogeneously microstructured surfaces does not fit the correlation very well. Besides the different shapes of the boiling curves, the deviations between the experimental results and the correlation are large as well, with 20 to 25 % for the short microstructured surface and 23 to 40 % for the long microstructured surface. These large deviations are mainly caused by the changes in boiling curve shape discussed in the previous paragraph. The parameter set for the Rohsenow correlation of the short microstructured surface are $a_{\text{EtOH}} = 0.33$, $b_{\text{EtOH}} = 1$, and $C_{\text{sf,EtOH}} = 0.004$.

Compared to the smooth copper surface, the same parameters $a_{\text{EtOH,FC-72}}$ and $b_{\text{EtOH,FC-72}}$ are used. However, the value of $C_{\text{sf,EtOH}}$ is significantly smaller $\left(C_{\text{sf,EtOH,10cu}} = 0.004,\ C_{\text{sf,EtOH,Scu}} = 0.0095\right)$. The same is true for the experiments with FC-72 $\left(C_{\text{sf,FC-72,10cu}} = 0.0015 \text{ and } C_{\text{sf,FC-72,Scu}} = 0.0038\right)$.

5.2.2.2 Heat transfer coefficients

The difference in the fitted parameters observed above is presumably caused by the significantly smaller wall superheats obtained by measurements using the homogeneously structured surfaces compared to the smooth surface. In turn, this results in higher heat transfer coefficients at specific heat fluxes, which is shown in Figure 5.19. There, the heat transfer coefficients for specific heat fluxes for the short microstructured surface 10cu at various system pressures using ethanol (a) and FC-72 (b) are presented. For comparison, the results of the smooth copper surface Scu at system pressures of 0.4 and 5.0 bar are shown as well. Similar to the results of the smooth copper surface, the heat transfer coefficients increase for increasing heat flux and system pressure. At a specific system pressure and heat flux, the heat transfer coefficients measured for the short microstructured surface are significantly higher, than the heat transfer coefficients of the smooth copper surface. This is presumably caused by the higher surface roughness, the larger area in contact with the fluid, and the smaller bubble diameters for a specific system pressure, which is shown in Figure 5.17. The identification of the exact contribution of each parameter is not possible. However, it is clear that the increased surface area does not directly correlate with the heat transfer coefficient, since the overall heat transfer improvement is in the best-case scenario 2.8, while the area is increased by a factor of 9.3. The results of the long microstructured surface 20cu are presented in Figure A.8 in the appendix.

The Tables 5.1 and 5.2 show the heat transfer coefficient enhancement ratios at specific heat fluxes and various system pressures using ethanol and FC-72 as boiling fluids, respectively. The enhancement ratios, which compare the heat transfer coefficients of the microstructured surfaces 20cu and 10cu to the smooth copper surface Scu, reach 2.8 for both fluids. At lower system pressures, the enhancement ratios of the long microstructured surface are slightly larger compared to the short microstructured surface and vice versa at higher system pressures. When comparing the enhancement ratios of the two microstructured surfaces to the technical copper surface Tcu using FC-72 as boiling fluid, they are smaller because the technical copper surface's roughness enhances the boiling process, as discussed in section

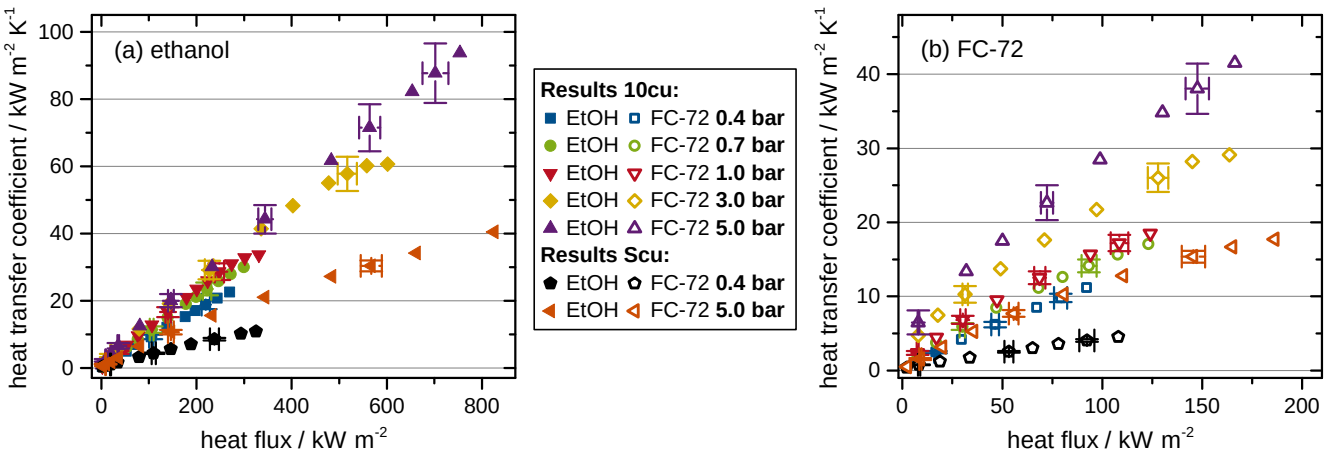

Figure 5.19: Heat transfer coefficients for specific heat fluxes obtained for the short microstructured surface 10cu and smooth copper surface Scu using ethanol (a) and FC-72 (b) at various system pressures.

Table 5.1: Heat transfer coefficient enhancement ratios at a specific heat flux and various system pressures using ethanol as boiling fluid.

	$\alpha_{10cu}/\alpha_{Scu}$	$\alpha_{10cu}/\alpha_{Tcu}$	$\alpha_{20cu}/\alpha_{Scu}$	$\alpha_{20cu}/\alpha_{Tcu}$
$\dot{q}_{el} = 220\,kW\,m^{-2}$				
0.4 bar	2.20	2.00	2.43	2.20
1.0 bar	2.48	2.42	2.81	2.50
5.0 bar	1.93	1.96	1.72	1.75

Table 5.2: Heat transfer coefficient enhancement ratios at specific heat fluxes and various system pressures using FC-72 as boiling fluid.

	$\alpha_{10cu}/\alpha_{Scu}$	$\alpha_{10cu}/\alpha_{Tcu}$	$\alpha_{20cu}/\alpha_{Scu}$	$\alpha_{20cu}/\alpha_{Tcu}$
$\dot{q}_{el} = 92\,kW\,m^{-2}$				
0.4 bar	2.75	1.78	2.77	1.80
1.0 bar	2.59	1.75	2.33	1.58
$\dot{q}_{el} = 130\,kW\,m^{-2}$				
5.0 bar	2.26	1.40	1.54	0.96

5.1.2.3. Overall, the enhancement ratios are larger at lower system pressures, which correlates to the larger reduction in bubble diameter, shown in Figure 5.17.

Focusing on the pressure dependency of the heat transfer coefficients of the two homogeneously structured surfaces, the experimental data is compared to Gorenflo's correlation (Equations 2.6) [140]. The reference heat transfer coefficients necessary for the correlation are experimental values at 30 and $80\,kW\,m^{-2}$ for FC-72 and ethanol, respectively, both at 1.0 bar. Figure 5.20 shows the ratios of the experimentally determined heat transfer coefficients to the mentioned references at different reduced pressures. The results of the long microstructured surface 20cu are presented in Figure A.9 in the appendix. For both surfaces, it is observable that the pressure dependency of the heat transfer coefficients is significantly lower than the dependency predicted by the correlation. At higher reduced pressures, the deviations between the results of the microstructured surfaces and the correlation are larger compared to deviations of the uncoated surfaces, for both fluids respectively. In addition, deviations at lower system pressures and higher heat fluxes are observable as well for the microstructured surfaces. Besides the reduced pressure dependency of the measured heat transfer coefficients, the roughness of the microstructured surfaces could be another important factor resulting in deviations between the measured data and the correlation. In Gorenflo's correlation, the roughness of a surface is accounted for by its mean arithmetic roughness. However, it is assumed that the correlation considers the surface roughness to be caused by scratches and grooves. While having similar arithmetic surface roughness, this surface structure is very different compared to the microstructures investigated in this thesis. The impact of microstructures on the boiling process is not limited to the roughness value, but other effects like liquid imbibition into the structures could have a significant impact [110].

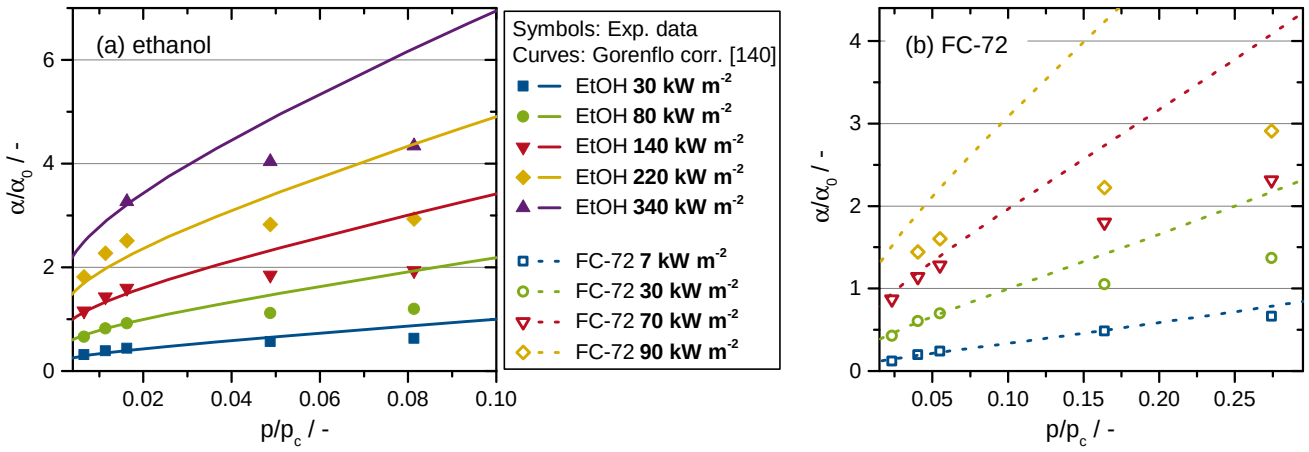

Figure 5.20: Ratios of heat transfer coefficient to reference heat transfer coefficient for specific heat fluxes at reduced pressures obtained for the short microstructured surface 10cu using ethanol (left) and FC-72 (right) compared to Gorenflo's correlation [140].

The correlations of Gorenflo and Rohsenow were established for smooth and rough uncoated surfaces. They are only partially suited to predict the boiling process for a microstructured surface. Therefore, the experimental data is compared to two correlations developed for a nanostructured surface [88] and a surface with micropillars [50]. Unfortunately, a correlation could not be found that was developed using a microstructure with higher geometrical similarities to the two homogeneously structured surfaces. Li et al. [88] did experiments using nickel surfaces with different surface treatments, ranging from chemical enhancement of the wettability to nanostructuring with nano cones. They used water as boiling fluid at atmospheric pressure and established the following correlation (Equations 5.2), which is based on Rohsenow's correlation [124]:

$$\Delta T_{\mathrm{sup}} = 0.013 \frac{\Delta h_v}{c_{p,\mathrm{l}}} C_{\mathrm{sf}}^{-0.33} \left[\frac{\dot{q}_{\mathrm{el}}}{\Delta h_v \eta_{\mathrm{l}}} \sqrt{\frac{\sigma}{g\,(\rho_{\mathrm{l}} - \rho_{\mathrm{v}})}} \right]^{0.33} Pr, \tag{5.2a}$$

$$C_{\mathrm{sf}} = r\sqrt{1-\cos\Theta} \left[1 + \frac{5.45}{(Ra-3.5)^2 + 2.61} \right] \left(\frac{\lambda_{\mathrm{w}} \rho_{\mathrm{w}} c_{\mathrm{w}}}{\lambda_{\mathrm{l}} \rho_{\mathrm{l}} c_{p,\mathrm{l}}} \right)^{-0.02}, \quad \Theta = max\,(\Theta, 15°). \tag{5.2b}$$

Ho et al. [50] did measurements using FC-72 at atmospheric pressure with different micropillared surfaces made of AlSi10Mg. They also based their correlation (Equations 5.3) on Rohsenow's correlation:

$$\Delta T_{\mathrm{sup}} = \frac{\Delta h_v}{c_{p,\mathrm{l}}} C_{\mathrm{sf}} \left[\frac{\dot{q}_{\mathrm{el}}}{\Delta h_v \eta_{\mathrm{l}}} \sqrt{\frac{\sigma}{g\,(\rho_{\mathrm{l}} - \rho_{\mathrm{v}})}} \right]^{n} Pr^{3.5}, \tag{5.3a}$$

$$C_{\mathrm{sf}} = 3.21 \times 10^{-5}\, r^{0.0469}, \tag{5.3b}$$

$$n = 1.2163 r^{-0.0743}. \tag{5.3c}$$

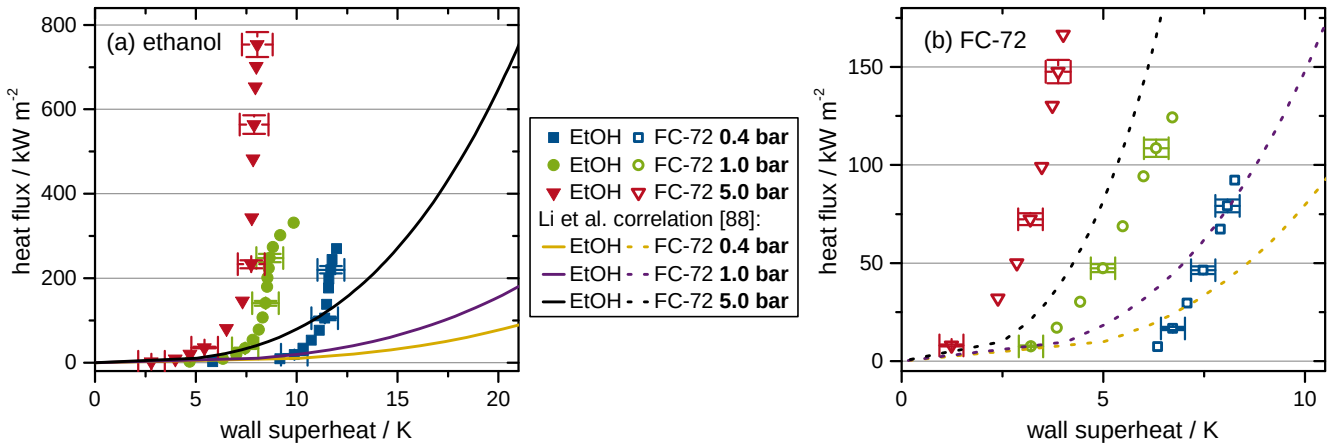

Figure 5.21: Nukiyama curves for the short microstructured surface 10cu at various system pressures obtained with ethanol (a) and FC-72 (b) in comparison to the correlation of Li et al. [88].

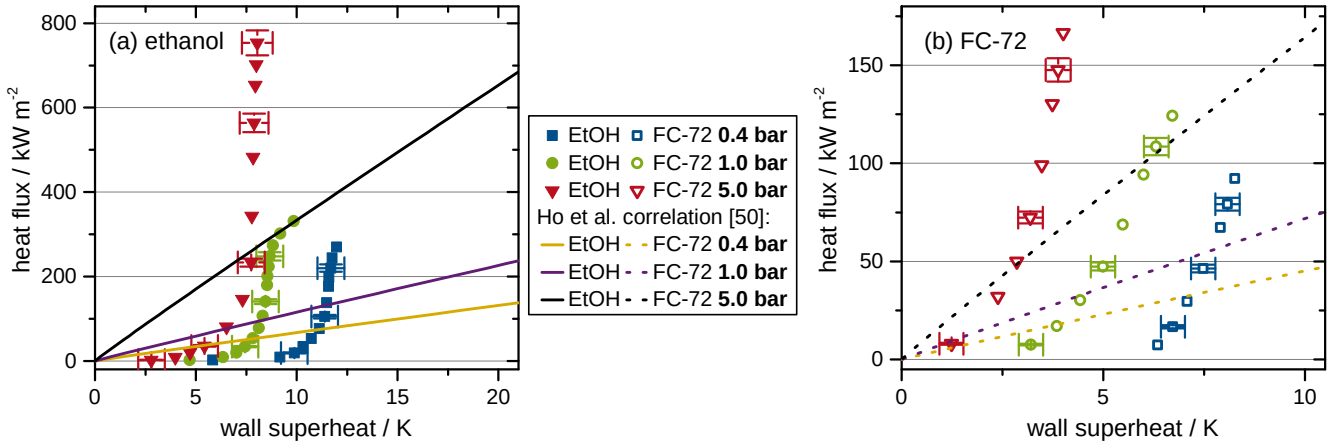

Figure 5.22: Nukiyama curves for the short microstructured surface 10cu at various system pressures obtained with ethanol (a) and FC-72 (b) in comparison to the correlation of Ho et al. [50].

Figures 5.21 and 5.22 show Nukiyama curves comparing the results of the short microstructured surface 10cu to the correlations of Li et al. (Equations 5.2) [88] and Ho et al. (Equations 5.3) [50] at various system pressure. The results using ethanol are shown on the left (a) and the ones using FC-72 on the right (b). Obviously, the experimental results fit neither correlation well. If FC-72 is used as boiling fluid, the mean deviations are smaller. However, they are still between 16 and 33 % for the correlation of Li et al. and between 74 and 81 % for the correlation of Ho et al. The large deviations between the experimental results and the correlations could be due to the large roughness factor of $r = 9.29$, the ratio of the wetted surface area to the surface area of a smooth surface with the same dimensions. This is a theoretical value, since the real value could not be analyzed in the scope of this thesis. The real value is likely smaller than the theoretical one, because the microneedles are slightly tilted and they form small agglomerations. Still, even if the real value is slightly smaller, it is presumably still significantly larger than the ones of the surfaces of Li et al. (approximately $r = 1.2$) and Ho et al. ($r = 1.25$ to $r = 3.74$). Besides the larger roughness factors, the microstructural geometry of the two homogeneously structured surfaces differs from the surfaces used by Li et al. and Ho et al., which can have a significant impact on the boiling process [71].

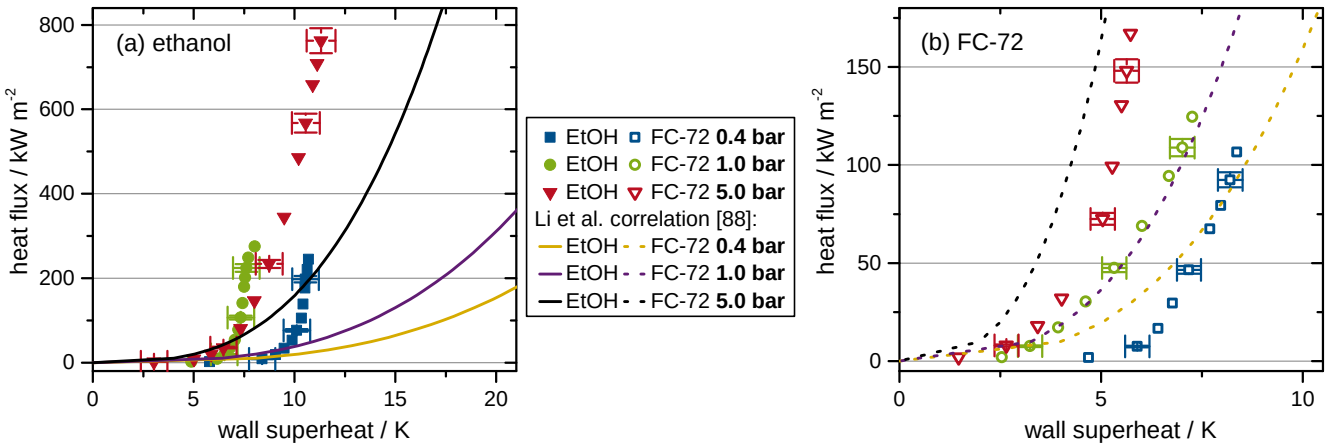

Figure 5.23: Nukiyama curves for the long microstructured surface 20cu at various system pressures obtained with ethanol (a) and FC-72 (b) in comparison to the correlation of Li et al. [88].

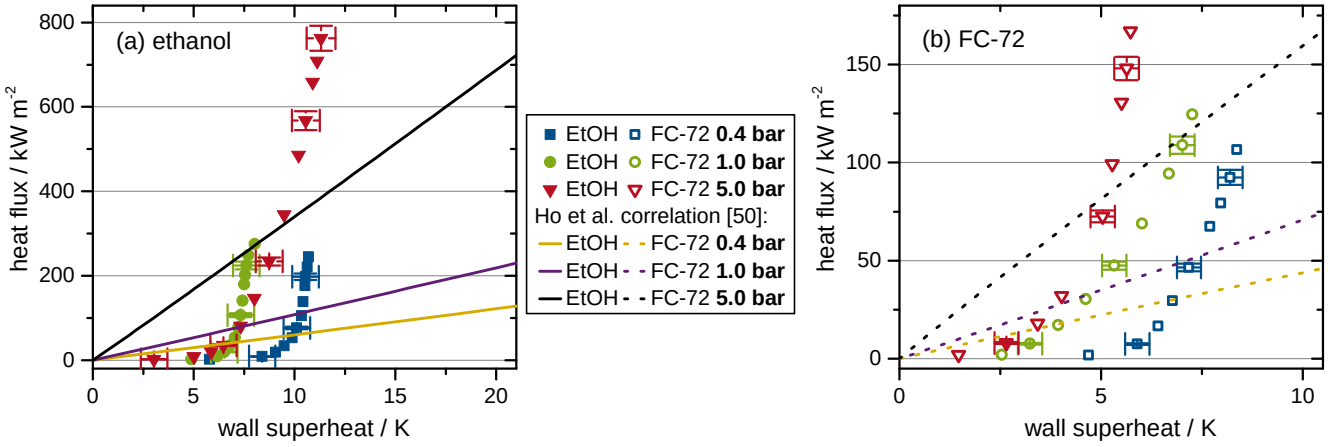

Figure 5.24: Nukiyama curves for the long microstructured surface 20cu at various system pressures obtained with ethanol (a) and FC-72 (b) in comparison to the correlation of Ho et al. [50].

Figures 5.23 and 5.24 show Nukiyama curves comparing the results of the long microstructured surface 20cu with the correlations of Li et al. (Equations 5.2) [88] and Ho et al. (Equations 5.3) [50] at various system pressures using ethanol (a) and FC-72 (b) as boiling fluids, respectively. Remarkably, the experimental results obtained for the long microstructured surface using FC-72 fit the correlation of Li et al. reasonably well (Figure 5.23b). However, the results measured with ethanol do not fit the correlation at all. As Li et al. [88] used water as boiling fluid and the physical properties of water and ethanol are less different compared to FC-72, it is assumed that an overlap of two effects is responsible for the good fit between correlation and results obtained with FC-72. Similar to the results of the short microstructured surface, the Nukiyama curves for the long microstructured surface do not fit the correlation of Ho et al. [50].

All in all, the homogeneously structured surfaces used in this thesis enhance the heat transfer coefficient significantly and correlations developed for smooth or structured surfaces do not fit the experimental data very well, especially if no fitted parameters are used in the correlations. This is because important parameters have not been identified yet and, therefore, cannot be accounted for in these correlations.

Additionally, the lack of measurements with microstructures at lower and higher system pressures than atmospheric pressure, reported in literature, results in the inability of correlations to account for pressure dependencies.

5.2.2.3 Critical heat fluxes

Figure 5.25 shows the critical heat fluxes for the short microstructured surface 10cu at various system pressures compared to the correlations of Zuber (Equations 2.7) [168], Kandlikar (Equation 2.8) [62] and Yagov (Equations 2.11) [158]. Additionally, the critical heat fluxes obtained for the smooth copper surface Scu are presented for comparison. The results using ethanol as boiling fluid are visible on the left and the ones with FC-72 on the right. Compared to the measurements of the smooth copper surface and the correlation of Zuber, the critical heat fluxes obtained using the short microstructured surface are smaller for most system pressures, especially for the measurements using ethanol. For FC-72, the differences are slightly smaller and the values fit the correlation of Yagov and Kandlikar well for a receding contact angle of $\Theta_{rec,10cu,FC\text{-}72} = 71°$. The critical heat fluxes using ethanol do not fit the correlation of Yagov at small system pressures and a receding contact angle of $\Theta_{rec,10cu,EtOH} = 77°$ is necessary to fit the correlation of Kandlikar. Those fitted receding contact angles are significantly larger than those obtained for the smooth copper surface $\left(\Theta_{rec,Scu} = 65°\right)$ and the technical copper surface using ethanol and especially FC-72 $\left(\Theta_{rec,Tcu,FC\text{-}72} = 43°\right)$. A similar trend is visible for the long microstructured surface, whose results are presented in Figure A.10 in the appendix.

The higher receding contact angles could be explained by two scenarios. On the one hand, Kandlikar's correlation might not incorporate the unknown microstructure-related phenomenon, which causes the reduced critical heat fluxes of the homogeneously structured surfaces. On the other hand, the receding contact angles actually increase, this, however, disagrees with two wetting phenomena. In case the system is in Wenzel state [156], where the fluid imbibes into the surface structure, the wetting behavior present on the smooth surface should be enhanced by additional roughness. This would result in reduced

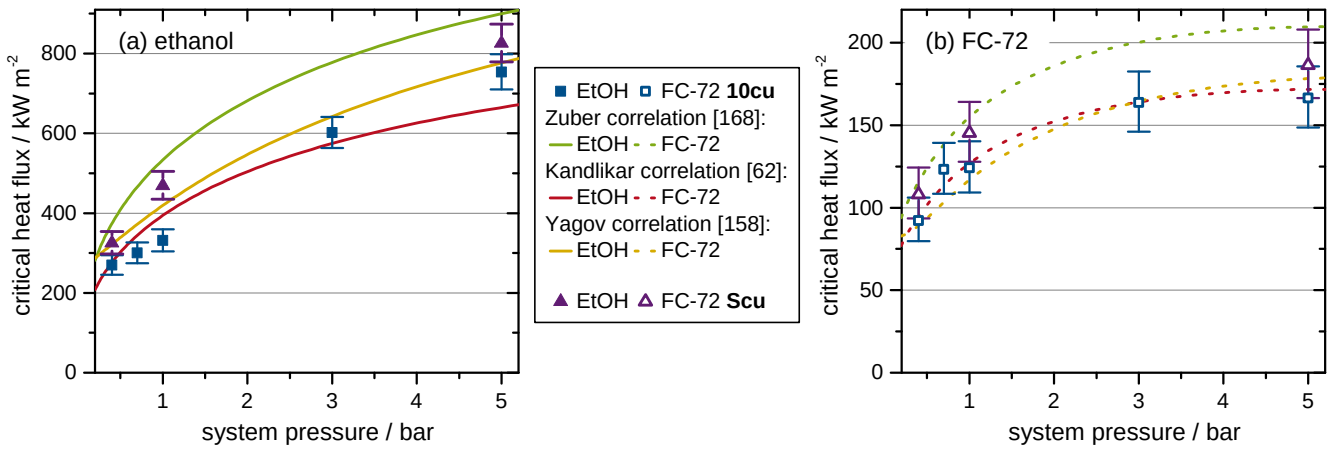

Figure 5.25: Critical heat fluxes for the short microstructured surface 10cu at various system pressures obtained with ethanol (a) and FC-72 (b) compared to correlations of Zuber [168], Kandlikar [62], Yagov [158], and the experimental results of the smooth copper surface Scu.

static contact angles compared to the smooth surface. Additionally, during the contact angle and imbibition experiments, described in section 3.2.2, the two homogeneously structured surfaces showed perfect wetting behavior and Wenzel state for both fluids. In addition, it is well-known that microstructuring has a significant impact on the receding contact angles [35, 164]. Typically, the receding contact angle decreases with increasing roughness [93, 100, 164]. However, there is a study showing the opposite behavior for high surface roughness [152]. In case the system is in Wenzel state, it is, therefore, very likely that the receding contact angles on the homogeneously structured surfaces are smaller than the ones on the uncoated surfaces. However, it could be possible that the wetting behavior of the microstructures changes from Wenzel to Cassie-Baxter state [17], where the fluid cannot imbibe into the surface structure, due to evaporation. In addition to the increasing contact angles under non-isothermal conditions [123], the microstructure could be completely filled with vapor shortly before burnout because of the densely packed microneedles. Being in Cassie-Baxter state should increase the receding contact angles compared to the uncoated surfaces, which remain in Wenzel state. Moon et al. [105] observed a change in the wetting behavior from Cassie-Baxter, which was present during drop impingement experiments, to Wenzel during boiling experiments on a surface with micropillars. A publication observing a change in the opposite direction could not be found by the author, however, a change from Wenzel state to Cassie-Baxter state should be possible, depending on the microstructure. In conclusion, it is not possible to determine whether or not the receding contact angle increases, since it is not possible to measure, and arguments can be made for both scenarios.

Additionally, there is the possibility that the presented correlations do not factor in the unknown microstructure-related phenomenon, which causes the lower critical heat fluxes, because they were established for smooth surfaces. Correlations predicting critical heat fluxes of microstructured surfaces can be separated into different groups. One group assume that vapor recoil triggers burnout based on the correlation of Kandlikar. Typically, those correlations include critical heat flux increasing effects caused by the microstructures. Chu et al. [22] assume that the surface tension force holding the bubble at the surface increases due to the longer effective contact line length caused by microstructures. Ahn et al. [3] assume that the dispersed liquid inside the microstructure causes an increase in critical heat flux. However, liquid spreading was also observed in the imbibition experiments, described in section 3.2.2. Nevertheless, the critical heat fluxes obtained with the homogeneously structured surfaces are smaller compared to the smooth copper surface, where no imbibition takes place, and whose evaporation rates are, therefore, significantly reduced. This leads to the conclusion that another phenomenon dictates the critical heat fluxes of the homogeneously structured surfaces.

Quan et al. [119] assume that a reduction in the Rayleigh-Taylor wavelength causes higher critical heat fluxes. Similar to Quan et al., several other studies [92, 111] report that a modified Rayleigh-Taylor wavelength might be responsible for the increased critical heat fluxes. This in turn would predict a larger Rayleigh-Taylor wavelength on the two homogeneously structured surfaces compared to the smooth copper surface.

Dhillon et al. [26] and Nguyen et al. [107] assume that an increased rewetting velocity prevents the formation of irreversible dry spots, which increases the critical heat flux. Since the microneedles presumably increase the flow resistance, a reduced dewetting velocity might be possible.

In conclusion, the mechanism causing the smaller critical heat fluxes of the two homogeneously structured surfaces cannot be identified, since several important parameters such as the receding contact angles, the wetting regime (Wenzel/Cassie-Baxter), or the rewetting velocities cannot be measured or identified.

Since the heat transfer coefficients increase with higher heat fluxes, the reduced critical heat fluxes also cause reduced heat transfer coefficients at maximum heat fluxes below CHF, compared to the two uncoated copper surfaces. This reduction, which is more prominent for higher system pressures, is visible in the Tables 5.3 and 5.4, showing the heat transfer coefficient enhancement ratios at maximum heat fluxes.

All in all, the two homogeneously structured surfaces have altered the boiling process drastically. The different needle length affects the measurements using ethanol, while having an insignificant influence on the measurements using FC-72. The influence of the system pressure on the boiling process is not as pronounced as for the two uncoated copper surfaces. Compared to the smooth copper surface, the two homogeneously structured surfaces could enhance the heat transfer coefficients up to a factor of 2.8 for both fluids. Compared to the technical copper surface, the two homogeneously structured surfaces could enhance the heat transfer coefficients up to a factor of 1.8 for FC-72 and 2.5 for ethanol, respectively. The enhancement ratios at maximum heat fluxes are, for the most part, lower than the enhancement ratios for a specific heat flux. This is because the critical heat fluxes of the two homogeneously structured surfaces are lower compared to the uncoated copper surfaces. Those findings answer the first scientific question—How is the boiling process affected by a microstructure, whose geometrical length scale is between the well-studied micropillars and nanowires?

Table 5.3: Heat transfer coefficient enhancement ratios at maximum heat fluxes below CHF and various system pressures using ethanol as boiling fluid.

	$\alpha_{max,10cu}/\alpha_{max,Scu}$	$\alpha_{max,10cu}/\alpha_{max,Tcu}$	$\alpha_{max,20cu}/\alpha_{max,Scu}$	$\alpha_{max,20cu}/\alpha_{max,Tcu}$
0.4 bar	2.08	1.46	2.11	1.48
1.0 bar	1.89	1.66	1.92	1.68
5.0 bar	2.32	1.95	1.67	1.40

Table 5.4: Heat transfer coefficient enhancement ratios at maximum heat fluxes below CHF and various system pressures using FC-72 as boiling fluid.

	$\alpha_{max,10cu}/\alpha_{max,Scu}$	$\alpha_{max,10cu}/\alpha_{max,Tcu}$	$\alpha_{max,20cu}/\alpha_{max,Scu}$	$\alpha_{max,20cu}/\alpha_{max,Tcu}$
0.4 bar	2.46	1.48	2.81	1.69
1.0 bar	1.98	1.37	1.99	1.27
5.0 bar	2.34	1.08	1.64	0.79

5.3 Results of the optimized surface

This leads to the second scientific question—Is it possible to improve the boiling performance of said microstructure by adding a macrostructure, creating a hierarchical structure? Since the primary goal is to increase critical heat flux, the desired hierarchical structure should increase the liquid flow into the microstructure, create different fluid inflow and outflow paths, and decrease the Rayleigh-Taylor wavelength. This is achieved by creating areas of lower boiling performance in between areas of higher boiling performance, similar to the surfaces of Rahman et al. [121]. The secondary goal is to increase heat transfer coefficients further. The optimized, hierarchical surface created to achieve these goals is described in section 3.2. The boiling performance of this optimized surface will be discussed in the following section.

5.3.1 Nukiyama curves

Figures 5.26, 5.27, and 5.28 show Nukiyama curves for the five copper surfaces used in this thesis at system pressures of 0.4 bar, 1.0 bar, and 5.0 bar. The experimental results using ethanol (a) as boiling fluid are presented on the left and the results using FC-72 (b) are shown on the right. The results for the system pressures of 0.7 bar and 3.0 bar are presented in Figures A.11 and A.12 in the appendix. For the most part, the two homogeneously structured surfaces 20cu and 10cu show the lowest wall superheats, corresponding to their high heat transfer coefficients. In addition, the low critical heat fluxes discussed in the last section are visible. The optimized, hierarchical surface Opt shows slightly higher wall superheats compared to the homogeneously structured surfaces, but lower wall superheats compared to the two uncoated surfaces Scu and Tcu, with the exception of the experiment with FC-72 at 5.0 bar. The critical heat fluxes for the optimized surface are higher compared to the other surfaces for all system pressures, which means that the first goal of the optimization is achieved. The possible reasons for this increased critical heat flux are discussed in the next section.

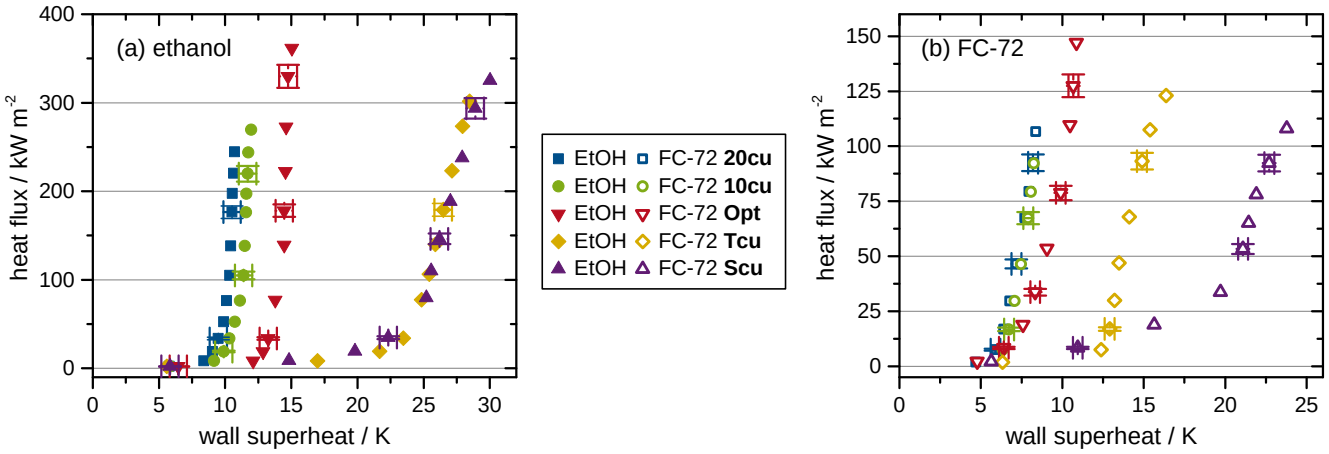

Figure 5.26: Nukiyama curves at 0.4 bar system pressure for the five different surfaces using ethanol (a) and FC-72 (b).

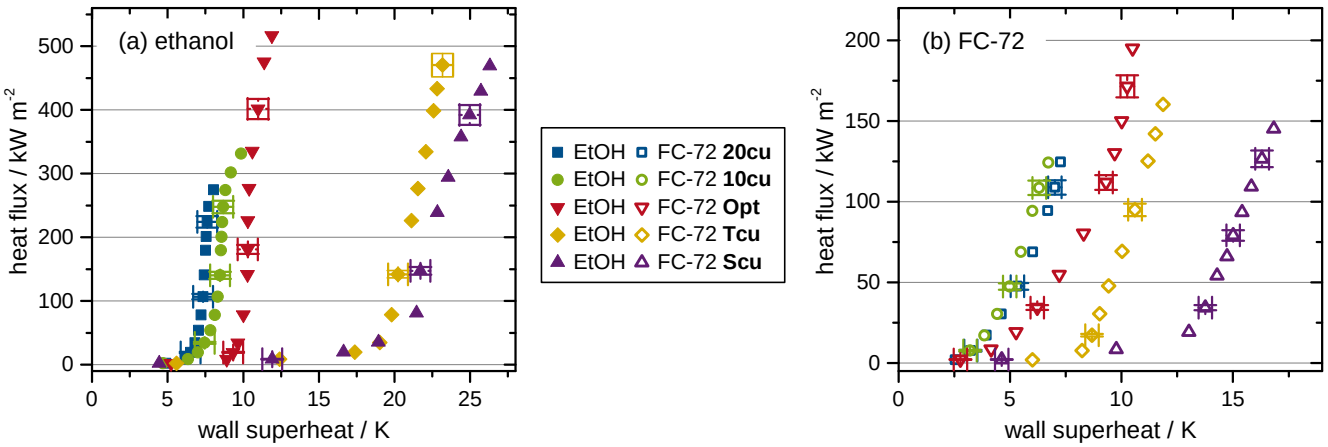

Figure 5.27: Nukiyama curves at 1.0 bar system pressure for the five different surfaces using ethanol (a) and FC-72 (b).

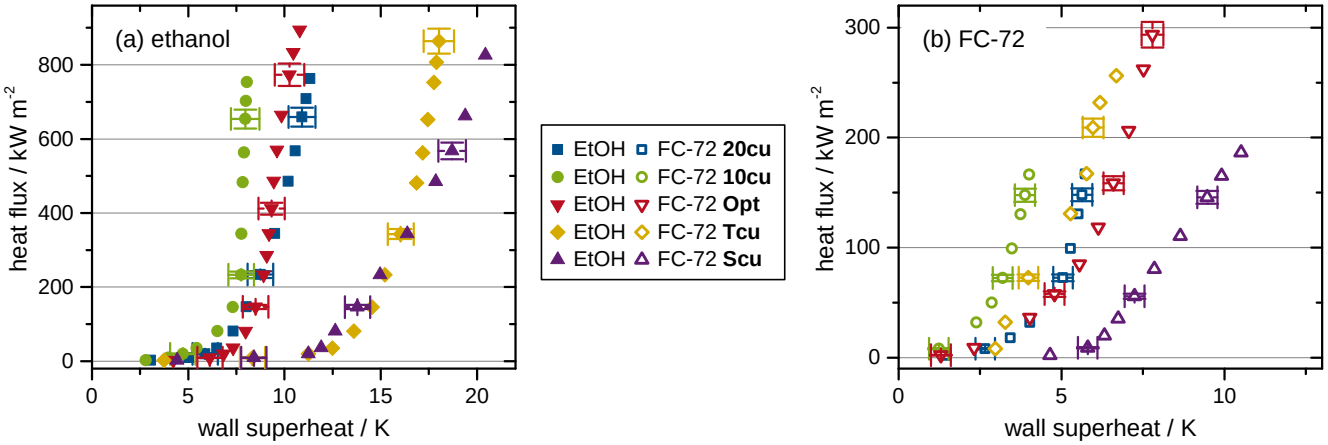

Figure 5.28: Nukiyama curves at 5.0 bar system pressure for the five different surfaces using ethanol (a) and FC-72 (b).

5.3.2 Critical heat fluxes

Upon closer inspection of the boiling phenomenon on the optimized, hierarchical surface Opt at low heat fluxes in Figure 5.29a, the bubbles seem to nucleate inside the darker, microstructured strips. However, the bubbles rise mostly above the brighter, smooth copper strips. This might suggest a separation of vapor outflow and liquid inflow, which is presented in Figure 5.29b. The images presented in this figure, however, are only taken at low heat fluxes. It is assumed that the behavior should stay the same for high heat fluxes. Proving this is difficult, since there are too many bubbles rising from the surface, thereby blocking the view on the surface, at high heat fluxes. The separation of vapor outflow and liquid inflow could be a reason for the increased critical heat fluxes. Additionally, the microstructure is interrupted, which could enable an easier rewetting, since the liquid can enter the microstructure from the sides and the top. This would delay the formation of an irreversible dry spot to higher heat fluxes. In addition, it would prevent the microstructure from being completely enveloped by vapor, impeding the Cassie-Baxter state of wetting.

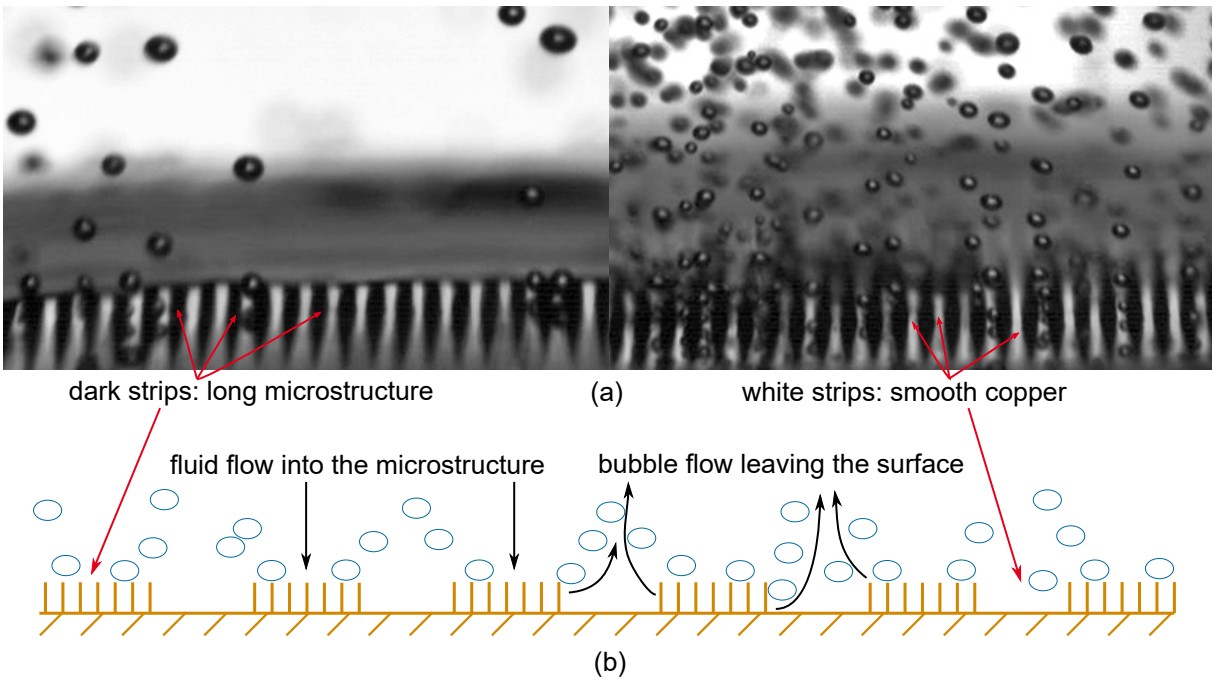

Figure 5.29: B&w images (a) and sketch (b) showing the boiling phenomenon at low heat fluxes on the optimized surface Opt.

Table 5.5: Enhancement ratios of the maximum heat fluxes below CHF and non-dimensional bubble diameters at various system pressures using ethanol as boiling fluid.

	$CHF_{\mathrm{Opt}}/CHF_{\mathrm{20cu}}$	$CHF_{\mathrm{Opt}}/CHF_{\mathrm{10cu}}$	$d_{\mathrm{b,Opt}}/P$
0.4 bar	1.45	1.31	2.42
0.7 bar	1.40	1.41	1.64
1.0 bar	1.85	1.53	1.17
3.0 bar	1.27	1.28	0.72
5.0 bar	1.15	1.17	0.56

Table 5.6: Enhancement ratios of the maximum heat fluxes below CHF and non-dimensional bubble diameters at various system pressures using FC-72 as boiling fluid.

	$CHF_{\mathrm{Opt}}/CHF_{\mathrm{20cu}}$	$CHF_{\mathrm{Opt}}/CHF_{\mathrm{10cu}}$	$d_{\mathrm{b,Opt}}/P$
0.4 bar	1.38	1.59	0.81
0.7 bar	1.57	1.57	0.63
1.0 bar	1.57	1.57	0.58
3.0 bar	1.77	1.57	0.54
5.0 bar	1.76	1.76	0.40

The Tables 5.5 and 5.6 contain enhancement ratios of the maximum heat fluxes below CHF of the optimized surface Opt compared to the ones of the two homogeneously structured surfaces 10cu and 20cu for both fluids. The enhancement ratios reach a maximum value of approximately 1.8 for both fluids. In addition to the enhancement ratios, a non-dimensional bubble diameter is shown. $d_{\mathrm{b,Opt}}$ is the

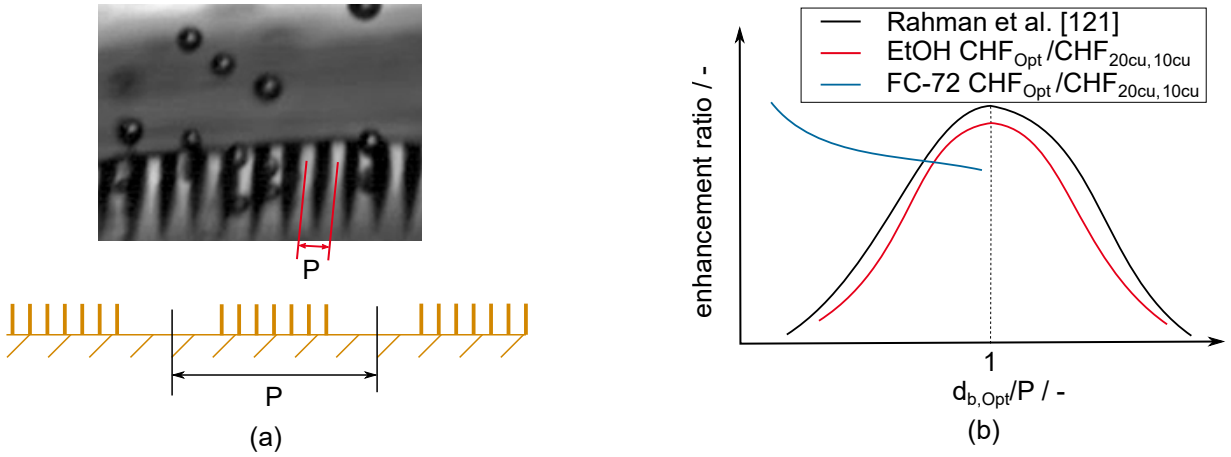

Figure 5.30: Sketch and image (a) illustrating the distance P and a qualitative sketch (b) of the enhancement ratio of the maximum heat flux below CHF as a function of the non-dimensional bubble diameter compared to the results of Rahman et al. [121].

mean bubble diameter measured for the optimized surface at low heat fluxes and P is the center-to-center distance between the smooth copper strips, which is shown in Figure 5.30a.

In Figure 5.30b, a qualitative sketch of the enhancement ratio of the maximum heat flux below CHF as a function of the non-dimension bubble diameter $\left(d_{b,Opt}/P\right)$ is shown for both fluids. The experimental results are compared to the ones of Rahman et al. [121], whose surfaces inspired the structure of the optimized, hierarchical surface. Qualitatively, the experimental results obtained using ethanol fit the results of Rahman et al. well. Quantitatively, the ratios of enhancement are comparable as well. However, the experimental results using FC-72 show a different behavior. An increasing enhancement ratio towards smaller non-dimensional bubble diameters $\left(d_{b,Opt}/P < 1\right)$ is visible in Figure 5.30b, while the results using ethanol and the ones of Rahman et al. show a decrease in enhancement ratio. This might suggest a dependency of the enhancement ratio on additional parameters other than the non-dimensional bubble diameter.

5.3.3 Heat transfer coefficients

Besides the enhancement of critical heat flux, Rahman et al. [121] observed a significant increase in heat transfer coefficients. Tables 5.7 and 5.8 show the heat transfer coefficient enhancement ratios of the optimized surface Opt at maximum heat fluxes (shortly below the critical heat fluxes, respectively) at various system pressures. In most cases, the heat transfer coefficient is increased by the optimized surface in comparison to the homogeneously structured surfaces 20cu and 10cu, however, the quantitative enhancement is a lot lower compared to Rahman et al. [121]. Additionally, if the heat transfer coefficients are compared for specific heat fluxes, it is obvious that, corresponding to the average wall superheats, the heat transfer coefficients of the optimized surface are in most cases smaller than the ones of the homogeneously structured surfaces, which is visible in Figures 5.31, 5.32, and 5.33.

In those figures, the heat transfer coefficients of the five different copper surfaces are presented at system pressures of $p_{sys} = 0.4\,\text{bar}$, $p_{sys} = 1.0\,\text{bar}$, and $p_{sys} = 5.0\,\text{bar}$. The results obtained using ethanol (a) are

Table 5.7: Heat transfer coefficient enhancement ratios at maximum heat fluxes below CHF and various system pressures using ethanol as boiling fluid.

	$\alpha_{max,Opt}/\alpha_{max,20cu}$	$\alpha_{max,Opt}/\alpha_{max,10cu}$	$\alpha_{max,Opt}/\alpha_{max,Tcu}$	$\alpha_{max,Opt}/\alpha_{max,Scu}$
0.4 bar	1.05	1.07	1.56	2.22
1.0 bar	1.27	1.29	2.14	2.45
5.0 bar	1.23	0.89	1.73	2.05

Table 5.8: Heat transfer coefficient enhancement ratios at maximum heat fluxes below CHF and various system pressures using FC-72 as boiling fluid.

	$\alpha_{max,Opt}/\alpha_{max,20cu}$	$\alpha_{max,Opt}/\alpha_{max,10cu}$	$\alpha_{max,Opt}/\alpha_{max,Tcu}$	$\alpha_{max,Opt}/\alpha_{max,Scu}$
0.4 bar	1.06	1.21	1.80	2.98
1.0 bar	1.08	1.01	1.38	2.15
5.0 bar	1.29	0.91	0.98	2.12

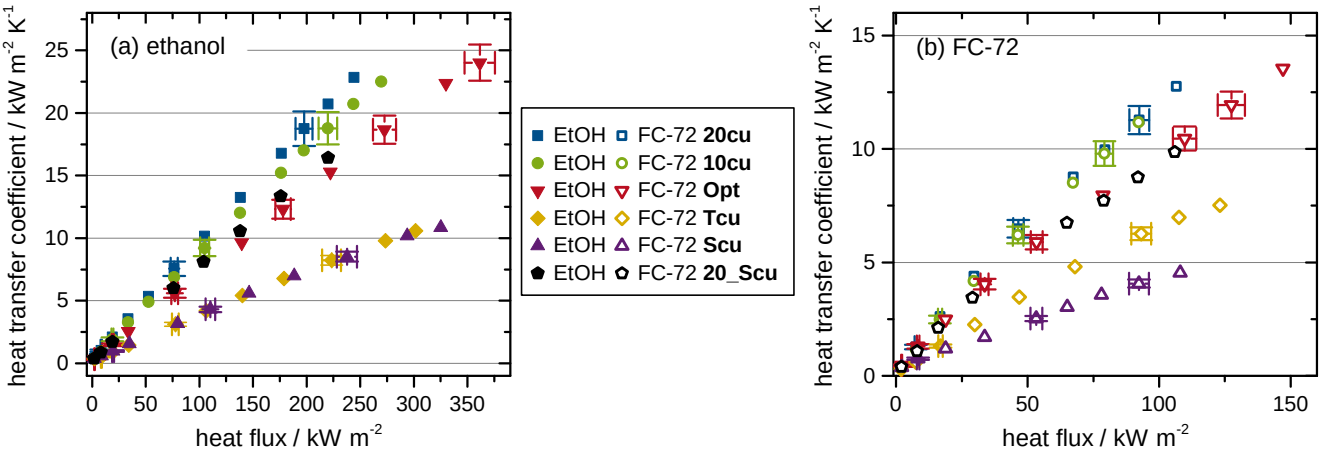

Figure 5.31: Heat transfer coefficients for specific heat fluxes obtained for the five different surfaces using ethanol (a) and FC-72 (b) at a system pressure of 0.4 bar.

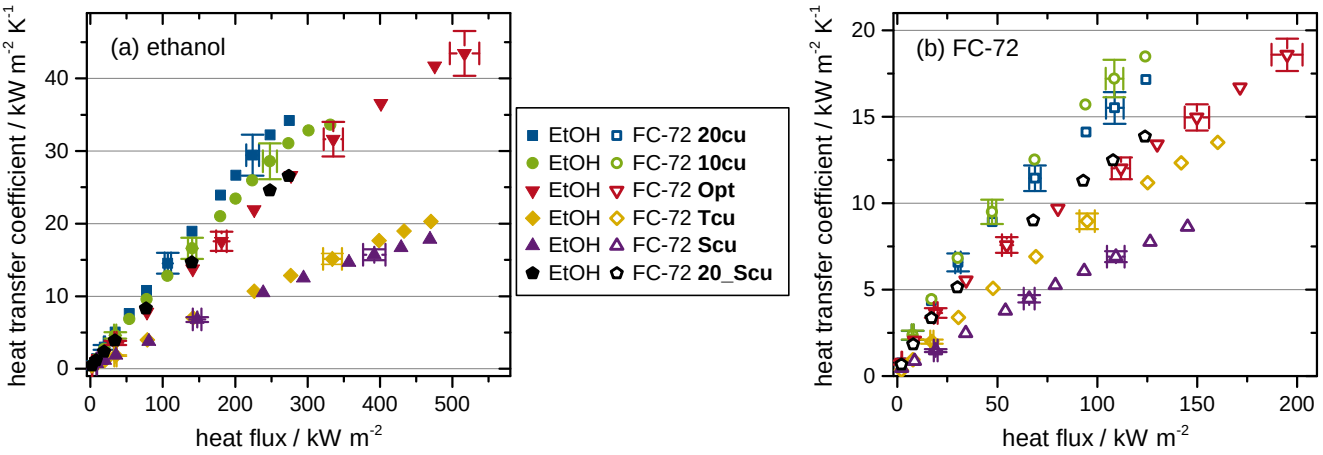

Figure 5.32: Heat transfer coefficients for specific heat fluxes obtained for the five different surfaces using ethanol (a) and FC-72 (b) at a system pressure of 1.0 bar.

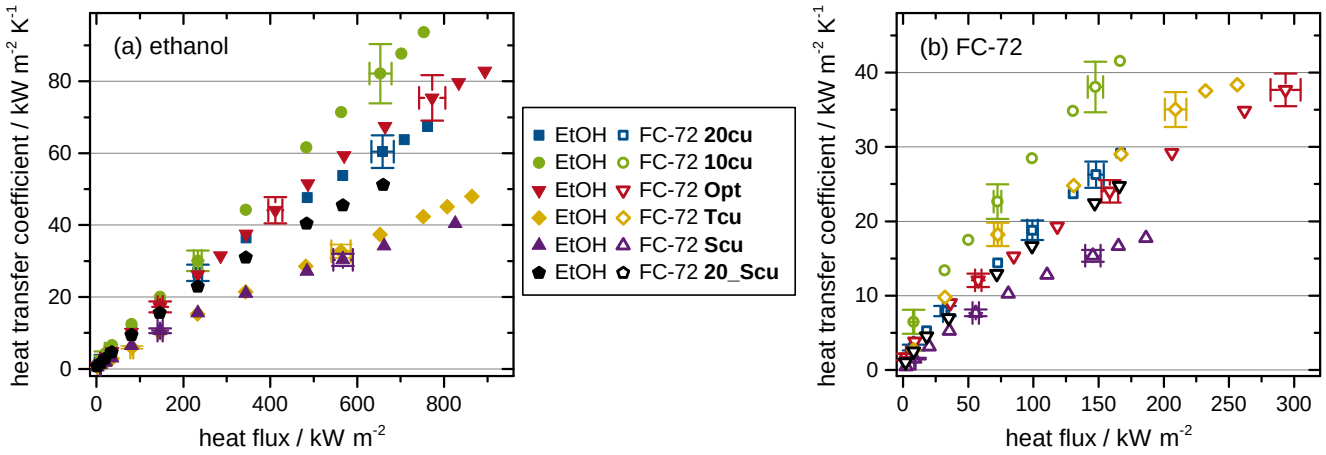

Figure 5.33: Heat transfer coefficients for specific heat fluxes obtained for the five different surfaces using ethanol (a) and FC-72 (b) at a system pressure of 5.0 bar.

presented on the left and the ones using FC-72 (b) on the right, while the results at $p_{sys} = 0.7$ bar and $p_{sys} = 3.0$ bar are presented in Figures A.13 and A.14 in the appendix. Although the heat transfer coefficients at specific heat fluxes for the optimized surface Opt are mostly smaller compared to the two homogeneously structured surfaces 20cu and 10cu, they are larger than those obtained with the uncoated copper surfaces Scu and Tcu, with the exception of the measurements at $p_{sys} = 3.0$ bar and $p_{sys} = 5.0$ bar using FC-72. However, the highest heat transfer coefficients are mostly obtained for the optimized surface, independent of the boiling fluid. In addition to the experimental results, heat transfer coefficients (20_Scu) based on the results of the long microstructured surface and the smooth copper surface are presented in the Figures 5.31, 5.32, and 5.33 as well. These heat transfer coefficients are calculated using the heat transfer coefficients of both surfaces multiplied by their corresponding portion of the optimized surface, which consists of approximately 65 % 20cu and 35 % Scu. Then those values are added, creating the presented heat transfer coefficients 20_Scu. Unfortunately, for the experiments using ethanol at 3.0 bar and 5.0 bar, the heat transfer coefficients of the optimized surface are larger than those of the long microstructured surface, due to the changing boiling behavior, which is discussed in section 5.2.2.1. However, with the exception of those results, the differences between the heat transfer coefficients of the optimized surface and the calculated ones (20_Scu) are smaller than the measurement uncertainties. This suggests two important conclusions.

Firstly, the boiling process of the optimized surface is dominated by the microstructured part of the surface, which coincides well with the measurements of the mean bubble diameters, shown in Figure 5.34. There, the mean bubble diameters of the five different surfaces are visible at various system pressures and for both fluids. It is obvious that the mean bubble diameters on the optimized surface are comparable to the ones of the two homogeneously structured surfaces.

Secondly, the improvement of the maximum heat transfer coefficients by the optimized surface is mainly due to the increased critical heat fluxes, and the fact that the heat transfer coefficient increases steadily with increasing heat flux. This is visible for example in Figure 5.32. An additional enhancement due to the separation of liquid inflow and vapor outflow is not visible, contrary to the findings of Rahman et al. [120, 121]. The difference in surface structure or boiling fluid might explain these divergent results.

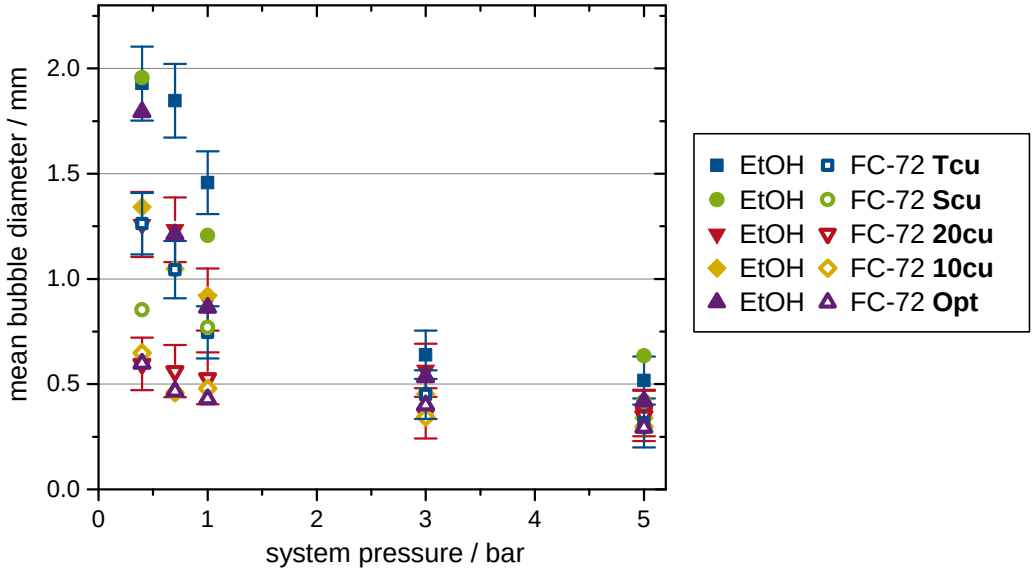

Figure 5.34: Mean bubble diameters at various system pressures obtained for the five different copper surfaces using ethanol and FC-72 as boiling fluids.

All in all, the measurements with the optimized surface prove that the boiling process of the homogeneously microstructured surfaces could be enhanced by adding a macrostructure, thereby creating a hierarchical structure. The critical heat fluxes were enhanced substantially, up to a factor of 1.8, in comparison to the homogeneously structured surfaces. Furthermore, the maximum heat transfer coefficients increased up to a factor of 1.3, in comparison to the homogeneously structured surfaces. However, this increase is mainly due to the already higher critical heat fluxes and an additional improvement due to the hierarchical structure could not be realized. The reason for this lack of improvement compared to literature data remains unknown. An analysis of the boiling behavior on a smaller length scale could help solving this problem. Nevertheless, those findings answer the second scientific question—Is it possible to improve the boiling performance of said microstructure by adding a macrostructure, creating a hierarchical structure?

5.4 Investigation on the influence of the boiling fluid on two different length scales

As mentioned in section 3.2, the construction of a microstructured infrared transparent heater has failed. However, it is visible in the sections 5.1.2.3, 5.2.2.1, and 5.3.2 that boiling fluids have a significant impact on the boiling behavior, which interacts and overlaps with the influence of the microstructures. To further analyze the influence of the boiling fluid, the phenomenon is studied on two different length scales. To avoid additional interactions with the surface, the measurements, which focus on the fluids' influence on nucleate boiling, are performed with smooth surfaces.

In the first section, the results of the smooth copper surface are presented. In the following section, it is established whether the results of the smooth chromium surface on the infrared transparent heater are comparable to those of the smooth copper surface, before presenting the results of the smooth chromium surface in the last section.

5.4.1 Smooth copper surface

Figure 5.35 shows Nukiyama curves (a) and heat transfer coefficients for specific heat fluxes (b), at various system pressures for the smooth copper surface Scu using both boiling fluids. It is apparent that the measurements with FC-72 show lower wall superheats and, therefore, higher heat transfer coefficients for a specific heat flux compared to the measurements with ethanol. However, critical heat fluxes are much lower than those obtained with ethanol. Those differences are caused by the different physical properties of the two fluids, such as, enthalpy of vaporization and liquid and vapor densities.

Figure 5.36 shows heat transfer coefficients of the smooth copper surface for specific vapor volume flows at various system pressures, using both fluids. It is remarkable that the differences in heat transfer coefficient between both fluids are very small at the same vapor volume flow and system pressure. A similar behavior is visible for the other copper surfaces as well. Their results are presented in Figures A.15, A.16, A.17, and A.18 in the appendix. The differences measured for the other surfaces are larger, but still within the measurement uncertainties, with the exception of the technical copper surface. This circumstance is discussed in section 5.1.2.3. The negligible difference in the heat transfer coefficient for both fluids should be analyzed further, using additional surfaces and fluids. If those surfaces and fluids show a similar trend, then this relation between the fluids could be used to enhance existing correlations.

The small difference between the heat transfer coefficients for the same vapor volume flows could imply that the improvement due to the slightly smaller bubble diameters obtained with FC-72 is quantitatively similar to the improvement due to higher physical properties like specific heat capacity $\left(c_{p,\mathrm{l,EtOH}} = 2.40\,\mathrm{kJ\,kg^{-1}\,K^{-1}}\right.$ and $\left.c_{p,\mathrm{l,FC\text{-}72}} = 1.04\,\mathrm{kJ\,kg^{-1}\,K^{-1}}\ @\ 20\,^{\circ}\mathrm{C}\right)$ and thermal conductivity of ethanol $\left(\lambda_{\mathrm{l,EtOH}} = 0.16\,\mathrm{W\,m^{-1}\,K^{-1}}\right.$ and $\left.\lambda_{\mathrm{l,FC\text{-}72}} = 0.06\,\mathrm{W\,m^{-1}\,K^{-1}}\ @\ 20\,^{\circ}\mathrm{C}\right)$. However, at low system pressures, the difference in bubble diameter and, therefore, nucleation site density is larger between the two fluids compared to the difference at high system pressures, as shown in Figure 5.5. This might be somewhat

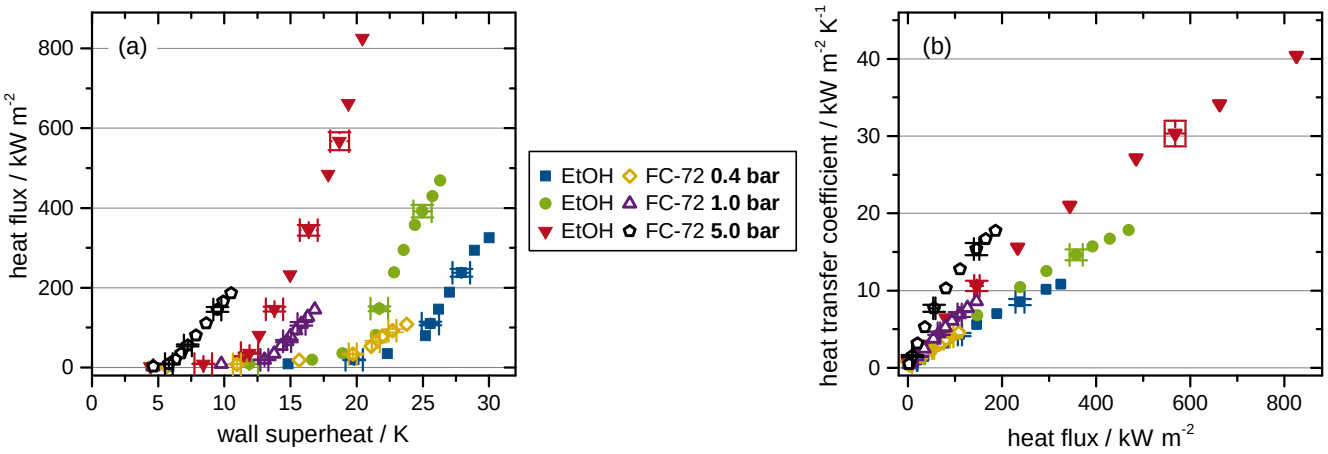

Figure 5.35: Nukiyama curves (a) and heat transfer coefficients for specific heat fluxes (b) of the smooth copper surface Scu at various system pressures using both boiling fluids.

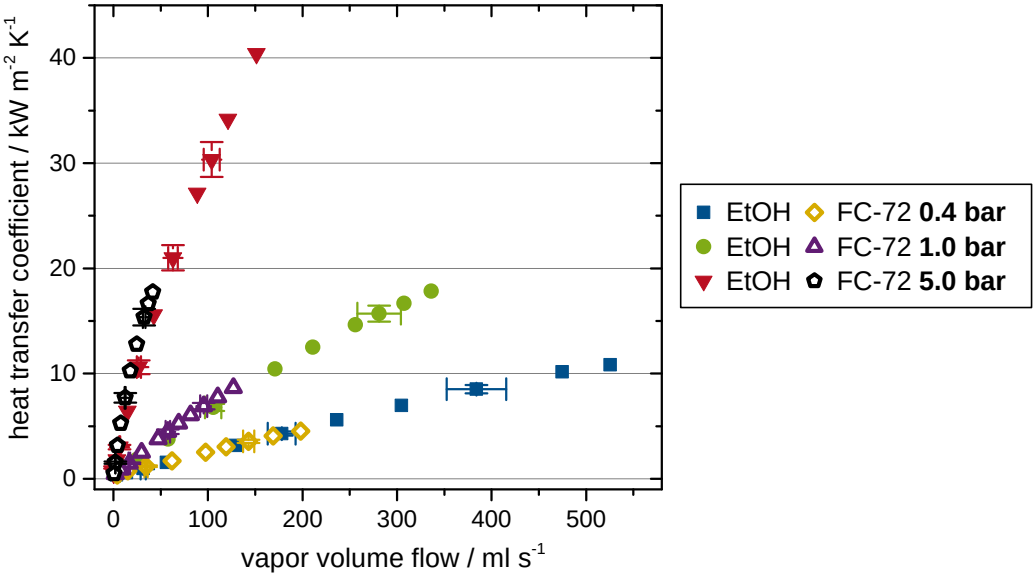

Figure 5.36: Heat transfer coefficients for specific vapor volume flows of the smooth copper surface Scu at various system pressures using both fluids.

balanced by the larger difference in physical properties at low system pressures. Additionally, another effect could improve the heat transfer coefficients of ethanol, especially at lower system pressures. Ethanol is known to show microlayer evaporation [54], while FC-72 shows mostly contact line evaporation [135] at ambient pressure. However, as shown by Sielaff [135] this behavior could change depending on the system pressure. Therefore, in order to interpret the boiling behavior of the smooth copper surface, it is necessary to understand the different evaporation regimes and their transition point depending on the system pressure. This will be addressed in the following sections.

5.4.2 Comparison between the smooth copper surface and the smooth chromium surface

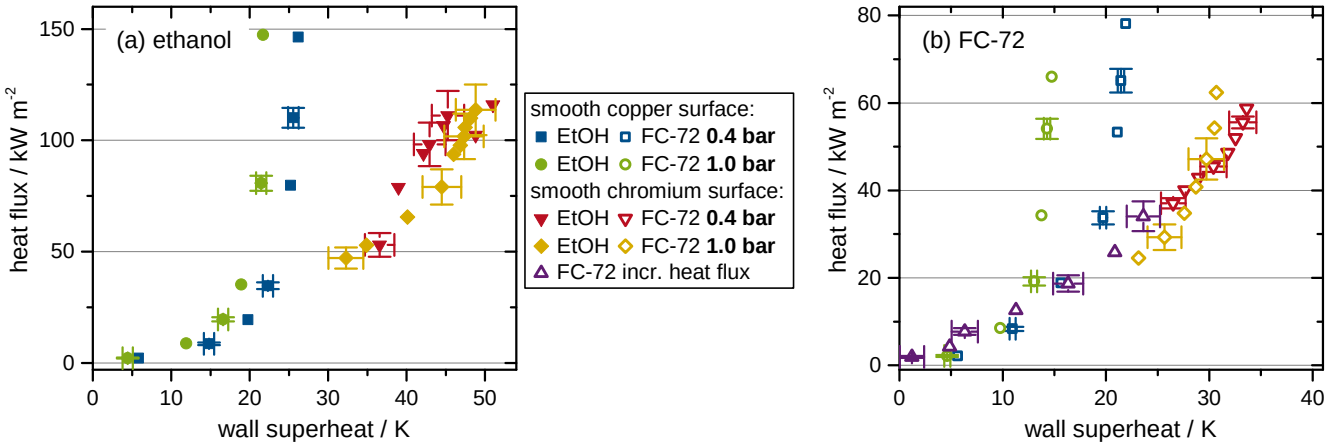

Figure 5.37: Nukiyama curves for the smooth copper surface Scu and the smooth chromium surface Scr at system pressures of 0.4 bar and 1.0 bar using ethanol (a) and FC-72 (b).

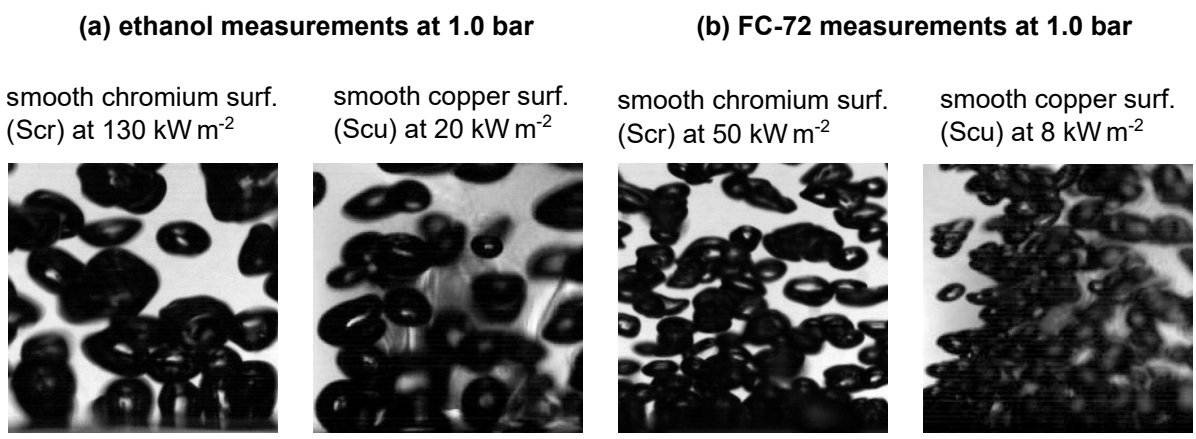

Figure 5.38: B&w images of the boiling phenomenon present on the smooth chromium surface Scr and the smooth copper surface Scu at different heat fluxes using ethanol (a) and FC-72 (b).

Figure 5.37 shows the Nukiyama curves for the smooth copper surface Scu and the smooth chromium surface Scr at system pressures of 0.4 bar and 1.0 bar. The experimental results using ethanol as boiling fluid are presented in Figure 5.37a, while the results using FC-72 are shown in Figure 5.37b. It is obvious that the wall superheats of the smooth chromium surface are significantly larger for both fluids than those of the smooth copper surface. While there are bubbles nucleating on the surface, it is assumed that most of the chromium surface is still in the natural convection regime, which dominates the boiling behavior, causing larger wall superheats. This assumption is supported by the results of an additional measurement using FC-72 with increasing heat fluxes. Up to a heat flux of 30 kW m^{-2}, no bubbles were present on the surface and the Nukiyama curve obtained with increasing heat fluxes fits the trend of the Nukiyama curves obtained with decreasing heat fluxes. The lowest heat fluxes for the decreasing heat flux measurements correspond to the last visible bubbles on the surface. In addition, the lower nucleation site density of the smooth chromium surface is apparent in Figure 5.38. There, the nucleation site densities visible in both images are approximately similar for both fluids. However, the heat flux necessary to maintain this density is significantly higher for the smooth chromium surface Scr, compared to the smooth copper surface Scu. This is probably due to the lower roughness of the chromium surface, which reduces the number of potential nucleation sites. Additionally, the heater material (Cu and CaF_2) has an influence on the boiling process. In regards to the entire surface, the boiling behavior on the smooth chromium surface cannot be compared to the smooth copper surface.

Figure 5.39 shows mean bubble diameters for the technical copper surface Tcu, the smooth copper surface Scu and the smooth chromium surface Scr at various system pressures, using both fluids. Within the measurement uncertainties, the mean bubble departure diameters measured on the smooth chromium surface are comparable to the ones obtained with the two uncoated copper surfaces. Thus, it is assumed that the processes, which govern the bubble ebullition cycle, should be comparable between the three surfaces. Therefore, further investigations using the smooth chromium surface should focus on single bubbles.

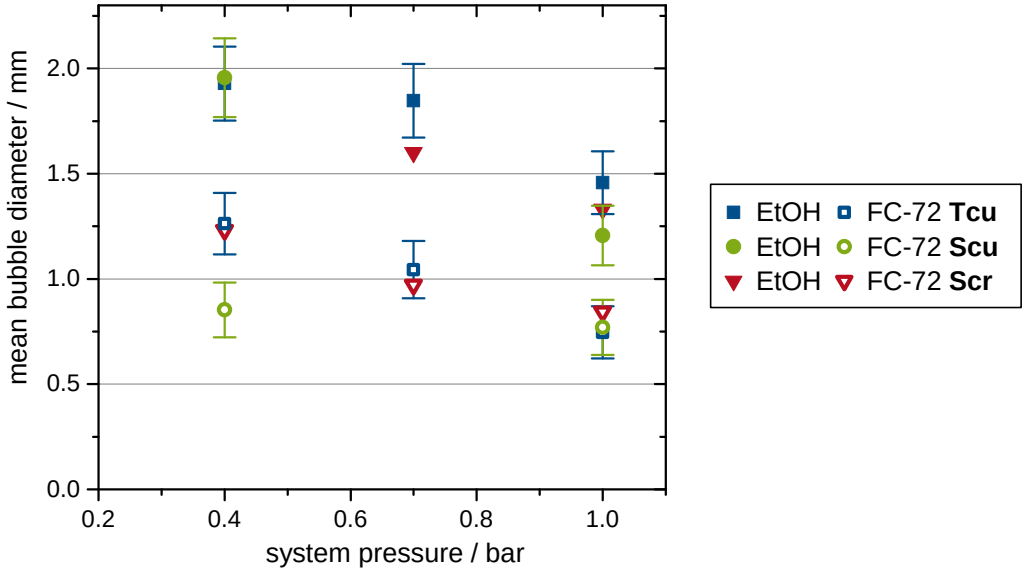

Figure 5.39: Mean bubble diameters at various system pressures obtained for the technical copper surface Tcu, the smooth copper surface Scu, and the smooth chromium surface Scr using ethanol and FC-72 as boiling fluids.

5.4.3 Investigation of single bubbles

Figure 5.40 shows temperature and corresponding heat flux fields beneath a growing bubble at different time steps after nucleation, using ethanol and FC-72 at a system pressure of 0.4 bar. It is observable that there are many differences in the temperature and heat flux fields. For one, the bubble size with ethanol as boiling fluid is significantly larger than for FC-72, as expected. For both fluids, the temperature and heat flux fields show an annulus shape, which is caused by the high evaporation rates at the three-phase contact line and the low heat transfer rates through the adsorbed layer beneath the bubble. The temperature drop caused by the high evaporation rates near the three-phase contact line is different for both fluids; this is due to the significant difference in the specific enthalpy of vaporization $\left(\Delta h_{v,\mathrm{EtOH}} = 926.16\,\mathrm{kJ\,kg^{-1}}\right.$ and $\left.\Delta h_{v,\text{FC-72}} = 94.37\,\mathrm{kJ\,kg^{-1}}\ @\ 20\,^{\circ}\mathrm{C}\right)$. The results obtained using ethanol show a varying shape of the annulus depending on the contact line movement. For an advancing contact line, the shape looks similar to the results obtained using FC-72. This shape is presumably caused by contact line evaporation. For a receding contact line, the area of the annulus is much larger. Additionally, there is a clear temperature and heat flux gradient visible. This shape is presumably caused by an evaporating microlayer with the contact line visible at its end.

To investigate if a microlayer was actually formed, the heat flux profiles, which are based on the intensity data of the infrared camera, are compared to the images of the synchronously operating b&w camera. If the apparent contact line positions in the b&w images match the extents of the circular shape in the heat flux data, it can be assumed that a microlayer is formed and convection effects can be ruled out. Figure 5.41 shows b&w images and heat flux fields of a growing bubble at various time steps after nucleation using ethanol as boiling fluid at a system pressure of 0.4 bar. It is observable that the extents of the

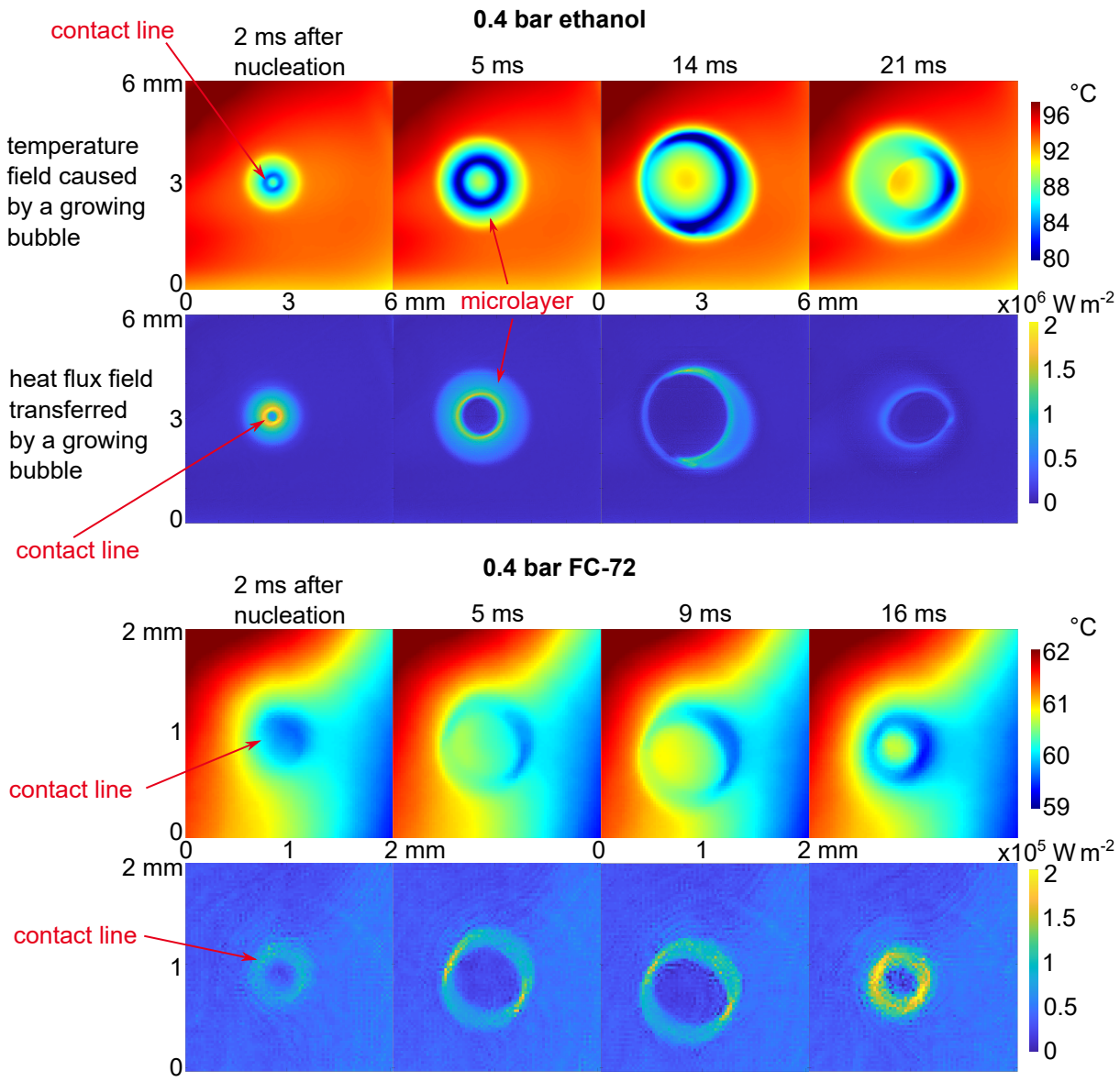

Figure 5.40: Temperature and heat flux fields beneath a growing bubble using ethanol and FC-72 at various time steps after nucleation and a system pressure of 0.4 bar.

bubble visible in the b&w images do not coincide with the heat flux fields. The data obtained with FC-72 shows the same inequality, which is presented in Figure A.19 in the appendix. This is mainly caused by the lack of optical access to the boiling surface, due to the different refraction indices of the superheated and the surrounding liquid, which is discussed in section 4.2. However, the bubble extents in the b&w images are larger compared to the annuli of the heat flux fields during bubble expansion on the surface. Thus, convection effects caused by the growing bubble cannot be responsible for the heat flux annuli and, therefore, are ruled out. Thus, it is assumed that the annuli are indeed caused by microlayer evaporation.

To investigate the microlayer further, the thickness of the microlayer is calculated using a simple 1-dimensional model reported by Giustini et al. [40]. In their model, they propose an additional heat

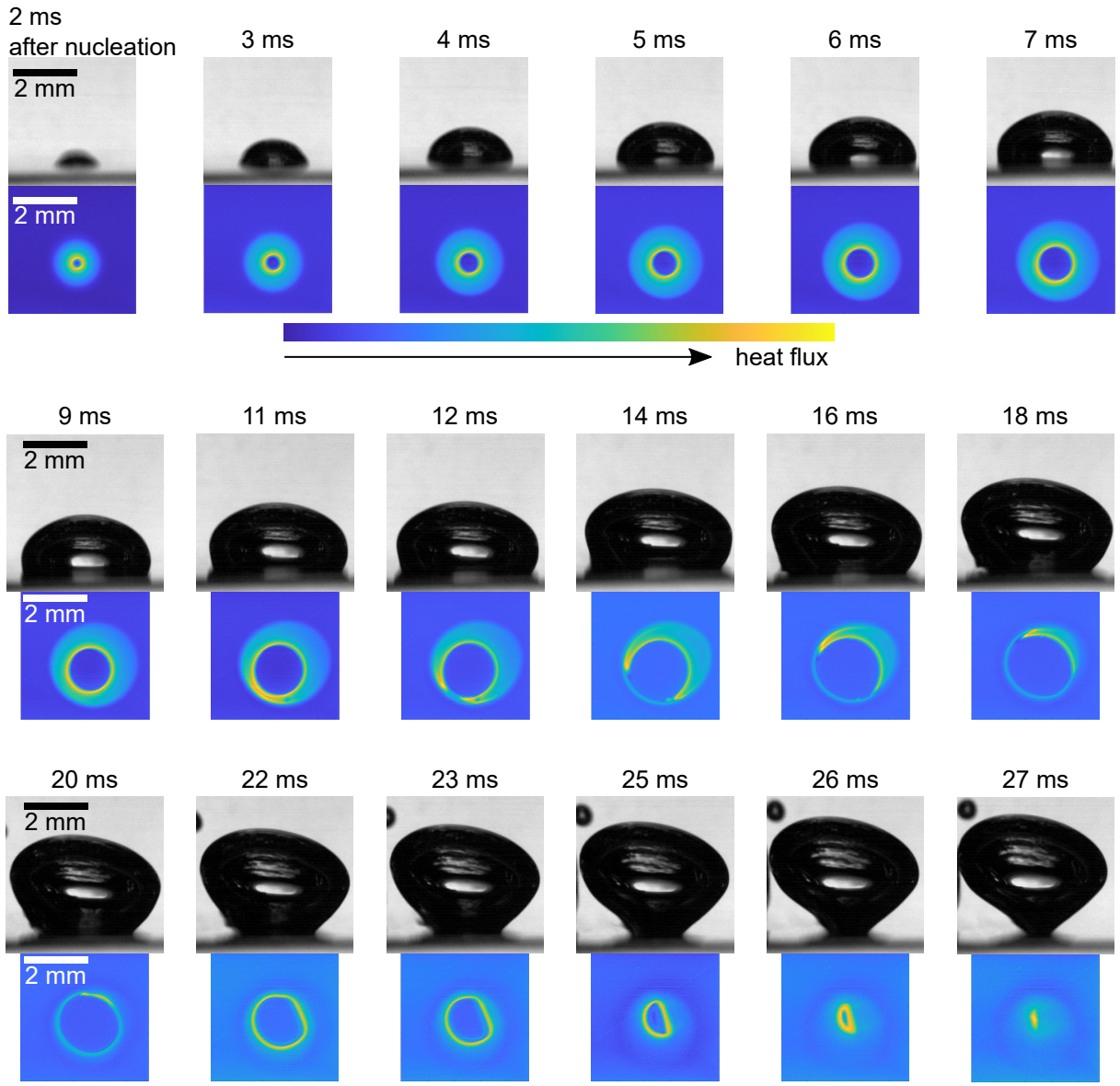

Figure 5.41: B&w images and heat flux fields of a growing bubble at various time steps after nucleation and a system pressure of $0.4\,\mathrm{bar}$ using ethanol as boiling fluid. The heat flux scale varies from time step to time step.

transfer resistance $\frac{1}{\alpha_{\mathrm{evap}}}$ at the boundary inside the bubble, which is shown in Figure 5.42. Additionally, they propose that convection inside the microlayer is negligible, since the Peclet number is smaller than unity. In case a no-slip boundary condition is used at the wall, simulations show that the velocity inside the microlayer is indeed very small [46]. Under the assumption that the temperature difference is negligibly small between the observed temperature at the bottom of the chromium nitride layer and the temperature on top to the chromium layer, the microlayer thickness can be calculated by the following Equation 5.4:

$$\gamma = \left[\frac{T_{\mathrm{w}} - T_{\mathrm{sat}}}{\dot{q}_{\mathrm{lc}}} - \frac{1}{\alpha_{\mathrm{evap}}} \right] \lambda_{\mathrm{l}}. \tag{5.4}$$

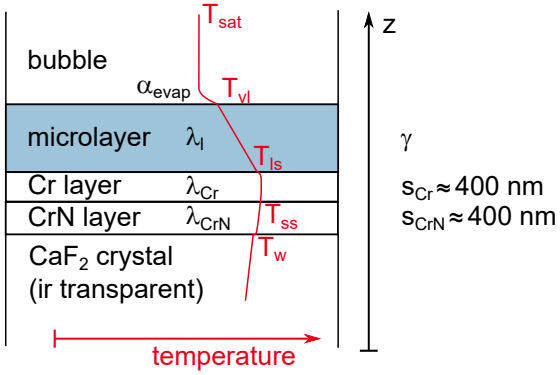

Figure 5.42: Sketch of the temperature gradient in the infrared transparent heater, the microlayer, and the bubble according to Giustini et al. [40].

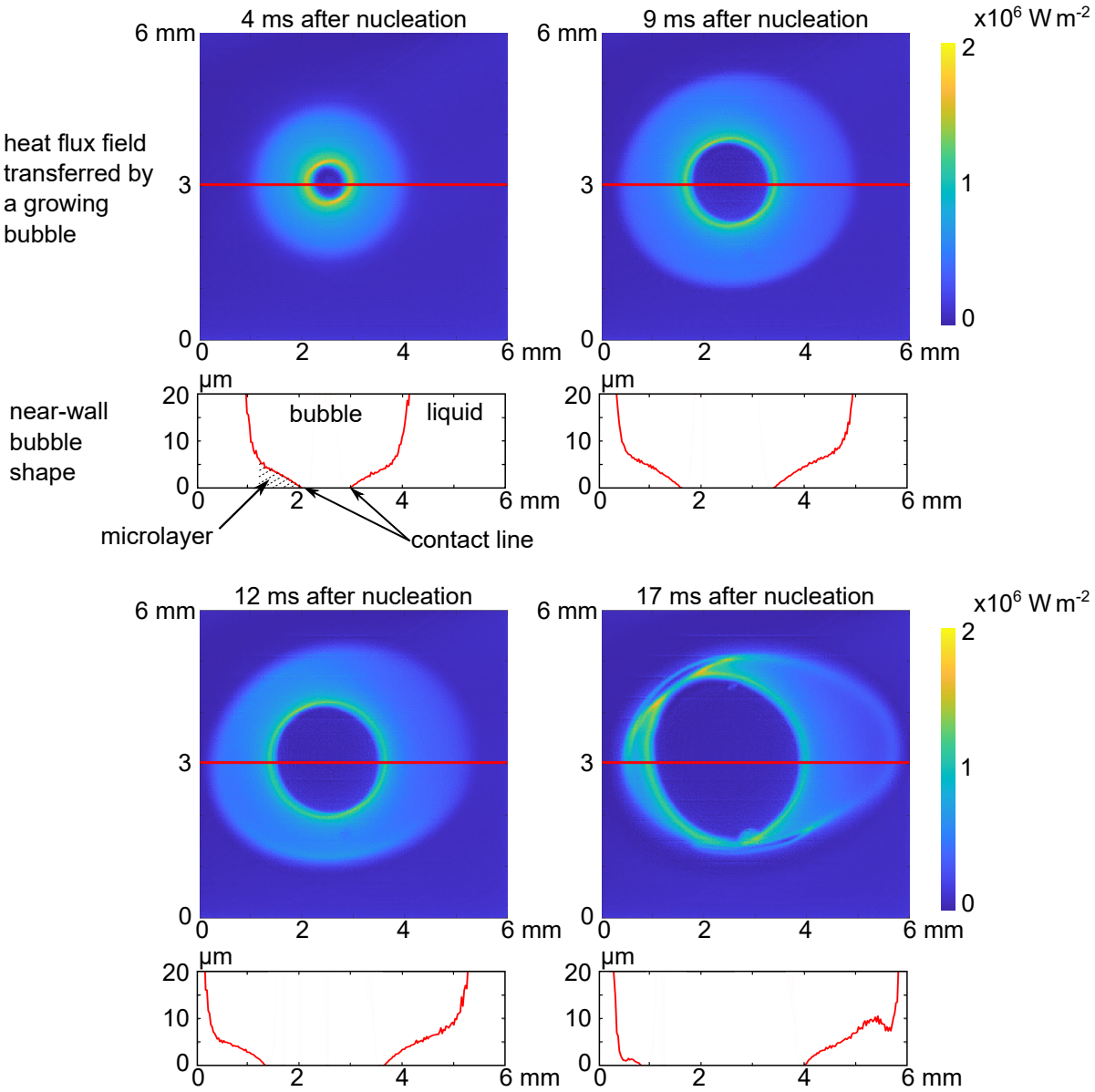

Figure 5.43: Heat flux fields and calculated microlayer thickness evolutions at $y = 3\,\mathrm{mm}$ (indicated by the red line) using ethanol as boiling fluid at different time steps after nucleation and a system pressure of $0.4\,\mathrm{bar}$.

$\dot{q}_{lc}$ and T_w are the calculated local heat flux and temperature data, respectively. Since α_{evap} is not measureable, it is used as a fitting parameter, to ensure a microlayer thickness of zero at the contact line. The resulting microlayer profiles are shown in Figure 5.43. There, heat flux fields are presented, which are obtained using ethanol as boiling fluid at a system pressure of 0.4 bar and different time steps after nucleation. The red lines in the heat flux fields indicate the segments, whose near-wall bubble shapes are calculated. The microlayer is the area below the boundary between liquid and vapor until the curvature increases drastically in the macroregion. Shortly after nucleation, the microlayer has a linear shape, which turns into a root shape once the microlayer starts evaporating (as expected), since thinner films evaporate faster. The microlayer thickness decreases over time and a hollow at the end of the microlayer becomes visible, which is in agreement with the measured microlayer profiles of Utaka et al. [147]. According to Schweikert [127], this hollow is created by the reducing bubble expansion velocity, which creates a thinner microlayer before the maximum expansion of the bubble is reached. The hollow increases over time, due to thermocapillary convection, since the surface tension is smaller in the hollow.

Besides the experimental results at a system pressure of 0.4 bar, microlayer profiles were calculated for the experiments at 0.7 bar and 1.0 bar, which are shown in Figures A.20 and A.21 in the appendix. The calculated microlayer thicknesses are in agreement with the ones reported by Utaka et al. [147]. It is observable that the microlayer thickness and length decreases with increasing system pressure. This is also observable in the heat flux profiles, which are caused by microlayer and contact line evaporation, in Figure 5.44. It shows heat flux fields and heat flux profiles, which correspond to the colored lines in the heat flux fields, at different time steps after nucleation using ethanol as boiling fluid. The results at system pressures of 0.4 bar, 0.7 bar, and 1.0 bar are presented. However, the results at 0.4 bar are discussed first. At 4 ms, the heat flux profile corresponding to the red line shows two peaks, surrounded outwards by a slowly decreasing area of increased heat flux. This profile is presumably caused by microlayer evaporation. The peak heat fluxes occur at the three-phase contact line, since the microlayer is thinnest in this region, which results in high evaporation rates. The heat flux then decreases with increasing film thickness. The heat flux profiles obtained in this thesis match the heat flux profiles measured by some researchers [142] but differ, compared to other researchers [59]. The measurements of Schweikert [127] indicate that this might by caused by different wall materials. Depending on the physical properties of the material, the thermal boundary layer developing inside the wall is responsible for the different heat flux profiles.

At 14 ms, the thickness of the microlayer decreased significantly. This smaller and thinner microlayer increases the heat flux, which is visible in the left peak of the red heat flux profile. Compared to the heat flux peak at 4 ms, the peak broadened due to a larger extent of a thin microlayer, while the overall extent of the microlayer decreased. However, if the microlayer is evaporated completely, the peak at the contact line is decreased significantly compared to a peak with a still present microlayer, which is observable in the green heat flux profile. The same phenomenon is also observable at 17 ms in the red heat flux profile. The difference in maximum heat flux at the contact line, depending on the presence of a microlayer, is reported by Schweikert et al. [128]. After 22 ms, the microlayer is evaporated completely, and smaller peaks caused by contact line evaporation are visible. In cases where the contact lines are advancing, the

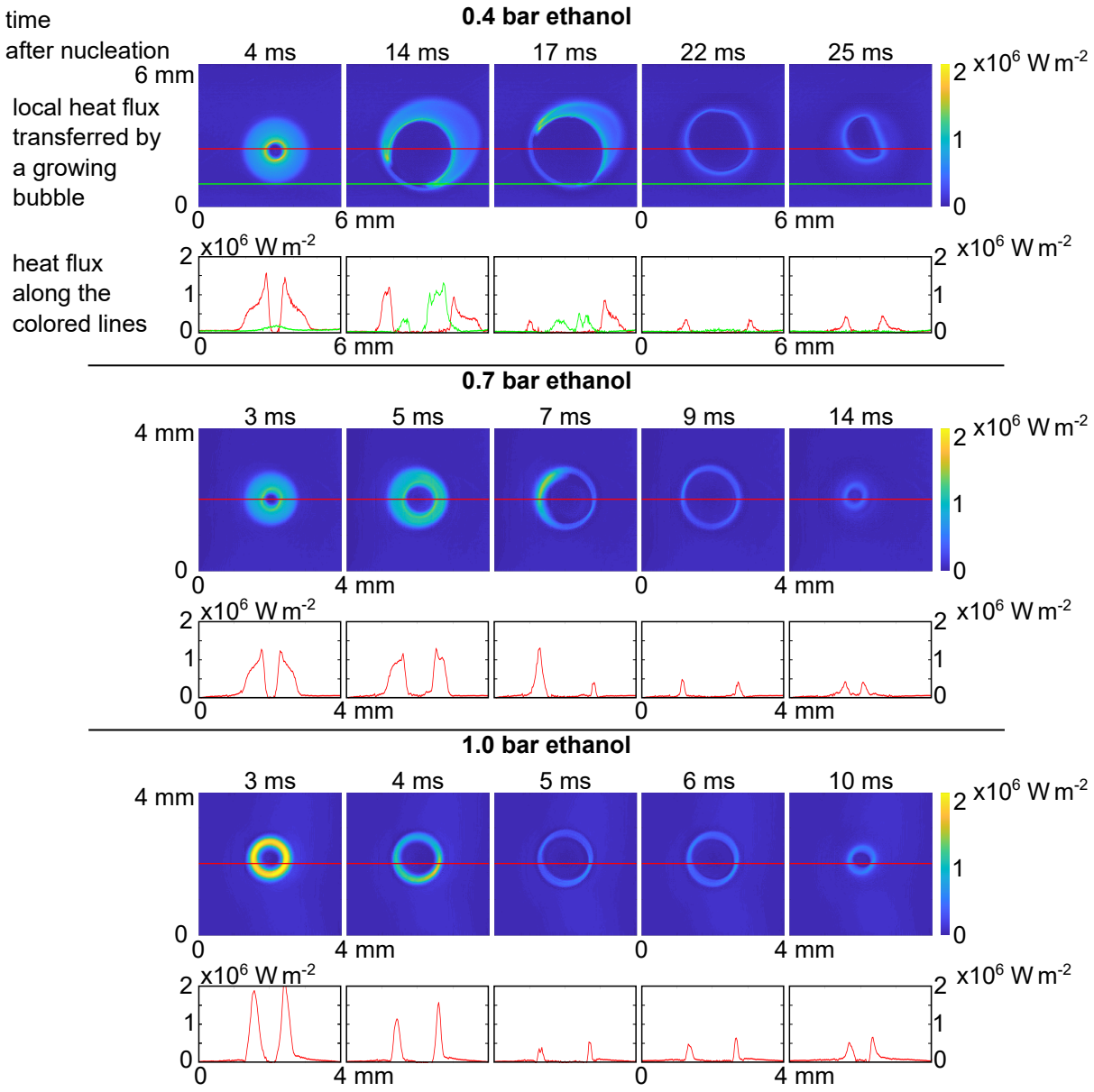

Figure 5.44: Heat flux fields and corresponding heat flux profiles using ethanol as boiling fluid at different time steps after nucleation and system pressures of 0.4 bar, 0.7 bar, and 1.0 bar.

associated peaks increase again, which is caused by cooler liquid being transported towards the wall, according to Kunkelmann et al. [77]. This is observable at 25 ms after bubble nucleation.

Similar evolutions of the heat flux profiles are visible in the experimental results at 0.7 bar and 1.0 bar as well. However, the microlayer thickness and width, as well as the bubble diameter, decrease with increasing system pressure due to lower dewetting [81] or higher bubble expansion velocities at higher system pressures, respectively, as shown in Table 5.9.

Similar to the results at 0.4 bar, if there is a microlayer present, then the heat flux profiles at higher system pressures show a higher maximum heat flux peak at the contact line. This might be caused by the spatial resolution of the infrared camera, which is 25 µm. In case of contact line evaporation, high heat fluxes are transferred in the microregion, according to Stephan and Hammer [138]. This microregion

Table 5.9: Bubble expansion velocities shortly after nucleation for the experiments using ethanol at various system pressures.

system pressure	0.4 bar	0.7 bar	1.0 bar
$u_{b,exp}$ in m s^{-1}	0.63 ± 0.08	0.42 ± 0.05	0.35 ± 0.08

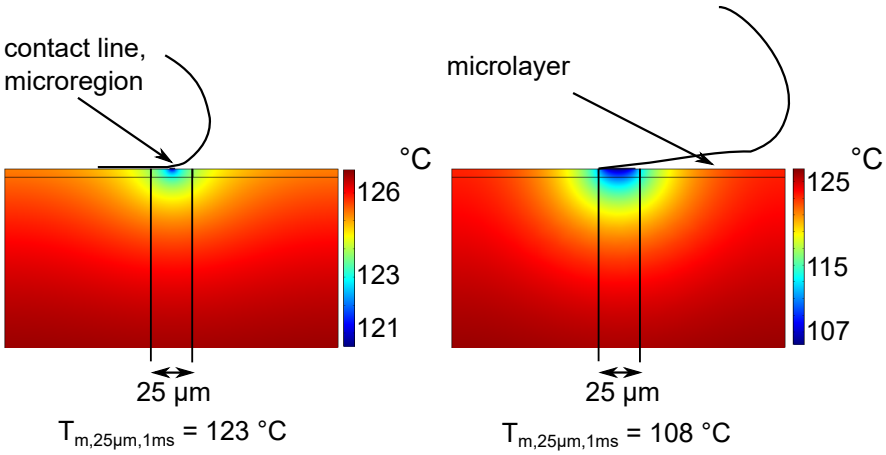

Figure 5.45: Simulation results visualizing the possible consequences of the spatial resolution of the infrared camera. Different temperature drops are observable, which are caused by contact line evaporation and microlayer evaporation.

is only 0.5 µm wide [126] and, therefore, significantly smaller compared to the spatial resolution of the infrared camera. In case of microlayer evaporation, the area which is covered by a very thin microlayer is much larger compared to the microregion of contact line evaporation, as seen in the experiments conducted at 0.4 bar. If the maximum local heat fluxes are comparable in both cases, the larger extent of a thin microlayer results in a lower intensity and, therefore, higher temperature drop.

Figure 5.45 shows the results of a simulation, used to visualize the possible differences in microlayer and contact line evaporation. In both cases, the same section of the infrared transparent heater with a homogeneous temperature of 127 °C is cooled by a heat flux of 10 MW m^{-2}. In case of contact line evaporation, this heat flux is applied over the width of 0.5 µm and in case of microlayer evaporation over 20 µm. After 1 ms, the mean temperature drop over 25 µm, the spatial resolution of the infrared camera, is significantly higher for microlayer evaporation, as expected. This higher temperature drop then leads to a higher calculated heat flux, although the maximum local heat flux is the same in both cases.

This simulation does not describe the phenomena of contact line evaporation or microlayer evaporation, but it does visualize the possible consequences of the spatial resolution of the infrared camera. The different maximum heat fluxes at the contact line depending on the presence of a microlayer are helpful to decide whether a microlayer is formed or not. This is especially helpful if the microlayer is short, which is observable in the experimental results using ethanol at a system pressure of 1.0 bar and FC-72 at 0.4 bar, as demonstrated in Figure 5.46.

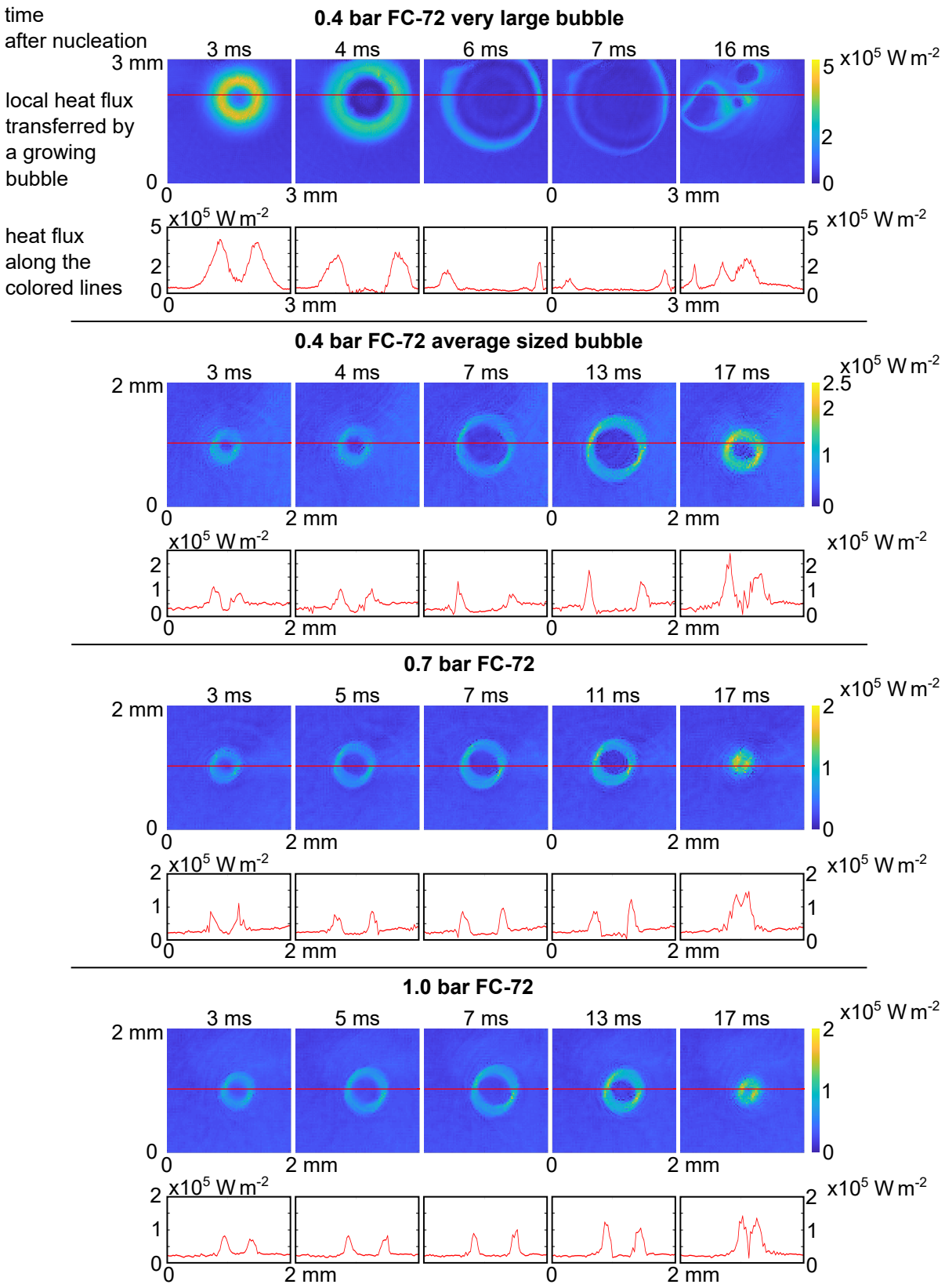

Figure 5.46: Heat flux fields and corresponding heat flux profiles using FC-72 as boiling fluid at different time steps after nucleation and system pressures of 0.4 bar, 0.7 bar, and 1.0 bar.

Table 5.10: Bubble expansion velocities shortly after nucleation for the experiments using both boiling fluids at various system pressures.

	EtOH 0.4 bar	EtOH 0.7 bar	EtOH 1.0 bar	FC-72 very large bubble 0.4 bar	FC-72 average sized bubbles 0.4 bar	FC-72 0.7 bar	FC-72 1.0 bar
$u_{b,exp}$ in m s^{-1}	0.63 ± 0.08	0.42 ± 0.05	0.35 ± 0.08	0.50	0.20 ± 0.16	0.09 ± 0.06	0.07 ± 0.05
microlayer evap. observed	yes	yes	yes	yes	no	no	no

There, the heat flux fields and profiles, which correspond to the red lines in the heat flux fields, are presented at different time steps after bubble nucleation using FC-72 as boiling fluid. The results at system pressures of 0.4 bar, 0.7 bar and 1.0 bar are presented; however, for a system pressure of 0.4 bar, the results for a very large bubble and an average sized bubble are shown. The heat flux fields and profiles for those two cases differ significantly. The heat flux fields and profiles of the very large bubble are similar to the results obtained at 1.0 bar using ethanol, suggesting microlayer evaporation. The heat flux fields and profiles of average sized bubble, on the other hand, show increasing heat fluxes for an advancing contact line, but no significant evolution of the heat flux peaks during bubble expansion. Kunkelmann et al. [77] described a similar behavior, which is attributed to contact line evaporation. The same behavior is visible for the results obtained with FC-72 at system pressures of 0.7 bar and 1.0 bar.

According to Blake and Ruschak [12] for an isothermal system and Schweikert et al. [129] for a non-isothermal system, one of the deciding parameters whether microlayer formation occurs is the dewetting velocity. Table 5.10 shows dewetting velocities, which correspond to bubble expansion velocities for the experiments presented in Figures 5.44 and 5.46. The expansion velocity of the very large bubble using FC-72 does not have a standard deviation, since it was the only one of its size to be measured. Microlayer formation was observed for the ethanol measurements, independent of the system pressure, and for the very large bubble using FC-72 at 0.4 bar. Using FC-72, small and average sized bubbles at 0.4 bar and the measurements at higher system pressures showed sole contact line evaporation. It is obvious that the bubble expansion velocities of the experiments showing microlayer formation are significantly larger compared to the ones without a microlayer. This supports the assumption of microlayer evaporation for the experiments using ethanol.

Kai Schweikert, a colleague in the CRC 1194, performed generic, non-isothermal dewetting experiments [127]. He measured the critical dewetting velocity as a function of the fluid properties and the wall superheat. He developed fluid specific correlations, which determine whether microlayer formation occurs based on the capillary number and the Jakob number. The experimental results obtained in this thesis are compared to the correlations of Schweikert, to establish whether the relationships found in the generic experiments of Schweikert can be applied to nucleate boiling.

Figure 5.47 shows experimentally determined capillary numbers and Jakob numbers at various system pressures, compared to the correlation of Schweikert [127]. The results using ethanol as boiling fluid are shown in Figure 5.47a, while the results using FC-72 are shown in Figure 5.47b. The capillary number

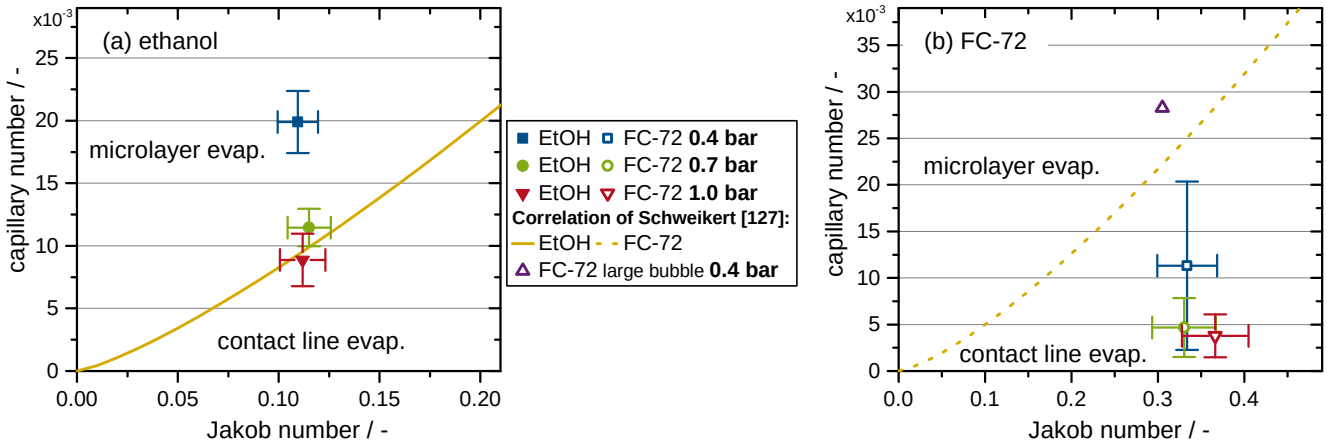

Figure 5.47: Capillary numbers and Jakob numbers obtained in experiments using the smooth chromium surface Scr at various system pressures using ethanol (a) and FC-72 (b) as boiling fluids. The experimental results are compared to the fluid specific correlations of Schweikert [127].

Ca, shown in Equation 5.5, is calculated using the bubble expansion velocity $u_{\mathrm{b,exp}}$, the dynamic viscosity of the liquid and the surface tension at saturation temperature.

$$Ca = \frac{\eta_{\mathrm{l}} u_{\mathrm{b,exp}}}{\sigma} \tag{5.5}$$

$$Ja = \frac{c_{p,\mathrm{l}} (T_{\mathrm{w}} - T_{\mathrm{sat}})}{\Delta h_{\nu}} \tag{5.6}$$

The Jakob number Ja, shown in Equation 5.6, is calculated using the mean wall temperature at the nucleation site shortly before the next bubble nucleates. Since this temperature cannot be determined accurately, an uncertainty of $\Delta T_{\mathrm{w}} = 3\,\mathrm{K}$ is chosen.

All in all, the calculated capillary and Jakob numbers are located in their corresponding evaporation regime, according to the fluid specific correlations of Schweikert. For a specific Jakob number, the correlation determines microlayer formation for capillary numbers larger than the critical capillary number, which is presented by the yellow polynomials in Figure 5.47. The calculated capillary number at a system pressure of 1.0 bar is slightly lower, compared to the correlation polynomial. However, the correlations were established for lower capillary numbers $Ca < 3 \times 10^{-3}$ and Jakob numbers $Ja < 0.03$. Thus, some deviations due to extrapolation are likely. Additionally, the microlayer length at 1.0 bar is already very small, and the transition from microlayer evaporation to sole contact line evaporation will probably happen at a slightly higher system pressure than 1.0 bar. Nevertheless, this comparison indicates that the results of the generic experiments of Schweikert can be applied to nucleate boiling.

In conclusion, two different evaporation regimes could be identified. The experiments using ethanol at system pressures of 0.4 bar, 0.7 bar, and 1.0 bar show microlayer evaporation, while the experiments using FC-72 show mostly contact line evaporation. These findings are in agreement with the correlations of Schweikert. These correlations, and the observations at 1.0 bar using ethanol, suggest that there

is a regime change shortly above 1.0 bar. This could explain the higher heat transfer coefficients at lower system pressures observed for ethanol, which is discussed in section 5.4.1. At system pressures of 0.4 bar and 5.0 bar, the heat transfer coefficients of ethanol and FC-72 are comparable for the same vapor volume flow. However, the differences in nucleation site density could be higher at lower system pressures due to the larger differences in bubble diameter between the two fluids, which is observable in Figure 5.34. Thus, there has to be an additional phenomenon increasing the heat transfer coefficients of the ethanol measurements at low system pressures. This phenomenon might be microlayer evaporation, which results in enhanced heat transfer due to the high local heat fluxes transferred by the microlayer. This shows the importance of a multiscale approach when investigating nucleate boiling, since many important phenomena, which influence the boiling process on a larger length scale, can only be identified by investigations on a smaller length scale. Those findings answer the third scientific question—Can an investigation of the boiling process on different length scales enable a better understanding of the occurring boiling phenomena?

CHAPTER 6

Summary, Conclusion, and Outlook

In the scope of this thesis, the influence of microstructured surfaces and different fluids on the boiling process was investigated. While microstructures and nanostructures have proven to enhance heat transfer coefficient and critical heat flux significantly, as shown in section 2.4, the interactions between solid and fluid are numerous and not well understood. This prevents the development of universally applicable correlations, which include the influences of complex structures on the boiling process. Thus, it is important to analyze several parameters influencing the boiling process, besides just measuring the heat transfer coefficients and critical heat fluxes. Those parameters being surface roughness, wettability and wickability of the fluid-surface combination, bubble dynamics, nucleation site densities, as well as dynamics of the three-phase contact line.

To perform a multiscale and multiphenomena investigation on the influence of microstructures on nucleate boiling, a new experimental setup was built. Special care had to be taken to ensure saturated conditions and safety of operation, due to experiments being performed in a large range of system pressures and, therefore, temperatures. In order to investigate the boiling process on different length scales, two heater modules were constructed. The first heater is made of copper and is used to measure heat transfer coefficients, as well as critical heat fluxes, thereby judging the efficiency of the boiling process. The second heater consists of an infrared transparent crystal with two metallic layers sputtered on top of it for heating and to ensure high emissivity. By observing the back of the metallic layers, the local intensity field during nucleate boiling can be captured using a high speed infrared camera. This local intensity is converted into temperatures through calibration and then into local heat fluxes by a 3-dimensional simulation using COMSOL Multiphysics. This local heat flux data is used to identify the evaporation regime beneath a growing bubble, as well as the initial bubble expansion velocity. In addition to the infrared camera, a b&w camera is used to determine the bubble departure diameters.

To thoroughly investigate the influence of microstructures on nucleate boiling, ethanol and FC-72, a refrigerant, were used as boiling fluids and six different surfaces were studied. Two homogeneously microstructured surfaces were manufactured, made of copper needles with diameters of 1 μm and lengths of 10 μm and 20 μm, respectively. Additionally, a hierarchical structure consisting of 0.48 mm wide strips,

made of the same microneedles with lengths of 20 µm, alternating with 0.26 mm wide smooth copper strips, was constructed. Two uncoated copper surfaces with different surface roughness were manufactured for comparison. To study the boiling process on a smaller length scale, a smooth chromium surface on top of the infrared transparent crystal was used. The roughnesses of those different surfaces were evaluated using a confocal microscope. Contact angle measurements have shown that the boiling fluids wet all surfaces used in this investigation, perfectly. To determine the wicking behavior of the microstructured surfaces, experiments using the setup of a colleague in the CRC 1194, Michael Heinz, were performed.

First, the results obtained using the smooth copper surface are compared to literature data and to the correlation of Rohsenow [124], validating the new experimental setup. This ensures that the phenomena visible during nucleate boiling can be traced back to the surface's impact, excluding unwanted factors, like e.g. inert gases. The experiments using the uncoated copper surfaces show increased critical heat fluxes and decreased wall superheats at higher system pressures. This pressure dependency is described reasonably well by the correlations of Rohsenow [124] and Gorenflo [140]. The critical heat fluxes observed on the two uncoated surfaces for ethanol and FC-72 are similar to the values predicted by the correlations of Zuber [168] and Yagov [158]. However, the critical heat fluxes obtained for the technical copper surface using FC-72 as boiling fluid are an exception, as they are larger compared to both correlations. This discrepancy is attributed to the roughness of the technical copper surface. A correlation incorporating the influence of surface roughness fits the data reasonably well. Similar to the critical heat fluxes, the heat transfer coefficients of the technical copper surface are higher than those of the smooth copper surface, if FC-72 is used as boiling fluid. This enhancement is due to higher nucleation site densities, which are observable in b&w images. Using ethanol as boiling fluid, no significant difference in boiling behavior is observed between the two surfaces. This could imply that the cavities present on the technical copper surface cannot be activated easily if ethanol is used as boiling fluid, whereas activation happens if FC-72 is used.

In case of increasing heat flux measurements, an additional boiling regime, the so-called partially activated isolated bubble regime, is observed on the technical copper surface. This regime is defined by a stationary wall superheat for increasing heat fluxes, since the added heat is solely used to activate additional nucleation sites. This regime is especially pronounced for the long microstructured surface. No pressure dependency of the boiling process is observed on the long microstructured surface, since the effects causing the partially activated isolated bubble regime, as well as the pressure dependency, could be superimposed. Thus, the measurements in this thesis are performed for decreasing heat fluxes. The results of the two homogeneously microstructured surfaces show that the different needle length affects the measurements using ethanol, while having insignificant influence on the experimental results using FC-72. Compared to the results of the uncoated copper surfaces and the correlation of Gorenflo, a similar, but less pronounced influence of the system pressure is observed. For a specific heat flux, the two homogeneously microstructured surfaces enhance the heat transfer coefficient up to a factor of 2.8 for both fluids, compared to the smooth copper surface. This enhancement is due to smaller bubble departure diameters and presumably higher nucleation site densities. The critical heat fluxes of the two homogeneously microstructured surfaces are lower than those of the uncoated copper surfaces. Unfortu-

nately, the reason for this decrease could not be identified. Nevertheless, the presented findings answer the first scientific question—How is the boiling process affected by a microstructure, whose geometrical length scale is between the well-studied micropillars and nanowires?

In an attempt to enhance the critical heat fluxes of the two homogeneously microstructured surfaces, a hierarchical surface was manufactured, by interrupting the microstructured surface with smooth copper strips. The goal of this enhancement is to increase the liquid flow into the microstructure, create different fluid inflow and outflow paths, and decrease the Rayleigh-Taylor wavelength. Consequently, the critical heat fluxes of the hierarchical surface are enhanced by a maximum factor of 1.8, compared to the homogeneously microstructured surfaces. Additionally, the maximum heat transfer coefficients are enhanced up to a factor of 1.3 and 3, compared to the homogeneously microstructured surfaces and the smooth copper surface, respectively. This answers the second scientific question—Is it possible to improve the boiling performance of said microstructure by adding a macrostructure, creating a hierarchical structure?

Besides microstructured and hierarchical surfaces, different boiling fluids have a significant impact on the boiling process. This influence can interact and overlap with the influence of the surface structure. In order to understand the influence of the boiling fluid, measurements with the smooth copper surface are performed. The results suggest the existence of a phenomenon enhancing heat transfer coefficients at low system pressures, if ethanol is used as boiling fluid. Experiments with the smooth chromium surface suggest that this phenomenon might be microlayer evaporation, which transforms to sole contact line evaporation, presumably at system pressures slightly higher than 1.0 bar. According to Schweikert et al. [128], the cumulative heat transferred by an evaporating microlayer is larger compared to contact line evaporation, which is in agreement with the observations of this thesis. In turn, this could enhance the heat transfer coefficients of the ethanol measurements at low system pressures. In comparison, the measurements using FC-72 show mostly contact line evaporation, with the exception of a large bubble at a system pressure of 0.4 bar. These findings show that phenomena, which influence the boiling process on a large length scale, can only be identified on a smaller length scale. This answers the third scientific question—Can an investigation of the boiling process on different length scales enable a better understanding of the occurring boiling phenomena?

The occurrence of different evaporation regimes, contact line evaporation and microlayer evaporation, are in agreement with correlations of Schweikert [127], which are based on generic, non-isothermal dewetting experiments. This agreement suggests the transferability of the phenomena observed in the generic experiments to nucleate boiling.

Unfortunately, several phenomena could not be explained, due to unknown processes inside the microstructure. Thus, in the future, further efforts should be made to apply the microstructure onto an infrared transparent heater. This would enable insights into the processes occurring inside the microstructure. Additionally, there are several parameters, which could not be measured, like the nucleation site density, the bubble frequency, or the receding contact angle under non-isothermal and saturated conditions. These parameters could provide hints for understanding the boiling phenomena

observed in this thesis. Unfortunately, these parameters could not be measured in the scope of this thesis. Besides the additional parameters, experiments using water as boiling fluid could provide further insights, since the wettability of the microstructures by water is significantly worse, compared to the fluids used in this thesis. Additional changes to the experimental setup are necessary to facilitate experiments using water due to its corrosive nature, which could not be realized. Besides answering the open questions of this thesis, further experiments with various boiling fluids should be performed, linking the bubble expansion velocity to experimental parameters such as system pressure and heat flux. This would enable the optimization or development of novel correlations, since effects of the evaporation regimes are not currently considered directly in state of the art correlations.

Bibliography

[1] *AD 2000 Regelwerk: Taschenbuch-Ausgabe 2020*. Beuth, 12 edition, 2020. ISBN 3410299114.

[2] 70th ESA parabolic flight campaign. Participants: J. Krempel, P. Hänichen, K. Schweikert, M. Zimmermann, I. Nejati, A. Sielaff, P. Stephan, Bordeaux, 2018.

[3] H. S. Ahn, H. J. Jo, S. H. Kang, and M. H. Kim. Effect of liquid spreading due to nano/ microstructures on the critical heat flux during pool boiling. *Applied Physics Letters*, 98(7):071908, 2011. ISSN 0003-6951. doi: 10.1063/1.3555430.

[4] M. Akiyama, F. Tachibana, and N. Ogawa. Effect of pressure on bubble growth in pool boiling. *Bulletin of JSME*, 12(53):1121–1128, 1969. ISSN 0021-3764. doi: 10.1299/jsme1958.12.1121.

[5] K. H. Ardron, G. Giustini, and S. P. Walker. Prediction of dynamic contact angles and bubble departure diameters in pool boiling using equilibrium thermodynamics. *International Journal of Heat and Mass Transfer*, 114(1):1274–1294, 2017. ISSN 00179310. doi: 10.1016/j.ijheatmasstransfer.2017.07.013.

[6] H. D. Baehr and K. Stephan. *Wärme- und Stoffübertragung*. 10 edition, 2019. ISBN 9783662584415.

[7] W. Bailey, E. Young, C. Beduz, and Y. Yang. Pool boiling study on candidature of pentane, methanol and water for near room temperature cooling. In *Thermal and Thermomechanical Proceedings 10th Intersociety Conference on Phenomena in Electronics Systems, 2006. ITHERM 2006*, pages 599–603. IEEE, 2006. ISBN 0-7803-9524-7. doi: 10.1109/ITHERM.2006.1645400.

[8] S. Batzdorf. *Heat transfer and evaporation during single drop impingement onto a superheated wall*. Dissertation, Technische Universität Darmstadt, Darmstadt, 2015.

[9] P. J. Berenson. Experiments on pool-boiling heat transfer. *International Journal of Heat and Mass Transfer*, 5(10):985–999, 1962. ISSN 00179310. doi: 10.1016/0017-9310(62)90079-0.

[10] K. Bier, D. Gorenflo, and G. Wickenhäuser. Zum Wärmeübergang beim Blasensieden in einem weiten Druckbereich. *Chemie Ingenieur Technik*, 45(14):935–942, 1973. ISSN 0009286X. doi: 10.1002/cite.330451406.

[11] K. Bier, D. Gorenflo, M. Salem, and Y. Tanes. Effect of pressure and surface roughness on pool boiling of refrigerants. *International Journal of Refrigeration*, 2(4):211–220, 1979. ISSN 01407007. doi: 10.1016/0140-7007(79)90012-4.

[12] T. D. Blake and K. J. Ruschak. A maximum speed of wetting. *Nature*, 282(5738):489–491, 1979. ISSN 0028-0836. doi: 10.1038/282489a0.

[13] V. M. Borishansky. Correlation of the effect of pressure on the critical heat flux and heat transfer rates using the theory of thermodynamic similarity. *Problems of Heat Transfer and Hydraulics of Two-Phase Media*, pages 16–37, 1969.

[14] B. Bourdon, R. Rioboo, M. Marengo, E. Gosselin, and J. de Coninck. Influence of the wettability on the boiling onset. *Langmuir : the ACS journal of surfaces and colloids*, 28(2):1618–1624, 2012. doi: 10.1021/la203636a.

[15] L. Bureš and Y. Sato. On the modelling of the transition between contact-line and microlayer evaporation regimes in nucleate boiling. *Journal of Fluid Mechanics*, 916, 2021. ISSN 0022-1120. doi: 10.1017/jfm.2021.204.

[16] V. P. Carey. *Liquid Vapor Phase Change Phenomena: An Introduction to the Thermophysics of Vaporization and Condensation Processes in Heat Transfer Equipment, Second Edition*. Taylor & Francis Group, New York, 2nd ed. edition, 2008. ISBN 1-59169-035-8.

[17] A. B. D. Cassie and S. Baxter. Wettability of porous surfaces. *Transactions of the Faraday society*, 40:546–551, 1944.

[18] G. Chen and C. H. Li. Combined effects of liquid wicking and hydrodynamic instability on pool boiling critical heat flux by two-tier copper structures of nanowires and microgrooves. *International Journal of Heat and Mass Transfer*, 129:1222–1231, 2019. ISSN 00179310. doi: 10.1016/j.ijheatmasstransfer.2018.10.002.

[19] H. Chen, G. Chen, X. Zou, Y. Yao, and M. Gong. Experimental investigations on bubble departure diameter and frequency of methane saturated nucleate pool boiling at four different pressures. *International Journal of Heat and Mass Transfer*, 112(1):662–675, 2017. ISSN 00179310. doi: 10.1016/j.ijheatmasstransfer.2017.05.031.

[20] R. Chen, M.-C. Lu, V. Srinivasan, Z. Wang, H. H. Cho, and A. Majumdar. Nanowires for enhanced boiling heat transfer. *Nano letters*, 9(2):548–553, 2009. ISSN 1530-6984. doi: 10.1021/nl8026857.

[21] Z. Chen, A. Haginiwa, and Y. Utaka. Detailed structure of microlayer in nucleate pool boiling for water measured by laser interferometric method. *International Journal of Heat and Mass Transfer*, 108(1):1285–1291, 2017. ISSN 00179310. doi: 10.1016/j.ijheatmasstransfer.2017.01.003.

[22] K.-H. Chu, R. Enright, and E. N. Wang. Structured surfaces for enhanced pool boiling heat transfer. *Applied Physics Letters*, 100(24):241603, 2012. ISSN 0003-6951. doi: 10.1063/1.4724190.

[23] K.-H. Chu, Y. Zhu, N. Miljkovic, Y. Nam, R. Enright, and E. N. Wang. Enhanced boiling heat transfer with copper oxide hierarchical surfaces. In *2013 Transducers & Eurosensors XXVII: The 17th International Conference on Solid-State Sensors, Actuators and Microsystems (TRANSDUCERS & EUROSENSORS XXVII)*, pages 2272–2275. IEEE, 2013. ISBN 978-1-4673-5983-2. doi: 10.1109/Transducers.2013.6627258.

[24] M. Colombo and M. Fairweather. Prediction of bubble departure in forced convection boiling: A mechanistic model. *International Journal of Heat and Mass Transfer*, 85:135–146, 2015. ISSN 00179310. doi: 10.1016/j.ijheatmasstransfer.2015.01.103.

[25] D. Cooke and S. G. Kandlikar. Effect of open microchannel geometry on pool boiling enhancement. *International Journal of Heat and Mass Transfer*, 55(4):1004–1013, 2012. ISSN 00179310. doi: 10.1016/j.ijheatmasstransfer.2011.10.010.

[26] N. S. Dhillon, J. Buongiorno, and K. K. Varanasi. Critical heat flux maxima during boiling crisis on textured surfaces. *Nature communications*, 6:8247, 2015. doi: 10.1038/ncomms9247.

[27] V. K. Dhir. Nucleate and transition boiling heat transfer under pool and external flow conditions. *International Journal of Heat and Fluid Flow*, 12(4):290–314, 1991. ISSN 0142727X. doi: 10.1016/0142-727X(91)90018-Q.

[28] L. Dong, X. Quan, and P. Cheng. An experimental investigation of enhanced pool boiling heat transfer from surfaces with micro/nano-structures. *International Journal of Heat and Mass Transfer*, 71:189–196, 2014. ISSN 00179310. doi: 10.1016/j.ijheatmasstransfer.2013.11.068.

[29] J. Du, C. Zhao, and H. Bo. A modified model for bubble growth rate and bubble departure diameter in nucleate pool boiling covering a wide range of pressures. *Applied Thermal Engineering*, 145:407–415, 2018. ISSN 13594311. doi: 10.1016/j.applthermaleng.2018.09.063.

[30] EA Elektro-Automatik GmbH. Betriebsanleitung PS 9000 1U, DocID: PS91UDE. 2018. URL `https://www.datatec.de/media/pdf/f0/85/7d/EA_PS9000-1U_Betriebsanleitung-DEX96M3NgVfutpi.pdf`. [Online; accessed July 2, 2021].

[31] M. Elbaum, S. G. Lipson, and J. S. Wettlaufer. Evaporation preempts complete wetting. *Europhysics Letters*, 29(6):457–462, 1995.

[32] H. S. Fath and R. L. Judd. Influence of system pressure on microlayer evaporation heat transfer. *Journal of Heat Transfer*, 100(1):49–55, 1978. ISSN 0022-1481. doi: 10.1115/1.3450503.

[33] S. Fischer. *Experimental Investigation of Heat Transfer during Evaporation in the Vicinity of Moving Three-Phase Contact Lines*. Dissertation, Technische Universität Darmstadt, Darmstadt, 2015.

[34] R. W. L. Fong, G. A. McRae, C. E. Coleman, T. Nitheanandan, and D. B. Sanderson. Correlation between the critical heat flux and the fractal surface roughness of zirconium alloy tubes. *Journal of Enhanced Heat Transfer*, 8(2):137–146, 2001. ISSN 1563-5074. doi: 10.1615/JEnhHeatTransf.v8.i2.60.

[35] E. Forrest, E. Williamson, J. Buongiorno, L.-W. Hu, M. Rubner, and R. Cohen. Augmentation of nucleate boiling heat transfer and critical heat flux using nanoparticle thin-film coatings. *International Journal of Heat and Mass Transfer*, 53(1-3):58–67, 2010. ISSN 00179310. doi: 10.1016/j.ijheatmasstransfer.2009.10.008.

[36] H. K. Forster and N. Zuber. Dynamics of vapor bubbles and boiling heat transfer. *AIChE Journal*, 1(4):531–535, 1955. ISSN 1547-5905. doi: 10.1002/aic.690010425.

[37] W. Fritz. Berechnung des Maximalvolumens von Dampfblasen. *Physikalische Zeitschrift*, 36(11):379–384, 1935.

[38] J. E. Galloway and I. Mudawar. CHF mechanism in flow boiling from a short heated wall—II. theoretical CHF model. *International Journal of Heat and Mass Transfer*, 36(10):2527–2540, 1993. ISSN 00179310. doi: 10.1016/S0017-9310(05)80191-7.

[39] W. Gao, J. Qi, X. Yang, J. Zhang, and D. Wu. Experimental investigation on bubble departure diameter in pool boiling under sub-atmospheric pressure. *International Journal of Heat and Mass Transfer*, 134(5):933–947, 2019. ISSN 00179310. doi: 10.1016/j.ijheatmasstransfer.2019.01.024.

[40] G. Giustini, S. Jung, H. Kim, K. H. Ardron, and S. P. Walker. Microlayer evaporation during steam bubble growth. *International Journal of Thermal Sciences*, 137:45–54, 2019. ISSN 12900729. doi: 10.1016/j.ijthermalsci.2018.11.012.

[41] D. Gorenflo. *Wärmeübergang bei Blasensieden, Filmsieden und einphasiger freier Konvektion in einem großen Druckbereich*, volume 22 of *Abhandlungen des Deutschen Kälte- und Klimatechnischen Vereins*. Karlsruhe, 1977. ISBN 3-7880-7089-7.

[42] D. Gorenflo, P. Sokol, and S. Caplanis. Zum Wärmeübergang beim Blasensieden von Kohlenwasserstoffen und Halogen-Kältemitteln an einem Glattrohr und einem Hochleistungs-Rippenrohr. *Wärme- und Stoffübertragung*, 26(5):273–281, 1991. ISSN 0042-9929. doi: 10.1007/BF01589999.

[43] C.-K. Guan, J. F. Klausner, and R. Mei. A new mechanistic model for pool boiling CHF on horizontal surfaces. *International Journal of Heat and Mass Transfer*, 54(17-18):3960–3969, 2011. ISSN 00179310. doi: 10.1016/j.ijheatmasstransfer.2011.04.029.

[44] M. Ha and S. Graham. Pool boiling enhancement through hierarchical texturing of surfaces. In *2016 15th IEEE Intersociety Conference on Thermal and Thermomechanical Phenomena in Electronic Systems (ITherm)*. IEEE, 2016. ISBN 9781467381215. doi: 10.1109/itherm.2016.7517575.

[45] H. Haffner. Zum Wärmeübergang an Kältemittel bei hohen Drücken. *Chemie Ingenieur Technik*, 44(5):286–291, 1972. ISSN 0009286X. doi: 10.1002/cite.330440509.

[46] S. Hänsch and S. Walker. The hydrodynamics of microlayer formation beneath vapour bubbles. *International Journal of Heat and Mass Transfer*, 102:1282–1292, 2016. ISSN 00179310. doi: 10.1016/j.ijheatmasstransfer.2016.07.026.

[47] Y. Haramura and Y. Katto. A new hydrodynamic model of critical heat flux, applicable widely to both pool and forced convection boiling on submerged bodies in saturated liquids. *International Journal of Heat and Mass Transfer*, 26(3):389–399, 1983. ISSN 00179310. doi: 10.1016/0017-9310(83)90043-1.

[48] M. Heinz, P. Stephan, and T. Gambaryan-Roisman. Influence of nanofiber coating thickness and drop volume on spreading, imbibition, and evaporation. *Colloids and Surfaces A: Physicochemical and Engineering Aspects*, page 127450, 2021. ISSN 09277757. doi: 10.1016/j.colsurfa.2021.127450.

[49] R. C. Hendricks and R. R. Sharp. *Initiation of Cooling Due to Bubble Growth on a Heating Surface*. National Aeronautics and Space Administration, 1964.

[50] J. Y. Ho, K. K. Wong, and K. C. Leong. Saturated pool boiling of FC-72 from enhanced surfaces produced by selective laser melting. *International Journal of Heat and Mass Transfer*, 99:107–121, 2016. ISSN 00179310. doi: 10.1016/j.ijheatmasstransfer.2016.03.073.

[51] S. T. Hsu and F. W. Schmidt. Measured variations in local surface temperatures in pool boiling of water. *Journal of Heat Transfer*, 83(3):254–260, 1961. ISSN 0022-1481. doi: 10.1115/1.3682252.

[52] Y. Im, Y. Joshi, C. Dietz, and S. Lee. Enhanced boiling of a dielectric liquid on copper nanowire surfaces. *International Journal of Micro-Nano Scale Transport*, 1(1):79–96, 2010. ISSN 1759-3093. doi: 10.1260/1759-3093.1.1.79.

[53] M. Jakob and W. Fritz. Versuche über den Verdampfungsvorgang. *Forschung auf dem Gebiete des Ingenieurwesens*, 2(12):435–447, 1931. ISSN 0015-7899. doi: 10.1007/bf02578808.

[54] H. H. Jawurek. Simultaneous determination of microlayer geometry and bubble growth in nucleate boiling. *International Journal of Heat and Mass Transfer*, 12(8):843–848, 1969. ISSN 00179310. doi: 10.1016/0017-9310(69)90151-3.

[55] JCGM/BIPM. *Evaluation of measurement data—guide to the expression of uncertainty in measurement (ISO GUM 1995 with minor corrections)*. 2008.

[56] H. Jo, H. S. Ahn, S. H. Kang, and M. H. Kim. A study of nucleate boiling heat transfer on hydrophilic, hydrophobic and heterogeneous wetting surfaces. *International Journal of Heat and Mass Transfer*, 54(25-26):5643–5652, 2011. ISSN 00179310. doi: 10.1016/j.ijheatmasstransfer.2011.06.001.

[57] N. G. Johnson. original published by Karl Geisler on http://www.me.umn.edu/courses/me/me5348/fc72.html: Email, 03.04.2013.

[58] B. J. Jones, J. P. McHale, and S. V. Garimella. The influence of surface roughness on nucleate pool boiling heat transfer. *Journal of Heat Transfer*, 131(12), 2009. ISSN 0022-1481. doi: 10.1115/1.3220144.

[59] S. Jung and H. Kim. An experimental study on heat transfer mechanisms in the microlayer using integrated total reflection, laser interferometry and infrared thermometry technique. *Heat Transfer Engineering*, 36(12):1002–1012, 2015. ISSN 0145-7632. doi: 10.1080/01457632.2015.979109.

[60] S. Kabelac, M. Kind, H. Martin, D. Mewes, K. Schaber, and P. Stephan. *VDI-Wärmeatlas*. Springer-Verlag Berlin Heidelberg, Berlin, Heidelberg, 2013. ISBN 9783540255048. doi: 10.1007/978-3-540-32218-4.

[61] A. Kalani and S. G. Kandlikar. Enhanced pool boiling with ethanol at subatmospheric pressures for electronics cooling. *Journal of Heat Transfer*, 135(11), 2013. ISSN 0022-1481. doi: 10.1115/1.4024595.

[62] S. G. Kandlikar. A theoretical model to predict pool boiling CHF incorporating effects of contact angle and orientation. *Journal of Heat Transfer*, 123(6):1071–1079, 2001. ISSN 0022-1481. doi: 10.1115/1.1409265.

[63] S. G. Kandlikar and M. E. Steinke. Contact angles and interface behavior during rapid evaporation of liquid on a heated surface. *International Journal of Heat and Mass Transfer*, 45(18):3771–3780, 2002. ISSN 00179310. doi: 10.1016/S0017-9310(02)00090-X.

[64] Keithley Instruments. SPEC-2000 DocID: CT 16 Oct 18 Rev.M. 2018. URL `https://download.tek.com/document/SPEC-2000M_Oct_2018.pdf`. [Online; accessed June 25, 2021].

[65] B. S. Kim, S. Shin, D. Lee, G. Choi, H. Lee, K. M. Kim, and H. H. Cho. Stable and uniform heat dissipation by nucleate-catalytic nanowires for boiling heat transfer. *International Journal of Heat and Mass Transfer*, 70:23–32, 2014. ISSN 00179310. doi: 10.1016/j.ijheatmasstransfer.2013.10.061.

[66] D. E. Kim, D. I. Yu, S. C. Park, H. J. Kwak, and H. S. Ahn. Critical heat flux triggering mechanism on micro-structured surfaces: Coalesced bubble departure frequency and liquid furnishing capability. *International Journal of Heat and Mass Transfer*, 91:1237–1247, 2015. ISSN 00179310. doi: 10.1016/j.ijheatmasstransfer.2015.08.065.

[67] J. Kim. Review of nucleate pool boiling bubble heat transfer mechanisms. *International Journal of Multiphase Flow*, 35(12):1067–1076, 2009. ISSN 03019322. doi: 10.1016/j.ijmultiphaseflow.2009.07.008.

[68] J. Kim, S. Jun, R. Laksnarain, and S. M. You. Effect of surface roughness on pool boiling heat transfer at a heated surface having moderate wettability. *International Journal of Heat and Mass Transfer*, 101(1):992–1002, 2016. ISSN 00179310. doi: 10.1016/j.ijheatmasstransfer.2016.05.067.

[69] J. M. Kim, S. C. Park, B. T. Kong, H.-B.-R. Lee, and H. S. Ahn. Effect of porous graphene networks and micropillar arrays on boiling heat transfer performance. *Experimental Thermal and Fluid Science*, 93:153–164, 2018. ISSN 08941777. doi: 10.1016/j.expthermflusci.2017.12.029.

[70] S. Kim, H. D. Kim, H. Kim, H. S. Ahn, H. J. Jo, J. Kim, and M. H. Kim. Effects of nano-fluid and surfaces with nano structure on the increase of CHF. *Experimental Thermal and Fluid Science*, 34 (4):487–495, 2010. ISSN 08941777. doi: 10.1016/j.expthermflusci.2009.05.006.

[71] S. H. Kim, G. C. Lee, J. Y. Kang, K. Moriyama, M. H. Kim, and H. S. Park. Boiling heat transfer and critical heat flux evaluation of the pool boiling on micro structured surface. *International Journal of Heat and Mass Transfer*, 91(9):1140–1147, 2015. ISSN 00179310. doi: 10.1016/j.ijheatmasstransfer.2015.07.120.

[72] S. J. Kim, I. C. Bang, J. Buongiorno, and L. W. Hu. Surface wettability change during pool boiling of nanofluids and its effect on critical heat flux. *International Journal of Heat and Mass Transfer*, 50(19-20):4105–4116, 2007. ISSN 00179310. doi: 10.1016/j.ijheatmasstransfer.2007.02.002.

[73] KME Mansfeld GmbH. FACTSHEET Cu-OFE C10100. 2016. URL `https://www.kme-mansfeld.com/files/pdfs/MKMHE_Factsheet_CU-OFE_V08.pdf`. [Online; accessed April 26, 2021].

[74] Korth Kristalle. Physical properties of CaF2. URL `https://www.korth.de/en/materials/detail/Calcium%20Fluoride%20/%20RAMAN`. [Online; accessed August 9, 2021].

[75] U. G. Kumar, S. Suresh, M. R. Thansekhar, and D. P. Babu. Effect of diameter of metal nanowires on pool boiling heat transfer with fc-72. *Applied Surface Science*, 423:509–520, 2017. ISSN 01694332. doi: 10.1016/j.apsusc.2017.06.135.

[76] C. Kunkelmann. *Numerical Modeling and Investigation of Boiling Phenomena*. Dissertation, Technische Universität Darmstadt, Darmstadt, 2011.

[77] C. Kunkelmann, K. Ibrahem, N. Schweizer, S. Herbert, P. Stephan, and T. Gambaryan-Roisman. The effect of three-phase contact line speed on local evaporative heat transfer: Experimental and numerical investigations. *International Journal of Heat and Mass Transfer*, 55(7-8):1896–1904, 2012. ISSN 00179310. doi: 10.1016/j.ijheatmasstransfer.2011.11.044.

[78] H. M. Kurihara and J. E. Myers. The effects of superheat and surface roughness on boiling coefficients. *AIChE Journal*, 6(1):83–91, 1960. ISSN 1547-5905. doi: 10.1002/aic.690060117.

[79] S. S. Kutateladze. *Teploperedacha pri Kondensatsii i Kipenii (Heat transfer in condensation and boiling): Tanslated Form: AEC-tr-3770*. State Scientific and Technical Publishers of Literature on Machinery, Moscow-Leningrad, 1952.

[80] S. S. Kutateladze, A. I. Leont'ev, and A. G. Kirdyashkin. Theory of heat transfer in nucleate boiling. *Journal of Engineering Physics*, 8(1):4–6, 1965. ISSN 0022-0841. doi: 10.1007/BF00833665.

[81] L. Landau and B. Levich. Dragging of a liquid by a moving plate. *Acta Physicochimica U.R.S.S.*, Vol.XVII(No. 1-2), 1942.

[82] D. Lee, B. S. Kim, H. Moon, N. Lee, S. Shin, and H. H. Cho. Enhanced boiling heat transfer on nanowire-forested surfaces under subcooling conditions. *International Journal of Heat and Mass Transfer*, 120:1020–1030, 2018. ISSN 00179310. doi: 10.1016/j.ijheatmasstransfer.2017.12.100.

[83] J. Lee, J. Kim, and K. T. Kiger. Time- and space-resolved heat transfer characteristics of single droplet cooling using microscale heater arrays. *International Journal of Heat and Fluid Flow*, 22 (2):188–200, 2001. ISSN 0142727X. doi: 10.1016/S0142-727X(00)00082-5.

[84] S. Levy. Generalized correlation of boiling heat transfer. *Journal of Heat Transfer*, 81(1):37–42, 1959. ISSN 0022-1481. doi: 10.1115/1.4008126.

[85] C. Li and G. P. Peterson. Parametric study of pool boiling on horizontal highly conductive microporous coated surfaces. *Journal of Heat Transfer*, 129(11):1465–1475, 2007. ISSN 0022-1481. doi: 10.1115/1.2759969.

[86] C. Li, Z. Wang, P.-I. Wang, Y. Peles, N. Koratkar, and G. P. Peterson. Nanostructured copper interfaces for enhanced boiling. *small*, 4(8):1084–1088, 2008. doi: 10.1002/smll.200700991.

[87] Q. Li, W. Wang, C. Oshman, B. Latour, C. Li, V. M. Bright, Y.-C. Lee, and R. Yang. Enhanced pool boiling performance on micro-, nano-, and hybrid-structured surfaces. pages 633–640. American Society of Mechanical Engineers Digital Collection, 2012. doi: 10.1115/IMECE2011-64921.

[88] Y.-Y. Li, Z.-H. Liu, and B.-Z. Zheng. Experimental study on the saturated pool boiling heat transfer on nano-scale modification surface. *International Journal of Heat and Mass Transfer*, 84(5):550–561, 2015. ISSN 00179310. doi: 10.1016/j.ijheatmasstransfer.2014.12.064.

[89] G. Liang and I. Mudawar. Pool boiling critical heat flux (chf) – part 1: Review of mechanisms, models, and correlations. *International Journal of Heat and Mass Transfer*, 117:1352–1367, 2018. ISSN 0017-9310. doi: 10.1016/j.ijheatmasstransfer.2017.09.134.

[90] J. H. Lienhard. A semi-rational nucleate boiling heat flux correlation. *International Journal of Heat and Mass Transfer*, 6(3):215–219, 1963. ISSN 00179310. doi: 10.1016/0017-9310(63)90108-X.

[91] J. H. Lienhard and V. K. Dhir. *Extended hydrodynamic theory of the peak and minimum pool boiling heat fluxes*. National Aeronautics and Space Administration, 1973.

[92] S. G. Liter and M. Kaviany. Pool-boiling CHF enhancement by modulated porous-layer coating: Theory and experiment. *International Journal of Heat and Mass Transfer*, 44(22):4287–4311, 2001. ISSN 00179310. doi: 10.1016/S0017-9310(01)00084-9.

[93] Q. Liu, J. Yu, and H. Wang. The role of the substrate roughness in contact angle hysteresis and dynamic deviation. *International Journal of Heat and Mass Transfer*, 148(19–20):118985, 2020. ISSN 00179310. doi: 10.1016/j.ijheatmasstransfer.2019.118985.

[94] J. J. Lorenz. *The effects of surface conditions on boiling characteristics*. Dissertation, Massachusetts Institute of Technology, Cambridge, Massachusetts, 1972.

[95] M.-C. Lu, R. Chen, V. Srinivasan, V. P. Carey, and A. Majumdar. Critical heat flux of pool boiling on si nanowire array-coated surfaces. *International Journal of Heat and Mass Transfer*, 54(25-26): 5359–5367, 2011. ISSN 00179310. doi: 10.1016/j.ijheatmasstransfer.2011.08.007.

[96] M. Mann, K. Stephan, and P. Stephan. Influence of heat conduction in the wall on nucleate boiling heat transfer. *International Journal of Heat and Mass Transfer*, 43(12):2193–2203, 2000. ISSN 00179310. doi: 10.1016/S0017-9310(99)00292-6.

[97] W. R. McGillis, V. P. Carey, J. S. Fitch, and W. R. Hamburgen. Pool boiling enhancement techniques for water at low pressure. In *1991 Proceedings, Seventh IEEE Semiconductor Thermal Measurement and Management Symposium*, pages 64–72. IEEE, 1991. ISBN 0-87942-664-0. doi: 10.1109/STHERM.1991.152914.

[98] J. P. McHale and S. V. Garimella. Bubble nucleation characteristics in pool boiling of a wetting liquid on smooth and rough surfaces. *International Journal of Multiphase Flow*, 36(4):249–260, 2010. ISSN 03019322. doi: 10.1016/j.ijmultiphaseflow.2009.12.004.

[99] J. P. McHale and S. V. Garimella. Nucleate boiling from smooth and rough surfaces – part 2: Analysis of surface roughness effects on nucleate boiling. *Experimental Thermal and Fluid Science*, 44:439–455, 2013. ISSN 08941777. doi: 10.1016/j.expthermflusci.2012.08.005.

[100] T. S. Meiron, A. Marmur, and I. S. Saguy. Contact angle measurement on rough surfaces. *Journal of colloid and interface science*, 274(2):637–644, 2004. ISSN 0021-9797. doi: 10.1016/j.jcis.2004.02.036.

[101] D. Meschede. *Gerthsen Physik*. Springer Berlin Heidelberg, Berlin, Heidelberg, 2010. ISBN 978-3-642-12893-6. doi: 10.1007/978-3-642-12894-3.

[102] R. B. Mesler and J. T. Banchero. Effect of superatmospheric pressures on nucleate boiling of organic liquids. *AIChE Journal*, 4(1):102–113, 1958. ISSN 1547-5905. doi: 10.1002/aic.690040119.

[103] B. B. Mikic and W. M. Rohsenow. A new correlation of pool-boiling data including the effect of heating surface characteristics. *Journal of Heat Transfer*, 91(2):245–250, 1969. ISSN 0022-1481. doi: 10.1115/1.3580136.

[104] A. S. Moita, E. Teodori, and A. L. N. Moreira. Influence of surface topography in the boiling mechanisms. *International Journal of Heat and Fluid Flow*, 52:50–63, 2015. ISSN 0142727X. doi: 10.1016/j.ijheatfluidflow.2014.11.003.

[105] H. W. Moon, Y. J. Yoon, J. H. Park, B.-S. Myung, and D. E. Kim. Dynamic wetting and boiling characteristics on micro-structured and micro/nano hierarchically structured surfaces. *Experimental Thermal and Fluid Science*, 74:19–26, 2016. ISSN 08941777. doi: 10.1016/j.expthermflusci.2015.11.019.

[106] F. D. Moore and R. B. Mesler. The measurement of rapid surface temperature fluctuations during nucleate boiling of water. *AIChE Journal*, 7(4):620–624, 1961. ISSN 0001-1541. doi: 10.1002/aic.690070418.

[107] T.-B. Nguyen, D. Liu, Md I. Kayes, B. Wang, N. Rashin, P. W. Leu, and T. Tran. Critical heat flux enhancement in pool boiling through increased rewetting on nanopillar array surfaces. *Scientific reports*, 8(1):4815, 2018. doi: 10.1038/s41598-018-22693-z.

[108] K. Nishikawa and K. Yamagata. On the correlation of nucleate boiling heat transfer. *International Journal of Heat and Mass Transfer*, 1(2-3):219–235, 1960. ISSN 00179310. doi: 10.1016/0017-9310(60)90024-7.

[109] S. Nukiyama. The maximum and minimum values of the heat q transmitted from metal to boiling water under atmospheric pressure. *Journal Japan Soc. Mech. Engrs*, 37:367–374, 1934.

[110] H. O'Hanley, C. Coyle, J. Buongiorno, T. McKrell, L.-W. Hu, M. Rubner, and R. Cohen. Separate effects of surface roughness, wettability, and porosity on the boiling critical heat flux. *Applied Physics Letters*, 103(2):024102, 2013. ISSN 0003-6951. doi: 10.1063/1.4813450.

[111] S. D. Park and I. C. Bang. Experimental study of a universal CHF enhancement mechanism in nanofluids using hydrodynamic instability. *International Journal of Heat and Mass Transfer*, 70(7):844–850, 2014. ISSN 00179310. doi: 10.1016/j.ijheatmasstransfer.2013.11.066.

[112] J. L. Parker and M. S. El-Genk. Enhanced saturation and subcooled boiling of FC-72 dielectric liquid. *International Journal of Heat and Mass Transfer*, 48(18):3736–3752, 2005. ISSN 00179310. doi: 10.1016/j.ijheatmasstransfer.2005.03.011.

[113] H. T. Phan, N. Caney, P. Marty, S. Colasson, and J. Gavillet. How does surface wettability influence nucleate boiling? *Comptes Rendus Mécanique*, 337(5):251–259, 2009. ISSN 16310721. doi: 10.1016/j.crme.2009.06.032.

[114] I. L. Pioro. Experimental evaluation of constants for the Rohsenow pool boiling correlation. *International Journal of Heat and Mass Transfer*, 42(11):2003–2013, 1999. ISSN 00179310. doi: 10.1016/S0017-9310(98)00294-4.

[115] I. L. Pioro, W. M. Rohsenow, and S. S. Doerffer. Nucleate pool-boiling heat transfer. i: Review of parametric effects of boiling surface. *International Journal of Heat and Mass Transfer*, 47(23): 5033–5044, 2004. ISSN 00179310. doi: 10.1016/j.ijheatmasstransfer.2004.06.019.

[116] M. Potash and P. C. Wayner. Evaporation from a two-dimensional extended meniscus. *International Journal of Heat and Mass Transfer*, 15(10):1851–1863, 1972. ISSN 00179310. doi: 10.1016/0017-9310(72)90058-0.

[117] P. Preusser. *Wärmeübergang beim Verdampfen von Gemischen in natürlicher Strömung*. Dissertation, Ruhr-Universität, Bochum, 1978.

[118] A. Priarone. Effect of surface orientation on nucleate boiling and critical heat flux of dielectric fluids. *International Journal of Thermal Sciences*, 44(9):822–831, 2005. ISSN 12900729. doi: 10.1016/j.ijthermalsci.2005.02.014.

[119] X. Quan, L. Dong, and P. Cheng. A CHF model for saturated pool boiling on a heated surface with micro/nano-scale structures. *International Journal of Heat and Mass Transfer*, 76:452–458, 2014. ISSN 00179310. doi: 10.1016/j.ijheatmasstransfer.2014.04.037.

[120] Md M. Rahman and M. McCarthy. Boiling enhancement on nanostructured surfaces with engineered variations in wettability and thermal conductivity. *Heat Transfer Engineering*, 38(14-15): 1285–1295, 2016. ISSN 0145-7632. doi: 10.1080/01457632.2016.1242961.

[121] Md M. Rahman, J. Pollack, and M. McCarthy. Increasing boiling heat transfer using low conductivity materials. *Scientific reports*, 5:13145, 2015. doi: 10.1038/srep13145.

[122] K. N. Rainey, S. M. You, and S. Lee. Effect of pressure, subcooling, and dissolved gas on pool boiling heat transfer from microporous surfaces in FC-72. *Journal of Heat Transfer*, 125(1):75–83, 2003. ISSN 0022-1481. doi: 10.1115/1.1527890.

[123] R. Raj, C. Kunkelmann, P. Stephan, J. Plawsky, and J. Kim. Contact line behavior for a highly wetting fluid under superheated conditions. *International Journal of Heat and Mass Transfer*, 55 (9-10):2664–2675, 2012. ISSN 00179310. doi: 10.1016/j.ijheatmasstransfer.2011.12.026.

[124] W. M. Rohsenow. *A method of correlating heat transfer data for surface boiling of liquids*. Technial Report No.5. Cambridge, Massachusetts: Division of Industrial Cooperation, 1951.

[125] W. M. Rohsenow and P. Griffith. *Correlation of maximum heat flux data for boiling of saturated liquids*. Technial Report No.6. Cambridge, Massachusetts: Division of Industrial Cooperation, 1955.

[126] C. Schlawitschek. *Numerical simulation of drop impact and evaporation on superheated surfaces at low and high ambient pressures*. Dissertation, Technische Universität Darmstadt, Darmstadt, 2020.

[127] K. Schweikert. *Microlayer and contact line evaporation during the dewetting of a volatile liquid on a superheated solid*. Dissertation, Technische Universität Darmstadt, Darmstadt, 2022.

[128] K. Schweikert, A. Sielaff, and P. Stephan. Heat flux during dip-coating of a superheated substrate. *Interfacial Phenomena and Heat Transfer*, 7(3):269–281, 2019. ISSN 2169-2785. doi: 10.1615/InterfacPhenomHeatTransfer.2019032623.

[129] K. Schweikert, A. Sielaff, and P. Stephan. On the transition between contact line evaporation and microlayer evaporation during the dewetting of a superheated wall. *International Journal of Thermal Sciences*, 145(8):106025, 2019. ISSN 12900729. doi: 10.1016/j.ijthermalsci.2019.106025.

[130] N. Schweizer. *Multi-Scale Investigation of Nucleate Boiling Phenomena in Microgravity*. Dissertation, Technische Universität Darmstadt, Darmstadt, 2010.

[131] R. R. Sharp. *The Nature of Liquid Film Evaporation During Nucleate Boiling*. National Aeronautics and Space Administration, 1964.

[132] B. Shen, T. Hamazaki, W. Ma, N. Iwata, S. Hidaka, A. Takahara, K. Takahashi, and Y. Takata. Enhanced pool boiling of ethanol on wettability-patterned surfaces. *Applied Thermal Engineering*, 149:325–331, 2019. ISSN 13594311. doi: 10.1016/j.applthermaleng.2018.12.049.

[133] B. Shi, Y.-B. Wang, and K. Chen. Pool boiling heat transfer enhancement with copper nanowire arrays. *Applied Thermal Engineering*, 75:115–121, 2015. ISSN 13594311. doi: 10.1016/j.applthermaleng.2014.09.040.

[134] S. Shin, B. S. Kim, G. Choi, H. Lee, and H. H. Cho. Double-templated electrodeposition: Simple fabrication of micro-nano hybrid structure by electrodeposition for efficient boiling heat transfer. *Applied Physics Letters*, 101(25):251909, 2012. ISSN 0003-6951. doi: 10.1063/1.4772539.

[135] A. Sielaff. *Experimental Investigation of Single Bubbles and Bubble Interactions in Nucleate Boiling*. Dissertation, Technische Universität Darmstadt, Darmstadt, 2014.

[136] B. E. Staniszewski. *Nucleate boiling bubble growth and departure*. Technial Report No.16. Cambridge, Massachusetts: Division of Industrial Cooperation, 1959.

[137] K. Stephan and M. Abdelsalam. Heat-transfer correlations for natural convection boiling. *International Journal of Heat and Mass Transfer*, 23(1):73–87, 1980. ISSN 0017-9310. doi: 10.1016/0017-9310(80)90140-4.

[138] P. Stephan and J. Hammer. A new model for nucleate boiling heat transfer. *Wärme- und Stoffübertragung*, 30(2):119–125, 1994. ISSN 0042-9929. doi: 10.1007/BF00715018.

[139] P. Stephan, A. Sielaff, S. Fischer, J. Dietl, and S. Herbert. A contribution to the basic understanding of nucleate boiling phenomena: generic experiments and numerical simulations. *Thermal Science & Engineering*, 21(2), 2013.

[140] P. Stephan, S. Kabelac, M. Kind, D. Mewes, K. Schaber, and T. Wetzel. *VDI-Wärmeatlas*. Springer Berlin Heidelberg, Berlin, Heidelberg, 2019. ISBN 978-3-662-52988-1. doi: 10.1007/978-3-662-52989-8.

[141] Y. Takata, S. Hidaka, J. M. Cao, T. Nakamura, H. Yamamoto, M. Masuda, and T. Ito. Effect of surface wettability on boiling and evaporation. *Energy*, 30(2-4):209–220, 2005. ISSN 03605442. doi: 10.1016/j.energy.2004.05.004.

[142] T. Tanaka, K. Miyazaki, and T. Yabuki. Observation of heat transfer mechanisms in saturated pool boiling of water by high-speed infrared thermometry. *International Journal of Heat and Mass Transfer*, 170(6):121006, 2021. ISSN 00179310. doi: 10.1016/j.ijheatmasstransfer.2021.121006.

[143] T. G. Theofanous and T. N. Dinh. High heat flux boiling and burnout as microphysical phenomena: Mounting evidence and opportunities. *Multiphase Science and Technology*, 18(3):251–276, 2006. ISSN 0276-1459. doi: 10.1615/MultScienTechn.v18.i3.30.

[144] T. G. Theofanous, T. N. Dinh, J. P. Tu, and A. T. Dinh. The boiling crisis phenomenon: part I: Nucleation and nucleate boiling heat transfer. *Experimental Thermal and Fluid Science*, 26(6-7): 775–792, 2002. ISSN 08941777. doi: 10.1016/S0894-1777(02)00192-9.

[145] T. G. Theofanous, T. N. Dinh, J. P. Tu, and A. T. Dinh. The boiling crisis phenomenon: part II: Dryout dynamics and burnout. *Experimental Thermal and Fluid Science*, 26(6-7):793–810, 2002. ISSN 08941777. doi: 10.1016/S0894-1777(02)00193-0.

[146] S. J. Thiagarajan, S. Narumanchi, C. King, W. Wang, and R. Yang. Enhancement of heat transfer with pool and spray impingement boiling on microporous and nanowire surface coatings. In *2010 14th International Heat Transfer Conference, Volume 6*, pages 819–828. ASMEDC, 08082010. ISBN 978-0-7918-4941-5. doi: 10.1115/IHTC14-23284.

[147] Y. Utaka, K. Hu, Z. Chen, and T. Morokuma. Measurement of contribution of microlayer evaporation applying the microlayer volume change during nucleate pool boiling for water and ethanol. *International Journal of Heat and Mass Transfer*, 125(747):243–247, 2018. ISSN 00179310. doi: 10.1016/j.ijheatmasstransfer.2018.04.044.

[148] R. I. Vachon, G. H. Nix, and G. E. Tanger. Evaluation of constants for the Rohsenow pool-boiling correlation. *Journal of Heat Transfer*, 90(2):239–246, 1968. ISSN 0022-1481. doi: 10.1115/1.3597489.

[149] H. J. van Ouwerkerk. Burnout in pool boiling the stability of boiling mechanisms. *International Journal of Heat and Mass Transfer*, 15(1):25–34, 1972. ISSN 00179310. doi: 10.1016/0017-9310(72)90163-9.

[150] S. J. D. van Stralen, R. Cole, W. M. Sluyter, and M. S. Sohal. Bubble growth rates in nucleate boiling of water at subatmospheric pressures. *International Journal of Heat and Mass Transfer*, 18 (5):655–669, 1975. ISSN 00179310. doi: 10.1016/0017-9310(75)90277-X.

[151] E. Wagner. *Hochauflösende Messungen beim Blasensieden von Reinstoffen und binären Gemischen*. Dissertation, Technische Universität Darmstadt, Darmstadt, 2008.

[152] J. Wang, Y. Wu, Y. Cao, G. Li, and Y. Liao. Influence of surface roughness on contact angle hysteresis and spreading work. *Colloid and Polymer Science*, 298(8):1107–1112, 2020. ISSN 0303-402X. doi: 10.1007/s00396-020-04680-x.

[153] P. C. Wayner and C. L. Coccio. Heat and mass transfer in the vicinity of the triple interline of a meniscus. *AIChE Journal*, 17(3):569–574, 1971. ISSN 0001-1541. doi: 10.1002/aic.690170317.

[154] P. C. Wayner, Y. K. Kao, and L. V. LaCroix. The interline heat-transfer coefficient of an evaporating wetting film. *International Journal of Heat and Mass Transfer*, 19(5):487–492, 1976. ISSN 00179310. doi: 10.1016/0017-9310(76)90161-7.

[155] R. Wen, Q. Li, W. Wang, B. Latour, C. H. Li, C. Li, Y.-C. Lee, and R. Yang. Enhanced bubble nucleation and liquid rewetting for highly efficient boiling heat transfer on two-level hierarchical surfaces with patterned copper nanowire arrays. *Nano Energy*, 38:59–65, 2017. ISSN 22112855. doi: 10.1016/j.nanoen.2017.05.028.

[156] R. N. Wenzel. Resistance of solid surfaces to wetting by water. *Industrial & Engineering Chemistry*, 28(8):988–994, 1936.

[157] K. T. Witte. *Experimentelle Untersuchungen zum Sieden in Metallfaserstrukturen im Bereich niederer Drücke*. Dissertation, Technische Universität Darmstadt, Darmstadt, 2016.

[158] V. V. Yagov. Is a crisis in pool boiling actually a hydrodynamic phenomenon? *International Journal of Heat and Mass Transfer*, 73(11):265–273, 2014. ISSN 00179310. doi: 10.1016/j.ijheatmasstransfer.2014.01.076.

[159] M. Yamada, B. Shen, T. Imamura, S. Hidaka, M. Kohno, K. Takahashi, and Y. Takata. Enhancement of boiling heat transfer under sub-atmospheric pressures using biphilic surfaces. *International Journal of Heat and Mass Transfer*, 115:753–762, 2017. ISSN 00179310. doi: 10.1016/j.ijheatmasstransfer.2017.08.078.

[160] S. R. Yang, Z. M. Xu, J. W. Wang, and X. T. Zhao. On the fractal description of active nucleation site density for pool boiling. *International Journal of Heat and Mass Transfer*, 44(14):2783–2786, 2001. ISSN 00179310. doi: 10.1016/S0017-9310(00)00311-2.

[161] Z. Yao, Y.-W. Lu, and S. G. Kandlikar. Effects of nanowire height on pool boiling performance of water on silicon chips. *International Journal of Thermal Sciences*, 50(11):2084–2090, 2011. ISSN 12900729. doi: 10.1016/j.ijthermalsci.2011.06.009.

[162] B. Yu and P. Cheng. A fractal model for nucleate pool boiling heat transfer. *Journal of Heat Transfer*, 124(6):1117–1124, 2002. ISSN 0022-1481. doi: 10.1115/1.1513580.

[163] D. I. Yu, H. J. Kwak, H. Noh, H. S. Park, K. Fezzaa, and M. H. Kim. Synchrotron x-ray imaging visualization study of capillary-induced flow and critical heat flux on surfaces with engineered micropillars. *Science advances*, 4(2):e1701571, 2018. doi: 10.1126/sciadv.1701571.

[164] Y. Yu, Q. Wu, K. Zhang, and B. H. Ji. Effect of triple-phase contact line on contact angle hysteresis. *Science China Physics, Mechanics and Astronomy*, 55(6):1045–1050, 2012. ISSN 1674-7348. doi: 10.1007/s11433-012-4736-3.

[165] L. Z. Zeng, J. F. Klausner, and R. Mei. A unified model for the prediction of bubble detachment diameters in boiling systems— 1. pool boiling. *International Journal of Heat and Mass Transfer*, 36(9):2261–2270, 1993. ISSN 00179310. doi: 10.1016/S0017-9310(05)80111-5.

[166] B. J. Zhang, R. Ganguly, K. J. Kim, and C. Y. Lee. Control of pool boiling heat transfer through photo-induced wettability change of titania nanotube arrayed surface. *International Communications in Heat and Mass Transfer*, 81:124–130, 2017. ISSN 07351933. doi: 10.1016/j.icheatmasstransfer.2016.12.007.

[167] M. Zimmermann, M. Heinz, A. Sielaff, T. Gambaryan-Roisman, and P. Stephan. Influence of system pressure on pool boiling regimes on a microstructured surface compared to a smooth surface. *Experimental Heat Transfer*, 33(4):318–334, 2020. ISSN 0891-6152. doi: 10.1080/08916152.2019.1635228.

[168] N. Zuber. *Hydrodynamic Aspects of Boiling Heat Transfer*. Dissertation, University of California, Los Angeles, 1959.

List of Figures

List of Tables

Chapter A

Appendix

A.1 Experimental results

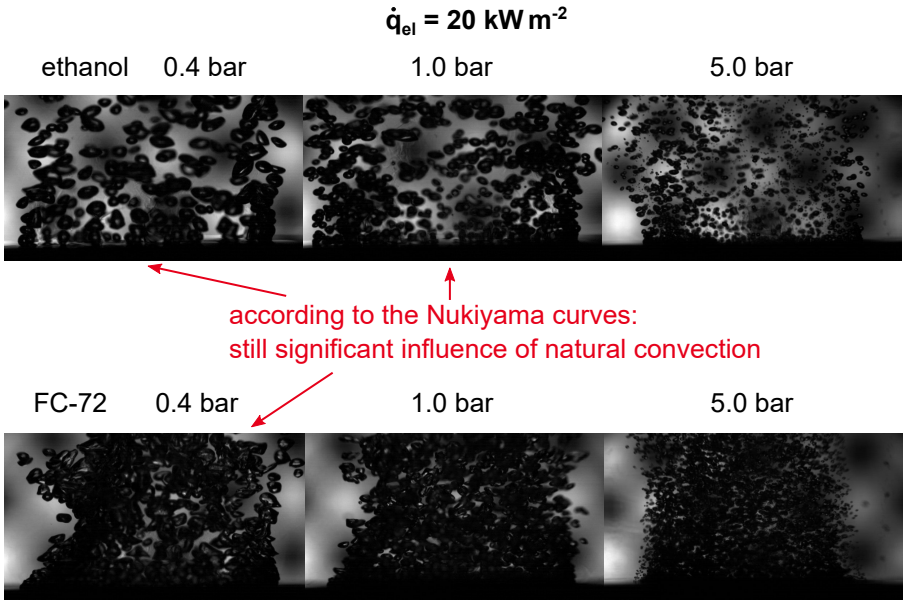

Figure A.1: Images showing the boiling phenomenon at a heat flux of $20\,\mathrm{kW\,m^{-2}}$ and various system pressures obtained for the smooth copper surface Scu, using ethanol and FC-72 as boiling fluids.

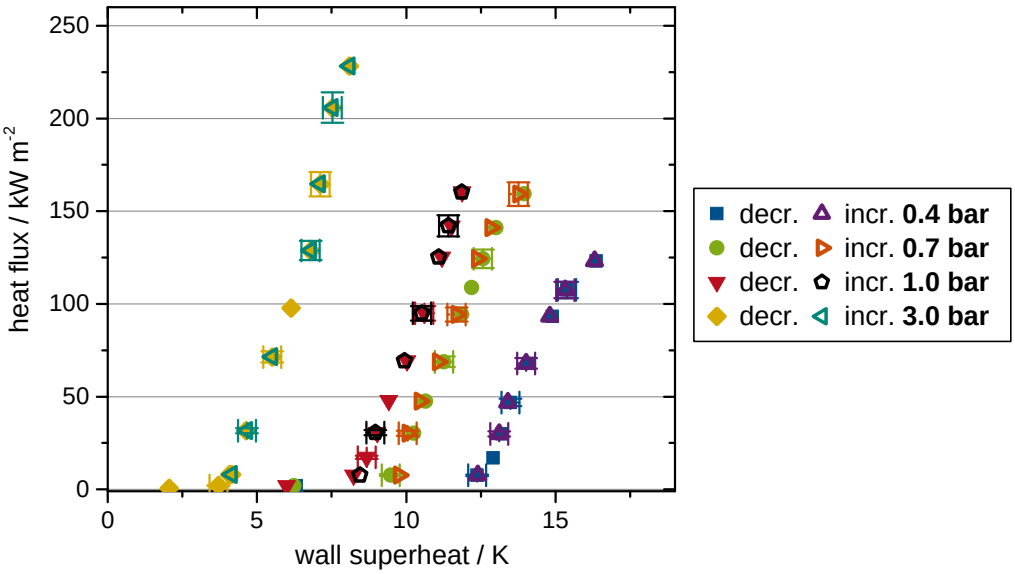

Figure A.2: Nukiyama curves for the technical copper surface Tcu using FC-72 at various system pressures for increasing and decreasing heat fluxes.

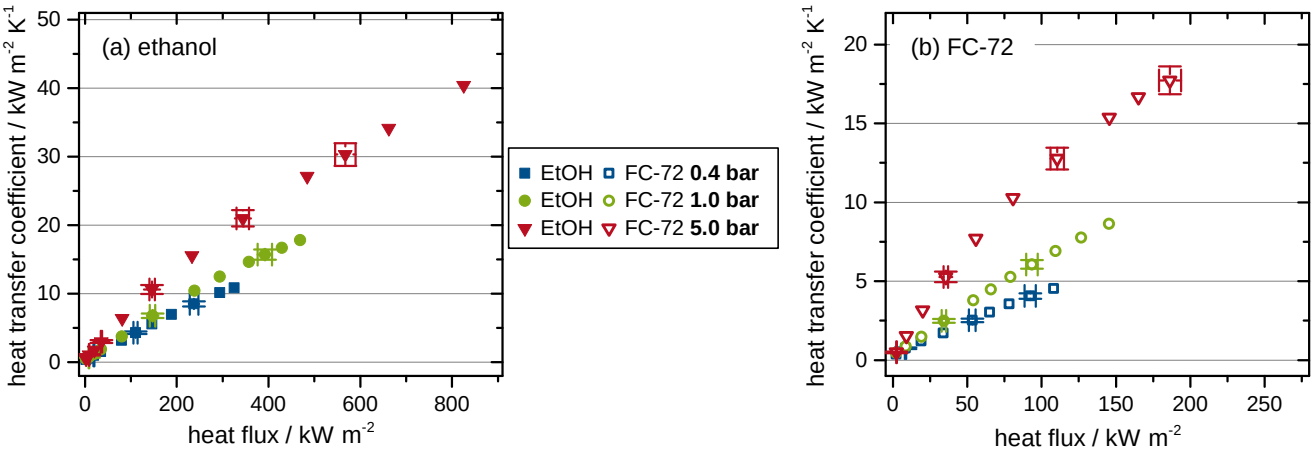

Figure A.3: Heat transfer coefficients for specific heat fluxes obtained for the smooth copper surface Scu using ethanol (a) and FC-72 (b).

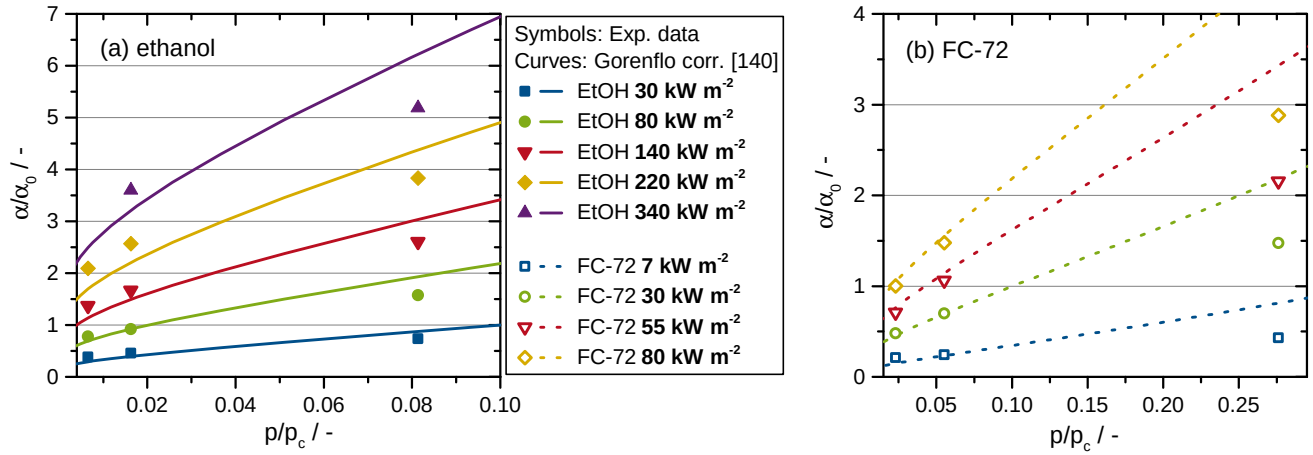

Figure A.4: Ratios of heat transfer coefficient to reference heat transfer coefficient for specific heat fluxes obtained for the smooth copper surface Scu using ethanol (a) and FC-72 (b) at reduced pressures compared to the Gorenflo correlation [140].

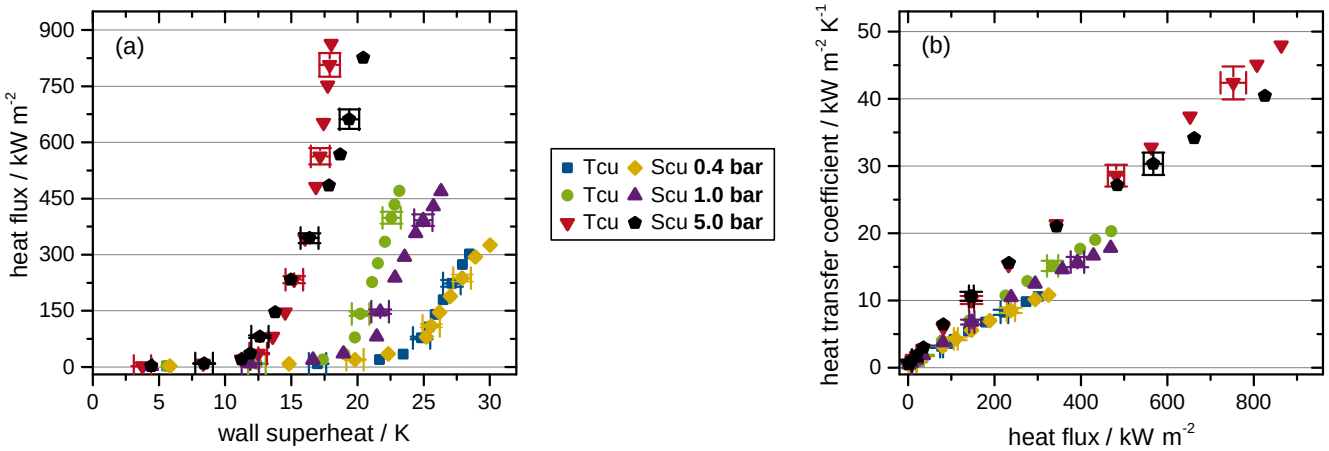

Figure A.5: Comparison of the results for the technical copper surface Tcu and the smooth copper surface Scu with ethanol as boiling fluid at various system pressures. The Nukiyama curves are presented in (a), while the heat transfer coefficients are shown in (b).

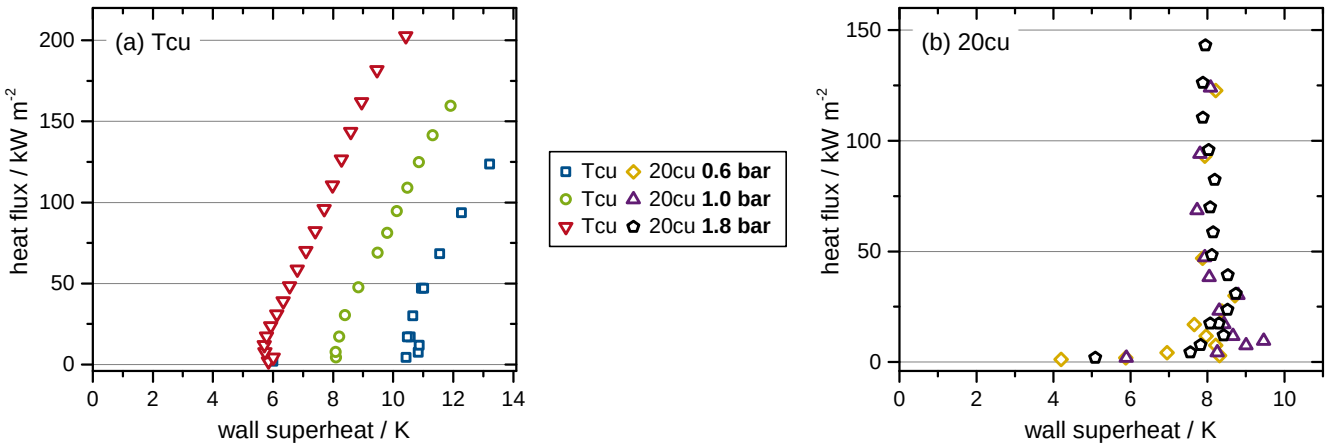

Figure A.6: Nukiyama curves for the technical copper surface Tcu (a) and the long microstructured surface 20cu (b) at various system pressures using FC-72.

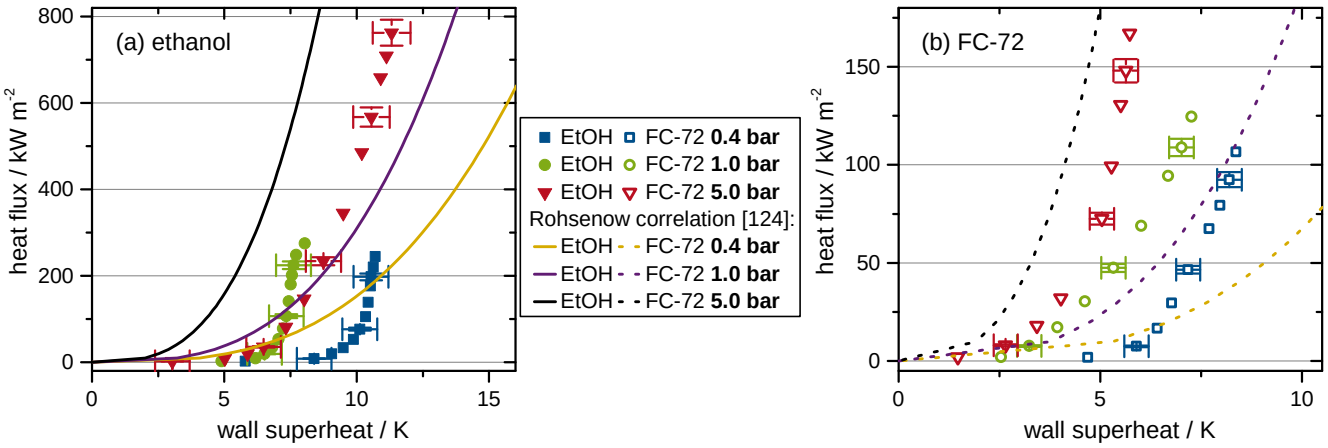

Figure A.7: Nukiyama curves for the long microstructured surface 20cu at various system pressures using ethanol (a) and FC-72 (b) in comparison to Rohsenow's correlation [124].

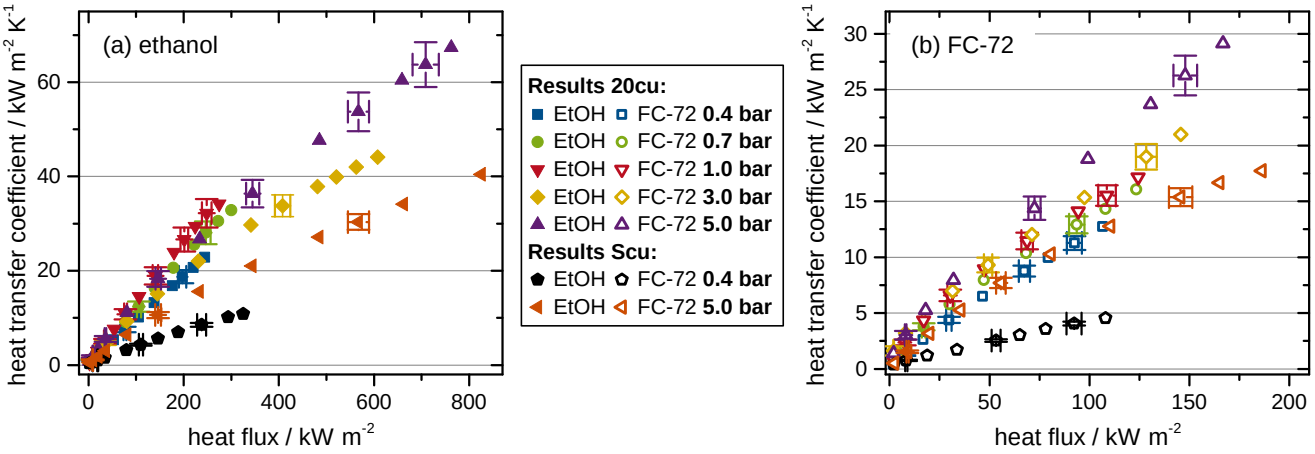

Figure A.8: Heat transfer coefficients for specific heat fluxes obtained for the long microstructured surface 20cu and smooth copper surface Scu using ethanol (a) and FC-72 (b) at various system pressures.

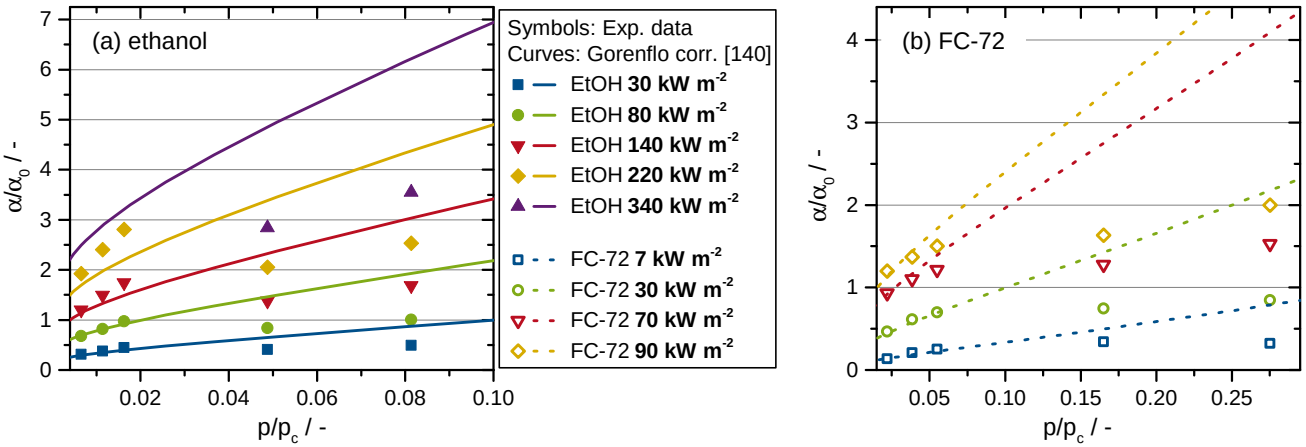

Figure A.9: Ratios of heat transfer coefficient to reference heat transfer coefficient for specific heat fluxes obtained for the long microstructured surface 20cu using ethanol (a) and FC-72 (b) at reduced pressures compared to Gorenflo's correlation [140].

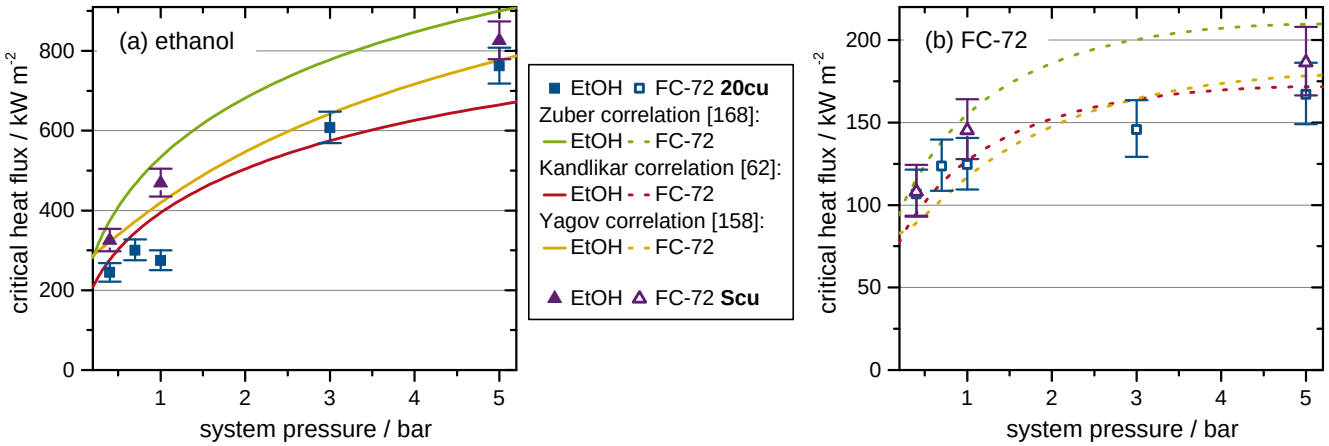

Figure A.10: Critical heat fluxes for the long microstructured surface 20cu at various system pressures using ethanol (a) and FC-72 (b) compared to correlations of Zuber [168], Kandlikar [62], Yagov [158], and the experimental results of the smooth copper surface Scu.

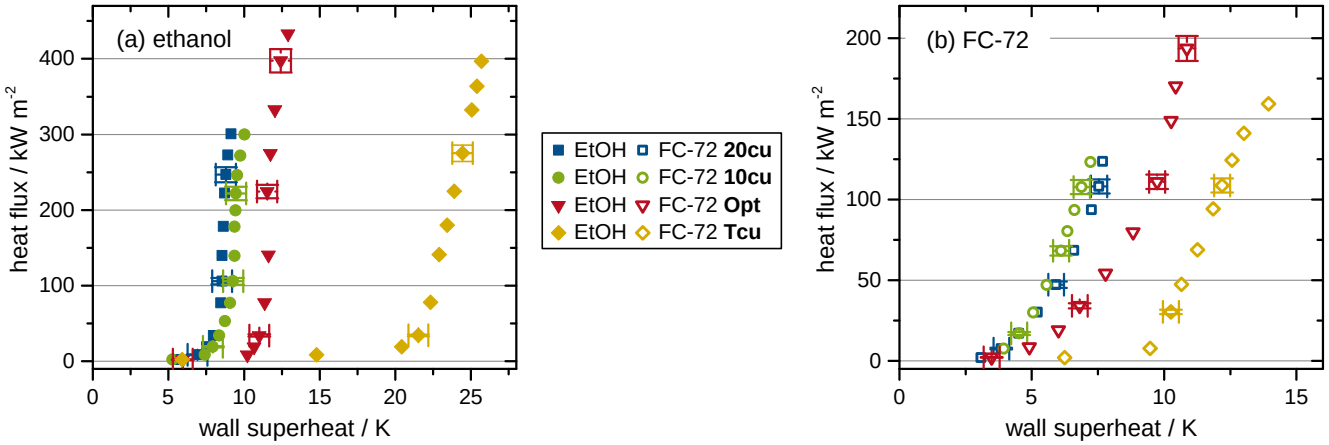

Figure A.11: Nukiyama curves at $0.7\,\mathrm{bar}$ system pressure for four different surfaces using ethanol (a) and FC-72 (b).

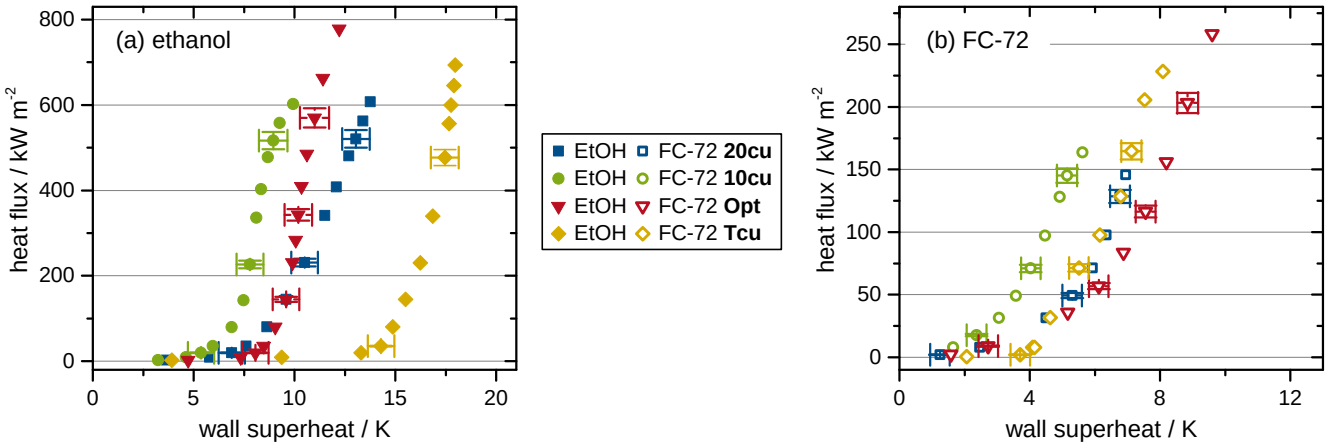

Figure A.12: Nukiyama curves at $3.0\,\mathrm{bar}$ system pressure for four different surfaces using ethanol (a) and FC-72 (b).

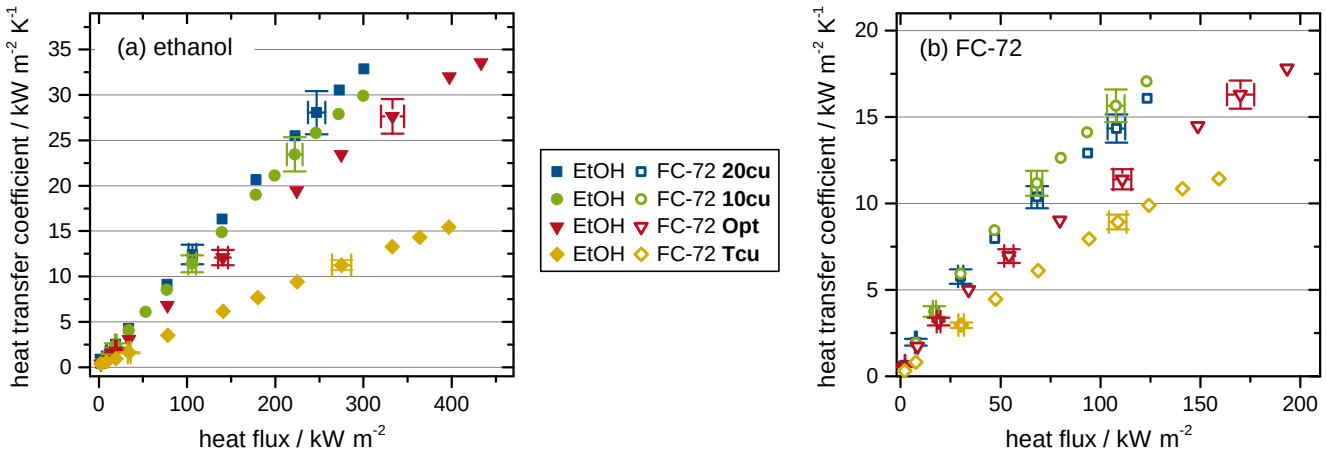

Figure A.13: Heat transfer coefficients for specific heat fluxes obtained for four different surfaces using ethanol (a) and FC-72 (b) at a system pressure of 0.7 bar.

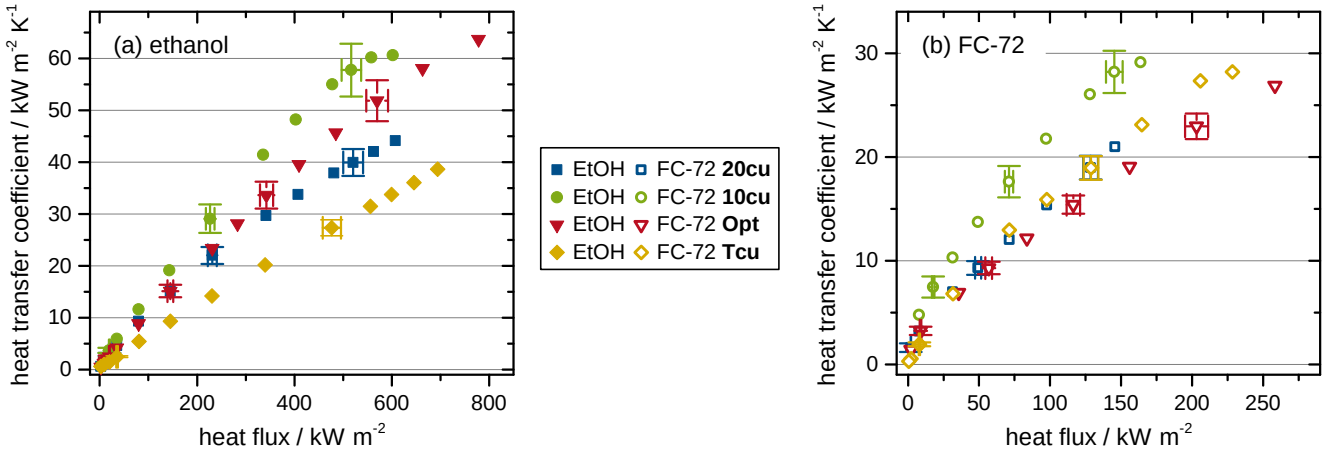

Figure A.14: Heat transfer coefficients for specific heat fluxes obtained for four different surfaces using ethanol (a) and FC-72 (b) at a system pressure of 3.0 bar.

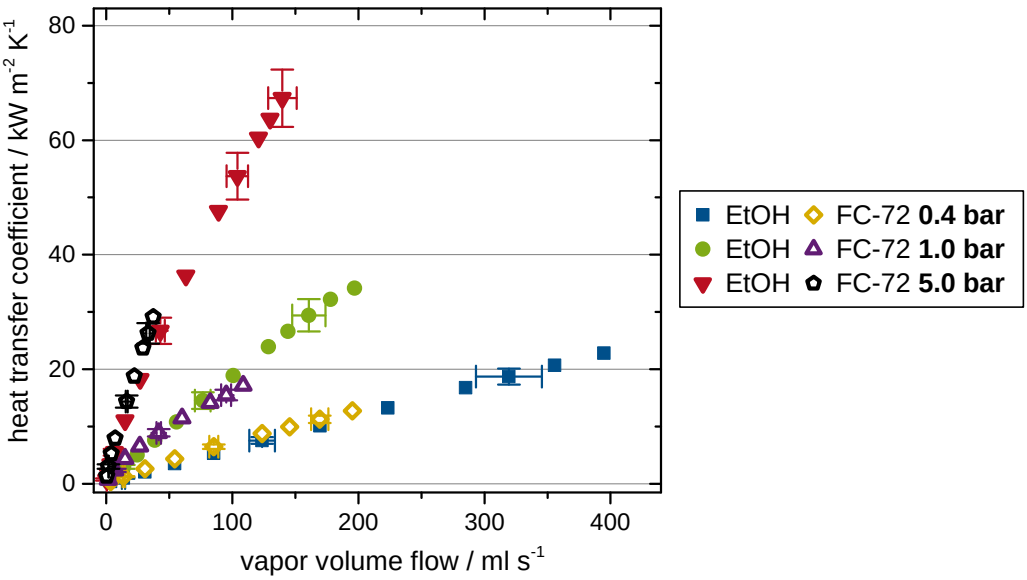

Figure A.15: Heat transfer coefficients for specific vapor volume flows at various system pressures for the long microstructured surface 20cu and both fluids.

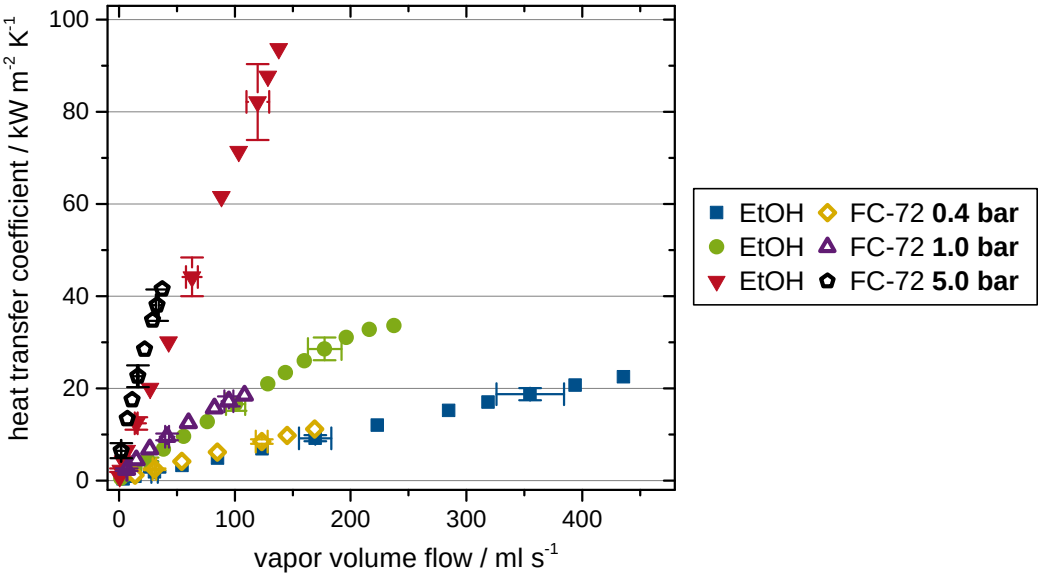

Figure A.16: Heat transfer coefficients for specific vapor volume flows at various system pressures for the short microstructured surface 10cu and both fluids.

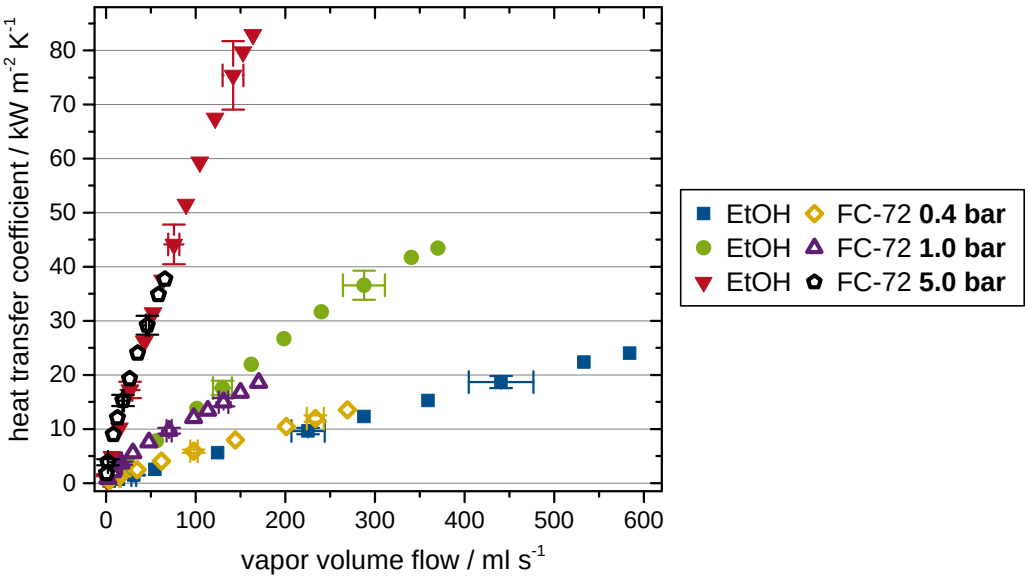

Figure A.17: Heat transfer coefficients for specific vapor volume flows at various system pressures for the optimized, hierarchical surface Opt and both fluids.

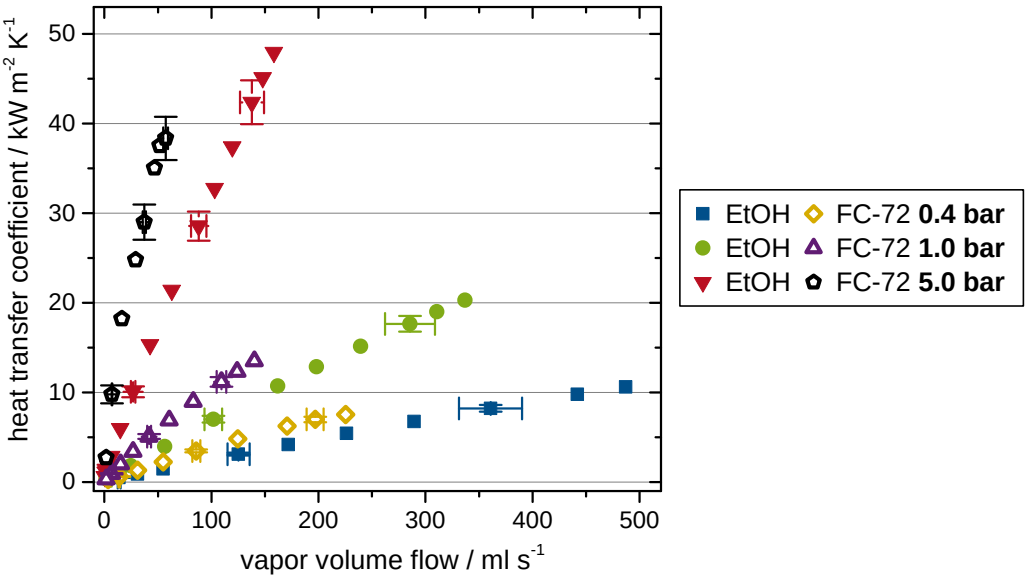

Figure A.18: Heat transfer coefficients for specific vapor volume flows at various system pressures for the technical copper surface Tcu and both fluids.

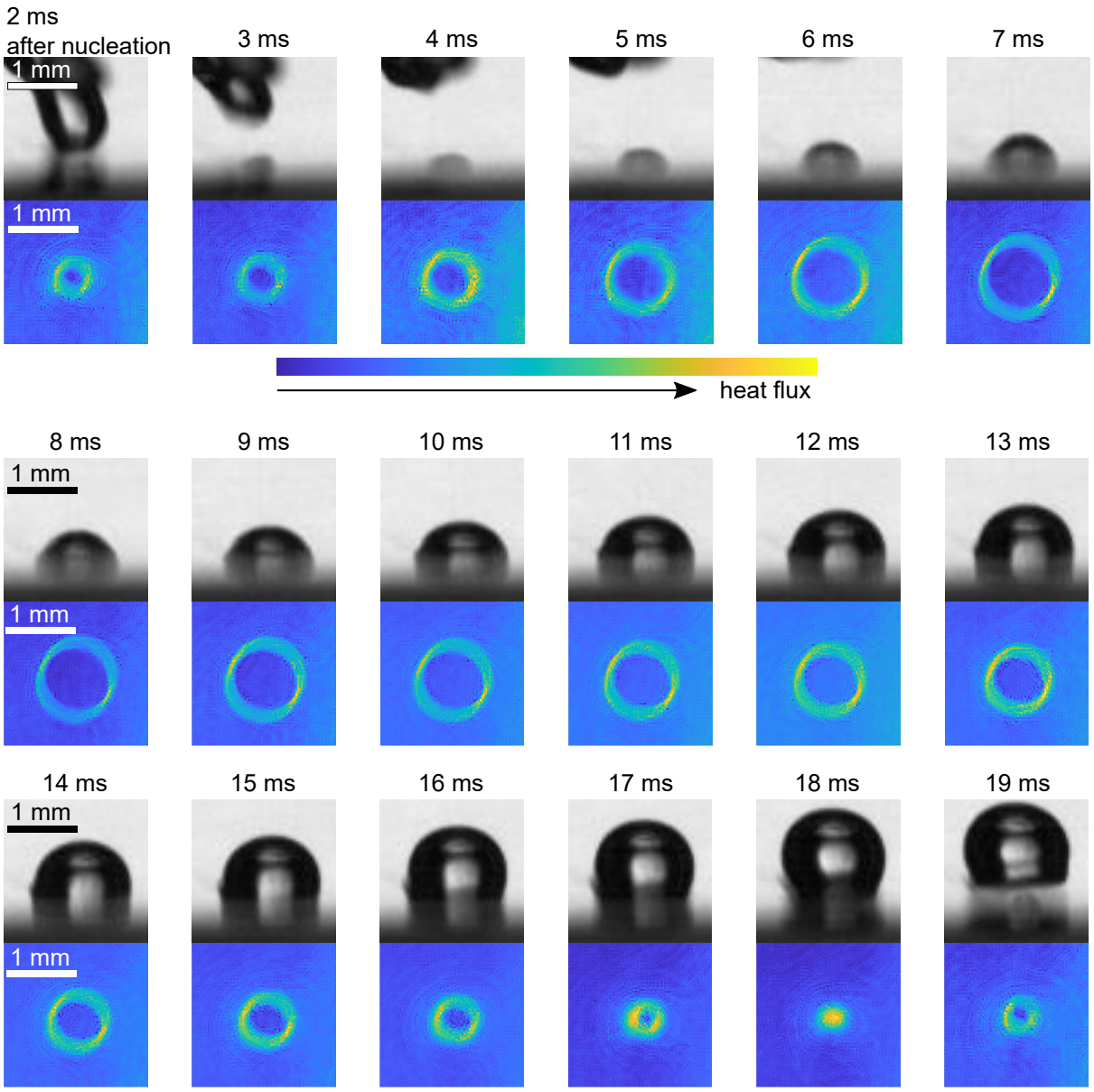

Figure A.19: B&w images and heat flux fields of a growing bubble at various time steps after bubble nucleation and a system pressure of $0.4\,\mathrm{bar}$ using FC-72 as boiling fluid . The heat flux scale varies from time step to time step.

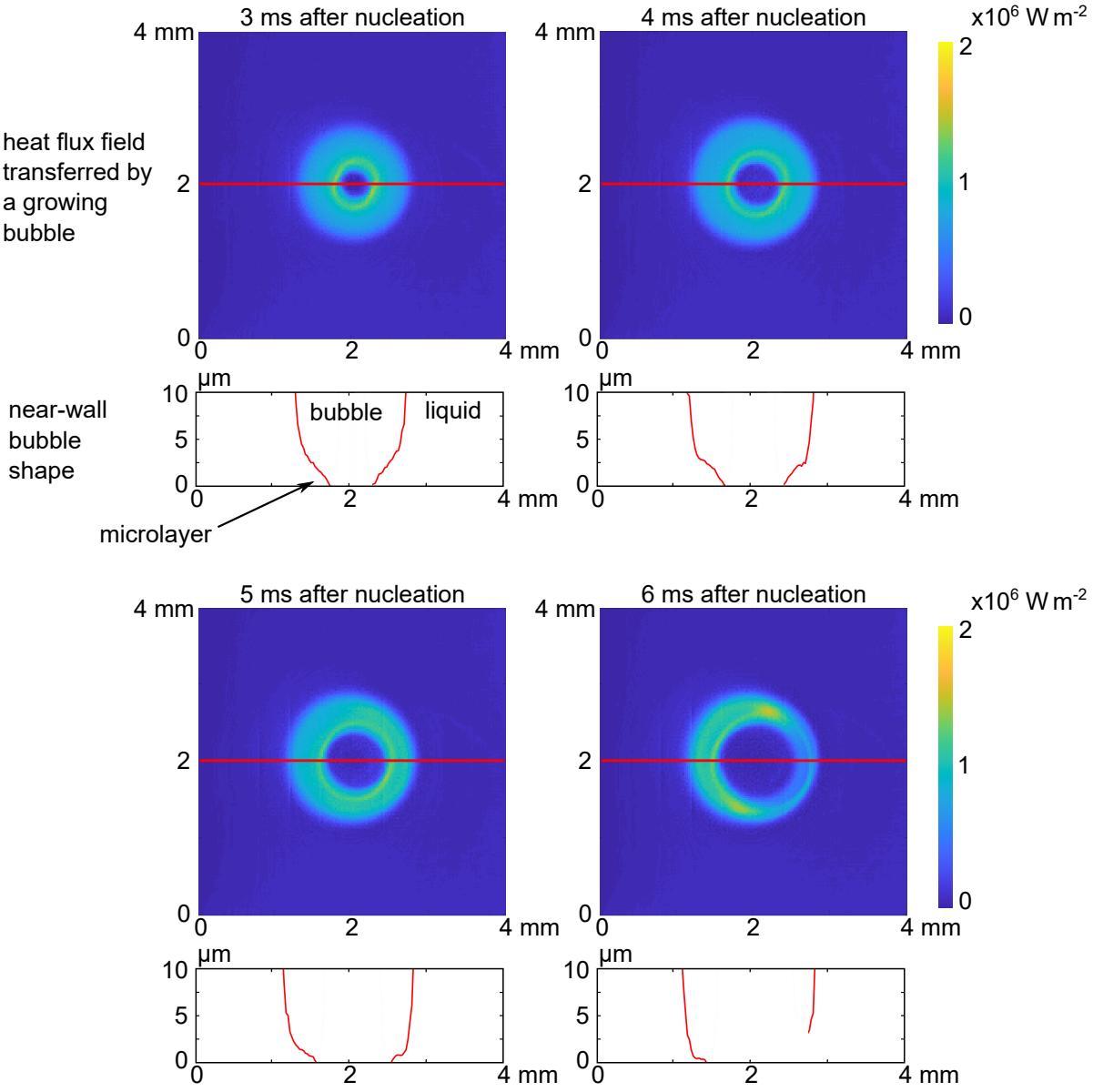

Figure A.20: Heat flux fields and calculated microlayer thickness evolutions at $y = 2\,\mathrm{mm}$ (indicated by the red line) using ethanol as boiling fluid at different time steps after nucleation and a system pressure of $0.7\,\mathrm{bar}$.

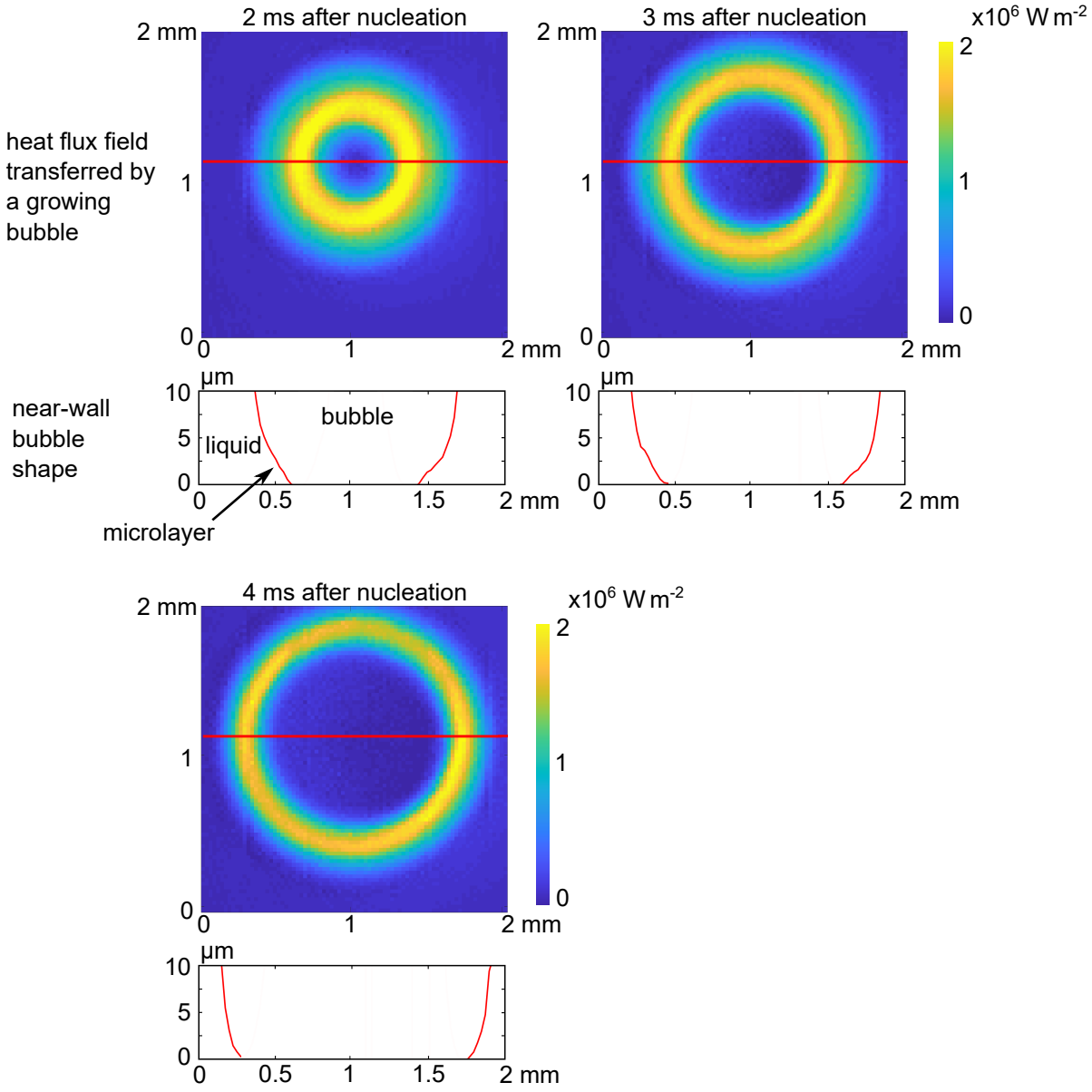

Figure A.21: Heat flux fields and calculated microlayer thickness evolutions at $y = 1.15\,\mathrm{mm}$ (indicated by the red line) using ethanol as boiling fluid at different time steps after nucleation and a system pressure of $1.0\,\mathrm{bar}$.

A.2 Comparison to literature data

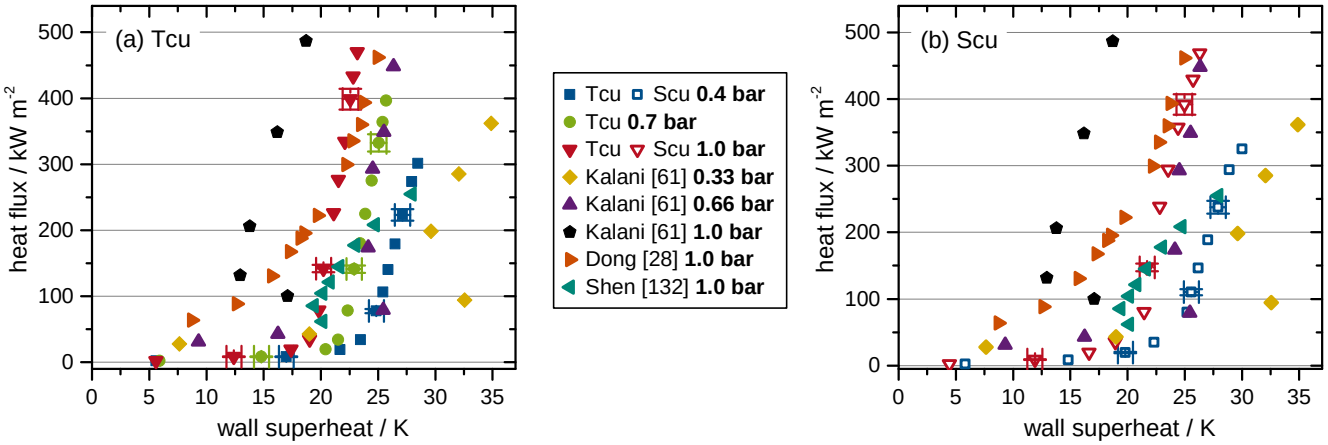

Figure A.22: Nukiyama curves for the technical copper surface Tcu (a) and the smooth copper surface Scu (b) at various system pressures using ethanol as boiling fluid compared to literature data.

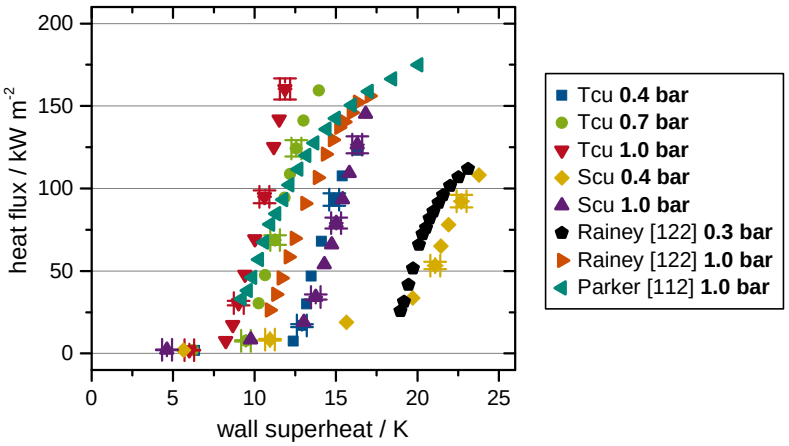

Figure A.23: Nukiyama curves for the technical copper surface (Tcu) and the smooth copper surface (Scu) at various system pressures using FC-72 as boiling fluid compared to literature data.

In Figures A.22 and A.23, Nukiyama curves are presented at various system pressures for the technical copper surface Tcu and the smooth copper surface Scu using ethanol and FC-72 as boiling fluids. Additionally, literature data is shown of Dong et al. [28], Kalani and Kandlikar [61], Parker and El-Genk [112], Rainey et al. [122], and Shen et al. [132]. It is obvious, while some literature data sets match the results obtained in this thesis, others do not. Several factors could cause these deviations and the scattering of the literature data. In many publications, the roughness of the smooth surface is unknown. However, roughness can have a large impact on the boiling process, which is visible in section 5.1.2.3 and in Figure A.23. The results obtained using the technical copper surface show significantly smaller wall superheats compared to the results of the smooth copper surface. Although their roughness values are different, the technical copper surface could still be considered smooth, since it is uncoated and

polished by emery paper of a small grain size[1]. Besides the roughness of the surface, the purity of the boiling fluid has a significant impact. Especially the amount of inert gases dissolved in the liquid can change the boiling behavior drastically. However, most researchers do not provide a leakage rate of their experimental setup, which makes it impossible to determine, whether the boiling fluid is degassed. Additionally, other characteristics of the experimental setup could have an influence as well, since the quantitative impact of many error sources cannot be determined. All those factors are responsible for the scattered nucleate boiling data.

A.3 Material properties

Table A.1: Temperature dependent equations used to calculate the physical properties of ethanol as suggested by the *VDI-Wärmeatlas* [60]. The temperature has to be inserted in Kelvin und the pressure in Pascal.

property	symbol	value
vapor pressure[2]	p	$\left\{61.48\exp\left[513.9/T\left(-8.33801L+0.08719L^{1.5}-3.30578L^{2.5}-0.25986L^{5}\right)\right]\right\}$ bar
liq. density[2]	ρ_l	$\left\{276+748.619L^{0.35}-412.3645L^{2/3}+776.4385L-436.6754L^{4/3}\right\}$ kg m^{-3}
vap. density[3]	ρ_v	$\left\{p/180.4645T\right\}$ kg m^{-3}
spec. enthalpy of vaporization[2]	Δh_v	$\left\{92740.712\left(14.68765L^{1/3}-15.27119L^{2/3}+26.062304L-20.049661L^{2}+15.816495L^{6}\right)\right\}$ J kg^{-1}
liq. heat capacity[2]	$c_{p,\mathrm{l}}$	$\left\{180.4645\left(0.5036/L+22.442-36.7832L+160.3732L^{2}-466.4327L^{3}+396.028L^{4}\right)\right\}$ J kg^{-1} K^{-1}
liq. thermal conductivity	λ_l	$\left\{0.251-3.16\times10^{-4}T+2.04\times10^{-7}T^{2}-2.57\times10^{-10}T^{3}\right\}$ W m^{-1}K^{-1}
liq. dyn. viscosity	η_l	$\left\{3.8\times10^{-7}\exp\left(6.16824[(740.289-T)/(T-90.765)]^{1/3}-0.0012[(740.289-T)/(T-90.765)]^{4/3}\right)\right\}$ Pa s
surface tension[2]	σ	$\left\{0.06374L^{2.46625-3.21891(1-L)+1.91455(1-L)^{2}-0.10017(1-L)^{3}}\right\}$ N m^{-1}

[1] approximately 12 µm grain size

[2] To reduce the length of the equation, the factor $L=(1-T/513.9)$ is used, with the temperature T in Kelvin.

[3] Using a virial expansion instead results in a mean density difference of 5 % to the ideal gas law, which is similar to the assumed overall uncertainty of the physical properties. Therefore, it is estimated that the ideal gas law is useable without significant errors.

Table A.2: Physical properties of FC-72 adapted from [57, 135].

sat. pressure / atm	sat. temp. / °C	liquid density / kgm^{-3}	vapor density / kgm^{-3}	heat capacity (c_p) / $J\,kg^{-1}K^{-1}$	enthalpy of evaporation / $J\,kg^{-1}$	surface tension x 10^{-2} / Nm^{-1}	ther. cond. x 10^{-2} / $Wm^{-1}K^{-1}$	dyn. visc. x 10^{-4} / Pas
0.085	0	1755.29	1.371	1011.01	99181.7	1.334	5.877	9.496
	5	1737.54	1.802	1018.73	98000	1.288	5.818	8.742
0.144	10	1719.78	2.234	1026.45	96818.2	1.241	5.76	8
	15	1705.66	2.859	1034.17	95593.4	1.195	5.702	7.43
0.232	20	1691.54	3.484	1041.89	94368.5	1.15	5.643	6.868
	25	1680.33	4.357	1049.61	93094.4	1.104	5.585	6.437
0.361	30	1669.12	5.231	1057.34	91820.3	1.059	5.526	6.011
	35	1659.4	6.41	1065.06	90497	1.015	5.468	5.68
0.54	40	1649.68	7.589	1072.78	89173.6	0.9708	5.41	5.353
	45	1640.58	9.136	1080.5	87788.8	0.9271	5.351	5.091
0.785	50	1631.48	10.683	1088.22	86403.9	0.8838	5.293	4.831
	55	1622.58	12.738	1095.94	84969.8	0.8409	5.234	4.608
1	56.6	1619.73	13.396	1098.41	84510.9	0.8273	5.216	4.537
1.109	60	1613.67	14.793	1103.66	83535.7	0.7985	5.176	4.388
	65	1603.46	17.516	1111.39	82046.2	0.7565	5.118	4.183
1.529	70	1593.25	20.238	1119.11	80556.6	0.715	5.059	3.982
	75	1581.12	23.721	1126.83	79024.1	0.6739	5.001	3.799
2.062	80	1568.99	27.203	1134.55	77491.5	0.6334	4.942	3.618
	85	1554.08	31.59	1142.27	75928.1	0.5933	4.884	3.432
2.726	90	1539.16	35.976	1149.99	74364.7	0.5538	4.826	3.249
	95	1520.13	41.486	1157.71	72782.9	0.5149	4.767	3.195
3.541	100	1501.1	46.996	1165.44	71201	0.4766	4.709	3.14
	105	1477.05	53.811	1173.16	69446.9	0.4388	4.65	3.084
4.529	110	1452.99	60.625	1180.88	67692.7	0.4018	4.592	3.028
	115	1423.5	69.061	1188.6	65993.9	0.3654	4.534	2.963
5.713	120	1394.01	77.496	1196.32	64295.1	0.3297	4.475	2.898
	125	1357.46	88.023	1204.04	62214.8	0.2947	4.417	2.82
7.117	130	1320.9	98.55	1211.77	60134.4	0.2606	4.358	2.742
	135	1276.84	112.068	1219.49	57641.6	0.2274	4.3	2.649
8.771	140	1232.78	125.586	1227.21	55148.8	0.1952	4.242	2.557
	145	1180.24	143.815	1234.93	52059	0.1639	4.183	2.447
10.71	150	1127.69	162.044	1242.65	48969.2	0.1339	4.125	2.337
	155	1065.47	188.631	1250.37	45048.5	0.1051	4.066	2.207
12.96	160	1003.25	215.217	1258.09	41127.7	0.0779	4.008	2.077
	165	930.49	259.178	1265.82	35692.9	0.0525	3.95	1.926
15.58	170	857.72	303.138	1273.54	30258	0.0294	3.891	1.775
	175	714.06	485.117	1281.26	12459.2	0.0097	3.833	1.477
18.17	178.5	613.5	612.502	1286.66	0	0	3.792	1.269

Table A.3: Physical properties of copper at $T = 20\,°C$ according to [73].

property	symbol	value
density	ρ	$8900\,kg\,m^{-3}$
thermal conductivity	λ	$393\,W\,m^{-1}K^{-1}$
spec. heat capacity	c	$390\,J\,kg^{-1}K^{-1}$

Table A.4: Physical properties of CaF_2 at $T = 20\,°C$ according to [74].

property	symbol	value
density	ρ	$3180\,kg\,m^{-3}$
thermal conductivity	λ	$9.71\,W\,m^{-1}K^{-1}$
spec. heat capacity	c	$854\,J\,kg^{-1}K^{-1}$

A.4 Condenser

The necessary condenser length was calculated using a piecewise 2-dimensional calculation, as seen in Figure A.24. The step size is $\Delta l = 0.1\,mm$ and the calculation is stopped once the entire vapor mass flow is condensed. The heat transfer phenomena of the boiling fluid side are calculated using a correlation for local film condensation with co-current vapor flow, which is published in the *VDI-Wärmeatlas* [60]. The heat transfer through the wall is calculated using 1-dimensional Fourier's law. The heat transfer on the silicone oil side is calculated using a correlation for forced convection through an annulus. The silicone oil temperature is assumed constant over the condenser length. It is calculated by averaging the

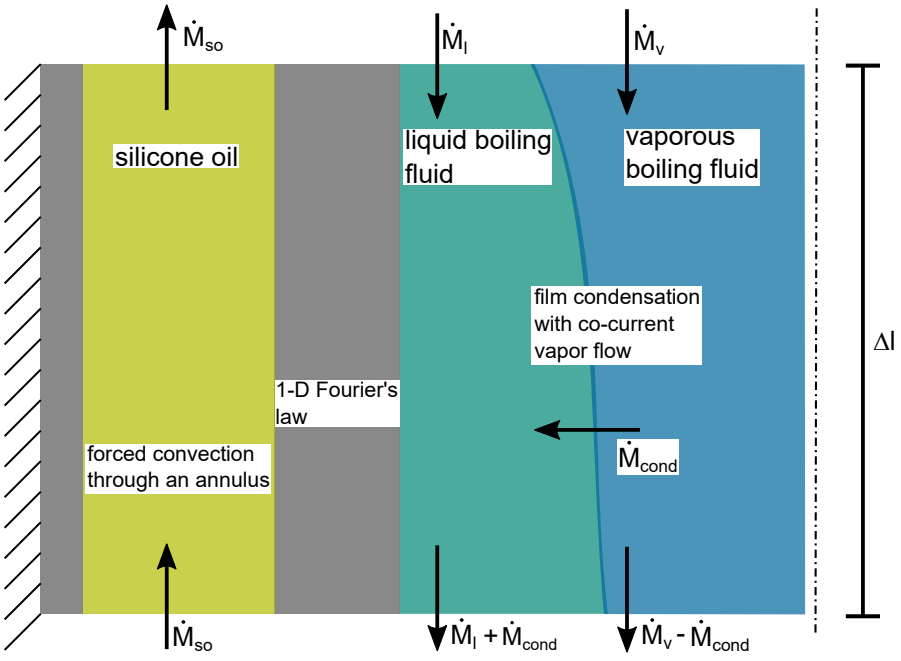

Figure A.24: Sketch of a calculated condenser section.

temperature of the arriving silicone oil and the temperature of the departing silicone oil, which is based on the arrival temperature and the overall removed heat flow. The outside of the shell is assumed to be adiabatic. In order to find the perfect length for the condenser, two extreme cases are evaluated for boiling heat fluxes between 10 and 1000 $kW\,m^{-2}$ using the copper heater:

- water boiling at 30 °C with varying silicone oil temperatures and flowrates,
- FC-72 boiling at 180 °C with varying silicone oil temperatures and flowrates.

A condenser with a total length of 2 m is able to transfer most of the heat fluxes in those two cases. As the physical properties of ethanol are situated between the properties of water and FC-72, the condenser is able to work with ethanol as well. Due to a limited size of the experiment, the condenser consists of two pipes each 1 m long.